INFORMATION TO USERS

This manuscript has been reproduced from the microfilm master. UMI films the text directly from the original or copy submitted. Thus, some thesis and dissertation copies are in typewriter face, while others may be from any type of computer printer.

The quality of this reproduction is dependent upon the quality of the copy submitted. Broken or indistinct print, colored or poor quality illustrations and photographs, print bleedthrough, substandard margins, and improper alignment can adversely affect reproduction.

In the unlikely event that the author did not send UMI a complete manuscript and there are missing pages, these will be noted. Also, if unauthorized copyright material had to be removed, a note will indicate the deletion.

Oversize materials (e.g., maps, drawings, charts) are reproduced by sectioning the original, beginning at the upper left-hand corner and continuing from left to right in equal sections with small overlaps. Each original is also photographed in one exposure and is included in reduced form at the back of the book.

Photographs included in the original manuscript have been reproduced xerographically in this copy. Higher quality 6" x 9" black and white photographic prints are available for any photographs or illustrations appearing in this copy for an additional charge. Contact UMI directly to order.

U·M·I

University Microfilms International
A Bell & Howell Information Company
300 North Zeeb Road, Ann Arbor, MI 48106-1346 USA
313/761-4700 800/521-0600

Order Number 9218271

The application of liquid junctions for characterization of semiconductor materials

Shen, Wu-mian, Ph.D.

City University of New York, 1992

U·M·I
300 N. Zeeb Rd.
Ann Arbor, MI 48106

The Application of Liquid Junctions for Characterization of Semiconductor Materials

by

Wu-mian Shen

A dissertation submitted to the Graduate faculty in Physics in partial fulfillment of the requirements for the degree of Doctor of Philosophy, The City University of New York.

1992

This manuscript has been read and accepted for the Graduate Faculty in Physics in satisfaction of the dissertation requirement for the degree of Doctor of Philosophy.

Sept. 26, 1991
Date

Micha Tomkiewicz
Chair of Examining Committee

Oct 1, 1991
Date

Joseph B. Krieger
Executive Officer

Fred H. Pollak

George Skorinko

Frederick W. Smith

Jeff P. Gambino
Supervisory Committee

The City University of New York

ABSTRACT

The Application of Liquid Junctions for

Characterization of Semiconductor Materials

by

Wu-mian Shen

Advisor: Professor Micha Tomkiewicz

In this study, liquid junctions were used to characterize silicon and silicon subjected to various reactive ion etching (RIE); surface optimization of $CuInSe_2$; and photo-modification of InSe. Impedance spectroscopy and modulation spectroscopies such as electrolyte electroreflectance (EER), photoreflectance (PR), and photoreflectance in the presence of electrolyte (EPR) were the major methodologies that were used for investigating the dielectric properties of the semiconductors and their interface with the ambients. It was shown that the above experimental techniques provide information about the flat-band potential, doping density, Fermi level pinning, the density and distribution of surface states, energy gap and broadening parameter related to the lifetime of majority carriers, etc. The effective medium analysis of the frequency dispersion of the impedance provides the information on the microstructure of the composite at the interface. The analysis of the constant phase angle (CPA) elements reveals the origin of disorder such as diffusion of minority carriers. The change of the line shape of the modulation spectrum provides a sensitive probe for analyzing the tensile strain, the

quality of the crystal, etc. Both techniques can be complementary and cross-checked, which comprise a versatile system of characterization for the dielectric properties of semiconducting materials.

To My Father and Mother

ACKNOWLEDGEMENT

I wish to express my deepest gratitude to Professor Micha Tomkiewicz of Brooklyn College, CUNY, my thesis advisor, for his invaluable guidance and constant encouragement throughout my research. His enthusiasm and creativity in exploring and understanding physics and chemistry will always be an inspiration.

I also would like to express my sincere appreciation to the distinguished members of Supervisory Committee, in particular, to Professor Fred H. Pollak of Brooklyn College, CUNY, for his wonderful lectures and valuable advice during the course of this work. To Professor George Skorinko of Brooklyn College, CUNY, Professor Frederick W. Smith of City College, CUNY, and Dr. Jeff P. Gambino of IBM, I wish to thank them for their careful reading of this manuscript and their helpful advice.

I greatly appreciate Dr. David Cahen of The Weizmann Institute of Science, Israel for providing the $CuInSe_2$ samples; Dr. Claude Levy-Clement of the Laboratoire de Physique des Solides, CNRS, France for providing the InSe samples; and Dr. Jeff P. Gambino of IBM East Fishkill for providing the silicon and various RIE samples. Without the collaboration with the above scientists, it would have been impossible to succeed with my research.

I have been fortunate to have had the opportunity to work closely with two excellent colleagues Dr. Benedict Aurian-Blajeni and Dr. M.C.A. Fantini, former research associates at Brooklyn College. Their team spirit and helpful suggestions

were fortifying.

I wish to acknowledge with sincere gratitude the Department of Physics at Brooklyn College for providing me with this opportunity, the Solar Energy Research Institute and IBM for their support of this work, and NATO for the travelling grant to France.

Finally I am sincerely indebted to Professor Bi-ruo Sun of Shanghai Jiao-tung University for introducing me to this research field and recommending me to Professor Micha Tomkiewicz, and lastly, to my wife, Li-li Yang, for her devoted support and patient sacrifice during the years of my doctoral study.

Wu-mian Shen

Brooklyn, New York

June, 1991

TABLE OF CONTENTS

Chapter 1: Introduction 1

Chapter 2: Theoretical background 8

2.1 Semiconductor-electrolyte junctions 8

2.1.1 Comparison of the liquid junction with Schottky barrier contact 8

2.1.2 Potential distribution 11

Space-charge layer 11

Surface states 15

2.1.3 Photoresponse 17

2.1.4 Generalized equivalent circuit model 24

2.1.5 Effective medium theory 32

2.2 Modulation spectroscopy 38

2.2.1 Dielectric function 39

2.2.2 Modulated reflectivity 43

2.2.3 Third derivative spectra in low field regime 44

2.2.4 Photoreflectance 48

2.2.5 Flat-band determination 51

2.2.6 Fermi level pinning 52

2.2.7 Surface trap states 56

Chapter 3: Experimental techniques 59

3.1 Impedance spectroscopy 59

3.1.1 Impedance measuring setup 60

3.1.2 Extract of the parameters in the equivalent circuit 62

3.2 Modulation spectroscopy 68

3.2.1 Universal workstation for optical characterization 68

3.2.2 Experimental detail of modulation spectroscopy 71

3.3 Dark and photo I-V 73

3.4 Sample preparation and experimental cell 74

3.4.1 Silicon 74

3.4.2 $CuInSe_2$ 77

3.4.3 InSe 79

Chapter 4: Silicon and its reactive ion etching 81

4.1 Potential distribution of silicon/methanol interface 81

4.1.1 Photo and dark I-V 81

4.1.2 Electroreflectance 84

4.1.3 Impedance 89

4.1.4 Proposed band diagram of Si/methanol system 95

4.2 The effect of media on photoreflectance 97

4.2.1 Low-field limit of PR and EER 97

4.2.2 Effect of electrolyte on line shape of modulation spectrum 101

4.2.3 Effect of electrolyte on relaxation time of surface states 105

4.2.4 summary 107

4.3 Characterization of the damage of Si due to RIE 108

4.3.1 Modulation spectra of Si subjected to various RIE 108

4.3.2 Impedance spectra of Si subjected to various RIE 116

4.3.3 The effect of the damage due to RIE 124

4.3.4 Damage profile analysis 135

4.4 Comparison of the liquid junction with solid-state devices 142

4.4.1 Experimental results of Schottky barrier (SB) devices 143

4.4.2 Experimental results of metal-oxide-semiconductor (MOS) devices 153

4.4.3 Comparison of SB with liquid junction 159

4.4.4 Comparison of MOS devices with liquid junction 163

Chapter 5: Surface optimization of n-$CuInSe_2$ 166

5.1 Experimental results 166

5.1.1 Photoelectrochemical performance characteristics 166

5.1.2 Electrolyte electroreflectance (EER) 166

5.1.3 Impedance 176

5.2 Discussion 185

5.2.1 Effects of chemical etching 185

5.2.2 Effects of air oxidation 189

5.2.3 Nature of oxidized layer 193

5.2.4 Effective medium description of oxidized layer-electrolyte composite 197

5.2.5 Potential distribution of $CuInSe_2$/polyiodide system 200

Chapter 6: n-InSe and its photo-modification 202

6.1 Experimental results 202

6.1.1 Photoreflectance 202

6.1.2 Impedance 206

6.2 Discussion 212

6.2.1 Effects of photo-modification 212

6.2.2 Origin of the CPA element 214

6.2.3 Potential distribution of InSe- and modified InSe-polyiodide system 217

6.2.4 The characteristics of modified layer $CuISe_3$ 217

Chapter 7: Conclusions and future work 221

7.1 Conclusions 221

7.1.1 Silicon and silicon subjected to various RIE 222

7.1.2 $CuInSe_2$ and its surface optimization 224

7.1.3 InSe and its photo-modification 225

7.2 Future work 226

Appendix: Publications related to the thesis 228

Bibliography 230

LIST OF TABLES

Table I. Energy gaps and linewidth parameters of PR of Si and various RIE samples at 77 K. 112

Table II. Energy gaps and linewidth parameters of PR of Si and various RIE samples at 300 K. 112

Table III. Energy gaps and linewidth parameters of EER and EPR of Si and various RIE samples at 300 K. 113

Table IV. Flat-band potential V_{fb} obtained from the electroreflectance measurements of Si and various RIE samples. 119

Table V. Flat-band potential V_{fb} and doping density N_d obtained from the impedance measurements of Si and various RIE samples. 123

Table VI. Short-circuit current density J_{sc} and open-circuit voltage V_{oc} of Si and various RIE samples in methanolic electrolyte for a light intensity of 100 mW/cm^2. 123

Table VII. Tensile strain and elastic compliance constant parameters for Si subjected to various RIE treatments. 127

Table VIII. Thickness of the residue layer l_1 and silicon damaged region l_2. 132

Table IX. Density of electrolyte molecules adsorbed in the substrate surface N_H and density of surface states N_3. Relaxation time τ_H related to N_H and relaxation time τ_3 related to N_3 at zero potential. 136

Table X. Built-in potential V_{bi}, doping density N_D, energy difference

between the bottom of the conduction band and the Fermi level V_n, barrier height V_{bn}, and series resistance R_s obtained from the impedance measurements of the SB samples. 148

Table XI. Diode ideality factor n, saturation current density J_{st}, barrier height V_{bn}, and shunt resistance R_{sh}, calculated based on the impedance results and thermionic emission theory for the SB devices. 150

Table XII. Diode ideality factor n, saturation current density J_{st}, barrier height V_{bn}, and series resistance R_s, calculated based on the current-voltage results and thermionic emission theory for the SB devices. 152

Table XIII. Fitting parameters for the photoreflectance of SB. E_1 is the energy gap and Γ_1 the phenomenological broadening parameter related to the lifetime of the majority carriers. 154

Table XIV. Built-in potential V_{bi}, doping density N_D, and thickness of the oxide layer l_o of the MOS samples. SCL denotes space-charge layer. 157

Table XV. Fitting parameters for electroreflectance and photoreflectance of the bare and MOS samples. 159

LIST OF FIGURES

Figure 2.1 Energy level diagram for semiconductor-electrolyte junction showing the relations between the electrolyte redox couple (H^+/H_2), the Helmholtz layer potential drop (V_H), and the semiconductor band gap (E_g), electron affinity (χ), work function (ϕ_{sc}), band bending (V_b), and flat-band potential (V_{fb}). The electrochemical and solid state energy scales are shown for comparisons; ϕ_{el} is the electrolyte work function [6]. 9

Figure 2.2 The generalized equivalent circuit of a single interface. R_p is the resistance associated with the Faradaic current flow, Z_d is a generalized impedance associated with disorder either in the structure or in the dynamic (diffusion), C_i and R_i are associated with parallel charge accumulation modes with different relaxation times than the majority carriers such as surface states or minority carriers, C_{sc} is the space-charge capacitance, and R_s is the series resistance. 30

Figure 2.3 The basic microstructure build-up process in the differential effective medium theory [90]. 37

Figure 2.4 The schematic representation of modulation field due to chopped laser beam in PR. 57

Figure 3.1 The experimental setup of the impedance spectroscopy. 61

Figure 3.2 The experimental arrangement of the modulation spectroscopy. 70

Figure 3.3 The experimental arrangement for measuring the surface photovoltage and spectral response. 71

Figure 4.1 Current-potential response with chopped white light for unetched <100> n-Si in methanolic solution of oxidized and reduced dimethylferrocene in the following concentrations: 0.2M $FeCp_2$, 1mM $FeCp_2^+$, and 1M $LiClO_4$ supporting electrolyte. Tungsten halogen ELH lamp with light intensity at the electrode surface of 100 mW/cm^2. The sweep rate is 10 mV/s. 81

Figure 4.2 Current-potential curves of two samples: one original and the other subjected to HF etching process. (a) Photoresponse of HF etched Si, (b) of unetched Si, and (c) dark response of both samples. Electrolyte and other experimental conditions are the same as in Fig. 4.1. Photovoltaic parameters extracted from these curves: J_{sc} = 12.4 mA/cm^2 and V_{oc} = -0.503 V (original); J_{sc} = 16.3 mA/cm^2; and V_{oc} = -0.519V (after HF etching). 82

Figure 4.3 Dark current-potential plot of the original sample in the methanolic solution of the same composition as described in Fig. 4.1. The calculated charge density associated with the peak is shown on the figure. 83

Figure 4.4 Electroreflectance spectra of HF etched Si in the same electrolyte as in Fig. 4.1 except for the dimethylferrocenes that were diluted by a factor of 20, as a function of the electrode potential vs Pt.

The modulation amplitude is 0.15 V_{pp} and the modulation frequency is 740 Hz. 84

Figure 4.5 Comparison of observed (points) and calculated (solid line) line shape of the spectrum at 0.0 V vs Pt. Fitting parameters: C= $6.4X10^6$; E_g = 3.407 eV; Γ = 0.17 eV; θ = 4.18 rad; and n = 3.0. 85

Figure 4.6 Variation of the amplitudes of the 3.4 eV EER peaks with the electrode potential: (a) after HF etching and (b) before etching. The potential sweep rate was 5 min. per experimental point. The lines are drawn for convenience of inspection. The arrows indicate the direction of the potential sweep. 86

Figure 4.7 The same as Fig. 4.6 but with the aqueous electrolyte with the following composition: 0.25M NH_4F/0.01M $K_3Fe(CN)_6$/ 0.01M $K_4Fe(CN)_6/H_2O$. 87

Figure 4.8 Impedance response curves for HF etched n-Si in the methanolic solution with the same composition as described in Fig. 4.1. Potential is -0.2 V vs Pt. The symbols represent experimental data for the real and imaginary parts of the impedance. The solid lines represent numerical fits to the equivalent circuit shown in the left-hand corner. 89

Figure 4.9 Mott-Schottky plots of n-Si in the methanolic solution described in Fig. 4.1. (a) HF etched sample. V_{fb} = -0.76 V vs Pt and

N_d = 4.7X10^{15}/cm^3. (b) Original sample. V_{fb} = -0.86 V vs Pt and N_d = 2.2X10^{15}/cm^3. 91

Figure 4.10 Mott-Schottky plots of n-Si in the aqueous electrolyte described in Fig.4.7. V_{fb} = -0.79 V vs Pt and N_d = 2.3X10^{15}/cm^3. 92

Figure 4.11 Potential dependence of C_H of the HF etched sample. The ordinate depicts the charge density/eV. 93

Figure 4.12 The potential dependence of *n* [Eq. (2.70)] of the HF etched sample. 95

Figure 4.13 The proposed band-structure diagram of the Si/methanol in this work. 96

Figure 4.14 Comparison of observed (points) and calculated (solid line) line shape of the PR spectra of n-Si at 77K. Modulation source: 7.5 mW He-Ne laser; modulation frequency: 750 Hz. Fitting parameters: in the E_1 region: E_g = 3.489 eV, Γ = 0.087 eV; in the E_2 region: $E_g(1)$ = 4.382 eV, $\Gamma(1)$ = 0.135 eV; $E_g(2)$ = 4.786 eV, $\Gamma(2)$ = 0.347 eV. 98

Figure 4.15 Dependence of the PR signal of n-Si on the light intensity of the modulated beam. 100

Figure 4.16 Comparison between PR, EPR, and EER of n-Si. The EPR and the EER were measured in the methanolic solution of oxidized and reduced dimethylferrocene in the following concentrations: 0.01M $FeCp_2$, 50μM $FeCp_2^+$, and 1M $LiClO_4$ supporting

electrolyte. The EPR was measured under open-circuit conditions and the EER at a potential of 0.0 V vs Pt. The chopping frequency in all cases is 750 Hz. 101

Figure 4.17 Comparison of the EER of n-Si in two different electrolytes: The same methanolic solution as in Fig.4.16 (solid line) and an aqueous electrolyte (open diamonds) with the same composition as in Fig. 4.7. The experimental conditions are the same as in Fig.4.16. 102

Figure 4.18 Comparison of the EPR spectra of the n-Si in (a) methanol and (b) the methanolic solution. Experimental conditions are the same as in Fig. 4.16. 103

Figure 4.19 The EPR of n-Si in the methanolic solution at different electrode potential. The spectra are normalized for the same amplitude. 104

Figure 4.20 The potential dependence of the amplitude of the EPR peak of n-Si in the methanolic solution. Arrows indicate the direction of the sweep. 105

Figure 4.21 EPR spectra of n-Si in the methanolic solution at two different chopping frequencies. 106

Figure 4.22 Comparison of the frequency dispersion of PR and EPR of n-Si in the methanolic solution and the theoretical fit of the EPR results to Eq.(2.162) with the following parameters: τ_1 = 0.5 ms, τ_2 = 6.5 ms, and the ratio of the two coefficients is 0.65. 107

Figure 4.23 Photoreflectance spectra of n-Si subjected to various RIE

	treatments. Temperature 77K. The modulation source is 7.5 mW He-Ne laser; modulation frequency is 750 Hz.	109
Figure 4.24	The same as Fig. 4.23 over an expanded energy scale.	109
Figure 4.25	(a) Comparison of observed and calculated E_1 line shape of the PR at 300K of the CF_4 RIE-treated n-Si. (b) The same as (a) for the E_2 region.	111
Figure 4.26	Comparison of the PR of n-Si at 77K and 300K. Same conditions as in Fig.4.14. The spectra are normalized for the same amplitude.	114
Figure 4.27	Comparison of the PR of CHF_3/Ar RIE-treated n-Si at 77K and 300K.	114
Figure 4.28	Comparison between PR, EPR, and EER for the CHF_3/Ar RIE-treated n-Si. The EPR and the EER were measured in the same methanolic solution as in Fig. 4.16.	115
Figure 4.29	The same as Fig. 4.28 for the $CClF_3/H_2$ RIE-treated n-Si.	115
Figure 4.30	Comparison of the frequency dispersion of PR and EPR of CHF_3/Ar RIE-treated n-Si in the methanolic solution.	117
Figure 4.31	Variation of the amplitude of the 3.4 eV EER peak with electrode potential for (a) untreated n-Si, (b) CHF_3/Ar, and (c) $CClF_3/H_2$, RIE-treated samples. The spectra were taken in the methanolic solution that was previously described.	117
Figure 4.32	(a) Bias dependence of the electroreflectance of the $CClF_3/H_2$ RIE sample. (b) Bias dependence of electroreflectance of the	

$CClF_3/H_2$ + O_2 ash sample. (c) Bias dependence of the electro-reflectance of the O_2 ash sample. 118

Figure 4.33 Impedance spectrum at -0.4V vs Pt of (a) CHF_3/Ar RIE and (b) $CClF_3/H_2$ RIE + O_2 ash. The equivalent circuits which represent the measured data are shown in the inserts. (□): Re(Z), (○): Im(Z), solid lines: theoretical fits to the proposed equivalent circuit with appropriate values of the elements that are summarized in subsequent figures. 120

Figure 4.34 Mott-Schottky plots of (a) original, (b) CHF_3/Ar RIE, and (c) CF_4 RIE samples. 121

Figure 4.35 Mott-Schottky plots of (a) $CClF_3/H_2$ RIE, (b) $CClF_3/H_2$ RIE + O_2 ash, and (c) O_2 ash samples. 122

Figure 4.36 The PR of CHF_3/Ar RIE-treated n-Si (points) and of a sample that was cleaned with a second RCA etch following the RIE treatment (solid line). 128

Figure 4.37 EPR at three different wavelength of the modulated beam for the CF_4 RIE-treated n-Si. (a) 4131 Å from Kr-ion laser; (b) 4880 Å from Ar-ion laser; and (c) 6328 Å from He-Ne laser. The spectra are normalized for the same amplitude. 129

Figure 4.38 Bias dependence of the exponent n of the CPA element. (a) $CClF_3/H_2$ RIE, (b) $CClF_3/H_2$ RIE +O_2 ash, and (c) O_2 ash. 134

Figure 4.39 (a) Short-circuit current density vs etching time in a buffered HF

solution for CHF_3/Ar RIE (1) and CF_4 RIE (2) samples.
(b) Open-circuit voltage vs etching time in a buffered HF solution for the same samples. 137

Figure 4.40 The same as Fig. 4.39 for etching with the KOH solution. 137

Figure 4.41 Forward sweep of chopped-light-induced photocurrent of (a) original Si substrate. (b) CHF_3/Ar RIE sample after etching process in the KOH solution. (c) CF_4 RIE sample after etching process in the KOH solution. Sweep rate = 10 mV/s. 139

Figure 4.42 Current density vs time during photoetching: (a) CHF_3/Ar RIE and (b) CF_4 RIE. 140

Figure 4.43 (a) Spectra of the real and imaginary parts of the impedance at 0 V of Ti/SB with untreated (control) Si sample. The equivalent circuit that represents the measured data is shown in the inset. The solid lines represent the theoretical fits to the equivalent circuit. (b) The same as (a) for the CHF_3/Ar RIE Ti/SB sample at 0 V. 144

Figure 4.44 (a) The same as Fig. 4.43 (a) for the Al/SB sample at 0 V. (b) The same as (a) for the $CClF_3$/H_2 RIE Al/SB sample. 145

Figure 4.45 The same as Fig. 4.43 (b) at 0.2 V. 146

Figure 4.46 Mott-Schottky plot of the space-charge layer capacitance of (a) the original Ti/SB sample, (b) the CHF_3/Ar RIE Ti/SB sample, and (c) the CF_4 RIE Ti/SB sample. 147

Figure 4.47 Mott-Schottky plot of the space-charge layer capacitance of (a) the original Al/SB sample, (b) the $CClF_3/H_2$ RIE Al/SB sample, and (c) the $CClF_3/H_2$ RIE $+O_2$ ash, Al/SB sample. 147

Figure 4.48 ln R_{sc} vs bias voltage for (a) the original Ti/SB, (b) the CHF_3/Ar RIE Ti/SB, and (c) the CF_4 RIE Ti/SB. 149

Figure 4.49 (a) The same as Fig. 4.48 (a) for the original Al/SB. (b) The same as (a) for the $CClF_3/H_2$ RIE Al/SB. (c) The same as (a) for the $CClF_3/H_2$ RIE $+O_2$ ash Al/SB. 149

Figure 4.50 (a) Current density vs voltage characteristics of the Ti/SB devices: (1) original, (2) CHF_3/Ar RIE, and (3) CF_4 RIE. (b) The same as (a) for the Al/SB devices: (1) original, (2) $CClF_3/H_2$ RIE, and (3) $CClF_3/H_2$ RIE + O_2 ash. 151

Figure 4.51 Current density vs voltage characteristics in the forward-bias region (+) and the theoretical fit to Eq.(4.4) (solid line) for (a) CHF_3/Ar RIE Ti/SB, and (b) $CClF_3/H_2$ RIE Al/SB. 151

Figure 4.52 Photoreflectance spectra of (a) bare Si (1) and untreated Ti/SB (2); (b) bare $CClF_3/H_2$ RIE Si (1) and $CClF_3/H_2$ RIE Al/SB (2); (c) Ti/SB devices with untreated Si (1), $CClF_3/H_2$ RIE (2), and O_2 ash (3). 153

Figure 4.53 Impedance spectra of MOS device with untreated Si at -0.5 V. The equivalent circuit is shown in the inset with the theoretical fits to this circuit (solid lines). 154

Figure 4.54 High-frequency capacitance C vs voltage for MOS devices with (1) untreated Si, (2) CHF_3/Ar RIE, and (3) CF_4 RIE. 155

Figure 4.55 The voltage dependence of the oxide layer capacitance, C_o, (a), and the space-charge layer capacitance, C_{sc}, (b), of the MOS device with the untreated Si. 156

Figure 4.56 Mott-Schottky plot of C_{sc} of (a) the untreated MOS sample, (b) the CHF_3/Ar RIE MOS sample, and (c) the CF_4 RIE MOS sample. 157

Figure 4.57 Electroreflectance (ER) spectra of (a) a MOS device with untreated Si, (b) a CHF_3/Ar RIE MOS sample, and (c) a CF_4 RIE MOS sample, and photoreflectance (PR) spectra of bare Si. 158

Figure 5.1 Current-potential response curves with chopped white light for n-$CuInSe_2$ in polyiodide solution with the following composition: 6M KI + 0.1M CuI_2 + 0.1M InI_3 + 0.0125M I_2 at pH 6.0. W/X source with intensity of 100 mW/cm^2. Etching in 2% Br_2/ methanol solution for 60s. Oxidation for 2h at 150°C in air. 167

Figure 5.2 EER spectra of n-$CuInSe_2$ in 1/1/1M aqueous polysulfide as function of electrode potential vs Pt. Modulation amplitude: 0.20 V. 168

Figure 5.3 EER spectra of n-$CuInSe_2$ in aqueous polyiodide with the same composition in Fig. 5.1. 169

Figure 5.4 Variation of the amplitude of peak A from Fig. 5.2 with the

electrode potential, before etching. 170

Figure 5.5 Variation of the amplitude of the three EER peaks in Fig. 5.2 with electrode potential after etching in Br_2/methanol and wash in 10% KCN. 171

Figure 5.6 Variation of the amplitude of the low energy EER peak from Fig. 5.3 with electrode potential, before (solid line) and after (broken line) etching. 172

Figure 5.7 EER spectra of n-$CuInSe_2$ in aqueous polyiodide with the same composition as in Fig. 5.1 after oxidation for 1.5h at 150°C. 173

Figure 5.8 Comparison of EER spectra of n-$CuInSe_2$ in aqueous polyiodide. Top: With a layer of indium oxide; potential = -0.245V vs Pt; modulation = 2.25 V_{p-p}. Middle: After oxidation for 1.5h at 150°C; potential = -0.2V vs Pt; modulation = 0.4 V_{p-p}. Bottom: As received; potential = -0.2V vs Pt; modulation = 0.2 V_{p-p}. 174

Figure 5.9 The amplitude of peak A from Fig. 5.2 as a function of the modulation amplitude. 175

Figure 5.10 Comparison of observed and calculated line shape of peak A in Fig. 5.2. Potential = -0.2V vs Pt. 175

Figure 5.11 Impedance response curves for n-$CuInSe_2$ in polyiodide solution with the same composition as in Fig. 5.1. In the right-hand corner is the equivalent circuit constructed in the manner explained in the text. 177

Figure 5.12 Mott-Schottky plots of C_{sc} (curve 1) and C_1 (curve 2). The data for C_{sc} were taken from the high frequency response of spectra like the one presented in Fig. 5.11. The data for C_1 were taken from the high frequency peak of the imaginary part in a response like the one shown in Fig. 5.14. 178

Figure 5.13 Variation of C_{ss}, taken from response curves like the one shown in Fig. 5.11, with electrode potential. The solid line is a theoretical fit to superposition of two Gaussian line shapes. 179

Figure 5.14 The impedance spectra of the n-$CuInSe_2$ crystal after heating in air for 1h at 150°C. In the right-hand corner is the equivalent circuit constructed as a reference point in a manner explained in the text. The full line is a theoretical fit to this equivalent circuit, based on Eq. (5.1). The parameters of the equivalent circuit were adjusted to fit only the imaginary part. 180

Figure 5.15 Impedance response curve of the surface-oxidized, n-$CuInSe_2$ with Ag front contact without electrolyte, prepared after heating the etched semiconductor in air for 2h at 150°C. 183

Figure 5.16 Mott-Schottky plot of the capacitance taken from the high frequency part of the low frequency peak of the imaginary part in the impedance response like the one shown in Fig. 5.14. Electrode area is 0.045 cm^2. 183

Figure 5.17 Mott-Schottky plot of capacitance taken from the high frequency

response of spectra like the one presented in Fig. 5.15. The voltage is applied between the back and the front contacts of the solid-state device. Electrode area is 0.020 cm^2. 184

Figure 5.18 Dark I-V characteristics of the n-$CuInSe_2$ solid-state junction without electrolyte, after heating in air for 2h at 150°C. The insert represents the arrangement of the electrode. 185

Figure 5.19 Plot of P/(1-P) vs potential U for untreated $CuInSe_2$. 187

Figure 5.20 Comparison of experiment (dotted line) and theory (solid line) for the light induced current-voltage characteristics of etched n-$CuInSe_2$ in the same electrolyte as in Fig. 5.1. The theoretical curve was calculated by using Eq. (5.2) in the manner explained in the text. 190

Figure 5.21 The same fit between theory and experiment as the one shown in Fig. 5.20, but for the oxidized $CuInSe_2$ crystal. Curve 1 shows the behavior with the same parameters as the one found for etched crystal except for the effective doping level, which was taken from the data in Fig. 5.12 to be $7.5X10^{15}cm^{-3}$. Curve 2 was calculated by using the same parameters but with no surface recombination. 191

Figure 5.22 Electron beam-induced current traces across the cleaved junction of an n-$CuInSe_2$/oxidized surface layer + oxidized In/Ti device. The right-hand part shows the region directly below that shown

on the left-hand side. Each side shows a ca. 25 μm length of the junction. Beam voltage: 10 kV; beam current: 15 pA. Junction region: Ti on the right; the junction stretches from the Ti, through the In(ox) into the $CuInSe_2$. 196

Figure 5.23 The impedance spectra of n-$CuInSe_2$, after heating in air for 1h at 150°C, in polyiodide solution with the same composition as in Fig. 5.1. Solid circles represent experimental points and circles represent theoretical results based on Eq. (5.5) and (5.8). 199

Figure 5.24 The band structure diagrams of n-$CuInSe_2$ in polyiodide solution before and after heating in air. 201

Figure 6.1 Photoreflectance spectrum of n-InSe in the low energy range and a theoretical fit to the line-shape function. Modulation source -- 6328 Å He-Ne laser; modulation frequency -- 517 Hz. Fitting parameters: E_{ex} = 1.196 eV, Γ_{ex} = 0.033 eV; E_g = 1.238 eV, Γ = 0.016 eV. 203

Figure 6.2 Comparison of PR of n-InSe and photomodified InSe after treatment in the polyiodide electrolyte containing Cu^+ with different modification time. a) n-InSe; b) modified InSe with modified time of 10 min.; c) modified InSe with modified time of 20 min. Same conditions as in Fig. 6.1. 203

Figure 6.3 PR of photomodified n-InSe at different wavelengths of the modulated beam. a) 6328 Å from He-Ne laser, and b) 6764 Å from

Kr ion laser. The spectra are normalized for the same amplitude. 204

Figure 6.4 Photoreflectance spectra of a) InSe and b) photomodified InSe; in the high energy range, and the theoretical fit (solid line) of the line-shape of the spectrum of the modified InSe. Modulation source -- 4067 Å Kr ion laser; modulation frequency -- 516 Hz. Fitting parameters: E_g = 1.93 eV; Γ = 0.221 eV. 205

Figure 6.5 The impedance spectra of n-InSe in the electrolyte: 1M KI/ 0.05M I_2/2M H_2SO_4 at potential of a) -0.1 V vs Pt, and b) +0.3V vs Pt. Electrode area is 0.12 cm^2. The solid lines are the theoretical fit to the equivalent circuit shown in the insert. 207

Figure 6.6 The impedance spectra of modified InSe in the same electrolyte as in Fig. 6.5 at potential of -0.05 V vs Pt. Electrode area is 0.257 cm^2. The solid lines are theoretical fits to the equivalent circuit shown in the insert. 208

Figure 6.7 Mott-Schottky plots of C_{sc} for a) InSe and b) modified InSe. 208

Figure 6.8 G_{ss}/ω and B_{ss} spectra of n-InSe in the same electrolyte as in Fig. 6.5. Electrode potential: 0 V vs Pt. The capacitive and resistive elements of the surface states are evaluated from the amplitude and the position of the peak. 209

Figure 6.9 Variation of C_{ss1} of the slow surface states, with electrode potential for a) n-InSe and b) modified InSe. The solid lines are theoretical fits to Gaussian line shapes. 210

Figure 6.10 Variation of C_{ss2} of the fast surface states, with electrode potential for n-InSe. Fast surface states of the modified InSe electrode were not observed. The solid line is a theoretical fit to a Gaussian line shape. 210

Figure 6.11 Variation of the CPA parameter N with the electrode potential for n-InSe (circles) and modified InSe (squares). The solid lines are the theoretical fits to Eq. (6.3). 214

Figure 6.12 The band structure diagrams of n-InSe and modified InSe in polyiodide solution. 218

CHAPTER 1

INTRODUCTION

The development of a new material technology for electronic and photovoltaic devices is often hindered by the lack of rapid quantitative techniques for determining the quality of the semiconductor as a function of growth parameters, doping levels and device processing procedures [1]. The evaluation of many bulk properties requires the presence of some sort of junction that will establish a strong electric field at the interface. The topology of many semiconductor surfaces is such that it is very difficult, if not impossible, to establish solid state junctions. In addition, even if construction of a solid state junction is feasible, it requires the additional surface preparation that can alter the surface situation of as-received samples. Also, it is extremely inconvenient for on-line diagnostic measurements [2]. It is attractive to search a technique to build up a junction conveniently and effectively for characterization of semiconductor materials.

The first studies of photoelectrochemistry were performed by Edmond Becquerel in 1839 [3], who observed that a voltage and an electric current were produced when a silver chloride electrode, immersed in an electrolyte and connected to a counter electrode, was illuminated. Brattain and Garrett [4] showed the rectifying properties of the semiconductor/electrolyte junctions in 1954. The major expansion of scientific interest in photoelectrochemistry occurred after Fujishima and Honda [5] studied the photo-electrolysis of water by TiO_2

photoanodes in 1972. Immediately following that work, the need to find an alternative fuel source rekindled interest in solar energy. As a result, the behavior of a variety of semiconducting materials had been investigated in contact with numerous electrolyte systems, and photoelcetrochemistry was formed as a separate discipline [6-11].

An electrolyte provides a convenient and reversible junction medium to form rectifying contact. It is necessary only to immerse a semiconductor into an electrolyte, perform the measurement, remove the sample from the liquid for cleaning or treatment, and return it again for measurements, etc. and, thus, liquid junctions can be used as an extremely versatile on-line characterization environment. The electrolytes are generally transparent to photons over a large energy range, therefore, the optical techniques based on effects induced by illumination are especially easy to perform. The interfacial chemistry of the liquid junctions can be modified and the transport and optical properties can be monitored in a non-destructive way.

Since bulk properties should be independent of the nature of the ambient, the liquid junction characterization should be compatible with solid state junctions. This is not the case for surface properties. Every conceivable parameter of the surface is influenced by the ambient. Since this is a problem with any junction technology that is being used for characterization purpose, a way must be found to correlate the surface properties at different ambients. In this study, we will try to investigate the correlation of characterization results using the same technique

with different media.

The liquid junctions will be used to study the following materials in this study:

1] n-Si and Si subjected to reactive ion etching.

Silicon is the most studied semiconducting material to date. The small indirect gap and the low electronegativity of Si make a detailed analysis of Si based devices by dielectric techniques among the most difficult of the conventional semiconductors. Yet, in terms of applications, both in photovoltaic and electronics, Si is without a significant rival.

The main problem for photoelectrochemical application of n-Si in aqueous media is the photoelectrochemical corrosion or passivation. The formation and continuous growth of the oxide layer suppress the charge transfer at the interface.

Recently, solar conversion efficiencies that exceed 14% were reported for n-Si in methanolic solutions of ferrocene/ferricenium with $LiClO_4$ as the supporting electrolyte [12-15]. These cells were reported to be stable therefore offering perhaps the best argument in favor of the competitiveness of liquid junction solar cells in comparison with their solid state counterparts. The mechanistic aspects of these cells were investigated primarily through a detailed analysis of their current-voltage characteristics. However, the study of the potential distribution of the n-Si/ methanol system will provide a clearer picture and understanding for the mechanism of the improved current-voltage performance.

Reactive ion etching (RIE) is the key factor in the race to shrink feature

sizes and to increase the scale of integration in very large scale integration (VLSI) circuit fabrication. Since the late 1970's, the conventional wet etching processes have been replaced by RIE. In the reactive ion etching, energetic positive ions produced by plasma are accelerated to remove material by physical sputtering. The chemically active species react with the material at the surface, which results in desired directionality and selectivity. Unfortunately, RIE introduces modifications near the silicon surface, which are reported to include: (1) residue film formation due to etching species deposition; (2) incorporation of impurities due to implanted plasma ions; (3) high degree of disorder due to intrinsic bonding damage [16-21]. As a result, devices fabricated on reactive ion etched silicon have often degraded electrical characteristics. Convenient methods for measuring the damage are highly desirable. Many analytical techniques, such as reflection high-energy electron diffraction (RHEED), Rutherford back-scattering (RBS), Auger electron spectroscopy (AES), x-ray photoelectron emission spectroscopy (XPS), Raman scattering, transmission electron microscopy (TEM), secondary ion mass spectroscopy (SIMS), deep level transient spectroscopy (DLTS), thermal waves (TW), and ellipsometry, have been used to determine the depth of damage, structure of the damage, and the chemistry of the implanted impurities. For a "routine" characterization of the electrical properties, metal-oxide-semiconductor (MOS) capacitors or Schottky barrier (SB) diodes are often used [18-19]. However, the fabrication of MOS capacitors and Schottky diodes alter the as-etched surface.

In this study, the liquid junction between Si and methanol is used for

screening and understanding the damage inflicted on Si during reactive ion etching. The dielectric properties of liquid junctions are compared with that of solid state junctions, such as SB and MOS devices.

2] $CuInSe_2$

Single crystal and thin film solar cells based on $CuInSe_2$ show appreciable energy conversion efficiency (>10%) and impressive stability [22-24]. These attractive features have prompted more extensive investigations [25], which were extended to include liquid junction photoelectrochemical cells [26]. It was reported that efficient and stable photoelectrochemical solar cells could be made using n-$CuInSe_2$ as the photoanode in contact with an aqueous electrolyte [26-44]. Particularly impressive results were reported in polyiodide solutions [32-43].

It was reported that there are two main approaches to improve the performance of the cells considerably. One is that, in acidic electrolyte, Se layer forms on the surface, which reacts with the electrolyte to generate a polycrystalline $CuISe_3$-Se interphase that forms a stable and efficient heterojunction with the substrate. Post-growth air annealing leads to the formation of restructured interphase comprising CuI, InI_3, and $CuISe_3$, which can convert to the quaternary compound, $CuIn_2ISe_3$, when exposed to the electrolyte. $CuIn_2ISe_3$, along with $CuISe_3$, raises efficiency and further increases stability. This type of photoelectrochemical surface modification can be extended to other systems such as InSe that will be discussed later.

The second approach for improving performance is that the surface was

optimized through air oxidation, which consisted mainly of indium oxide, and the optimized surface was used in a near-neutral electrolyte.

The dramatic effects of the surface modification stimulate the interest in studying the mechanism of light-induced charge separation across a chemically modified interface. For modified interfaces that amount to less than a monolayer, the electric field, which serves as the driving force for the light-induced charge separation process, is located at the solid-electrolyte interface thereby allowing the system to retain its photoelectrochemical character. On the other hand, if the modified interface constitutes a separate phase, with thickness that is considerably larger than a tunneling length, the location of the space-charge layer is less obvious, and an uncertainty persists whether the space-charge layer is at the solid-electrolyte interface or, alternatively, between two solid phases, in which case the system can be described best as a solid-state photovoltaic device, connected in series to an electrochemical cell.

In this study, the nature of charge accumulation and transfer at the interface between n-$CuInSe_2$ and aqueous electrolyte is investigated. The changes at the interface induced by surface optimization were characterized and these changes were correlated with the improvements in performance characteristics.

3] InSe

n-InSe reacts under illumination in a similar way to $CuInSe_2$ when placed in acidic copper-polyiodide solutions [45-48], since Se is also the main photocorrosion product of InSe. After modification, the photoelectrochemical response

is improved. The modified n-InSe photoelectrode shows improved stability (~ 1 hour) in contrast to $CuInSe_2$ that exhibits a truly long term stability. It is of significance to characterize the modified layer and elucidate the mechanism for the observed improvements in performance. Since InSe is a lamellar, two dimensional compound, the comparison of the behavior of $CuInSe_2$ and InSe to the same type of surface chemistry provides the unique opportunity to study the effects of dimensionality on the interfacial chemistry.

In this study, photoreflectance and impedance spectroscopies were used to characterize the InSe and modified InSe, aimed at elucidating the mechanism for the observed improvements in the photoelectrochemical response due to photo-modification.

CHAPTER 2

THEORETICAL BACKGROUND

2.1 Semiconductor-electrolyte junctions

When a semiconductor is immersed in an electrolyte, a semiconductor-electrolyte junction is formed. The junction is characterized by the presence of a space charge layer in the semiconductor adjacent to the interface with the electrolyte. A space charge layer generally develops in a semiconductor upon contact and equilibration with a second phase whenever the initial electrochemical potential of electrons is different in the two phases. For semiconductors, the electrochemical potential of electrons is given by the Fermi level in the semiconductor. For liquid electrolytes, the electrochemical potential of electrons is determined by the redox potential of the redox couples present in the electrolyte [6,49].

2.1.1 Comparison of the liquid junction with Schottky barrier contact

From a phenomenological point of view, the behaviors of solid Schottky barrier contact and the liquid junction appear to be similar. The main difference is in the conduction mechanism. In metals, the conduction is due to electrons; while in liquids the charge carriers are ions.

Figure 1 illustrates the diagram of energy levels for semiconductor-electrolyte junctions.

Compared with the solid Schottky barrier, the charge separating processes on the solution side exhibit unique features not known in solids. Among them:

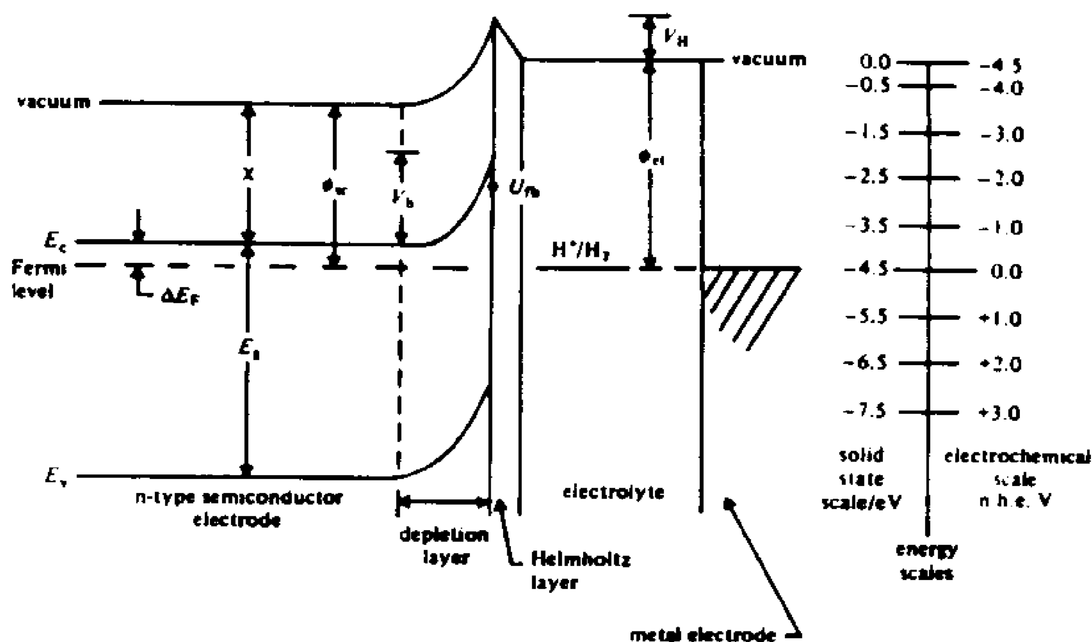

Figure 2.1 **Energy level diagram for semiconductor-electrolyte junction showing the relations between the electrolyte redox couple (H^+/H_2), the Helmholtz layer potential drop (V_H), and the semiconductor band gap (E_g), electron affinity (χ), work function (ϕ_{sc}), band bending (V_b), and flat-band potential (V_{fb}). The electrochemical and solid state energy scales are shown for comparisons; ϕ_{el} is the electrolyte work function [6].**

(1) There is a Franck-Condon shift of the energy levels of ions in the electrolyte. The energy of an ion in solution is changed by the arrangement of the solvent molecules to reduce the coulomb energy of the ion. When the charge of the ion is changed due to charge transfer, the dipoles of the solvent change their orientation to minimize the energy of the new charged state. This rearrangement energy shifts the equilibrium energy of the filled or reduced state relative to that of the empty or oxidized state.

(2) Energy levels fluctuate with time. This fluctuation stems from the thermal

motion of the polar solvent molecules. The probability that the energy level is at any particular energy is given by a Gaussian distribution [50]:

$$W_{ox}(E) = (4\pi\lambda k_B T)^{-1/2} \exp[-(E - E^o_{ox})^2/4\lambda k_B T] \qquad (2.1)$$

$$W_{red}(E) = (4\pi\lambda k_B T)^{-1/2} \exp[-(E - E^o_{red})^2/4\lambda k_B T] \ , \qquad (2.2)$$

where k_B is the Boltzmann constant, T the temperature, E^o_{ox} and E^o_{red} are the most probable energies of the unoccupied and occupied states in solution, λ is the rearrangement or reorientation energy, which represents the activation energy for the process of transforming the solvation shell structure from the equilibrium situation of one species to the most probable structure of the other. E^o_{ox}, E^o_{red}, and λ are related by:

$$E^o_{ox} - E^o_{red} = 2\lambda \ . \qquad (2.3)$$

(3) The electron transfer across the interface is isoenergetic, i.e., it takes place between states of equal energy [50,51].

(4) An electrolyte is composed of a non-conducting solvent, aqueous or non-aqueous, in which the supporting electrolyte and redox couple are dissolved. The redox couple possesses different oxidation states that correspond to the electro-chemical equilibrium such as:

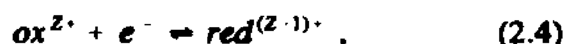

$$ox^{Z+} + e^- \rightleftharpoons red^{(Z-1)+} \ , \qquad (2.4)$$

where ox^{Z+} and $red^{(Z-1)+}$ are the ox and the red form of the same chemical species. The standard redox potential represents the relative position of the energy level of the ion in solution under same standard conditions.

2.1.2 Potential distribution

The potential distribution of the semiconductor/electrolyte interface is a key factor for photoelectrochemical applications.

Space-charge layer [51,52]

The potential $\Phi(x)$ must obey Poisson's equation, which in one dimension takes the following form:

$$\frac{d^2\Phi(x)}{dx^2} = -\frac{\varrho(x)}{\varepsilon_o \varepsilon} , \qquad (2.5)$$

where ε is the dielectric constant, ε_o is the permittivity of free space and $\rho(x)$ is the charge density distribution in x direction perpendicular to the surface, which can be represented by

$$\varrho(x) = e\,[n_b - p_b + p(x) - n(x)] , \qquad (2.6)$$

where n_b and p_b are the bulk concentration of electrons and holes, respectively, assuming that all acceptors and donors are fully ionized. $p(x)$ and $n(x)$ are concentrations of holes and electrons within the space charge layer. Under the assumption that the Fermi level is far from the band edges, the Fermi function can be approximated by a Boltzmann distribution, and the electron density $n(x)$ and

hole density p(x) in the space charge layer can be written as

$$n(x) = n_b \exp[-e(\phi_b - \phi(x))/k_B T] \qquad (2.7)$$

$$p(x) = p_b \exp[e(\phi_b - \phi(x))/k_B T] \ , \qquad (2.8)$$

where Φ_b is the potential of the bulk semiconductor.

Now, defining

$$V(x) = \phi_b - \phi(x) \ , \qquad (2.9)$$

Poisson's equation becomes

$$\frac{d^2V(x)}{dx^2} = \frac{e}{\varepsilon_o \varepsilon} [n_b - p_b + p_b e^{\frac{eV(x)}{k_B T}} - n_b e^{-\frac{eV(x)}{k_B T}}] \ . \qquad (2.10)$$

The equation can be integrated once analytically by multiplying each side by 2(dV/dx) and applying the boundary condition that V=0 and dV/dx=0 when x=W, where W is the width of space charge layer, to yield:

$$\left(\frac{dV}{dx}\right)^2 = \frac{2e}{\varepsilon_o \varepsilon}[(n_b - p_b)V + \frac{k_B T}{e} p_b(e^{\frac{eV}{k_B T}} - 1) - 1 + \frac{k_B T}{e} n_b(e^{-\frac{eV}{k_B T}} - 1)]. \ (2.11)$$

For n-type semiconductor, $p_b \rightarrow 0$ and all terms including p_b can be neglected, and for completely ionized donors, $n_b = N_d$, therefore, the above equation at the surface (x=0) becomes

$$\left(\frac{dV}{dx}\right)^2\bigg|_{x=0} = \frac{2eN_d}{\varepsilon_o \varepsilon}[V_{sc} - \frac{k_B T}{e}(1 - e^{-\frac{eV_{sc}}{k_B T}})] \, , \qquad (2.12)$$

where V_{sc} is the potential drop across the space charge layer.

In the depletion mode, $V_{sc} > 0$ and $eV_{sc}/k_B T \gg 1$, therefore neglecting the exponential term in equation (2.12), and taking into account that dV/dx>0, one obtains

$$\frac{dV}{dx}\bigg|_{x=0} = \sqrt{\frac{2eN_d}{\varepsilon_o \varepsilon}(V_{sc} - \frac{k_B T}{e})} \, . \qquad (2.13)$$

Recalling from Gauss's theorem that the surface charge is given by

$$\begin{aligned} Q_{sc} &= -A\varepsilon_o \varepsilon \frac{d\phi}{dx}\bigg|_{x=0} = A\varepsilon_o \varepsilon \frac{dV}{dx}\bigg|_{x=0} \\ &= A\sqrt{2eN_d \varepsilon_o \varepsilon}\left(V_{sc} - \frac{k_B T}{e}\right)^{1/2} \end{aligned} \, , \qquad (2.14)$$

where A is the area of semiconductor, the differential capacitance is

$$C_{sc} = \frac{dQ_{sc}}{dV_{sc}} = A\sqrt{\frac{\varepsilon_o \varepsilon e N_d}{2}}\left(V_{sc} - \frac{k_B T}{e}\right)^{-1/2} \, . \qquad (2.15)$$

Hence,

$$\frac{1}{C_{sc}^2} = \frac{2}{\varepsilon_o \varepsilon e N_d A^2}\left(V_{sc} - \frac{k_B T}{e}\right). \qquad (2.16)$$

Assuming that all voltage changes occur across the depletion layer of the semiconductor, one obtains:

$$V_{sc} = U - U_{fb}\,, \qquad (2.17)$$

where U is the electrode potential and U_{fb} the flat-band potential. It follows that

$$\frac{1}{C_{sc}^2} = \frac{2}{\varepsilon_o \varepsilon e N_d A^2}\left(U - U_{fb} - \frac{k_B T}{e}\right). \qquad (2.18)$$

Equation (2.18) is known as the Mott-Schottky relationship [53,54], which predicts a linear C^{2} vs U plot, the intercept with U axis, U_o, being given by

$$U_o = U_{fb} + \frac{k_B T}{e}\,, \qquad (2.19)$$

from which U_{fb} can be obtained. The slope yields N_d if ε and A are known.

The flat-band potential U_{fb} is a critical parameter characterizing the semiconductor electrode, that is, the electrode potential at which the semiconductor bands are flat (zero space charge in the semiconductor). The flat-band potential locates the Fermi level relative to the electrolyte level and thereby locates the band edges. The position of the band edges relative to the electrolyte levels is important in determining whether the desired electron transfer reactions can take place and

whether there is sufficient inherent band bending to allow the barrier to form without bias. Based on flat-band potential, potential distribution on the interface can be established.

If one approximates the depletion layer by a capacitor, the width W of which varies with applied voltage, then W is given by

$$W = \frac{\varepsilon_o \varepsilon A}{C_{sc}} = \sqrt{\frac{2\varepsilon_o \varepsilon}{eN_d}} \left(U - U_{fb} - \frac{k_B T}{e}\right)^{1/2} . \qquad (2.20)$$

Surface states [55,56]

Surface states are localized electronic energy levels present at the surface of the material. Because these localized energy levels are active in exchanging or sharing electrons with the bulk of the material and thus actively participate in the electronic and other related properties of the interface, the density of surface states and their distribution may strongly influence the potential distribution of semiconductor/electrolyte interface and the dielectric and optical properties of the junction.

Assuming that the surface states at the semiconductor/electrolyte interface exhibit a Gaussian density distribution, which can be expressed as:

$$N_{ss}(E) = \frac{N_t}{e\sigma\sqrt{2\pi}} \exp\left[-\frac{(E_t - E)^2}{2(e\sigma)^2}\right], \qquad (2.21)$$

where E is the energy, E_t is the most probable energy, $e\sigma$ the standard deviation

in energy distribution and N_t the total concentration of surface states, and the occupation of the surface states under equilibrium is governed by Fermi-Dirac statistics, the surface charge is given by

$$\begin{aligned} q_{ss} &= e \int_{E_v}^{E_c} \frac{N_{ss}(E)}{1 + \exp[(E - E_F)/k_B T]} \, dE \\ &= \frac{N_t}{\sigma\sqrt{2\pi}} \int_{E_v}^{E_c} \frac{\exp[-(E_t - E)^2/2(e\sigma)^2]}{1 + \exp[(E - E_F)/k_B T]} \, dE \end{aligned} \quad . \qquad (2.22)$$

For $e\sigma \gg k_B T$,

$$\frac{1}{1 + e^{\frac{E - E_F}{k_B T}}} = \Gamma(E - E_F) = \begin{cases} 0 & for \quad E > E_F \\ 1/2 & for \quad E = E_F \\ 1 & for \quad E < E_F \end{cases} . \qquad (2.23)$$

Substituting Eq.(2.23) into Eq.(2.22) leads to:

$$q_{ss} = \frac{eN_t}{2}\left[erf\left(\frac{E_t - E_v}{\sqrt{2}e\sigma}\right) - erf\left(\frac{E_t - E_F}{\sqrt{2}e\sigma}\right)\right] , \qquad (2.24)$$

where

$$erf\, x = \frac{2}{\sqrt{\pi}} \int_0^x e^{-x^2} \, dx . \qquad (2.25)$$

Using

$$E_t = -eU_t \quad , \qquad E_v = -eU_v \quad , \qquad (2.26)$$
$$E_F = -eU \quad , \quad U - U_{fb} = \Delta\phi_s$$

where U is the electrode potential, U_{fb} the flat-band potential, $\Delta\Phi_s$ the potential drop across the space charge layer and U_t the most probable potential of surface state, one obtains

$$q_{ss} = \frac{eN_t}{2}\left[erf\left(\frac{U_v - U_t}{\sqrt{2}\sigma}\right) - erf\left(\frac{U_{fb} + \Delta\phi_s - U_t}{\sqrt{2}\sigma}\right)\right] . \qquad (2.27)$$

The differential capacitance due to these states is given by

$$C_{ss} = -\frac{dq_{ss}}{d\Delta\phi_s} = \frac{eN_t}{\sigma\sqrt{2\pi}} \exp\left[-\frac{(U - U_t)^2}{2\sigma^2}\right] . \qquad (2.28)$$

The differential capacitance due to surface states has the same kind of potential distribution as surface state density itself. Therefore, the density and distribution parameters, such as probable potential and standard deviation, can be deducted from the potential distribution of the surface state capacitance.

2.1.3. Photoresponse

For monochromatic photons incident upon the interface, the generation rate G(x) of the electron-hole pairs is a function of the distance x inward from the surface of the semiconductor and given by [57]

$$G(x) = \alpha I_o(1 - R)e^{-\alpha x} , \qquad (2.29)$$

where α is the absorption coefficient, I_o the incident photon flux, and R the reflectivity.

The electron-hole pairs generated within the space charge layer or depletion layer are separated by the electric field. The minority charge carriers are driven to the semiconductor/electrolyte interface before they can recombine with the majority carriers. For n-type semiconductor the minority carriers are holes. The hole flux coming toward the interface, which is generated within the space charge layer, F_f, is given by

$$F_f = \int_0^W G(x)\, dx = I_o(1 - R)(1 - e^{-\alpha W}) . \qquad (2.30)$$

The light that is not absorbed in the space charge layer is absorbed in the field-free bulk of the semiconductor. The density of those minority carriers generated in the bulk is controlled by recombination and diffusion. The concentration of holes, P, is determined by the following one-dimensional diffusion equation [58,59]

$$\frac{dP}{dt} = D_p \frac{d^2P}{dx^2} - \frac{P - P_o}{\tau} + G(x) , \qquad (2.31)$$

where D_p is the diffusion coefficient for holes, P_o the equilibrium hole density, and τ the lifetime of the holes. In the steady state, $dP/dt=0$ and then

$$D_p \frac{d^2P}{dx^2} - \frac{P-P_o}{\tau} + G(x) = 0 \ . \qquad (2.32)$$

Using the boundary conditions [58,60]

$$\begin{array}{lll} P = P_o & at & x = \infty \\ P = 0 & at & x = W \end{array} \ , \qquad (2.33)$$

the solution of Eq.(2.32) is

$$P(x) = P_o(1 - e^{\frac{W-x}{L_p}}) - \frac{L_p^2}{D_p} \frac{I_o\alpha(1-R)e^{-\alpha W}}{1-\alpha^2 L_p^2} [e^{\frac{W-x}{L_p}} - e^{\alpha(W-x)}] \ , \qquad (2.34)$$

where

$$L_p = \sqrt{D_p \tau} \qquad (2.35)$$

is the diffusion length of the holes. The diffusion flux of holes at x=W, F_d, is obtained as

$$\begin{aligned} F_d &= D_p \frac{dP(x)}{dx}\bigg|_{x=W} \\ &= P_o \frac{D_p}{L_p} + I_o(1-R) \frac{\alpha L_p}{1+\alpha L_p} e^{-\alpha W} \end{aligned} \ , \qquad (2.36)$$

which is the diffusion flux of the holes entering the depletion layer. Assuming that there is no recombination within the space charge layer, the diffusion flux of holes

is independent of the positions within the space charge layer. For the wide-band-gap semiconductor, the first term in the Eq.(2.36) can be neglected. The total hole flux, F, to the surface consists of two components: F_f generated in the space charge layer and the diffusing hole flux F_d.

$$F = F_f + F_d = I_o(1 - R)\left[1 - \frac{e^{-\alpha W}}{1 + \alpha L_p}\right] . \qquad (2.37)$$

The hole flux at the surface is divided into two parts [9,59]: the recombination flux, F_r, in which the holes recombine with electrons via surface states, and charge transfer flux, F_t, in which the holes transfer charge to the electrolyte. The recombination flux, F_r, can be written as [61]

$$\begin{aligned} F_r &= k_r n_t^* P_s \\ &= S_r P_s \end{aligned} , \qquad (2.38)$$

where S_r is the rate constant for surface recombination, k_r is the second order rate constant for surface recombination, P_s the surface density of holes, and n_t^* is the concentration of the occupied surface states given by

$$n_t^* = n_t + \delta n_t , \qquad (2.39)$$

where n_t is the equilibrium concentration of the occupied states and δn_t the non-equilibrium increment.

For surface states with energies closed to the flat-band potential, the electron exchange between the surface states and the conduction band is very

efficient and the surface recombination current is limited by the availability of holes. Under those conditions

$$\delta n_t \ll n_t \,, \qquad (2.40)$$

and

$$S_r = k_r n_t^* = k_r n_t \,. \qquad (2.41)$$

From Eq.(2.27)

$$n_t = \frac{q_{ss}}{e} = \frac{N_t}{2}\left[erf\left(\frac{U_v - U_t}{\sqrt{2}\,\sigma}\right) - erf\left(\frac{U - U_t}{\sqrt{2}\,\sigma}\right)\right] . \qquad (2.42)$$

For surface states close to the bottom of the conduction band,

$$\frac{U_t - U_v}{\sigma} \gg 1 \qquad and \qquad erf\left(\frac{U_v - U_t}{\sqrt{2}\,\sigma}\right) \approx 1 \,, \qquad (2.43)$$

therefore,

$$S_r = \frac{k_r N_t}{2}\left[1 - erf\left(\frac{U - U_t}{\sqrt{2}\,\sigma}\right)\right] . \qquad (2.44)$$

Obviously, the recombination contributes nothing to the external current. Similarly, the charge transfer flux, F_t, can be written as

$$F_t = S_t P_s \,, \qquad (2.45)$$

where S_t is the charge transfer parameter. S_t can be described as [59]

$$S_t = \int_{E_v}^{E_c} v_{th}\,\sigma_t N_t(E)\; dE \,, \qquad (2.46)$$

where v_{th} is the thermal velocity of the holes, σ_t the interaction cross section of the holes at the surface, and $N_t(E)$ the area density of reaction centers in the electrolyte.

In steady state, the hole flux reaching the surface is equal to the sum of the recombination flux, F_r, and the charge transfer flux, F_t, i.e.,

$$F = F_r + F_t = (S_r + S_t)\,P_s \,. \qquad (2.47)$$

The photocurrent, J_{photo}, is given by:

$$J_{photo} = \frac{F_t}{F_r + F_t}\,eF = \frac{S_t}{S_r + S_t}\,eI_o(1 - R)\left[1 - \frac{e^{-\alpha W}}{1 + \alpha L_p}\right]. \qquad (2.48)$$

Hence, the quantum efficiency, Φ, can be written as

$$\Phi = \frac{J_{photo}}{eI_o} = \frac{S_t}{S_r + S_t}(1 - R)\left[1 - \frac{e^{-\alpha W}}{1 + \alpha L_p}\right]. \qquad (2.49)$$

The photocurrent-potential behavior is implicit through the potential dependent parameters: the width of space charge layer, W, and the surface recombination

rate, S_r. Also, one can analyze the photocurrent versus photon energy characteristics at fixed electrode potential, which is called photocurrent spectroscopy, or its normalized form that is called spectral response.

A number of theoretical models were developed. Reichman [62] took carrier recombination in the space charge layer into account. F. El Guibaly et al. [63-65] and S. Chandra et al. [66] included the effects of dark current, space charge recombination, surface state, and the charge transfer kinetics at the interface. Recently H. Kobayashi et al. [67] introduced the hole quasi-Fermi level to accommodate the slow diffusion transfer at the semiconductor/liquid interface and the slow diffusion of redox species between the interface and the bulk of the solution.

Neglecting surface recombination, some simplification can be made to determine important physical parameters from the photoresponse [68-70]:

a) If $W \ll 1/\alpha$, then

$$J_{photo} = e I_o \alpha \frac{L_p + W}{1 + \alpha L_p} , \qquad (2.50)$$

but near the band edge, the optical absorption coefficient, α, of a semiconductor can be expressed as [60]

$$\alpha = A \frac{(h\nu - E_g)^{n/2}}{h\nu} , \qquad (2.51)$$

where A is a constant, $h\nu$ the photon energy, E_g the energy gap of the semicon-

ductor, and n depends on whether the transition is direct (n=1) or indirect (n=4). Therefore, if $L_p \ll 1/\alpha$, then

$$\Phi = \frac{J_{photo}}{e I_o} \propto \alpha \propto \frac{(h\nu - E_g)^{n/2}}{h\nu} . \qquad (2.52)$$

From the linearity of $(\Phi h\nu)^{2/n}$ versus $h\nu$ (n=1 or 4), one can determine whether the semiconductor has direct transition feature or indirect, and the energy gap, E_g, can be obtained by linear extrapolation to the abscissa in the corresponding plot.

b) If $W \ll 1/\alpha$ and $L_p \ll 1/\alpha$, then

$$J_{photo} = e I_o \alpha (L_p + W) . \qquad (2.53)$$

A plot of J_{photo} versus W should give a straight line whose intercept on the abscissa gives $-L_p$, the diffusion length of the minority carrier.

c) If $L_p \ll W \ll 1/\alpha$, then

$$J_{photo} = e I_o \alpha W = I_o \alpha \left[\frac{2 e \varepsilon_o \varepsilon}{N_d}\right]^{1/2} \left[U - U_{fb} - \frac{k_B T}{e}\right]^{1/2} . \qquad (2.54)$$

The flat-band potential, U_{fb}, can be determined through linearly extrapolating the plot of J^2_{photo} vs potential to zero photocurrent.

2.1.4 Generalized equivalent circuit model

A photoelectrochemical system can be characterized in terms of charge

transfer across the interface between semiconductor electrode and the electrolyte. The driving force for the charge transfer is the potential drop across the interface. This requires that the electric current flowing between the semiconductor and the electrolyte is a unique function of the voltage drop across the interface. All the mechanistic information about the rate limiting steps in such a system is contained in the function I(E), where E is the voltage drop across the interface, usually measured against a reference electrode, and I is the current. If a small time-dependent perturbation in the voltage, ΔE, is introduced, the resulting change in the current can be expanded into the Taylor series such as [71]

$$I(E+\Delta E) = I(E) + \left(\frac{\partial I}{\partial E}\right)_{E,I} \Delta E + \left(\frac{\partial^2 I}{\partial E^2}\right)_{E,I} \Delta E^2 \ . \qquad (2.55)$$

If the amplitude of the perturbation is small enough so that the higher derivatives can be neglected, then the resulting change in the current can be expressed as

$$\Delta I = \left(\frac{\partial I}{\partial E}\right)_{E,I} \Delta E \ . \qquad (2.56)$$

The admittance of the system is defined as

$$Y(\omega) = \frac{1}{Z(\omega)} = \left(\frac{\partial I}{\partial E}\right)_{E,I} \ , \qquad (2.57)$$

and $Z(\omega)$ is the impedance of the system. ω is the angular frequency of the perturbation.

To gain useful information about the system from the impedance measurements, one builds a model for the mechanism of charge transfer in the system, expresses the model in terms of I(E) relation, superposes a small time dependent perturbation E, calculates the resulting change in I, from which the frequency dispersion of the impedance is obtained, fits it to the experimental results to determine the validity of the model, and gets the physical parameters that appear in the model.

The diffusion capacitance is such an example. When a small ac signal is applied to the junction that is forward biased to a voltage V_o and current density J_o, the total voltage and current are given by [72]

$$V(t) = V_o + V_1 e^{j\omega t} \qquad (2.58)$$

$$J(t) = J_o + J_1 e^{j\omega t} , \qquad (2.59)$$

where V_1 and J_1 are small-signal amplitude of voltage and current density, respectively.

The small-signal ac component, $\tilde{p}_n(x,t)$, of the hole density is given by

$$\tilde{p}_n(x,t) = p_{n1}(x) e^{j\omega t} . \qquad (2.60)$$

It obeys the continuity equation,

$$\frac{\partial \tilde{p}_n}{\partial t} = -\frac{\tilde{p}_n}{\tau_p} + D_p \frac{\partial^2 \tilde{p}_n}{\partial x^2} , \qquad (2.61)$$

where D_p and τ_p are diffusion coefficient and lifetime, respectively. Eq.(2.61) can be written as

$$\frac{\partial^2 \tilde{p}_n}{\partial x^2} - \frac{\tilde{p}_n}{D_p \tau_p / (1 + j\omega\tau_p)} = 0 . \qquad (2.62)$$

The hole density at the depletion layer boundary is

$$\begin{aligned} p_n &= p_{no} \exp\left(\frac{eV}{k_B T}\right) = p_{no} \exp\left[\frac{e(V_o + V_1 e^{j\omega t})}{k_B T}\right] \\ &= p_{no} \exp\left(\frac{eV_o}{k_B T}\right) + p_{no} \exp\left(\frac{eV_o}{k_B T}\right) \frac{eV_1}{k_B T} e^{j\omega t} . \end{aligned} \qquad (2.63)$$

Therefore, the boundary condition becomes

$$\tilde{p}_n = p_{no} \exp\left(\frac{eV_o}{k_B T}\right) \frac{eV_1}{k_B T} e^{j\omega t} \qquad at \quad x = W . \qquad (2.64)$$

The ac component of the hole density is then

$$\tilde{p}_n = p_{no} \exp\left(\frac{eV_o}{k_B T}\right) \frac{eV_1}{k_B T} e^{-\frac{x - W}{L_p^*}} e^{j\omega t} , \qquad (2.65)$$

where

$$L_p^* = \frac{L_p}{(1 + j\omega\tau_p)^{1/2}} . \qquad (2.66)$$

At x=W, the ac component of hole diffusion current density is

$$\tilde{J} = -eD_p \frac{\partial \tilde{p}_n}{\partial x}\bigg|_{x=W} = \frac{eD_p p_{no}}{L_p^*} \frac{eV_1}{k_B T} \exp\left(\frac{eV_o}{k_B T}\right) e^{j\omega t} . \qquad (2.67)$$

Hence,

$$J_1 = \frac{eD_p p_{no}}{L_p} \frac{eV_1}{k_B T} (1 + j\omega\tau_p)^{1/2} e^{\frac{eV_o}{k_B T}} , \qquad (2.68)$$

and

$$Z_d = \frac{V_1}{J_1} = \frac{k_B T}{e} \frac{L_p}{eD_p p_{no}} (1 + j\omega\tau_p)^{-1/2} e^{-\frac{eV_o}{k_B T}} . \qquad (2.69)$$

The alternative to this approach is to try to represent the system in terms of electrical circuit elements, such as capacitors and resistors. The capacitive elements are associated with charge accumulation modes and the resistive elements with charge transfer modes. The product of a capacitive and a resistive element in a set, τ=RC, is associated with the corresponding relaxation time of the charge accumulation mode. The response of this network is compared with the measured response over a wide frequency regime. However, sometimes the passive lumped elements cannot give an adequate description of the real physical process.

Here, a generalized equivalent circuit is introduced. For such a simple case

as an abrupt junction between a semiconductor and a metal, or abrupt junction between a semiconductor and a concentrated electrolyte, where the electrolyte charge accumulation in the Helmholtz layer can be neglected, such a generalized equivalent circuit is shown in figure 2.2 [73]. C_{sc} is usually the capacitance due to the space charge layer, assumed to be the fastest relaxing element. C_i and $\tau_i=R_iC_i$ are the capacitances and the corresponding relaxation times of charge accumulation modes such as various surface states, minority carriers and bulk states. Z_d is a generalized constant phase angle (CPA) element given by [74]:

$$Z_d = N(1 + j\omega\tau)^{-n} , \qquad (2.70)$$

where ω is the angular frequency and N, τ, and n are parameters. R_s is the series resistance and R_p is the shunt resistance. The real and imaginary parts of Z_d can be written as:

$$R_d = N(1 + \omega^2\tau^2)^{-n/2} \cos n\theta \qquad (2.71)$$

$$X_d = -N(1 + \omega^2\tau^2)^{-n/2} \sin n\theta , \qquad (2.72)$$

where $\tan\theta = \omega\tau$.

CPA refers to the fact that the phase angle ϑ_z is independent of frequency ω [75]. Therefore, the imaginary part Im(Z) and the real part Re(Z) of the impedance have the same frequency dependence. In general, CPA-like response appears only over a finite range of frequency. In this model, for $\omega\tau \gg 1$,

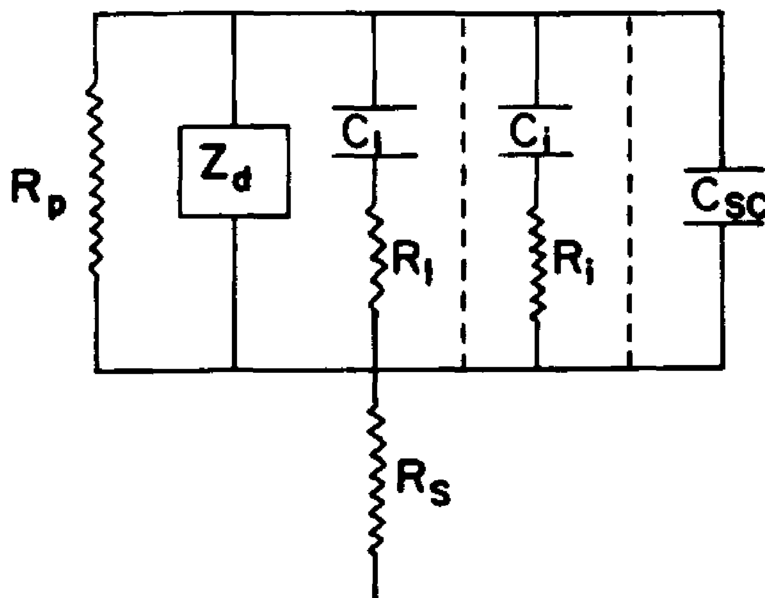

Figure 2.2 The generalized equivalent circuit of a single interface. R_p is the resistance associated with the Faradaic current flow, Z_d is a generalized impedance associated with disorder either in the structure or in the dynamic (diffusion), C_i and R_i are associated with parallel charge accumulation modes with different relaxation times than the majority carriers such as surface states or minority carriers, C_{sc} is the space-charge capacitance, and R_s is the series resistance.

$$R_d = N(\omega\tau)^{-n}\cos\frac{n\pi}{2} \qquad (2.73)$$

$$X_d = -N(\omega\tau)^{-n}\sin\frac{n\pi}{2}\,, \qquad (2.74)$$

which exhibits CPA behavior. For $\omega\tau \ll 1$,

$$R_d = N \qquad (2.75)$$

$$X_d = -Nn\omega\tau \ , \qquad (2.76)$$

which exhibits the passive element behavior.

Z_d in this form can include contributions from static disorder such as porosity [77], random mixture of conductor and insulator that can be described by the effective medium approximation at percolation [78], or an interface that can be described by a fractal geometry [79]. It also can include contributions from dynamic disorder, such as diffusion. To provide one specific example connected with our previous discussion: if Z_d originates from diffusion capacitance in the semiconductor [see Eq.(2.69)], then τ is the minority carriers diffusion time, n=0.5 and

$$N = \frac{k_B T}{e} \frac{L_p}{e D_p P_{no}} \exp\left(- \frac{e V_o}{k_B T} \right) , \qquad (2.77)$$

[80] where T is the temperature, k_B the Boltzmann constant, e the electronic charge, L_p the minority carrier's diffusion length, D_p their diffusion coefficient, P_{no} their concentration in the bulk and V_o is the forward bias.

The equivalent circuit model does not provide any information concerning physical processes taking place in the system. It just separates the processes according to their relaxation times. To correlate the elements of the equivalent circuit with the physical processes, their dependence on external parameters such as voltage, temperature, electrolyte etc. must be investigated.

2.1.5 Effective medium theory

For solid-liquid interface, one can model the interface as a capacitor with a composite dielectric, in particular, for the polycrystalline electrodes or electrodes with a porous layer on the surface. In those cases, the liquid can penetrate into the solid, forming an interface characterized by a three dimensional morphology.

In polycrystalline or disorder materials, grain boundaries, disordered regions, voids etc. significantly affect their dielectric and optical properties. The macroscopic dielectric response of disordered materials is connected intimately with the compositional and microstructural parameters. In principle, the dielectric response of a material can be calculated via a two-step process: the electrostatic solution for a given microstructure to obtain the local electric field and dipole moment per unit volume at every point in the material; and average of these microscopic solutions to obtain the macroscopic observables. But the microstructure is not known exactly and in fact the macroscopic average dielectric response function seems to be more useful than a knowledge of the microscopic field. Effective medium theory defines an effective dielectric function, which is described by the dielectric function of its constituents [81,82], to represent the complicated system such as disorder or heterogeneous materials. The average microstructure is included obviously through volume fractions of different constituents. The detailed microstructure is implicitly included through screening effects which depending on the shape and orientation of the grains or particles.

The description of the effective medium theory can start with the familiar

Clausius-Mosotti equation,

$$\frac{\epsilon - 1}{\epsilon + 2} = \frac{4\pi}{3} n\alpha \ , \qquad (2.78)$$

where ε is the dielectric function, n the volume density, and α the polarizability.

Now let two different materials be mixed. It is assumed that the sizes of the particles are much smaller than the wavelength λ so that as the light travels through the medium it cannot distinguish between materials **a** and **b** and only some sort of averaging behavior is observed, but are large enough so that they can be characterized by macroscopic dielectric functions ε_a and ε_b, respectively. Since the right hand side of the Eq.(2.78) is additive, the dielectric function of the mixture obeys [83]

$$\frac{\epsilon - 1}{\epsilon + 2} = \frac{4\pi}{3} (n_a \alpha_a + n_b \alpha_b) \ , \qquad (2.79)$$

where α_a and α_b are the polarizabilities of phase **a** and **b**, respectively, n_a and n_b are the volume densities of phase **a** and **b**, respectively, and $n_a + n_b = n$.

From the Clausius-Mosotti Equation for material **a**,

$$\frac{\epsilon_a - 1}{\epsilon_a + 2} = \frac{4\pi}{3} n \alpha_a \ , \qquad (2.80)$$

it follows that

$$\frac{4\pi}{3} n_a \alpha_a = \frac{n_a}{n_a + n_b} \frac{\epsilon_a - 1}{\epsilon_a + 2} = f_a \frac{\epsilon_a - 1}{\epsilon_a + 2} . \qquad (2.81)$$

Similarly,

$$\frac{4\pi}{3} n_b \alpha_b = f_b \frac{\epsilon_b - 1}{\epsilon_b + 2} , \qquad (2.82)$$

then

$$\frac{\epsilon - 1}{\epsilon + 2} = f_a \frac{\epsilon_a - 1}{\epsilon_a + 2} + f_b \frac{\epsilon_b - 1}{\epsilon_b + 2} , \qquad (2.83)$$

where f_i represents the volume fraction of the I th phase:

$$f_i = \frac{n_i}{\sum_j n_j} \quad , \quad \sum_i f_i = 1 . \qquad (2.84)$$

Considering the two components, **a** and **b**, to be embedded in a polarizable host medium with dielectric function ε_h rather than in vacuum, it is necessary to construct a cavity filled with the host dielectric in calculating the local electric field, instead of a completely evacuated cavity, as happens in the derivation of classical Clausius-Mosotti equation. As a result, a generalized equation is obtained

$$\frac{\epsilon - \epsilon_h}{\epsilon + 2\epsilon_h} = f_a \frac{\epsilon_a - \epsilon_h}{\epsilon_a + 2\epsilon_h} + f_b \frac{\epsilon_b - \epsilon_h}{\epsilon_b + 2\epsilon_h} , \qquad (2.85)$$

where ε_h is the dielectric function of a host medium.

For $\varepsilon_h=1$, Eq.(2.85) has the same form as Eq.(2.83), which is called Lorentz-Lorenz effective medium approximation [84,85]. For $\varepsilon_h=\varepsilon_b$, Eq.(2.85) becomes

$$\frac{\epsilon - \epsilon_b}{\epsilon + 2\epsilon_b} = f_a \frac{\epsilon_a - \epsilon_b}{\epsilon_a + 2\epsilon_b} , \qquad (2.86)$$

which is the Maxwell-Garnett effective medium approximation [86].

Bruggeman suggested replacing ε_h in Eq.(2.85) with ε, i.e., letting the effective medium itself act as host medium, which results in

$$f_a \frac{\epsilon_a - \epsilon}{\epsilon_a + 2\epsilon} + f_b \frac{\epsilon_b - \epsilon}{\epsilon_b + 2\epsilon} = 0 . \qquad (2.87)$$

This is known as the Bruggeman effective medium approximation [87], the self-consistent approximation or the coherent potential approximation.

In the Maxwell-Garnett approximation, the grains of one component are assumed to be embedded in the matrix of the other component, which treats the two components in an asymmetric manner. For a single type of inclusion in a host background, ε has different values if the roles of host and inclusion are interchanged - even if the respective volume fractions are held constant.

In the Bruggeman effective medium approximation, the two components, **a** and **b**, are assumed to be embedded in an effective medium itself, whose dielectric function is ε. The two components, **a** and **b**, are treated in an equivalent manner. Equation (2.87) can be rewritten as a quadratic equation in ε as following

$$2\epsilon^2 - [(3f_a - 1)\epsilon_a + (3f_b - 1)\epsilon_b]\epsilon - \epsilon_a\epsilon_b = 0 \ . \qquad (2.88)$$

Obviously, the equation is symmetric in ε_a and ε_b and it resolves the ambiguity in the Maxwell-Garnett approximation. The above derivation is based on the assumption that the inclusions are spherical and non-interacting. However, the shapes of the particles determine how effectively they are screened, which affect the microscopic polarizations and fields, therefore, in turn, determining the functional relationship between ε and the dielectric functions of the constituents [83]. As an extension, it is assumed that ellipsoidal particles are aligned with the direction of polarization parallel to a principal axis of an ellipsoid. The effect can be described by the depolarization factor d. After substituting the results for the polarizability of an ellipsoid immersed in a dielectric medium, equation (2.87) then becomes [88]

$$f_a \frac{\epsilon_a - \epsilon}{d\epsilon_a + (1 - d)\epsilon} + f_b \frac{\epsilon_b - \epsilon}{d\epsilon_b + (1 - d)\epsilon} = 0 \ , \qquad (2.89)$$

where d is depolarization factor, which ranges between 0 and 1 and depends on the geometry of the inclusion in the composite. For spheres, d equals to 1/3, for needles or long cylinders with axes parallel to the field, d is 0, and for flat plates with their normals parallel to the field, d is 1.

Recent refinement of the Bruggeman's approximation is the differential effective medium approximation, or the self-similar effective medium approximation. The structure is built up by starting from homogeneous component **a** and using the

iterative process shown in figure 2.3: replace an infinitesimal amount of starting component **a** by the second component **b**, and then regard the resulting "effective" material as the homogeneous component for succeeding substitution step [89-91].

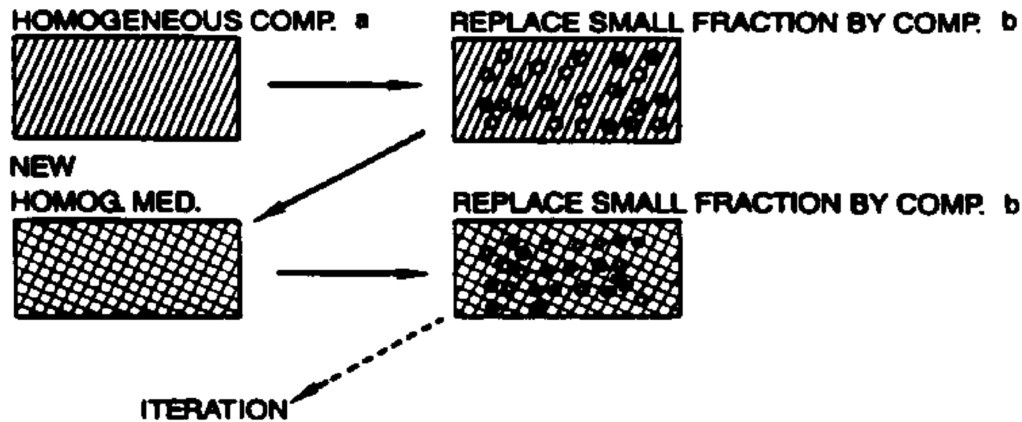

Figure 2.3 The basic microstructure build-up process in the differential effective medium theory [90].

The Bruggeman's effective medium approximation gives

$$(1-\Delta\psi_b)\frac{\epsilon_a-\epsilon}{d\epsilon_a+(1-d)\epsilon}+\Delta\psi_b\frac{\epsilon_b-\epsilon}{d\epsilon_b+(1-d)\epsilon}=0\,, \qquad (2.90)$$

where $\Delta\psi_b$ is the replacement amount of component **b** in the replacement step. Let $\Delta\varepsilon=\varepsilon-\varepsilon_a$ and consider the terms to first order in $\Delta\psi_b$; it follows that

$$\Delta\epsilon=\frac{(\epsilon_b-\epsilon)\epsilon}{d\epsilon_b+(1-d)\epsilon}\Delta\psi_b\,. \qquad (2.91)$$

Since $\Delta\psi_b$ stands for the amount of the composite replaced by component **b**, the real increment of component **b** in the replacement step is given by

$$\Delta\psi = (1 - \psi)\Delta\psi_b , \qquad (2.92)$$

where ψ denotes the volume fraction of component **b** in the mixture. The correct differential effective medium equation, therefore, is given by

$$\left[\frac{d(\epsilon_b - \epsilon) + \epsilon}{\epsilon(\epsilon_b - \epsilon)}\right] d\epsilon = \frac{d\psi}{(1 - \psi)} . \qquad (2.93)$$

Integrating Eq.(2.93) yields

$$1 - \psi = \left(\frac{\epsilon_b - \epsilon}{\epsilon_b - \epsilon_a}\right)\left(\frac{\epsilon_a}{\epsilon}\right)^d . \qquad (2.94)$$

This demonstrates that based on the effective medium theory, the dielectric response of a composite material is related to the dielectric functions of its constituents and some parameters characteristic of the structure of the composite, such as porosity and the depolarization factor.

2.2 Modulation spectroscopy

Modulation spectroscopy is accomplished by applying a small perturbation in a periodic fashion and measuring the corresponding change in the optical properties with a phase sensitive detector [92-96]. The perturbation parameters can be the electric field, magnetic field, temperature, stress, wavelength of the probe beam etc. The derivative nature of modulation spectra suppresses uninteresting background effects and emphasizes structure localized in the energy

region of inter-band transitions at critical points in the Brillouin zone.

Among all kinds of modulations the electromodulations, including electroreflectance (ER), electrolyte electroreflectance (EER), and photoreflectance (PR), are the most widely used technique. Its sharp, derivative-like features are directly sensitive to the conditions in the space charge region and, hence, can be used as an optical probe of field distribution in the junction.

2.2.1 Dielectric function

The fundamental quantity used to describe the optical properties of a solid is the dielectric function

$$\epsilon(\omega) = \epsilon_1(\omega) + i\,\epsilon_2(\omega) = N^2 , \qquad (2.95)$$

where $\varepsilon_1(\omega)$ and $\varepsilon_2(\omega)$ are the real and imaginary components of the dielectric function $\varepsilon(\omega)$, and N is the complex refraction index,

$$N = n + iK , \qquad (2.96)$$

where n and K are the real and imaginary components of N. Thus,

$$\epsilon_1(\omega) = n^2(\omega) - K^2(\omega) \qquad (2.97)$$

$$\epsilon_2(\omega) = 2\,n(\omega)\,K(\omega) . \qquad (2.98)$$

The absorption coefficient α depends on the above optical constants via

$$\alpha = \frac{2K\omega}{c} = \frac{\omega}{nc}\epsilon_2 . \qquad (2.99)$$

Based on the quantum theory of band-to-band transition and the definition of the absorption coefficient, the microscopic expression for the absorption coefficient is given by [97]:

$$\alpha(\omega) = \frac{4\pi^2 e^2}{ncm^2\omega}\sum_{v,c}\int_{BZ}\frac{2d\vec{k}}{(2\pi)^3}\left|\hat{\epsilon}\cdot M_{cv}(\vec{k})\right|^2 \delta(E_c(\vec{k}) - E_v(\vec{k}) - \hbar\omega), \quad (2.100)$$

and using (2.99)

$$\epsilon_2(\omega) = \frac{4\pi^2 e^2}{m^2\omega^2}\sum_{v,c}\int_{BZ}\frac{2d\vec{k}}{(2\pi)^3}\left|\hat{\epsilon}\cdot M_{cv}(\vec{k})\right|^2 \delta(E_c(\vec{k}) - E_v(\vec{k}) - \hbar\omega), \quad (2.101)$$

where e is the absolute value of the electron charge, m the effective mass of the electron, ω the angular frequency of the photon, $\hat{\epsilon}$ is the unit polarization vector of the photon's electric field, c and v denote conduction (empty) and valence (filled) bands, respectively,

$$M_{cv}(\vec{k}) = \langle c,\vec{k}\,|\,\vec{p}\,|\,v,\vec{k}\rangle \qquad (2.102)$$

is the momentum matrix element between states in conduction band and valence band at wave vector **k**, representing the transition probability, $E_c(\mathbf{k})$ and $E_v(\mathbf{k})$ are the energy of conduction band and valence band, respectively, and the integration is performed over the Brillouin zone. The $\epsilon_1(\omega)$ can be obtained using the Kramers-Kronig dispersion relation

$$\epsilon_1(\omega) = 1 + \frac{2}{\pi} P \int_0^{\infty} \omega' \epsilon_2(\omega) \frac{1}{\omega'^2 - \omega^2} d\omega' \quad , \qquad (2.103)$$

where P indicates the principal part,

$$\epsilon_1(\omega) = 1 + \frac{8\pi e^2}{m^2} \sum_{v,c} \int \frac{2d\vec{k}}{(2\pi)^3} \frac{\left|\hat{e}\cdot M_{cv}(\vec{k})\right|^2}{[E_c(\vec{k}) - E_v(\vec{k})]/\hbar} \times \frac{1}{[E_c(\vec{k}) - E_v(\vec{k})]^2/\hbar^2 - \omega^2} \quad . \qquad (2.104)$$

Incorporating the thermal broadening and replacing the integration variables by the energy E, and two variables k_1 and k_2 locating a point on the constant-energy surface S defined by $E_{cv}(\mathbf{k})$=E, then [95]

$$\epsilon(E,\Gamma) = 1 + \frac{e^2\hbar^2}{\pi^2 m^2 E^2} \int dE \int_S dk_1 dk_2 \frac{\left|\hat{e}\cdot M_{cv}(\vec{k})\right|^2}{\left|\nabla E_{cv}(\vec{k})\right|} \times \left[\frac{1}{E_{cv}(\vec{k}) - E - i\Gamma} - \frac{1}{E_{cv}(\vec{k}) + E + i\Gamma}\right] , \qquad (2.105)$$

where $E_{cv}(\mathbf{k})$ is the inter-band energy difference given by

$$E_{cv}(\vec{k}) = E_c(\vec{k}) - E_v(\vec{k}) \ , \qquad (2.106)$$

and Γ is the phenomenological broadening parameter related to the lifetime. Eq.(2.105) shows that $\varepsilon(E,\Gamma)$ has a singularity at every **k** for a given pair c, v for which

$$\nabla_k E_{cv}(\vec{k}) = 0 \ . \qquad (2.107)$$

These singular points are called Van Hove singularities. It is around these critical points that the structure in the dielectric function spectra and modulation spectra appears as peaks, which provides a probe for the band structure of the semiconductor.

Within the parabolic approximation for $E_{cv}(\mathbf{k})$,

$$E_{cv}(\vec{k}) = E_g + \frac{1}{2}\hbar^2\left(\frac{k_x^2}{\mu_{xx}} + \frac{k_y^2}{\mu_{yy}} + \frac{k_z^2}{\mu_{zz}}\right) \qquad (2.108)$$

the dielectric function can be written as a superposition of local functions [95]:

$$\epsilon(E,\Gamma) = \frac{e^2\hbar^2|\hat{e}\cdot M_{cv}|^2}{\pi^2 m^2 E^2}\int_{BZ}\frac{d^3\vec{k}}{E_{cv}(\vec{k}) - E - i\Gamma} \ . \qquad (2.109)$$

Because the region is local, $M_{cv}(\mathbf{k})$ may be assumed to be independent of $\mathbf{k}$. Performing the integral in Eq.(2.109) explicitly for one, two, and three dimensions, for which two, one, or none of the reduced inter-band effective masses μ_{ii} are infinite, yields

$$\epsilon(E,\Gamma) = \begin{cases} \frac{Q}{E^2} D_x K_y K_z i^{l+1} (E - E_g + i\Gamma)^{-1/2} \\ \frac{Q}{E^2} D_x D_y K_z i^{l+2} \ln(E - E_g + i\Gamma) \\ \frac{Q}{E^2} D_x D_y D_z i^{l+1} (E - E_g + i\Gamma)^{1/2} \end{cases} , \qquad (2.110)$$

where

$$Q = \frac{e^2 \hbar^2}{\pi m^2} |\hat{\epsilon} \cdot M_{cv}|^2 \qquad (2.111)$$

$$D_i = \left(\frac{2|\mu_{ii}|}{\hbar^2} \right)^{1/2} \qquad i = x, y, z \qquad (2.112)$$

$K_i = K_y$ or K_z are the cutoff lengths in the Brillouin zone for one and two dimensional critical points, and l is the critical point type that is equal to the number of negative masses μ_{ii}.

2.2.2 Modulated reflectivity

For near normal incidence, the reflectivity at the discontinuous interface between two different, but homogeneous media (substrate/ambient) can be written using Fresnel's equation as

$$R = \left| \frac{(N - N_a)^2}{(N + N_a)^2} \right| \qquad (2.113)$$

$$= \left| \frac{(n - n_a)^2 - (K + K_a)^2}{(n + n_a)^2 + (K + K_a)^2} \right| = R(\epsilon, \epsilon_a) \; , \qquad (2.114)$$

where N and N_a are the refractive indices of the material and the ambient, respectively, n and K are the real part and the imaginary part of N, and n_a and K_a are the real part and imaginary part of N_a.

The relative change of reflectivity due to perturbation is [95,98,99]

$$\frac{\Delta R}{R} = Re\left[\frac{2N_a}{N(\epsilon - \epsilon_a)} \Delta\epsilon \right] \qquad (2.115)$$

$$= Re\left[(\alpha - i\beta)\, \Delta\epsilon \right] \qquad (2.116)$$

$$= \alpha(\epsilon_1, \epsilon_2, \epsilon_a)\, \Delta\epsilon_1 + \beta(\epsilon_1, \epsilon_2, \epsilon_a)\, \Delta\epsilon_2 \; , \qquad (2.117)$$

where ε_a and ε are the dielectric functions of the ambient and the material, respectively, $\Delta\varepsilon = \Delta\varepsilon_1 + i\Delta\varepsilon_2$ is the change in ε due to perturbation and α and β are the Seraphin coefficients, which have a characteristic photon energy dependence for semiconductors. The perturbation induces the change in dielectric functions, and, therefore, the change of reflectivity.

2.2.3 Third derivative spectra in low field regime

The mechanism responsible for electric field modulation is the coupling of the field to the electrons (or holes), causing them to accelerate through the lattice.

Thus, they occupy a range of k states, and hence energy states, before they undergo a collision. This energy assists the electrons tunnelling through the gap and effectively reduces the energy gap.

F.H. Pollak presented a simple and clear physical derivation of the effects of an electric field on the dielectric function [100]. The gain E(F) in energy of the electron and hole in an electric field **F** can be calculated by replacing **k** by **k**+eFt/ħ, i.e.,

$$E(\vec{F}) = \frac{e^2 F^2 t^2}{2\mu_{\parallel}} , \qquad (2.118)$$

where t is the time between two collisions, F is the electric field, and $\mu_{\parallel}$ is the reduced inter-band effective mass in the field direction.

The average energy (or average energy uncertainty) during -t/2 to t/2 is then

$$\overline{E(\vec{F})} = \frac{1}{t} \int_{-t/2}^{t/2} E(\vec{F})\, dt = \frac{e^2 F^2 t^2}{24\mu_{\parallel}} . \qquad (2.119)$$

Considering the structure near a local critical point with energy E_g, the local dielectric function has the form

$$\epsilon = \epsilon(E - E_g + i\Gamma) . \qquad (2.120)$$

The change in dielectric function due to electric field, Δε, is

$$\Delta\epsilon = \epsilon(E - E_g + \overline{E(\vec{F})} + i\Gamma) - \epsilon(E - E_g + i\Gamma) . \qquad (2.121)$$

If the field is low enough so that, $\overline{E(\vec{F})} \ll \Gamma$ (low field regime), the Taylor's series expansion of Eq.(2.121) yields [100]

$$\Delta\epsilon = \overline{E(\vec{F})} \frac{\partial}{\partial E} \epsilon(E - E_g + i\Gamma) \qquad (2.122)$$

$$= \frac{e^2 F^2 t^2}{24 \mu_l} \frac{\partial}{\partial E} \epsilon(E - E_g - i\Gamma) . \qquad (2.123)$$

In quantum mechanics, the time, t, is also an operator:

$$t = i\hbar \frac{\partial}{\partial E} \qquad (2.124)$$

and hence Eq.(2.123) becomes

$$\Delta\epsilon = \frac{e^2 F^2 \hbar^2}{24 \mu_l} \frac{\partial^3}{\partial E^3} \epsilon(E - E_g + i\Gamma) \qquad (2.125)$$

$$= \frac{1}{3} (\hbar\Omega)^3 \frac{\partial^3}{\partial E^3} \epsilon(E - E_g + i\Gamma) , \qquad (2.126)$$

where

$$(\hbar\Omega)^3 = \frac{e^2 F^2 \hbar^2}{8 \mu_l} \qquad (2.127)$$

is the electro-optic energy. Eq.(2.125) has all the essential features of low field electromodulation, i.e., proportional to F^2, inversely proportional to μ_l and the third derivative nature.

The generalized expression for the "low field" electromodulated reflectance spectra can be written as

$$\frac{\Delta R(\omega_m)}{R} = F_{SCR}^2(\omega_m)\, Re\left[C e^{i\theta} (\hbar\omega - E_g + i\Gamma)^{-n} \right] \qquad (2.128)$$

$$= F_{SCR}^2(\omega_m)\, L(\hbar\omega) \quad , \qquad (2.129)$$

where $F_{SCR}(\omega_m)$ is the electric field in the space charge region (SCR) being modulated at ω_m, C and θ are the amplitude and phase factor, n is a number characteristic of the inter-band critical point, for 3 dimensional, n=2.5, for 2 dimensional, n=3.0, and for 1 dimensional, n=3.5. E_g is the energy gap and $L(\hbar\omega)$ is a spectral line-shape function, characteristic of a particular material. If the form of dielectric function ε is a Lorentzian, then

$$L(\hbar\omega) = Re\left[C e^{i\theta} (\hbar\omega - E_g + i\Gamma)^{-n} \right] . \qquad (2.130)$$

From the analysis of the spectral line shape, the band structure parameters can be deduced and the presence of defects acting as scattering centers could be reflected by the broadening of the width of line shape.

In a fully depletion SCR [101],

$$F_{SCR}^2 = \frac{2eN_d}{\epsilon}\left(V_{int} + \eta V_{ext} \quad \frac{k_B T}{e} \right) , \qquad (2.131)$$

where e is the electronic charge, N_d is the carrier concentration, ε is the static dielectric constant, V_{int} is the internal barrier potential, V_{ext} is the external applied

potential and η is a coefficient that determines what fraction of V_{ext} appears across the SCR. The k_BT/e term represents the Debye length correction. V_{ext} consists of a dc component, V_{dc} and an ac component at frequency ω_m, ΔV, which is called the modulating voltage, i.e.,

$$V_{ext} = V_{dc} + \Delta V(\omega_m) \ . \qquad (2.132)$$

If modulation from flat-band is considered, the modulated electric field in SCR is

$$F^2_{SCR}(\omega_m) = -\frac{2eN_d}{\epsilon}\eta\, \Delta V(\omega_m) \qquad (2.133)$$

and

$$\frac{\Delta R(\omega_m)}{R} = -\frac{2eN_d}{\epsilon}\eta\, \Delta V(\omega_m)\, L(\hbar\omega) \ . \qquad (2.134)$$

This indicates that the signal $\Delta R/R$ is proportional to the modulating voltage in the low field regime.

2.2.4 Photoreflectance

Photoreflectance (PR) is a contactless form of electroreflectance (ER) in which a built-in surface electric field is not modulated by changing the bias voltage across the device, but instead, periodically modulated by the photovoltage between the surface and the bulk due to irradiation with a second chopped pumping beam [102,103]. This form of modulation has the same type of effect on the optical constants as produced in ER; therefore, it is possible to analyze the spectra using the

theoretical machinery developed for ER.

Under the illumination of the pumping beam, which results in a forward bias, the dark current density J_D is

$$J_D = J_s(e^{\frac{eV}{k_BT}} - 1) , \qquad (2.135)$$

where J_s is the saturation current density, e is the electronic charge, V is the voltage, k_B is Boltzmann constant, and T is the temperature.

The total current density, J, is [72]

$$J = J_s(e^{\frac{eV}{k_BT}} - 1) - J_L , \qquad (2.136)$$

where J_L is photocurrent density. At open circuit condition, J=0, and assuming $J_L \gg J_s$, then

$$V_{oc} = \frac{k_BT}{e}\ln\left(\frac{J_L}{J_s} + 1\right) \approx \frac{k_BT}{e}\ln\left(\frac{J_L}{J_s}\right) . \qquad (2.137)$$

From Eq.(2.50), for $\alpha W \ll 1$ and $W \ll L_p$,

$$J_L = eI_o\alpha\frac{L_p + W}{1 + \alpha L_p} \approx eI_o\alpha\frac{L_p}{1 + \alpha L_p} \quad ,$$

$$V_{oc} = \frac{k_BT}{e}\ln\left[\frac{L_p}{1 + \alpha L_p}\frac{\alpha I_o e}{J_s}\right] . \qquad (2.138)$$

The photovoltage has the logarithmic dependence on the intensity of the pumping

beam. The modulation of beam intensity I_o results in the modulation of the voltage across the space charge region.

The precondition of PR is the existence of space charge region or band bending near the surface of the semiconductor, which can be induced by the surface state. At equilibrium, charge neutrality requires that the amount of charge needed to form the space charge layer originates from the surface [51]. Within the Schottky approximation for an abrupt junction, the barrier height at the surface is given by

$$V_s = \frac{eN_d W^2}{2\epsilon} , \qquad (2.139)$$

where e is the electronic charge, N_d is the concentration of the donors, W is the thickness of the space charge layer and ϵ is the dielectric constant. The number of charge per unit area on the surface, N_{ss}, arising from electrons or holes exhausted from a distance W from the surface, is given by

$$N_{ss} = -N_d W . \qquad (2.140)$$

Therefore,

$$V_s = \frac{eN_{ss}^2}{2\epsilon N_d} . \qquad (2.141)$$

For charge neutrality to be maintained, only a small modulation of the surface charge can produce a large modulation of the surface potential and hence a large

PR signal.

2.2.5 Flat-band determination [101]

If a small modulation signal $V_{-}=V_{a}\sin(\omega_{m}t)$ is applied on a n-type semiconductor biased into depletion, from 1/4 to 3/4 cycle, V_{-} is decreased, therefore, the bending of the band is increased, and the modulation field in the SCR is increased, while from 3/4 to 5/4 cycle, V_{-} is increased, and the modulation field in SCR is decreased. As a result, it produces a $\Delta R/R$ signal with a given phase. If the sample is biased into accumulation, from 1/4 to 3/4 cycle, V_{-} is decreased, hence the bending of the band is decreased and the modulation field in SCR is decreased, while from 3/4 to 5/4 cycle, the field in SCR is increased, i.e., in accumulation mode, the field in SCR varies opposite with that in depletion mode. Then, the $\Delta R/R$ signal in accumulation mode has the opposite phase from that in the depletion mode. Thus, when the space charge region is biased through flat-band potential, the ER signal changes sign and ER signal is zero at the flat-band potential.

If the line-shape does not change with dc bias, then keeping the photon energy at the value of the transition peak, and keeping the modulation amplitude and frequency unchanged, $\Delta R/R$ signal is measured when the dc bias potential is scanned from the reverse to forward, the flat-band potential V_{fb} can be determined from the potential at which $\Delta R/R$ signal is zero or change its sign. which is a direct measurement of V_{fb}.

2.2.6 Fermi level pinning [106]

At the semiconductor electrode, the electroreflectance signal is due to the change of the electric field in the space charge region of the semiconductor. If the Fermi level is completely pinned, the band edges move up and down as the potential is changed and the bending of the bands in the SCR is kept unchanged. As a result, there is no modulation in the electric field of the SCR of the semiconductor and hence there is no modulative reflectivity. The ER signal will reach a zero level at this situation.

The potential drop $\Delta\Phi_s$ across the space charge layer can be expressed as

$$\Delta\Phi_s = U - U_{fb} , \qquad (2.142)$$

where U is the electrode potential, and U_{fb} is the flat band potential. Assuming no IR drop, the change in electrode potential due to the modulation is divided between the space charge layer and the Helmholtz layer according to [104]

$$\Delta V = \delta\Delta\Phi_s + \delta\Phi_o = \Delta V_{sc} + \delta\Phi_o , \qquad (2.143)$$

where Φ_o is the potential drop across the Helmholtz layer. The change in the potential drop across the Helmholtz layer due to a change in the number of ionized surface states is given by [105]

$$\delta\Phi_o = \frac{e}{C_H}\delta N_{ss} , \qquad (2.144)$$

where C_H is the capacitance of the Helmholtz layer, and N_{ss} is the area density of

the ionized surface states.

Comparing Eqs.(2.143) and (2.144),

$$\Delta V_{sc} = \Delta V - \frac{e}{C_H}\delta N_{ss} = \left(1 - \frac{e}{C_H}\frac{dN_{ss}}{dU}\right)\Delta V \qquad (2.145)$$
$$= \eta \Delta V \ ,$$

where

$$\eta = 1 - \frac{e}{C_H}\frac{dN_{ss}}{dU} \ . \qquad (1.146)$$

Recalling Eq.(2.134), it follows that [106]

$$\frac{\Delta R(\omega_m)}{R} = -\frac{2eN_d}{\epsilon}\left(1 - \frac{e}{C_H}\frac{dN_{ss}}{dU}\right)\Delta V(\omega_m)\, L(\hbar\omega) \ . \qquad (2.147)$$

If the surface states are fast enough to equilibrate at the modulation frequency, i.e., the relaxation times of these states are faster than $1/\omega_m$, then the surface states cause part of the potential drop to fall across the Helmholtz layer, thus modulating the position of the band edges relative to the reference electrode, resulting in a decreased modulation amplitude on the space charge layer, and, therefore, a decreased electroreflectance signal. $(e/C_H)(dN_{ss}/dU)=0$ represents the condition when the Fermi level is unpinned by surface states and any change in the electrode potential results in corresponding change in the potential drop across the space charge layer. ER signal should be independent of the dc potential. If $(e/C_H)(dN_{ss}/dU)>0$, then, for n type semiconductors, anodic shift of the electrode

potential, i.e., the variation of bias from near flat-band to reverse, results in incremental ionization of the surface states, and the decrease in ER amplitude. $(e/C_H)(dN_{ss}/dU)=1$ represents the condition in which the Fermi level is completely pinned and the ER signal is reduced to zero. Therefore, the bias dependence of ER signal provides optical evidence for Fermi level pinning.

Thereby, the degree of Fermi level pinning P can be expressed as

$$P = \frac{e}{C_H}\frac{dN_{ss}}{dU} = 1 - \frac{\Delta R/R}{(\Delta R/R)_{max}} , \qquad (2.148)$$

which is valid provided that $(\Delta R/R)_{max}$, which occurs when $dN_{ss}/dU=0$, is still within the low field regime. Because changes in flat-band potential originate from changes in the potential drop across the Helmholtz layer, i.e., $\delta U_{fb}=\delta\Phi_o$, it follows from Eqs.(2.144) and (2.148) that

$$P = \frac{dU_{fb}}{dU} \qquad (2.149)$$

and

$$U_{fb} = U_{fb}^o + \int_{U_{max}}^{U} P\, dU , \qquad (2.150)$$

where U_{max} is the potential at which $\Delta R/R$ is maximum and U^o_{fb} is the flat-band potential at $U=U_{max}$.

Assuming that the surface state has a Gaussian density distribution as

Eq.(2.21), then the number of ionized state is given by [55]

$$N_{ss}^{+}(E_F) = \frac{N_t}{2}\left[erf\left(\frac{E_t - E_F}{\sqrt{2}e\sigma} \right) - erf\left(\frac{E_t - E_c}{\sqrt{2}e\sigma} \right) \right] . \qquad (2.151)$$

Neglecting the energy difference between the Fermi level and the bottom of the conduction band in the bulk of the semiconductor, then

$$E_F = -eU \qquad (2.152)$$

$$E_c = -eU_{fb} = -eU_{fb}^{o} - e\int_{U_{max}}^{U} P\, dU \qquad (2.153)$$

$$E_t - E_c = E_t^{o} - E_c^{o} = -eU_t^{o} + eU_{fb}^{o} \qquad (2.154)$$

$$E_t - E_F = E_t^{o} - E_c^{o} + E_c - E_F = -eU_t^{o} + eU - e\int_{U_{max}}^{U} P\, dU . \qquad (2.155)$$

This results in

$$N_{ss}^{+}(U) = \frac{N_t}{2}\left[erf\left(\frac{-U_t^{o} + U - \int_{U_{max}}^{U} P\, dU}{\sqrt{2}\sigma} \right) - erf\left(\frac{-U_t^{o} + U_{fb}^{o}}{\sqrt{2}\sigma} \right) \right] . \qquad (2.156)$$

Differentiation of Eq.(2.156) with respect to U and application of Eqs.(2.148) and (2.149) yield

$$P = \frac{e}{C_H} \frac{N_t}{\sigma\sqrt{2\pi}} e^{-\frac{1}{2\sigma^2}\left(U_t^\circ - U + \int_{U_{max}}^{U} P dU\right)^2} (1 - P) . \qquad (2.157)$$

Then it leads to

$$\frac{P}{1 - P} = \frac{eN_t}{C_H \sigma\sqrt{2\pi}} e^{-\frac{1}{2\sigma^2}\left(U_t^\circ - U + \int_{U_{max}}^{U} P dU\right)^2} . \qquad (2.158)$$

After fitting the curve of P/(1-P) vs U in the reverse bias condition, the ratio of surface state density to capacitance of Helmholtz layer, N_t/C_H, the probable energy position of the surface state, U_t°, and the standard derivation in the Gaussian distribution of surface state can be extracted.

2.2.7 Surface trap states

It has been demonstrated [107] that the frequency dispersion of the PR signal can yield information about surface trap states, which are modulated by the pumping beam in the PR experiment through their equilibration with the space charge layer. In their model the assumptions are the following:

(a) The chopped pumping beam is approximated by a square wave source.

(b) The light induced carriers are captured quickly by the surface traps and the built-in electric field is changed abruptly.

(c) These carriers are released slowly when the light is turned off. The release of the carriers follows kinetics that can be expressed as the sum of exponentials with

characteristic relaxation time τ_i and the electric field does so.

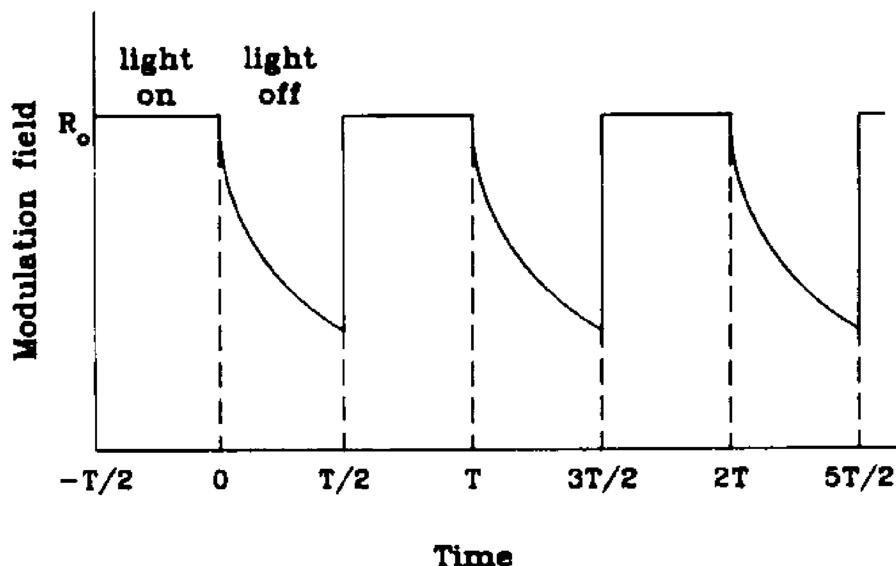

Figure 2.4 **The schematic representation of modulation field due to chopped laser beam in PR.**

Following these assumptions, the effective modulation field can be shown schematically on figure 2.4, and expressed as

$$f(t) = \begin{cases} R_o & -\frac{T}{2} \le t \le 0 \\ \sum_i C_i e^{-\frac{t}{\tau_i}} & 0 \le t \le \frac{T}{2} \end{cases}, \qquad (2.159)$$

where R_o is the change in built-in electric field due to the pumping beam, C_i are the coefficients of the exponential expansion such that $\Sigma C_i = R_o$, and τ_i are the characteristic relaxation times. Based on the above considerations, the real, $R(\omega)$,

and the imaginary, $X(\omega)$, parts of the first Fourier component of the PR intensity take the following form [108]:

$$R(\omega) = \omega \sum_i \frac{C_i \tau_i}{1 + \omega^2 \tau_i^2} \left[1 + \exp\left(- \frac{\pi}{\omega \tau_i} \right) \right] \qquad (2.160)$$

$$X(\omega) = A(0) - \omega^2 \sum_i \frac{C_i \tau_i^2}{1 + \omega^2 \tau_i^2} \left[1 + \exp\left(- \frac{\pi}{\omega \tau_i} \right) \right] . \qquad (2.161)$$

The measured amplitude of the PR signal is

$$A(\omega) = (R^2 + X^2)^{1/2} , \qquad (2.162)$$

where $A(0)$ is the dc amplitude, $A(0)=2R_o$, and ω is chopping frequency.

CHAPTER 3

EXPERIMENTAL TECHNIQUES

The methodology for investigating the semiconductor/liquid interface is based on electric field modulation of the system's response. The main techniques used in this study are impedance spectroscopy and modulation spectroscopy. The conventional current-voltage measurements are performed to complement the above measurements.

3.1 Impedance spectroscopy

The system's response is the dark current. The technique is based on a generalized representation of the frequency dispersion of simultaneously measured real and imaginary parts of the impedance. The charge accumulation modes and corresponding equivalent circuits can be deduced from the analysis of impedance spectroscopy.

In principle, if the frequency range is broad enough, the technique is sensitive to all the charge accumulation modes and to the charge transfer kinetics and mechanism. The physical nature of the elements in the equivalent circuit can be determined from their dependence on external parameters such as voltage, electrolyte etc.

3.1.1 Impedance measuring setup

The impedance measurement setup is shown in figure 3.1, which is based on the circuit arrangement proposed by Tomkiewicz [76]. The electrochemical cell is connected to a reference circuit in series. The generator output of the Solartron 1250 Frequency Response Analyzer, which includes ac and dc potential, was applied to the cell. The signals on the two terminals across the cell are transmitted to channels 1 and 2 of the analyzer of Solartron 1250, respectively. The analyzer gives the response of Channel 1 with respect to Channel 2. The dc bias is monitored through a Keithley 192 programmable DMM multimeter. If the spectroscopy extends to the frequency above 65 kHz, the cell is transferred to the HP measuring system at the setting frequency. The HP measuring system is composed of the following instruments: HP 3325A Synthesizer/function generator is used as an ac source, HP 6200B DC Power Supply is used as dc bias source, which is controlled by computer through HP 59501A HP-IB Isolated D/A Power Supply Programmer. The signals across the cell are picked up by HP 3575A Gain-Phase Meter, which has BCD (binary coded decimal) output. Model 4833 IEEE 488 Parallel Interface (ICS Electronics Corp.) is used to convert BCD data from HP 3575A into 8 bit characters for transmission over IEEE-488 bus and vice versa. The frequency scanning and data acquisition are controlled by IBM PC computer through IEEE 488 GPIB (General Purpose Interface Bus). The data are treated, shown on the monitor and stored in the diskette automatically by the software. A complete software package was written by the author. The software includes the

setting of the measuring parameters, impedance spectroscopy measurement, display on the monitor, storage of data in the diskette, print-out of data and the plotting of spectrum. The software also includes the option to use potentiostat and obtain the impedance by directly measuring V and I.

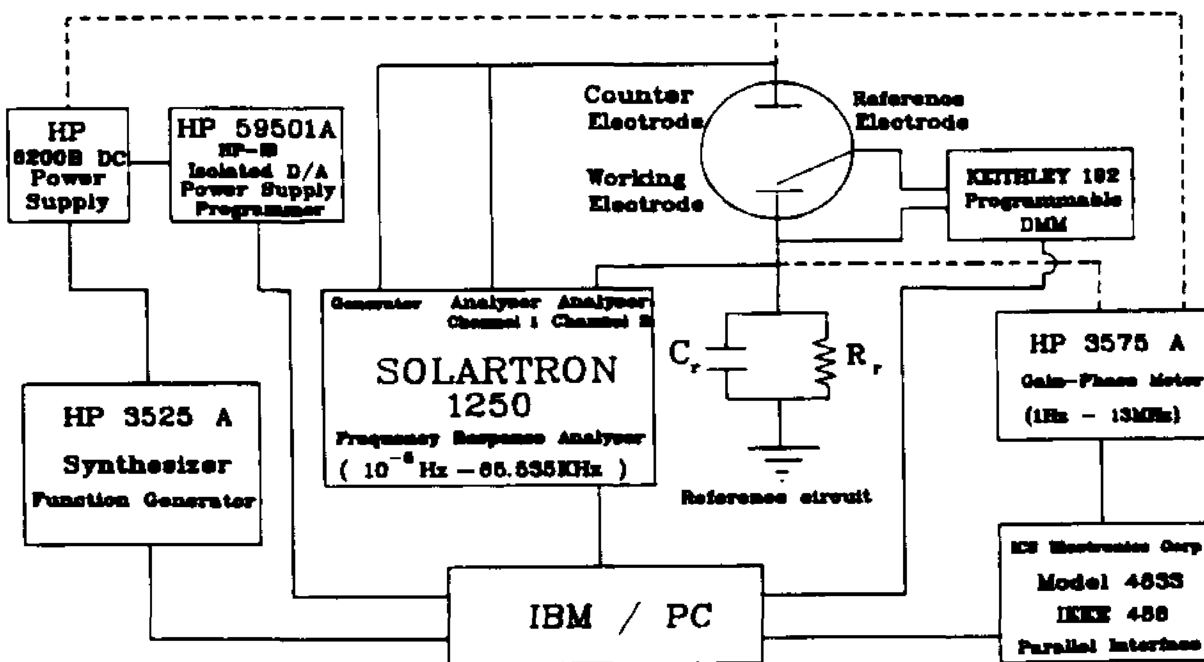

Figure 3.1 **The experimental setup of the impedance spectroscopy.**

The analyzer measures the relative magnitude, M, and the phase difference, θ, of the two signals across the cells. It is equivalent to the complex voltage ratio

$$\frac{E_1}{E_2} = M e^{i\theta} = \frac{Z + Z_r}{Z_r} , \qquad (3.1)$$

where Z is the impedance of the electrochemical cell,

$$Z = R + jX \qquad (3.2)$$

and Z_r is the impedance of the reference circuit,

$$\frac{1}{Z_r} = \frac{1}{R_r} + j\omega C_r \, . \qquad (3.3)$$

Then

$$Z_r = \frac{R_r(1 - j\omega\tau_r)}{1 + \omega^2\tau_r^2} \, , \qquad (3.4)$$

where τ_r=C_rR_r is the relaxation time of the reference circuit, ω is the angular frequency. The real and imaginary parts of the impedance of the cell can be deducted from Eq.(3.1)

$$R = \frac{R_r}{1 + \omega^2\tau_r^2}\,[\,M(\cos\theta + \omega\tau_r\sin\theta) - 1\,] \qquad (3.5)$$

$$X = \frac{R_r}{1 + \omega^2\tau_r^2}\,[\,M(\sin\theta - \omega\tau_r\cos\theta) + \omega\tau_r\,] \, . \qquad (3.6)$$

The spectroscopy is represented as log R and log(2πX) vs log f.

3.1.2 Extract of the parameters in the equivalent circuit

For a single abrupt junction between a semiconductor and a metal or a

concentrated electrolyte, a generalized equivalent circuit is shown in Fig.2.2 and discussed in § 2.1.4. The procedure of extracting the parameters in the equivalent circuit is the following:

(1) series resistance R_s and capacitance of space charge layer C_{sc}.

For a sufficiently concentrated electrolyte, the space charge layer has the smallest relaxation time, $\tau_s = R_s C_{sc}$. At the high frequency end, the system behaves as a single capacitor, C_{sc}, and resistor, R_s, connected in series and the impedance is given by:

$$Z_{HF} = R_s - j \frac{1}{\omega C_{sc}} . \qquad (3.7)$$

Thus, the real part R at high frequency is independent of frequency and the value of R_s can be determined. According to Eq.(3.7)

$$\log(2\pi X) = -\log f - \log C_{sc} . \qquad (3.8)$$

Therefore, the curve of $\log(2\pi X)$ vs $\log f$ should have a slope of -1 and C_{sc} can be evaluated from the intercept.

(2) Shunt resistance R_p.

At the low frequency end, all the elements of accumulation modes approach open circuit and the response of the system is

$$Re(Z)_{LF} = R_s + R_p . \qquad (3.9)$$

Then, R_p can be determined from the difference between the real parts of the

impedance at the low frequency end and at the high frequency end.

(3) Parameters of constant phase angle (CPA) element.

If one subtracts the frequency-independent high frequency resistance from the impedance

$$Z' = Z - R_s , \qquad (3.10)$$

and calculates the resulting admittance, it is easy to show that

$$\frac{1}{Z'} = \frac{1}{R_p} + j\omega C_{\infty} + \omega^2 \sum_i \frac{C_i \tau_i}{1 + \omega^2 \tau_i^2} + j\omega \sum_i \frac{C_i}{1 + \omega^2 \tau_i^2} + N^{-1} (1 + \omega^2 \tau^2)^{n/2} (\cos n\theta + j \sin n\theta) \quad , \qquad (3.11)$$

where the last term is due to a generalized CPA element given by

$$Z_d = N (1 + j\omega\tau)^{-n} , \qquad (2.70)$$

where N, τ, and n are parameters [73]. For $\tau \gg 1$, Eq.(3.11) can be viewed as the superposition of a constant term, linear term, power-law term, and Lorentzian terms with respect to the frequency.

The real part, G, of the above admittance 1/Z' is

$$G = \frac{1}{R_p} + \omega^2 \sum_i \frac{C_i \tau_i}{1 + \omega^2 \tau_i^2} + N^{-1} (1 + \omega^2 \tau^2)^{n/2} \cos n\theta , \qquad (3.12)$$

and imaginary part, B, of the admittance 1/Z' subtracted by the fastest relaxation

term, ωC_{sc}, is

$$B = \omega \sum_i \frac{C_i}{1 + \omega^2 \tau_i^2} + N^{-1} (1 + \omega^2 \tau^2)^{n/2} \sin n\theta \ . \qquad (3.13)$$

In the high frequency limit,

$$\lim_{\omega \to \infty} G = \frac{1}{R_p} + \sum_i \frac{C_i}{\tau_i} + N^{-1} \omega^n \tau^n \cos \frac{n\pi}{2} \approx N^{-1} \omega^n \tau^n \cos \frac{n\pi}{2} \qquad (3.14)$$

and

$$\lim_{\omega \to \infty} B = \frac{1}{\omega} \sum_i \frac{C_i}{\tau_i^2} + N^{-1} \omega^n \tau^n \sin \frac{n\pi}{2} \approx N^{-1} \omega^n \tau^n \sin \frac{n\pi}{2} \ . \qquad (3.15)$$

In the region satisfied by the above condition, log G and log B have a linear relation with log f and n and τ^n/N can be evaluated from the slope and intercept of the linear part of the above relationship.

In the low frequency limit,

$$\lim_{\omega \to 0} G = \frac{1}{R_p} + N^{-1} \approx N^{-1} \ . \qquad (3.16)$$

To extract τ, assuming $R_p \to \infty$, then N can be obtained from the real part of the admittance in the low frequency limit and τ can be deducted from τ^n/N, n, and N.

(4) parallel elements R_i , C_i .

The parallel elements R_i, C_i can be most conveniently obtained through the

remaining terms from the real and imaginary parts of the above admittance,

$$\frac{G_{ss}}{\omega} = \omega \sum_i \frac{C_i \tau_i}{1 + \omega^2 \tau_i^2} \qquad (3.17)$$

and

$$B_{ss} = \omega \sum_i \frac{C_i}{1 + \omega^2 \tau_i^2} \ . \qquad (3.18)$$

Both are the superposition of Lorentzian line shapes. If the separation between the time constants is large enough, then a series of maxima that characterize each R_iC_i element exhibit on the plot of G_{ss}/ω and B_{ss} with ω. At the maximum of i th G_{ss}/ω peak,

$$\frac{\partial (G_{ss}/\omega)_i}{\partial \omega} = \frac{C_i \tau_i (1 - \omega^2 \tau_i^2)}{(1 + \omega^2 \tau_i^2)^2} = 0 \ , \qquad (3.19)$$

then,

$$\omega_{max}^i \tau_i = 1 \ . \qquad (3.20)$$

From Eq.(3.17),

$$\left(\frac{G_{ss}}{\omega} \right)_{max}^i = \frac{C_i}{2} \ , \qquad (3.21)$$

therefore,

$$C_i = 2\left(\frac{G_{ss}}{\omega}\right)^i_{max} \qquad (3.22)$$

and

$$R_i = \frac{1}{4\pi f^i_{max}\left(\frac{G_{ss}}{\omega}\right)^i_{max}} . \qquad (3.23)$$

At the maximum of j th B_{ss} peak,

$$\frac{\partial (B_{ss})_j}{\partial \omega} = \frac{C_j(1-\omega^2\tau_j^2)}{(1+\omega^2\tau_j^2)^2} = 0 , \qquad (3.24)$$

then also

$$\omega^j_{max}\tau_j = 1 . \qquad (3.25)$$

From Eq.(3.18),

$$(B_{ss})^j_{max} = \frac{\omega^j_{max} C_j}{2} , \qquad (3.26)$$

therefore,

$$C_j = \frac{(B_{ss})^j_{max}}{\pi f^j_{max}} \qquad (3.27)$$

and

$$R_j = \frac{1}{2(B_{ss})_{max}} . \qquad (3.28)$$

Obviously, B_{ss} is sensitive to the fast relaxing elements since the amplitude of each B_{ss} peak is proportional to ω, and G_{ss}/ω is sensitive to the slow elements since the amplitude of each G_{ss}/ω peak is independent of ω.

This procedure is included in the impedance analysis software written by the author. If the separation between the time constants is not large enough and/or the system cannot be represented in terms of a simple abrupt junction due to film formation, multiple junctions, etc., the non-linear least square fitting of the data is necessary. In the latter case one can get some degree of confidence if one fits the real or imaginary components and check it against the other component. Since it is a dielectric technique in nature, which is highly model dependent, the uniqueness of the interpretation is then checked against other techniques. In this study, the optical techniques, modulation spectroscopies, are used to provide complementary information.

3.2 Modulation spectroscopy

3.2.1 Universal workstation for optical characterization [109]

The macroscopic characterization technique of semiconductors is highly sensitive to the model adopted for the particular system. To overcome it, the alternative is to use as many macroscopic techniques as one can on an identical

system and to arrive at a model that will quantitatively agree with all the results. Looking at the experimental requirements of many of these techniques one can see that many components are common. Most of the desired information about transport properties and potential distribution for the semiconductor/liquid interface is derived from the response of the system to a small perturbation of the space charge layer. This provides an opportunity to construct a "universal" experimental station in which with the same sample configuration one can apply great many, seemingly unrelated techniques. A cost effective universal workstation for optical characterization of semiconductor junction devices was built. The experiments that can be performed with this system include: photoreflectance (PR), electrolyte electroreflectance (EER), diffusion length measurement by surface photovoltage (SPV), surface photovoltage spectroscopy, 1st. and 2nd. harmonic, photoinduced current-voltage characteristics, spectral response and DC current-voltage characteristics. One can switch electronically between experiments and perform any number of techniques without moving the cell or removing the electrode from the electrolyte. The workstation is computerized completely with the control software written by the author. A variable neutral density filter is placed between the monochromator and the sample, which was introduced in the measuring setup of modulation spectroscopy by F.H. Pollak [110]. To fit the requirements of each experiment and raise the control precision, we use a stepping motor controlled by a computer to adjust the variable neutral density filter instead of a servo motor. For EER and PR experiments the filter is adjusted to keep the DC reflectivity constant.

For SPV experiments of measuring diffusion length the filter is adjusted to keep the open circuit voltage constant. For spectral response the filter is adjusted to keep the photon flux of the probe beam constant enabling direct measurements of unnormalized quantum efficiencies, and for SPV spectroscopy the filter is also adjusted to keep the photon flux of the probe beam constant.

The experimental arrangement of modulation spectroscopies is shown on figure 3.2. Figure 3.3 is the experimental arrangement of SPV and spectral response.

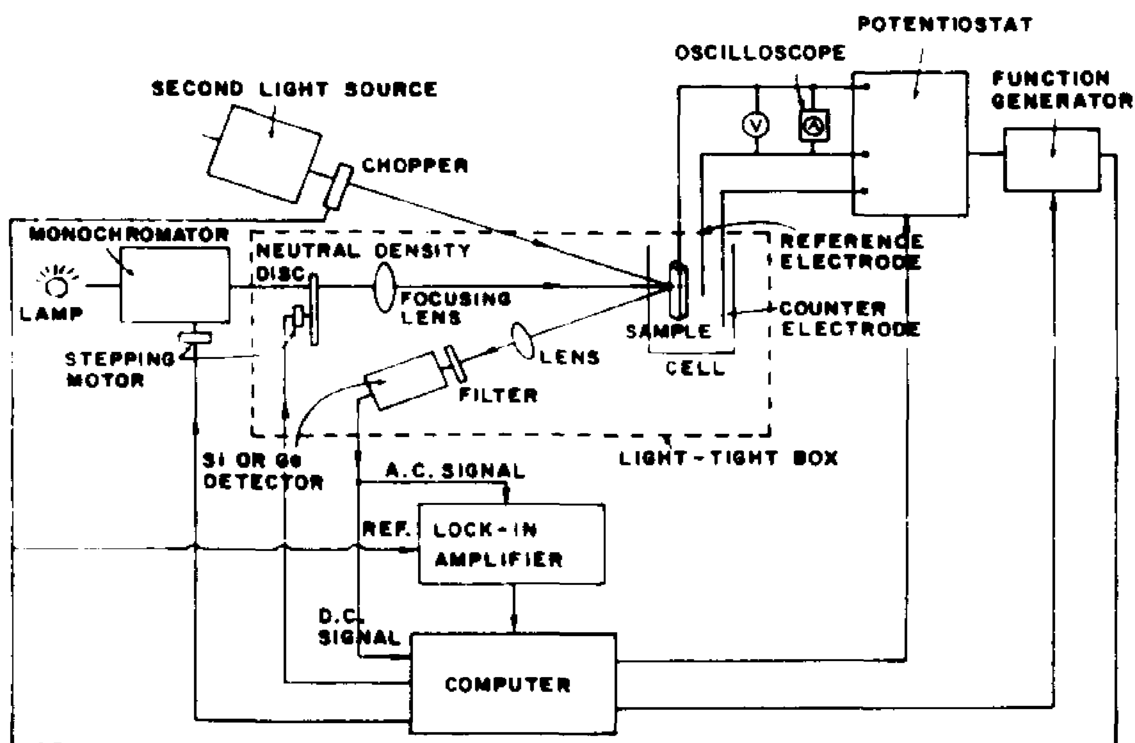

Figure 3.2 The experimental arrangement of the modulation spectroscopy.

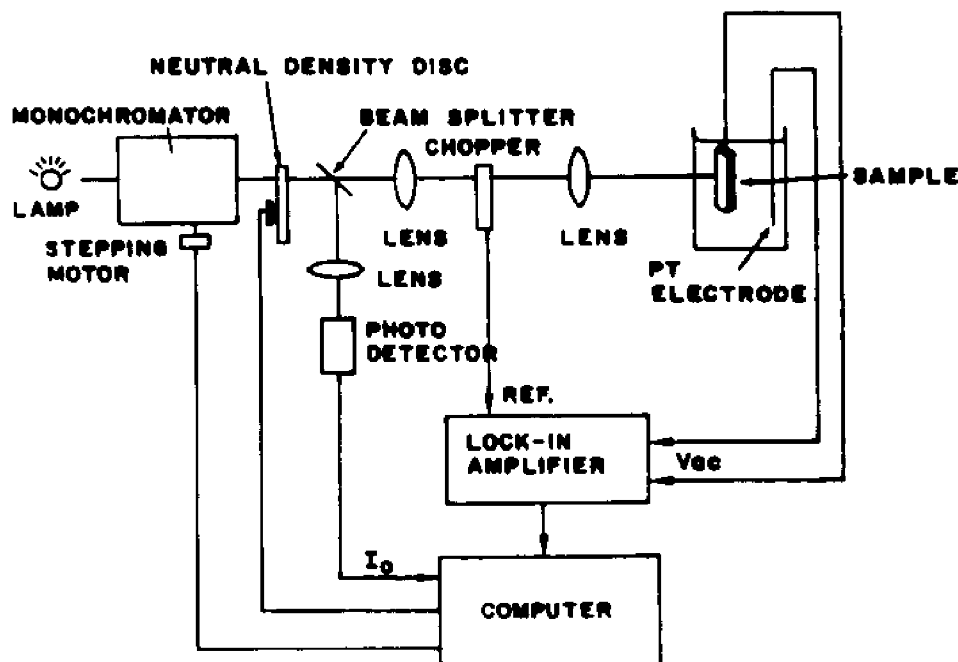

Figure 3.3 The experimental arrangement for measuring the surface photovoltage and spectral response.

3.2.2 Experimental detail of modulation spectroscopy [108]

The experimental arrangement for PR and EER is shown in Fig. 3.2. For PR the modulation source was the 6378 Å line of the 7.5 mW He-Ne laser (Hughes 3227H-PC). The modulating beam with 4880 Å wavelength is provided from Ar-ion laser (Coherent CR-6 Supergraphite). The modulating beams with 4067 Å, 4131 Å and 6764 Å are from the Krypton ion laser (Coherent Innova 100-K2). The optical chopper (Model SR540 Stanford Research Systems) is used for modulating the pumping beam with frequency 4 Hz-4 kHz. For EER, the EG&G Princeton Applied Research model 173 potentiostat was used to control the electrochemical potential

and a Hewlett-Packard 3311A function generator was used for the modulation voltage. The light source was a 150 W xenon lamp and a double-grating monochromator (Photon Technology International model 01-002) was used for scanning the spectral region of interest. The reflected light was detected by an operational amplifier/photodiode combination (HUV-4000B, EG&G Electro-Optics) for wavelengths of probing beam between 200nm and 1100nm. The GLN-050/E70 Ge detector/preamplifier combination at 77K (Electro-Optical Systems, Inc.) was used as detector for wavelengths between 800 nm and 1600 nm. A PbS detector is used for the wavelength range of 1000-3000 nm. The light striking the detector contains two signals: a DC or average value, $I_o(\lambda)R(\lambda)$, and a modulated AC value, $I_o(\lambda)\Delta R(\lambda)$, which varies with the modulation frequency ω_m. Here $I_o(\lambda)$ is the intensity of the probe beam from the monochromator, which is impinged on the sample and $R(\lambda)$ is the reflectivity of the sample and $\Delta R(\lambda)$ is the modulated reflectivity of the sample. The $I_o\Delta R$ was extracted from the output of the detector through a lock-in amplifier (Stanford Research Systems model SR-530). The DC intensity of the reflected light, $I_oR(\lambda)$, is kept constant with a continuously variable neutral density filter placed between the monochromator and the sample. The setup is controlled by an IBM PC/XT computer and the modulated reflectivity response was shown on the screen of the monitor directly and stored on diskettes. In the PR experiments of silicon an ultra violet transmitting visible absorbing filter was used to block the stray laser light and photoluminescence from the sample that have the same frequency as the signal of interest. For $CuInSe_2$ and InSe, the

corresponding long pass filter is selected for the same purpose and for rejecting the 2nd. harmonic component. The low temperature PR spectra were measured using a liquid N_2 dewar.

All the photoreflectance and electroreflectance spectra were measured in the "low field" regime, which is confirmed through the linear dependence of the modulated reflectivity signal $\Delta R/R$ on the modulating voltage. The spectra were fitted to the spectral line shape function [Eq.(2.130)] with the parameters, E_g, Γ, C, θ, and n.

Photoreflectance in the presence of an electrolyte (EPR) was measured to serve as a bridge between PR and its ability to characterize junctions with the ambient and the liquid junctions. It also serves to correlate the effects of different media on the spectroscopic properties.

3.3 Dark and photo I-V

The dark and photo I-V plots were obtained using an IBM EC/225 Voltammetric Analyzer in a three-electrode configuration connected with a X-Y recorder (815M-Plotamatic, MFE). The light source was a Sylvania tungsten halogen ELH lamp and the light intensity at the electrode surface was 100mW/cm^2. When the potential was scanned, the photocurrent was measured with a low frequency chopper (hand as a shutter) such that the light induced current and the dark current could be observed on the same chart.

3.4 Sample preparation and experimental cell

3.4.1 Silicon

The Si work was done in collaboration with Dr. M.C.A. Fantini and Dr. J.P. Gambino.

1] Sample [73,108,111-113]

The Si samples are n-type <100> wafers, with resistivity between 0.8 and 2 Ω-cm. The wafers were subjected to an RCA clean that consists of a 90 s etch with H_2O:H_2O_2:NH_4OH 5:1:1 at 65°C followed by 90 s of the same solution at the same temperature with HCl replacing the hydroxide. The samples were subjected to different RIE treatments in an asymmetric diode reactor with Si electrodes. The RIE treatment was performed at the IBM East Fishkill Facility.

CHF_3/Ar RIE samples were etched at a pressure of 40 mTorr, a gas flow rate of 25 sccm, and a voltage of 280 V for 4 min. CF_4 RIE was performed using a pressure of 40 mTorr, a gas flow rate 25 sccm, and a voltage of 280 V for 4 min, $CClF_3/H_2$ RIE was performed using pressure of 15 mTorr, a gas flow rate of 50/150 sccm, and a voltage of 600 V for 5 min. One set of samples was subjected to $CClF_3/H_2$ RIE followed by an O_2 ash in a barrel reactor at 200W for 35 min, and another set was subjected to O_2 ash alone.

To compare the sensitivity of liquid junction to detect the changes in the dielectric properties due to the RIE treatment with that of solid state devices such as metal-oxide-semiconductor (MOS) and Schottky barrier (SB) devices, the MOS and SB devices for Si and Si subjected to various RIE were made.

The MOS capacitors were fabricated by IBM according to the following procedure: After RIE, the wafers were cleaned using an O_2 ash, followed by an HF dip and an RCA cleaning, to remove metallic contaminants. The wafers were then oxidized (900°C, dry O_2), forming a 500 Å SiO_2 layer. Patterned aluminum was deposited on the front end and blanket aluminum on the back of the wafers; then the devices were annealed at 400°C for 20 h in forming gas (90% N_2 + 10% H_2).

Schottky barrier diodes were fabricated by a 15 s HF dip to remove the native oxide, followed by deposition of either patterned Al (5000 Å) or Ti (500 Å) on the front end of the wafers. Ti contacts were used always except on the series of samples that were exposed to $CClF_3/H_2$ RIE, where Al contacts were used.

The pattern and the thickness of the front metal contacts in the SB and MOS junctions, made for the impedance measurements, were different from those in the optical spectroscopy experiments; they were 500 Å metal dots and 75 Å metal blankets, respectively. For the impedance measurements the front metal contacts were made using a mask with dots of different areas. The largest ones have been chosen to make the electrical contact. Its area, measured with an optical microscope, was $0.0183 cm^2$. An untreated substrate was always used as a control in these configurations.

For liquid junction measurements, the ohmic contacts were made by rubbing Ga-In eutectic on the back surface of the sample and the sample was attached to a copper holder with silver print. The back and edges of the sample were covered with Miccrostop (trademark of Pyramid Plastics Incorporated, Tolber Division) and

only the front surface was exposed.

2] Cell configuration

In the liquid junction configurations these samples have been studied in a conventional three-electrode cell. Platinum foil with large area was used as a counter-electrode and a Pt wire, placed as close to the semiconductor as possible, as a reference electrode.

The methanolic solutions were prepared under nitrogen atmosphere, using methanol distilled over Mg and oxidized and reduced dimethylferrocene with $LiClO_4$ as the supporting electrolyte. This solution was shown to provide efficient and stable photovoltaic response for Si [15]. For the impedance and photo I-V measurements, the methanolic solution was used with the following composition: 0.2M $FeCp_2$, 1mM $FeCp_2^+$ and 1M $LiClO_4$. The potential of this solution was measured as 0.138V versus standard calomel electrode (SCE). For the electro-reflectance measurements, the methanolic solution was changed to the following composition: 0.01M $FeCp_2$, 50μM $FeCp_2^+$ and 1M $LiClO_4$. The potential of this solution was measured as 0.075V vs SCE. The low concentration of the ferrocene derivatives (5% of the regular solution that is used for photovoltaic applications) was used to reduce the absorption of the electrolyte and to facilitate the optical measurement. The aqueous electrolyte was composed of 0.25M NH_4F/0.01M $K_3Fe(CN)_6$/0.01M $K_4Fe(CN)_6$/H_2O [114].

3] Wet etching

(a) Silicon samples.

HF etching samples were subjected to 55% HF solution etching for 20 s to remove the native oxide layer on the surface.

(b) RIE samples.

Chemical etching was performed in a buffered HF (buff HF) and 2M KOH solutions. The composition of the buffered HF solution was 58.6% H_2O, 34.6% NH_4F, and 6.8% HF in weight [72]. Before and after dipping the samples in the 2M KOH solution, they were subjected to a quick etching in the buffered HF solution for about 1 s, to avoid the passivation of the surface.

4] Experimental conditions

(a) Impedance spectroscopies.

The frequency range was from 0.01 Hz to 10 MHz. The amplitude of the alternating field was 40 mV. In liquid junction configuration, the dc bias varies from -0.7 V to 0 V vs Pt for untreated silicon samples, and from -2.0 V to 0.5 V vs Pt for RIE samples. In SB configuration, the dc bias range from -0.5 V to 0.5 V with respect to the metal front contact and in the MOS configuration, the dc bias varies from -10 V to 3 V vs metal contact.

(b) Modulation spectroscopies.

The modulation frequency was 750 Hz. The modulation amplitude was 150 $mV_{p\text{-}p}$ for EER.

3.4.2 $CuInSe_2$ [115-117]

The $CuInSe_2$ work was done in collaboration with Dr. D. Cahen. The n-

$CuInSe_2$ single crystals were obtained from Rincon [118], and from Bachmann [119], through the Solar Energy Research Institute. They had a normal doping level of 10^{16}- 10^{17} cm^{-3}, Hall mobilities of 600-850 $cm^2V^{-1}s^{-1}$ and resistivities of 1-10 Ω-cm. Most of them were cut along the <112> orientation. The crystals were polished to 0.05 μm finish with alumina powder. The ohmic contacts and coverage of the electrodes with Miccrostop were similar to that of the Si samples. The electrodes were mounted in a N_2-purged solution of either Na_2S:S:NaOH 1/1/1M or 6M KI + 0.1M CuI_2 + 0.1M InI_3 + 0.0125M I_2 at pH 6.0. A Pt foil was used as the counter-electrode, and a Pt wire as the reference electrode. The redox potentials of the two solutions are -0.75 V and +0.3 V vs SCE, respectively.

The etching procedure was 2% Br_2/MeOH for 60 sec followed by rinsing with MeOH and then dipping in 10% KCN for 1 min. The KCN dip is used to dissolve any free Se that might precipitate on the surface after etching [43]. The air oxidation of the sample was done at 150°C for 2 h.

The impedance spectroscopies were carried out in the polyiodide solution and the EER measurements were carried out in both polysulfide and polyiodide solutions.

A solid-state junction was prepared using a sample heated 2 h in air at 150°C, and then contact was made with silver print on the front surface. The current-potential characteristics of the solid-state junction were measured using a Model 576 Curve Tracer (Tektronix).

3.4.3 InSe [45,80]

The InSe work was done in collaboration with Dr. C. Levy-Clement. The n-InSe crystals were obtained from A. Chevy; they were GaS-doped with 10^{15} cm^{-3} carriers and mobility of 600 $cm^2V^{-1}S^{-1}$. InSe is a lamellar compound; its two different crystalline surfaces exhibit different chemical and physical properties. The cleavage surface is the (001) plane, perpendicular to the c axis, and consists of selenium atoms bonded with covalent forces (⊥ electrode when exposed to the electrolyte). The other surface is the (110) plane parallel to the c axis and is made of selenium atoms bonded together by van der Waals bonds and of indium atoms bonded by metallic bonds (∥ electrode when exposed to the electrolyte). Ohmic contacts at the back of the InSe were made by soldering small rods of In at 350°C under H_2 atmosphere. The crystals were encapsulated in resin (Dow Corning 3145 RTV) with only the chosen surface left exposed to the electrolyte. Best results were obtained when the two types of surfaces were used without pretreatment.

A three-electrode airtight system was used to avoid oxidation of the electrolyte. The counter and reference electrodes were Pt wires. The electrolyte used for the modification of n-InSe is similar to the one used for $CuInSe_2$ by Menezes [36,38,39]: KI/HI/I_2/CuI in ratios of 1/y/0.05/x M. x was varied between 0.02 and 0.57M while y was equal to 2M for $0.02<x<0.2$M and 4M for $0.2<x<0.57$M. The increase in the concentration of acid was necessary to permit the dissolution of large amounts of CuI [45]. A polycrystalline compound is formed on the cleaved surface of InSe. The growth of this polycrystalline layer involves a

procedure very similar to the growth of the interfacial film on $CuInSe_2$. Several potentiostatic cycles between the open-circuit potential and short-circuit conditions lead to the same results compared with leaving the electrode at the maximum power point under a load.

Since the InSe has poor long term stability in electrolyte, PR was chosen to characterize it. The impedance measurements were carried out in an electrolyte with the following composition: 1M KI/0.05M I_2/2M H_2SO_4.

CHAPTER 4

SILICON AND ITS REACTIVE ION ETCHING

4.1 Potential distribution of silicon/methanol interface [73]

4.1.1 Photo and dark I-V

Figure 4.1 shows an example of the light-induced current-voltage characteristics of a Si sample in contact with the methanolic solution in which the light source was chopped at low frequency. The photocurrent-voltage plot for the original sample only starts to show photoeffect at potentials positive to -0.5 V. The turn-on potential, i.e., the most negative potential for which charge separation can be detected, can be extracted to be -0.58 V vs Pt.

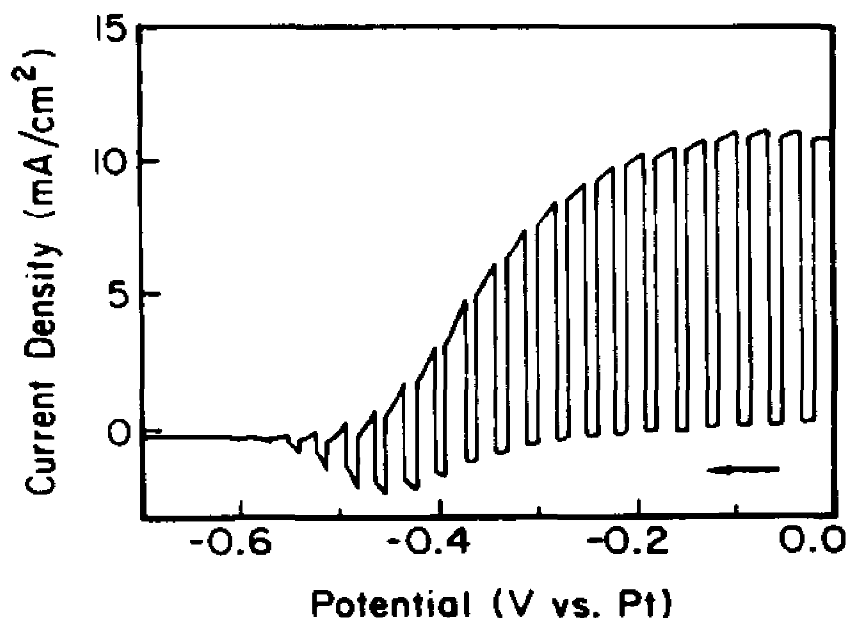

Figure 4.1 Current-potential response with chopped white light for unetched <100> *n*-Si in methanolic solution of oxidized and reduced dimethylferrocene in the following concentrations: 0.2M $FeCp_2$, 1mM $FeCp_2^+$, and 1M $LiClO_4$ supporting electrolyte. Tungsten halogen ELH lamp with light intensity at the electrode surface of 100 mW/cm^2. The sweep rate is 10 mV/s.

Figure 4.2 depicts the dark and photocurrent-voltage curves of the Si in the same electrolyte, before and after etching with HF. The main effects of etching are increases in the short-circuit current and in the fill factor. Typical values of the short-circuit current density (J_{sc}) and open-circuit voltage (V_{oc}) are about 15 mA/cm^2 and 0.5 V, respectively. The cells and the samples were not optimized for efficiency.

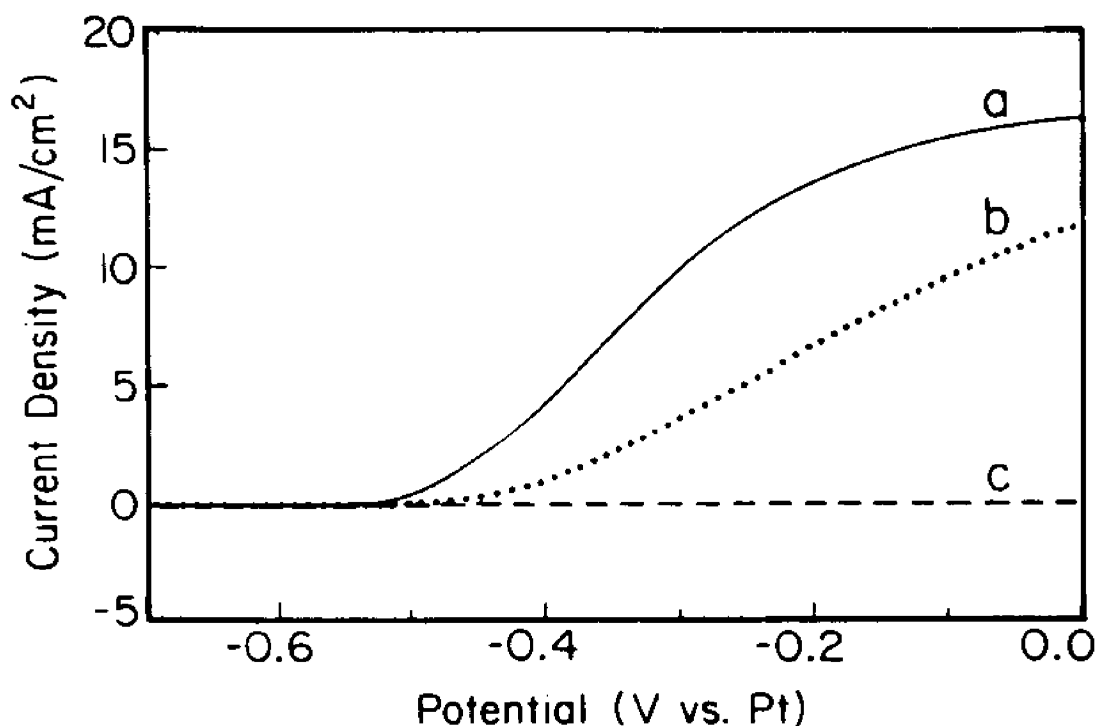

Figure 4.2 Current-potential curves of two samples: one original and the other subjected to HF etching process. (a) Photoresponse of HF etched Si, (b) of unetched Si, and (c) dark response of both samples. Electrolyte and other experimental conditions are the same as in Fig. 4.1. Photovoltaic parameters extracted from these curves: J_{sc} = 12.4 mA/cm^2 and V_{oc} = -0.503 V (original); J_{sc} = 16.3 mA/cm^2; and V_{oc} = -0.519V (after HF etching).

Figure 4.3 shows the dark current-voltage plot of the original sample. The same features were observed for the HF etched one. In this figure a peak occurs in the same bias region where the pinning of the Fermi level was observed from the EER data. The charge density that corresponds to this peak is about $1.1\times10^{16}/cm^2$. The dark current could not be fitted to the diode equation with any reasonable ideality factor.

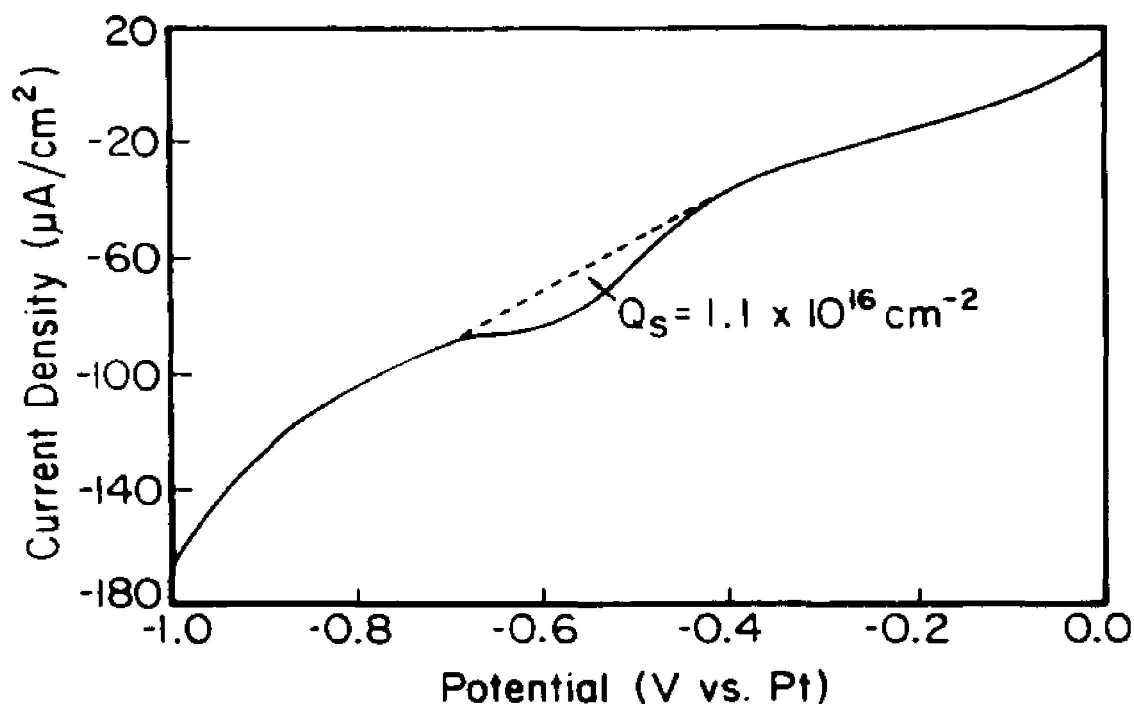

Figure 4.3 Dark current-potential plot of the original sample in the methanolic solution of the same composition as described in Fig. 4.1. The calculated charge density associated with the peak is shown on the figure.

4.1.2 Electroreflectance

Figure 4.4 shows the electroreflectance, under different bias conditions, for the sample subjected to the HF etching.

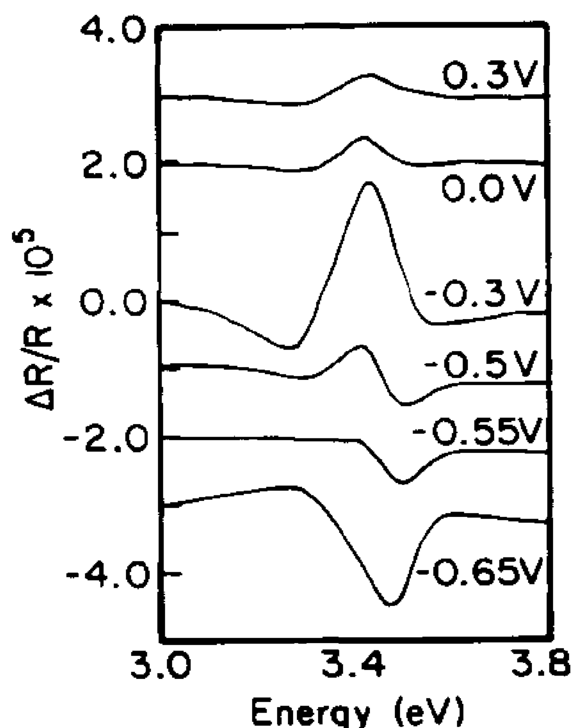

Figure 4.4 Electroreflectance spectra of HF etched Si in the same electrolyte as in Fig. 4.1 except for the dimethylferrocenes that were diluted by a factor of 20, as a function of the electrode potential vs Pt. The modulation amplitude is 0.15 V_{p-p} and the modulation frequency is 740 Hz.

The electroreflectance of Si in the 3.0-5.0 eV regime was analyzed in detail by numerous workers both in electrolyte configuration [120] and in Schottky barrier configurations [121]. The electrolytes were never chosen based on their stabilizing effect and as a result the state of the surface and the potential distribution at the interface were not well defined.

The electroreflectance of Si in the UV region is very complex. The 3.5 eV regime was proposed to be due to two critical points [121] E_0' and E_1 with the E_1

being the strongest high-energy transition. In the experiments with liquid junction these transitions never can be resolved. Since the primary interest is in the potential distribution and not in the spectroscopic features, the spectra in this study will be analyzed in terms of the number of resolved peaks only. Figure 4.5 is an example of a spectrum taken in the methanolic solution at a potential of 0.0 V vs Pt and the corresponding fit of the line shape to Eq.(2.130) with the following parameters: E_g = 3.407 eV, Γ = 0.17 eV, θ = 4.18 and n = 3.0, which indicates a two dimensional critical point. One can see that the fit is excellent and there is no need to invoke a second peak.

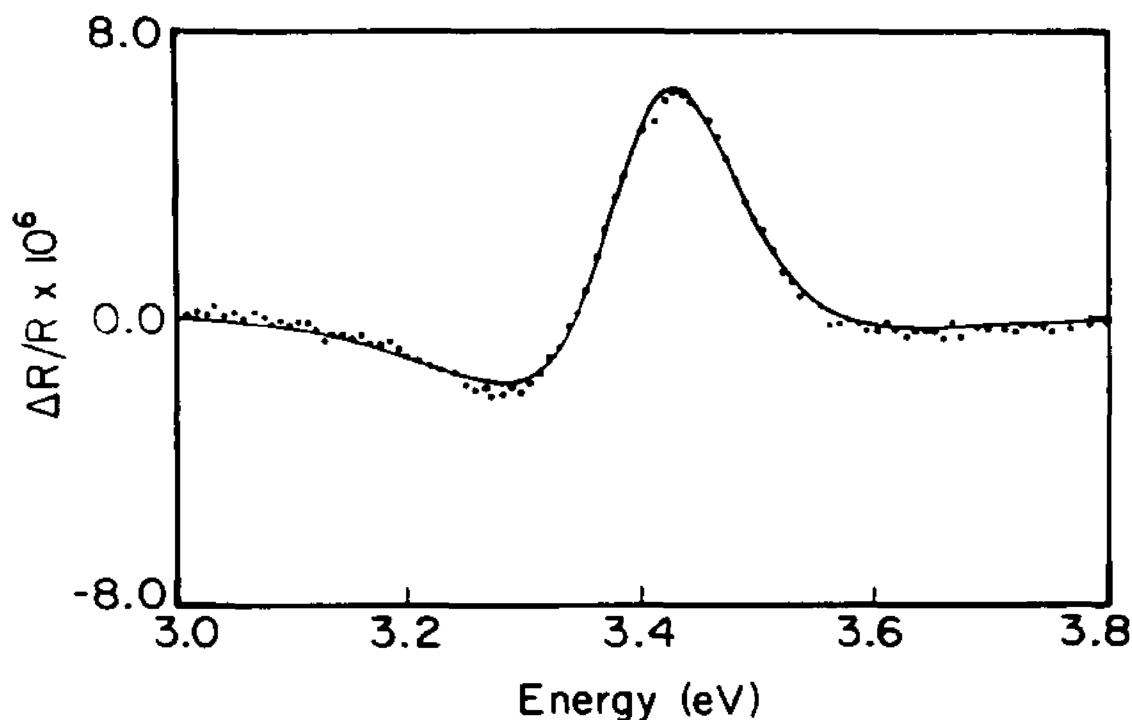

Figure 4.5 Comparison of observed (points) and calculated (solid line) line shape of the spectrum at 0.0 V vs Pt. Fitting parameters: C= 6.4×10^{-4}; E_g = 3.407 eV; Γ = 0.17 eV; θ = 4.18 rad; and n = 3.0.

Figure 4.6 shows the potential dependence of the amplitude of the peak for the Si sample before HF etching (b) and after (a). In this figure the potential dependence of the EER amplitude is plotted for two potential excursion directions. The data were taken after equilibrium was reached at each potential. Comparing Fig.4.6(a) and 4.6(b) it is observed that the original sample presents a broader bias distribution and a small hysteresis effect in the potential sweep. These features can be related to the presence of an oxide layer on the top of the semiconductor. For both samples the flat-band potential can be observed as the potential in which the signal changes sign. For the unetched sample the potential is between -0.66

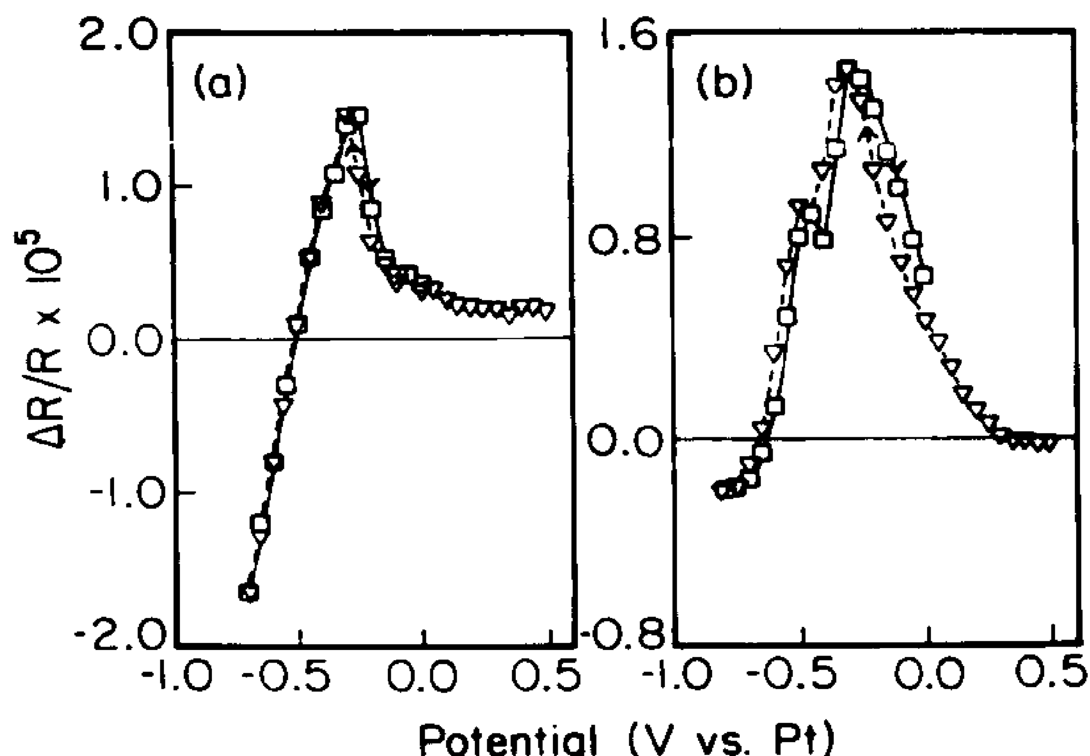

Figure 4.6 Variation of the amplitudes of the 3.4 eV EER peaks with the electrode potential: (a) after HF etching and (b) before etching. The potential sweep rate was 5 min. per experimental point. The lines are drawn for convenience of inspection. The arrows indicate the direction of the potential sweep.

V and -0.63 V vs Pt, depending on the direction of the sweep and for the etched sample it is at -0.51 V vs Pt. The Fermi level is partially pinned at a potential about -0.4 V vs Pt and it is completely pinned at positive potentials (reverse bias). HF etching reduces the pinning, both due to the states close to the conduction band and in the reverse bias region, and also decreases the hysteresis.

Figure 4.7 presents the potential dependence of the EER amplitude using the aqueous electrolyte with the composition described in the experimental section [114]. The electroreflectance was very noisy and the photocurrent very small. The behavior does not show the reverse bias pinning that was observed with the methanolic electrolyte. The flat-band potential is around -0.81 V vs Pt.

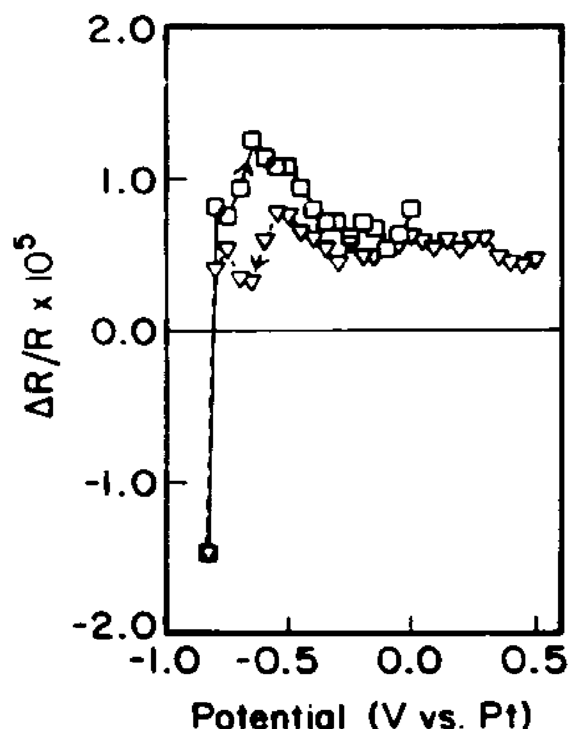

Figure 4.7 The same as Fig. 4.6 but with the aqueous electrolyte with the following composition: 0.25M NH_4F/0.01M $K_3Fe(CN)_6$/0.01M $K_4Fe(CN)_6$/H_2O.

The pinning at reverse bias is interpreted to be due to inversion of the surface [122] that is facilitated by the presence of the oxide layer. The Fermi level in this region is never completely pinned in the samples subjected to HF etching in which most of the oxide is removed. This effect is much more pronounced in the aqueous electrolyte in which the F^- ions dissolve any oxide that is being formed. The pinning region, observed at forward bias, is interpreted to be due to surface states. In principle, more quantitative information can be derived based on fitting these data to Eq.(2.147) [106], but since this equation is strictly valid for the low-field regime, none of the two pinning regimes fits the conditions for which this equation was derived.

The term "Fermi-level pinning" is used to describe a situation in which the difference between the electrode potential and the flat-band potential is independent of the electrode potential. This definition follows the electrochemical practice in which equilibrium experiments are performed as a function of the electrode potential that is measured relative to a nonpolarizable reference electrode. Within this framework the rest potential (zero bias) has no special significance. It is assumed here that the electrode potential is a measure of the position of the Fermi level relative to the standard electrode, and as a result Fermi level pinning describes the situation in which the Fermi level is pinned to the position of the band edges at the surface and the barrier height is independent of the position of the Fermi level relative to the reference electrode. This definition follows earlier practice [123] and it is a generalization of the definition often used to describe

solid-state devices in which the term Fermi level pinning is used only to describe the condition under zero bias. Following this practice the terminology of Fermi-level pinning and band-edge movement as a function of potential becomes synonymous.

4.1.3 Impedance

Figure 4.8 presents typical impedance data and the fitting with the equivalent circuit shown in the insert. Similar spectra were recorded for the etched and unetched samples over the potential range that corresponds to forward bias conditions.

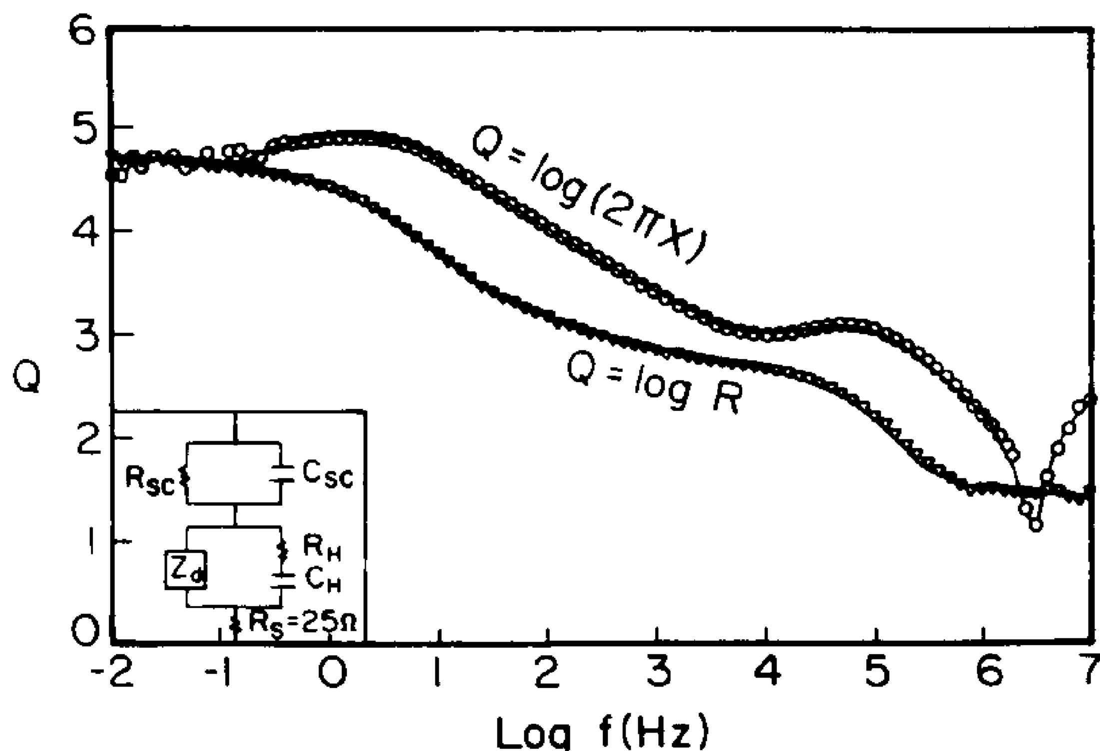

Figure 4.8 Impedance response curves for HF etched n-Si in the methanolic solution with the same composition as described in Fig. 4.1. Potential is -0.2 V vs Pt. The symbols represent experimental data for the real and imaginary parts of the impedance. The solid lines represent numerical fits to the equivalent circuit shown in the left-hand corner.

The impedance responses of Si/methanolic solution could not be fitted in terms of a single junction and the least square procedure should be used to the fitting. Figures 4.9-4.11 show the potential dependence of the two capacitive elements in Fig.4.8 for the various samples. Figures 4.9(a) and 4.9(b) depict the Mott-Schottky plots of the space charge layer capacitance C_{sc}, for the HF etched sample and for the unetched one. The flat-band potentials that were obtained from the intercept are -0.76 V vs Pt for the HF etched sample and -0.86 V vs Pt for the unetched one. The doping levels were obtained from the slopes, which yielded $4.7\times10^{15}/cm^3$ for the etched sample and $2.2\times10^{15}/cm^3$ for the unetched sample. The apparent difference in the doping level is due to the increase in roughness resulting from etching. The pinning of the Fermi level around -0.4 V vs Pt can be observed here better than with the EER results. The 0.1 V shift in flat band due to the removal of the oxide agrees well with the EER results. However, the flat bands are about 0.2 V more negative than those obtained from the EER. The primary reason for the discrepancy is the difference in the composition of the electrolyte, although some contribution due to the different amplitude of the ac signal cannot be ignored. This is supported by the results in the aqueous electrolyte shown in Fig.4.10. Here the flat band is -0.79 V vs Pt and the doping level is $2.2\times10^{15}/cm^3$. The flat-band here agrees within 0.02 V with the EER result taken in the same electrolyte. The doping level in this electrolyte is identical with the unetched sample in the methanolic solution and the pinning of the Fermi level is also evident here at about the same energy position from the conduction band

as in the methanolic solution. If one takes the capacitance of the Helmholtz layer to be ~20 μF/cm^2 then the number of surface states responsible for a shift of 0.1 V for the HF etched sample is 1.6×10^{13}/cm^2 and about double that for the unetched sample [55]. The fact that these states are present, with similar densities and energy, in the methanolic and the aqueous electrolytes and that similar states can be identified in the corresponding Schottky structure discussed in §4.4, suggests that they are not due to interactions with the electrolytes.

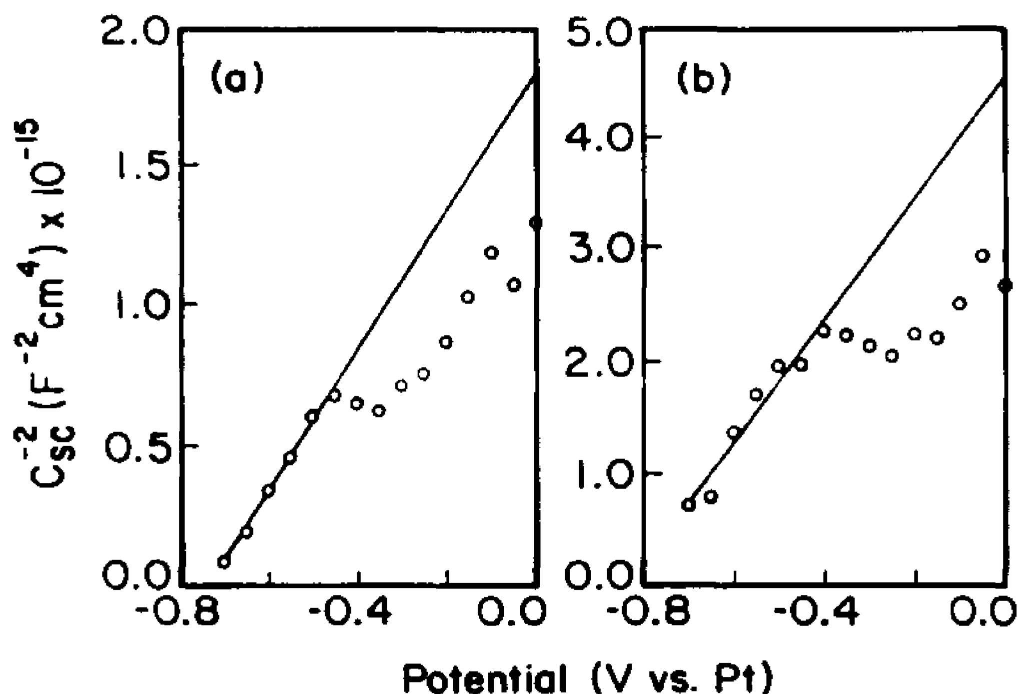

Figure 4.9 Mott-Schottky plots of n-Si in the methanolic solution described in Fig. 4.1. (a) HF etched sample. V_{fb} = -0.76 V vs Pt and N_d = 4.7×10^{15}/cm^3. (b) Original sample. V_{fb} = -0.86 V vs Pt and N_d = 2.2×10^{15}/cm^3.

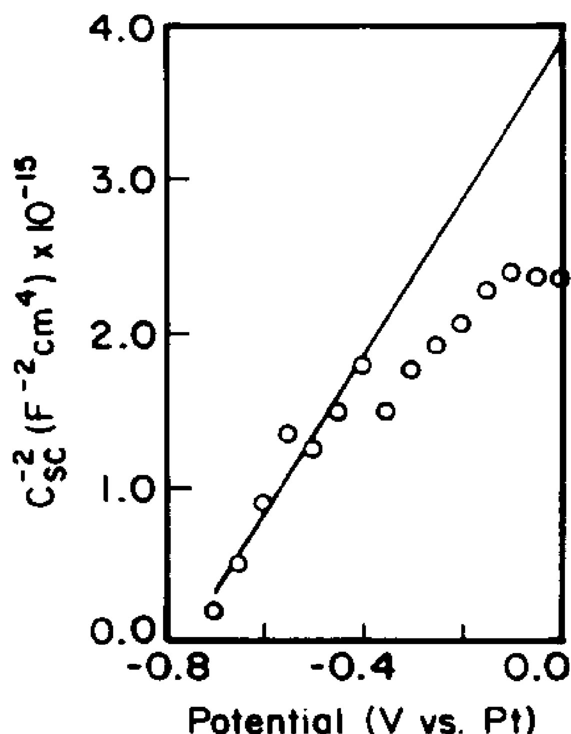

Figure 4.10 Mott-Schottky plots of n-Si in the aqueous electrolyte described in Fig.4.7. V_{fb} = -0.79 V vs Pt and N_d = 2.3X10^{15}/cm^3.

C_H and its corresponding R_H are interpreted in terms of adsorption of the electrolyte at potentials negative to the surface states that cause the Fermi level pinning. This interpretation is not based on the equivalent circuit, which places these elements in series with the space-charge layer. An almost equally good fit can be obtained by placing them in parallel to the space-charge layer that would have been the case if these elements were interpreted to result from the surface states that cause the Fermi-level pinning. The estimated coverage from Fig.4.11 is about 5×10^{14}/cm^2. This is an order of magnitude greater than the number of states calculated to be responsible for the Fermi-level pinning (or the corresponding negative shift in the flat-band potential). In addition, to account for the negative

shift in the flat band, one has to assume adsorption by the negatively charged counter ions. Since almost identical shifts are observed for the methanolic and aqueous electrolytes with no ions in common, one was forced to assume that the Fermi level pinning and its corresponding shift in the flat-band potential are due to negatively charged surface states that are filled as the Fermi level crosses the energy of these states. These states are not coupled with the electrolyte, but the filled states act as catalytic centers in the precipitation of the positively charged redox species.

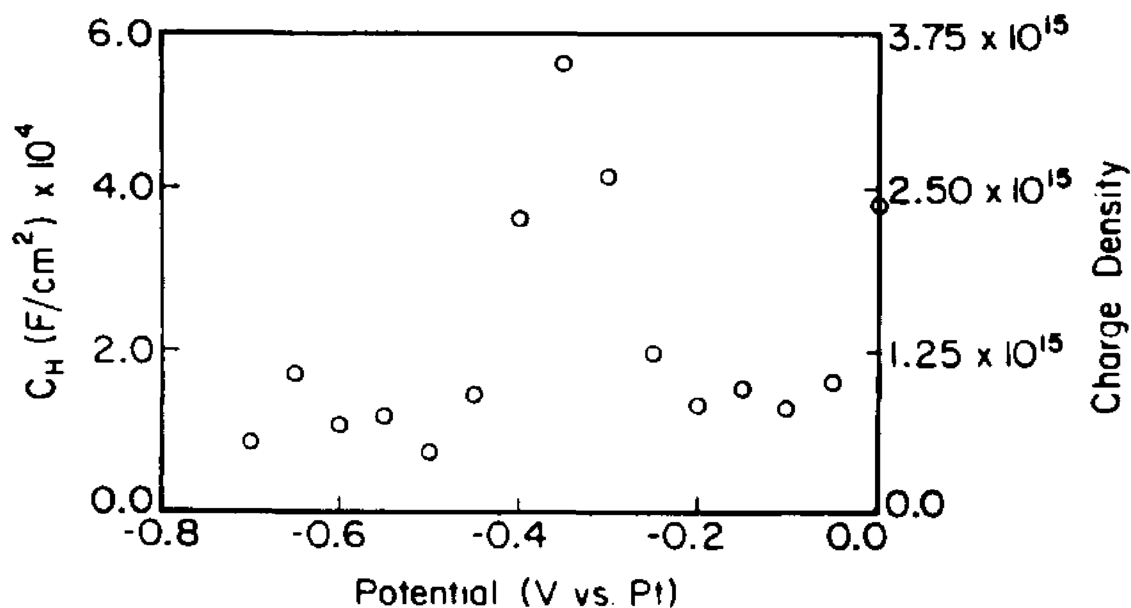

Figure 4.11 Potential dependence of C_H of the HF etched sample. The ordinate depicts the charge density/eV.

Z_d was identified as due to a porous oxide layer that can be almost completely removed by HF etching. N and $n\tau/N$ are the low frequency resistance ($\omega\tau \ll 1$) and the low frequency capacitance of this layer. The exponent n is related to the transport mechanisms within the material. Figure 4.12 shows that n is almost independent of potential, having a value close to 0.6. This, and the sensitivity to HF etching, strongly suggests that it results from transport through a porous layer. Using the limiting values for N and τ one can estimate the thickness of this porous oxide layer. For the HF etched sample this value is about 3 **Å** and for the original sample it is 26 **Å**. These numbers agree with the current understanding of the oxide on unetched Si [124] that predominantly originate from ex situ measurements. From the CPA data one can, in principle, build a more detailed analysis of the porosity profiles of this layer but the application of effective medium theories to a layer with atomic thickness is suspect enough to prevent any further "analysis". The presence of a porous oxide layer on the surface of the semiconductor is also supported by photo I-V and electroreflectance measurements. The photo I-V characteristics of the cell improve after HF etching (Fig.4.2), which is a well known procedure to remove SiO_2 [125]. The electroreflectance hysteresis effect in the potential sweep, and the broader bias dispersion for the original sample compared to the HF etched sample (Fig.4.6), are also consistent with the presence of an oxide layer on the original sample.

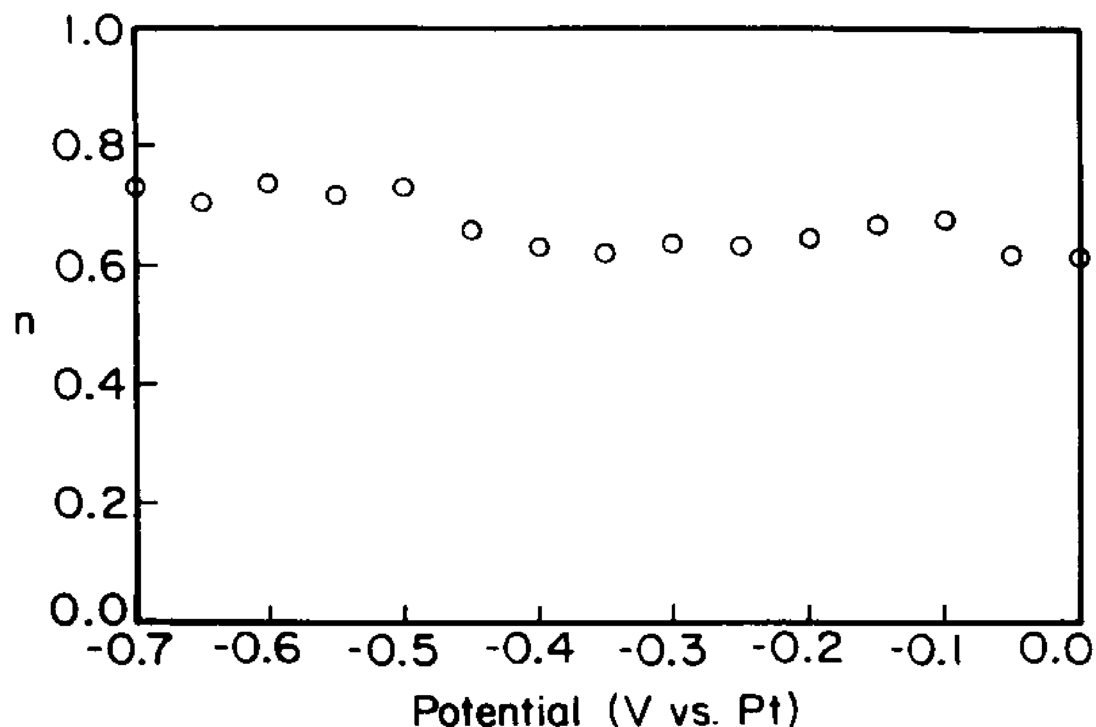

Figure 4.12 **The potential dependence of n [Eq. (2.70)] of the HF etched sample.**

4.1.4 Proposed band diagram of Si/methanol system

Summarizing the above results, the band diagram of the Si/methanol system can be represented in figure 4.13. Going from reverse to forward bias (V vs Pt increasing negatively) on Fig.4.13 one first observes the pinning of the Fermi level due to the presence of the minority carriers in the inversion region. The Fermi level is again partially pinned at 0.2 eV below the conduction band due to surface states. According to our results the pinning is more pronounced for non-treated surfaces. This indicates that these states are coupled to the oxide layer. Finally the potential reaches the flat-band value, which is about -0.8 V vs Pt. The potential distribution in aqueous electrolyte is very similar to the one in the methanolic

solutions.

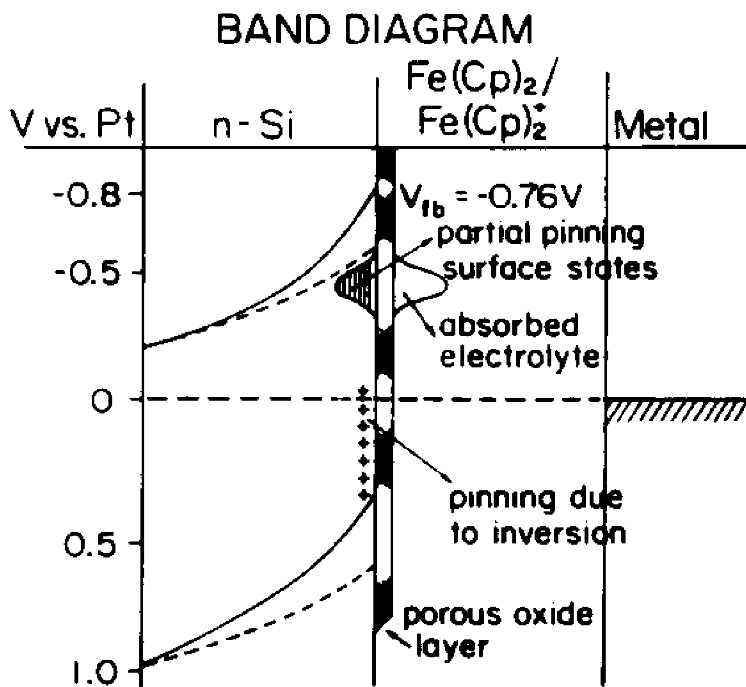

Figure 4.13 The proposed band-structure diagram of the Si/methanol in this work.

This potential distribution has to be reconciled with the results of Rosenbluth and Lewis [15] in which they obtained a linear dependence of the open-circuit voltage and the oxidation-reduction potential from which they conclude that the Fermi-level of this system is not pinned. First it has to be emphasized that the two experimental methods in question of analyzing Fermi-level pinning are sensitive to different pinning mechanisms. The method used by Rosenbluth and Lewis [15] to analyze the variations of the open-circuit voltage with the oxidation-reduction potential of the electrolyte, is analogous to the analysis of the open-circuit voltage as a function of the metal work function in metal-semiconductor junctions, and

monitors pinning due to coupling of the surface states with the electrolyte. The impedance and the EER data here monitor the charge accumulation in the space-charge layer as a function of the position of the Fermi level, and are sensitive to pinning of the space-charge layer to alternative charge equilibration mechanisms such as surface states, unpinning of the band edges through surface charging, pinholes, pinning through the electrolyte, or any other mechanism. Close analysis of Rosenbluth's results [15] reveals that the Fermi level is unpinned over a potential range of 0.4 eV that roughly corresponds to the energy difference between the short-circuit potential and the potential of the surface states, in full agreement with our data. Since they were monitoring the open-circuit voltage, which is zero for potentials negative to the potential of the surface states, one cannot compare the data at potentials negative to that of the surface states. The strong hysteresis that they observe can be interpreted to be due to adsorption of the electrolyte. The kind of pinning described here that results in a negative shift of the band edges due to charging of the surface states can be viewed as a combination of battery + photovoltaic cell and offers the possibility of a higher photovoltage.

4.2 The effect of media on photoreflectance [108]

4.2.1 Low-field limit of PR and EER

Photoreflectance (PR), at moderate light intensities, is currently understood in terms of light-induced modulation of the photovoltage that produces an

electroreflectance signal [102] so one expects that the ER and the PR spectra will be similar.

The features of electroreflectance of Si in the 3.5 eV regime were described in § 4.1.2. The ER in the 4.2-4.9 eV was analyzed in terms of a cluster of critical points (the E_2 region) of which only few were resolved experimentally and labeled $E_2(l)$ where l=1,2,3, etc., with the first transition being the strongest [126]. Figure 4.14 shows the PR over the energy range of 3.0-5.0 eV at 77K in which one can clearly observe the E_1 and the E_2 regions of Si. In our experiments, with few exceptions that will be mentioned later, both in liquid junctions and without any

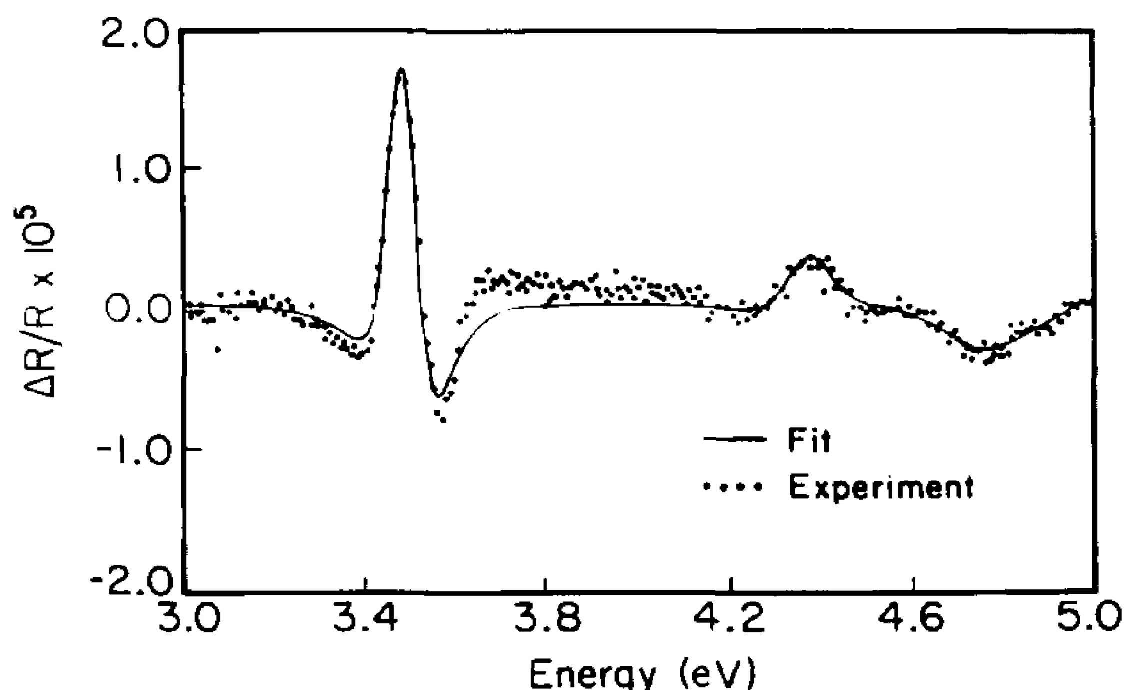

Figure 4.14 Comparison of observed (points) and calculated (solid line) line shape of the PR spectra of n-Si at 77K. Modulation source: 7.5 mW He-Ne laser; modulation frequency: 750 Hz. Fitting parameters: In the E_1 region: E_g = 3.489 eV, Γ = 0.087 eV; In the E_2 region: $E_g(1)$ = 4.382 eV, $\Gamma(1)$ = 0.135 eV; $E_g(2)$ = 4.786 eV, $\Gamma(2)$ = 0.347 eV.

junction, using EER, PR, or photoreflectance in the presence of an electrolyte (EPR), at room temperature or at 77K, our resolution was limited to a single peaks in the E_1 region and two peaks in the E_2 region.

Figure 4.14 also shows an example of such a fit of the line shapes in the two energy regions. In all cases the spectra were fitted with n=3.0, indicating two-dimensional critical points [121]. The fit is much better for the high-energy range than for the low-energy range. One obvious reason is that since the high-energy region is fitted for two peaks the number of adjustable parameters was doubled. The one peak fit in the low-energy region is obviously not perfect. One reason is the presence of unresolved peaks that was mentioned before. Another possible reason is that the line shape is dominated by the random distribution of electric fields due to defects. This is supported by the insensitivity of the line shape to temperature in the range 77-300K. This issue was addressed by Raccah et al.[127] in which they argue that under these conditions the third derivative line shape is not adequate and one has to add first- and second-derivative terms that were interpreted in terms of electrostricture and polarization of the defects. Attempts to fit our spectra to this generalized functional form have resulted in much better fitting. However, two more parameters are needed for these fits and in spite of the physical sense that this generalization makes in our case, it is our belief that our resolution does not justify inclusion of these terms that might only contribute to overinterpretation of the data. The same reasoning holds for not trying to assess any contribution from Gaussian line shapes that were recently suggested [128] for

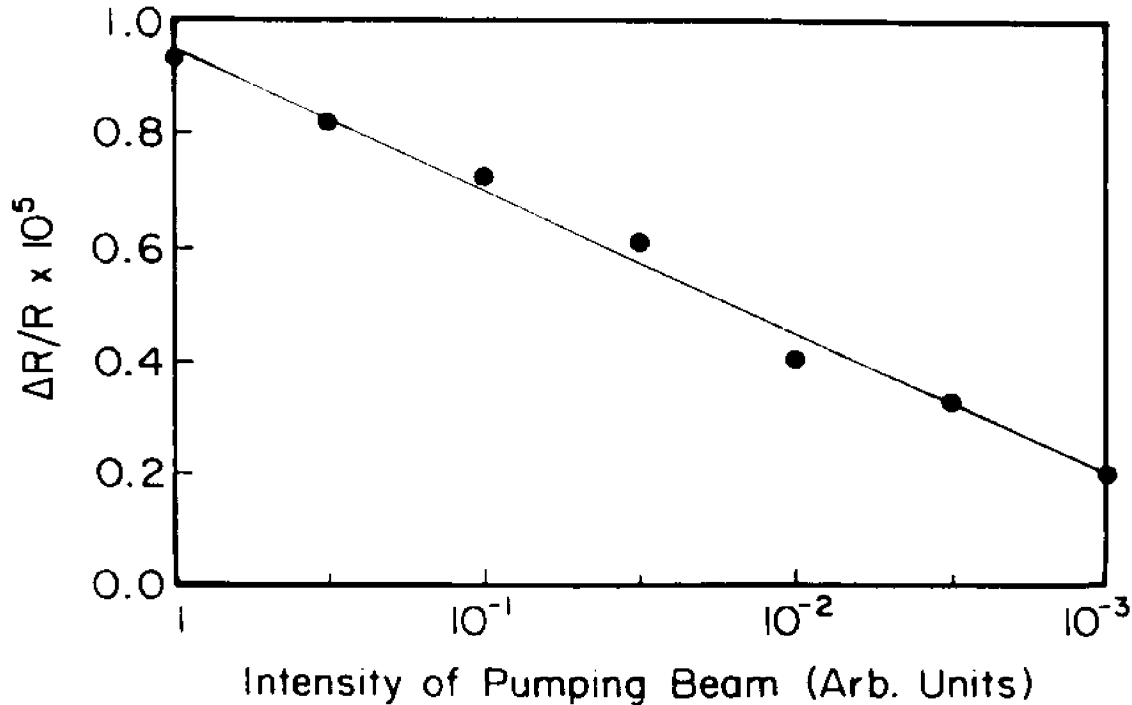

Figure 4.15 Dependence of the PR signal of n-Si on the light intensity of the modulated beam.

inhomogeneous broadening.

For the EER measurements it was verified that, around the rest potential, experiments were in the low-field regime by working only in the linear regime of amplitudes of the EER signal versus the modulation. The modulation amplitude was kept constant typically at 150 mV $_{p\text{-}p}$. The low-field regime is more difficult to verify with PR and EPR since the modulation is through the photovoltage.

Figure 4.15 shows, we believe for the first time, the expected logarithmic dependence of the PR signal on the light intensity of the pumping beam over more than three orders of magnitude of intensity. This result serves as a direct experimental verification of the origin of the modulation in the PR experiments and it also indicates that as long as one is in this linear regime the low-field approximation of the line shape should apply.

4.2.2 Effect of electrolyte on line shape of modulation spectrum

Figure 4.16 shows a comparison of the PR, EER, and EPR spectra of n-Si. Upon introduction of the electrolyte the signal broadens with an increase in Γ by more than a factor of 2. Figure 4.17 compares the EER spectra of untreated silicon in the methanolic and aqueous electrolytes. The spectrum in the aqueous electrolyte was noisy because the surface of Si is continuously oxidized by the light-induced minority carriers and the oxide is etched by the F^- ions. The peak position in the two electrolytes is exactly the same while the line broadening for the aqueous electrolyte is in between that of the PR and the methanolic solution.

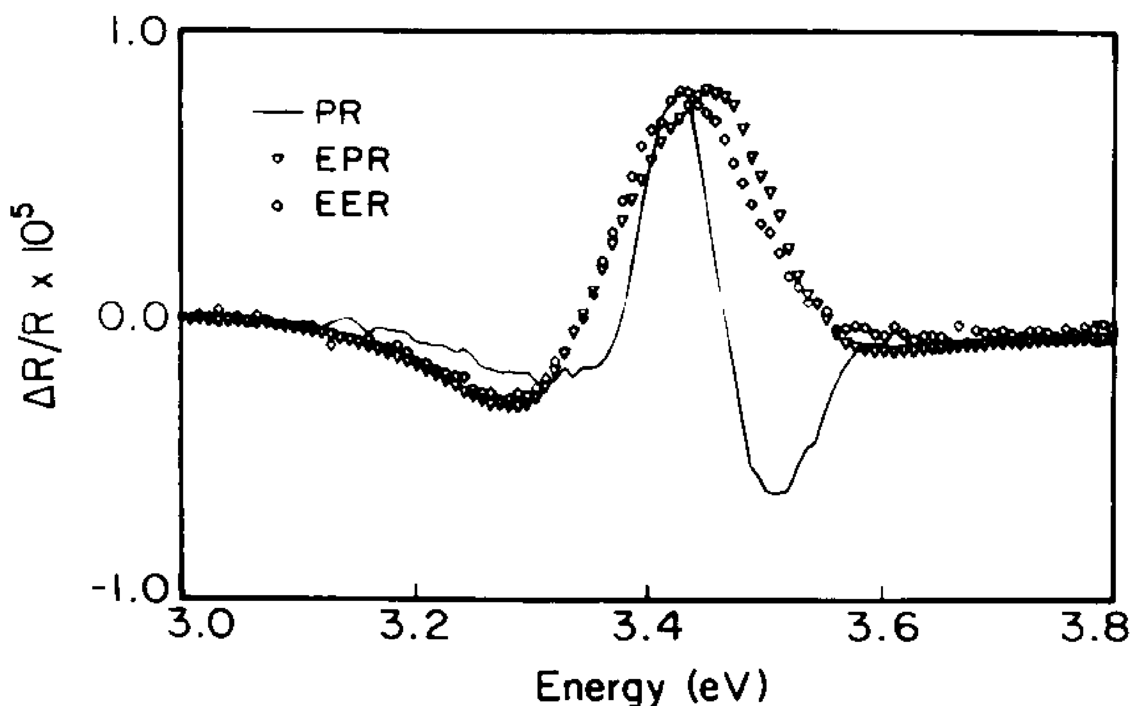

Figure 4.16 Comparison between PR, EPR, and EER of n-Si. The EPR and the EER were measured in the methanolic solution of oxidized and reduced dimethylferrocene in the following concentrations: 0.01M $FeCp_2$, 50μM $FeCp_2^+$, and 1M $LiClO_4$ supporting electrolyte. The EPR was measured under open-circuit conditions and the EER at a potential of 0.0 V vs Pt. The chopping frequency in all cases is 750 Hz.

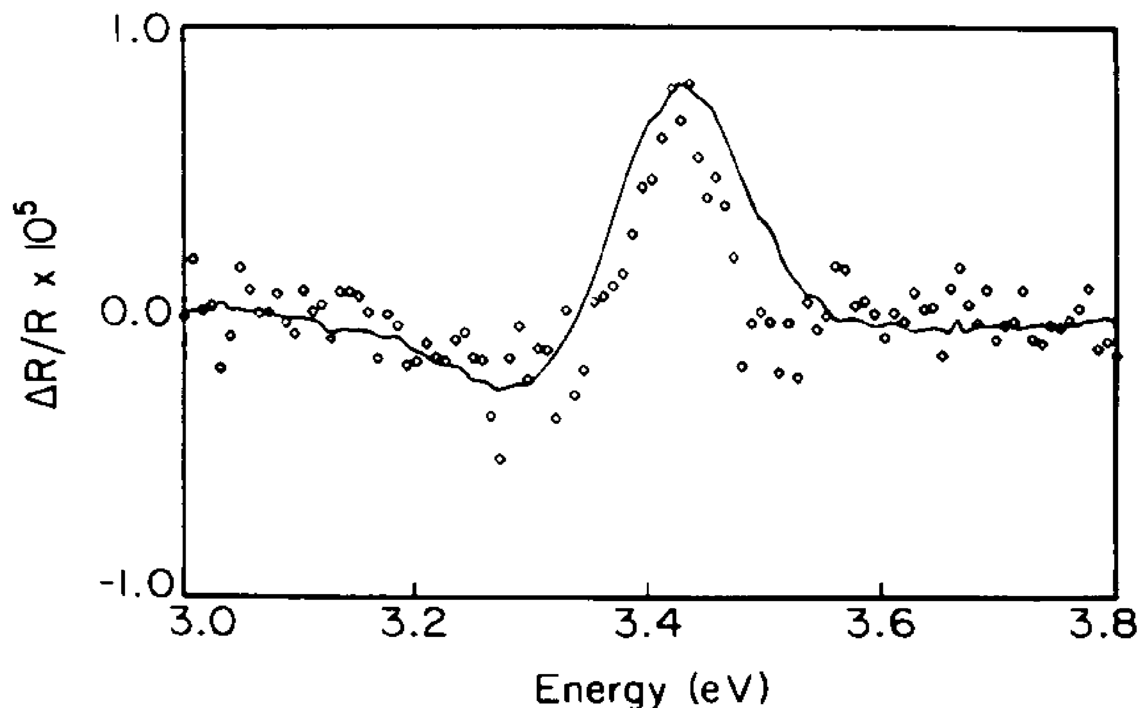

Figure 4.17 Comparison of the EER of n-Si in two different electrolytes: The same methanolic solution as in Fig.4.16 (solid line) and an aqueous electrolyte (open diamonds) with the same composition as in Fig. 4.7. The experimental conditions are the same as in Fig.4.16.

Figure 4.18 shows the EPR spectra only in methanol and in the methanolic ferrocene solution. These spectra are identical. To clarify further the effect of the electrolyte, the PR spectrum of the Si electrode in a cell without electrolyte was measured at first, then the methanolic solution was injected into the cell and the EPR spectrum was measured again. For another set of experiments, the EPR in the methanolic solution was measured, then the Si electrode was cleaned with methanol and after the surface of Si was dried, the PR measurement in the cell without electrolyte was taken. The PR spectra of both sets had the same line shape and the line-shape of the EPR spectra of both sets were the same but

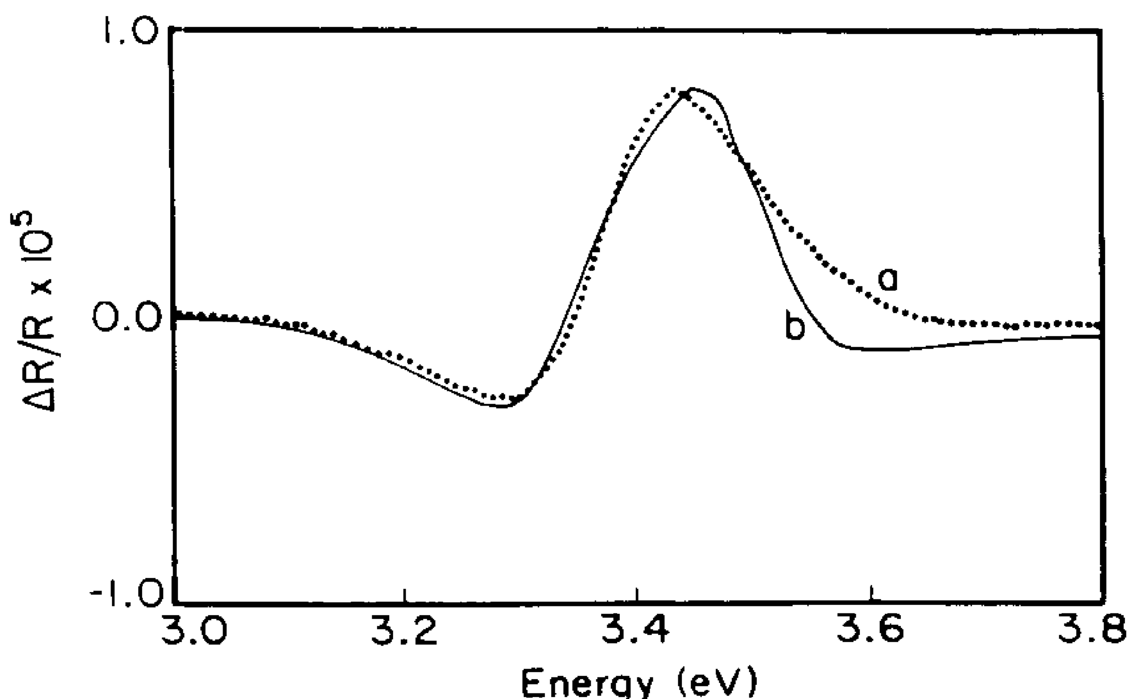

Figure 4.18 Comparison of the EPR spectra of the n-Si in (a) methanol and (b) the methanolic solution. Experimental conditions are the same as in Fig. 4.16.

different from that of PR. This indicates again that the distortion of the line shape results from the electrolyte and the process is reversible, with the line shape of the modulation spectrum recovering to that of the original Si after the electrolyte is removed from surface. These results strongly suggest that the broadening of the line shape upon introduction of the electrolyte is caused by surface states at the interface that are being modified by the solvent. One mechanism that can be associated with surface states that might cause such broadening is a deviation from the low-field regime due to an increase in the surface potential upon introduction of the electrolyte. This hypothesis can be directly tested by performing the EPR measurements as a function of the electrode potential. These results are

shown in figure 4.19 from which it is easy to see that the line shape is independent of the electrode potential over the entire relevant potential range. Figure 4.20 shows the dependence of the amplitude of the EPR peak on the electrode potential. The flat-band potential approximately agrees with the one that was obtained using EER. However, while EER results have shown strong Fermi-level pinning at reverse bias conditions, the EPR results show no pinning (the amplitude does not change with the electrode potential at positive potentials). The EER pinning was interpreted to be due to band shifts resulting from inversion at the surface. Apparently the inverted surface has no effect on the photovoltage created by the light-induced carriers.

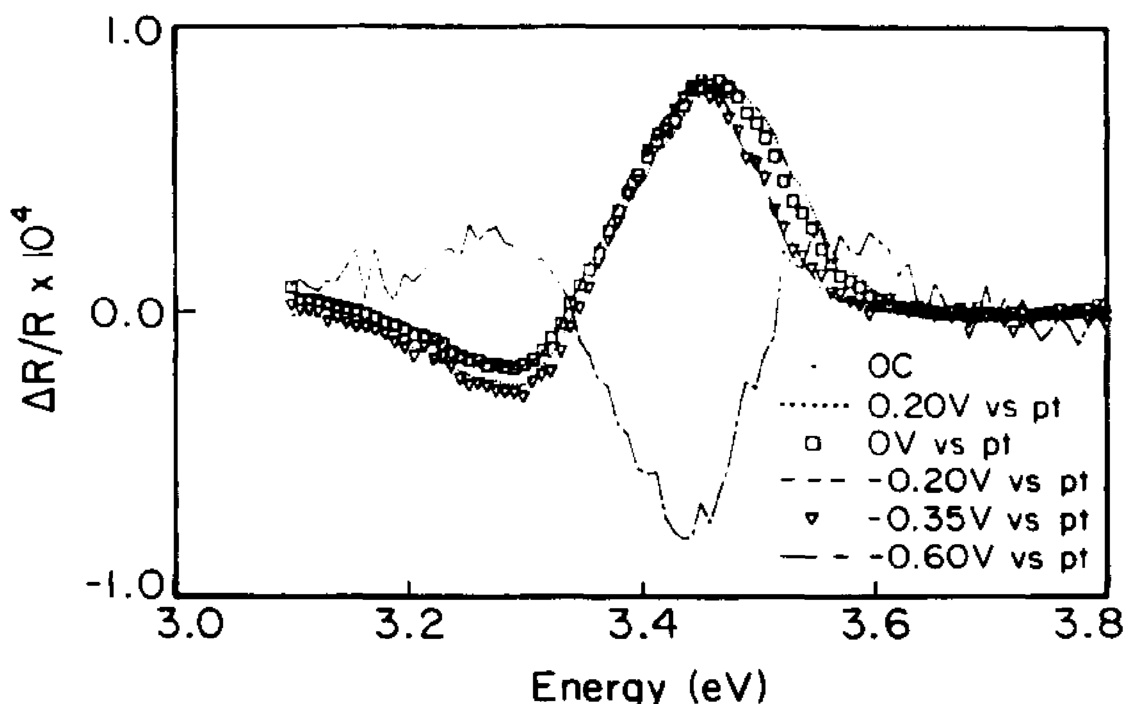

Figure 4.19 The EPR of n-Si in the methanolic solution at different electrode potential. The spectra are normalized for the same amplitude.

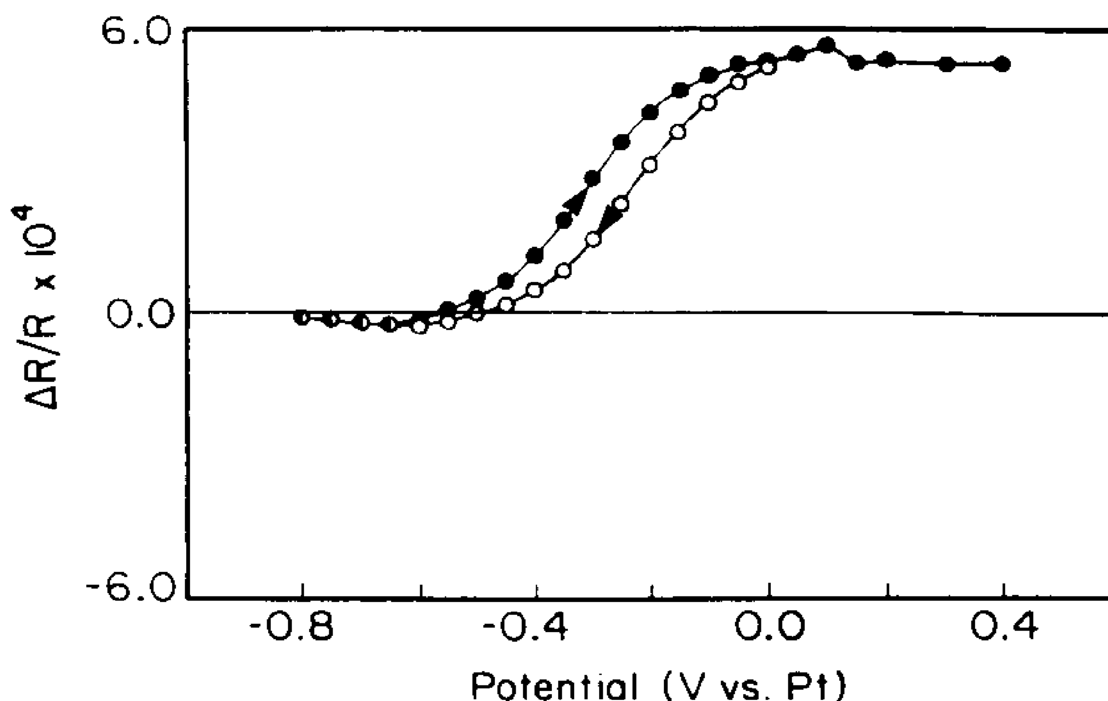

Figure 4.20 **The potential dependence of the amplitude of the EPR peak of n-Si in the methanolic solution. Arrows indicate the direction of the sweep.**

4.2.3 Effect of the electrolyte on the relaxation times of the surface states

Figure 4.21 compares the EPR spectra of n-Si in the methanolic solution at the high and low chopping frequency limits. The spectra are identical. Figure 4.22 compares the frequency dispersions of the amplitude of the PR and the EPR transitions. The PR response is flat except at the very low frequency limit. From this result it is assumed that the states responsible for the PR signal have relaxation times slower than 50 ms. The EPR response is shifted to the high frequencies and Fig.4.22 also shows the fit of the experimental results to Eqs.(2.160)-(2.162). The presence of the electrolyte is decreasing the relaxation times by more than an order of magnitude. These data were analyzed in terms of

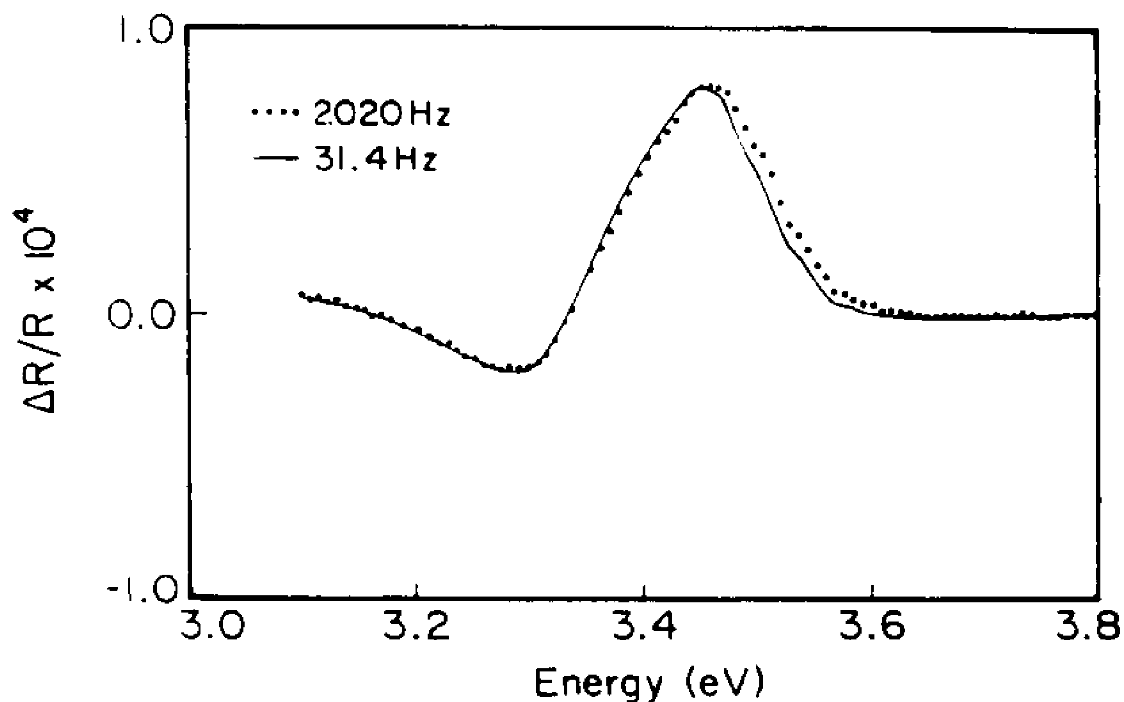

Figure 4.21 EPR spectra of n-Si in the methanolic solution at two different chopping frequencies.

two sets of surface states, one with relaxation time of 0.51 ms and the other with 6.5 ms with about 40% weight of the faster states. There is no way of determining the energy of these states. The temperature variation of the relaxation times should provide this information. The available temperature window in the presence of an electrolyte is very limited. The temperature dependence of the frequency dispersions of the PR and EPR of this system is not yet available. In the impedance studies of this system, the response of the surface states cannot be directly detected. The surface states were detected indirectly through their effect on Fermi-level pinning and their catalytic activity on the adsorption of the electrolyte. They were placed at about 0.2 eV below the conduction band. Since their

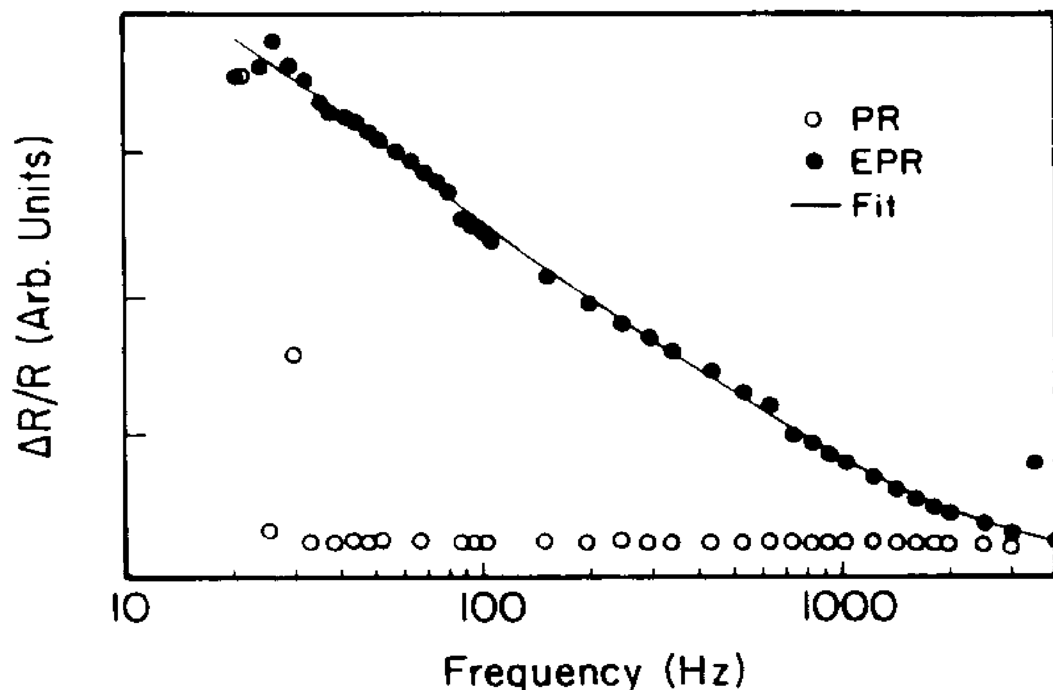

Figure 4.22 Comparison of the frequency dispersion of PR and EPR of n-Si in the methanolic solution and the theoretical fit of the EPR results to Eq.(2.162) with the following parameters: τ_1 = 0.5 ms, τ_2 = 6.5 ms, and the ratio of the two coefficients is 0.65.

relaxation times are not available from the impedance measurements, direct comparison to the present results is presently impossible.

4.2.4 Summary

The reversible changes in line shape of the photoreflectance signals occur upon introduction of the electrolyte. These changes are electrolyte dependent, being more pronounced in the methanolic solutions than in the aqueous electrolyte. The methanol itself proved to be the constituent that drives these changes. The effect of the electrolyte is interpreted to be due to modifications of the kinetics of equilibration between the surface states and the space-charge layer. This is

supported by the frequency dispersion experiments in which it is demonstrated that the presence of the methanolic electrolyte causes a decrease in the relaxation time of the surface states by more than an order of magnitude. The physical mechanism, through which the surface states induce the line-shape changes, has failed to be identified. It has been proved that it is not due to departure from the low-field regime due to changes in the surface electric field.

An additional point of interest, to the best of my knowledge, that was demonstrated here for the first time, is the difference in Fermi-level pinning as measured by EER and EPR. Again comprehensive theoretical reasoning cannot be proposed to explain this but it is suggested only that the effect is connected with the different carriers that are responsible for the modulated electric field in the two experiments.

4.3 Characterization of the damage of Si due to RIE [111,112]

4.3.1 Modulation spectra of Si subjected to various RIE

Figure 4.23 shows the PR spectra at 77K, over the spectral range of 2.6-5.0 eV, of the various RIE treated samples and the untreated Si, in which one can clearly observe the E_1 and E_2 regions of Si subjected to the various etching treatments. The response of the untreated n-Si served as a baseline for the discussion of the RIE treated samples. Figure 4.24 shows the magnification of these results for the energy range of 3.0-3.8 eV. The broadening and the red shifts of the peaks at about 3.4 and 4.3 eV for the samples subjected to different RIE

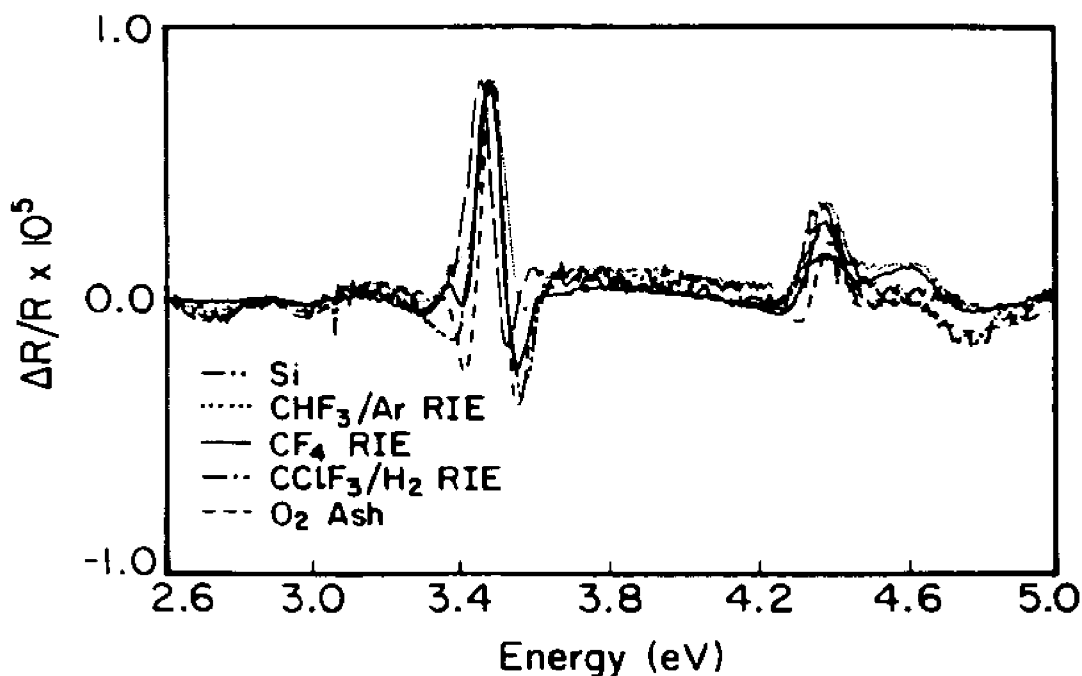

Figure 4.23 Photoreflectance spectra of n-Si subjected to various RIE treatments. Temperature 77K. The modulation source is 7.5 mW He-Ne laser; modulation frequency is 750 Hz.

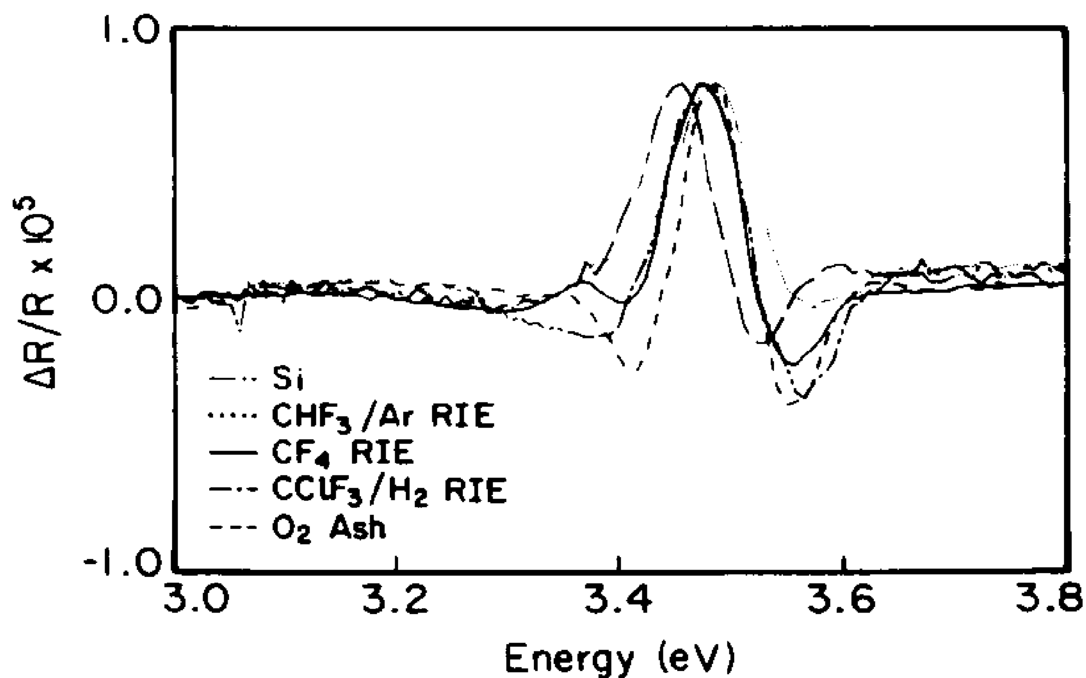

Figure 4.24 The same as Fig. 4.23 over an expanded energy scale.

treatments can be easily seen. Qualitatively similar results were obtained at room temperature using PR, EER, and EPR of the various RIE treated samples.

Figures 4.25(a) and (b) show an example of such a fit of the line shapes, in the two energy regions mentioned above, for an RIE treated Si. The results of these fits for the different experimental conditions are summarized in Table I-III.

Figure 4.26 is the comparison of the low-energy PR spectra of undamaged Si at 77K and room temperature (300K). A blue shift of 43 meV has been observed as the temperature was lowered. This shift agrees with previously published results [121] and corresponds to the increase in the band gap. The interesting feature there was that the line-width parameter Γ seemed to be temperature independent. This rules out phonon scattering [129] as the dominant mechanism that determines the line-width and leaves scattering by impurities as the most probable mechanism that determines the line-width for untreated Si. Figure 4.27 shows a similar comparison for CHF_3/Ar treated sample. The 300K spectrum is red shifted by about 40 meV compared to the untreated Si under the same condition and Γ is 145.5 meV, obviously broader than that of untreated one. Apparent narrowing in the line shape of the main peak and a shoulder at the lower energy end of the main peak can be seen at 77K. The 77K spectrum was analyzed in terms of two peaks one at 3.494 eV and the other at 3.364 eV. Γ of the main peak is 89.4 meV, not much different from that of the untreated sample. Similar results were also seen with the CF_4 treated samples.

Figure 4.28 compares the PR with that of the EER and EPR, taken in the

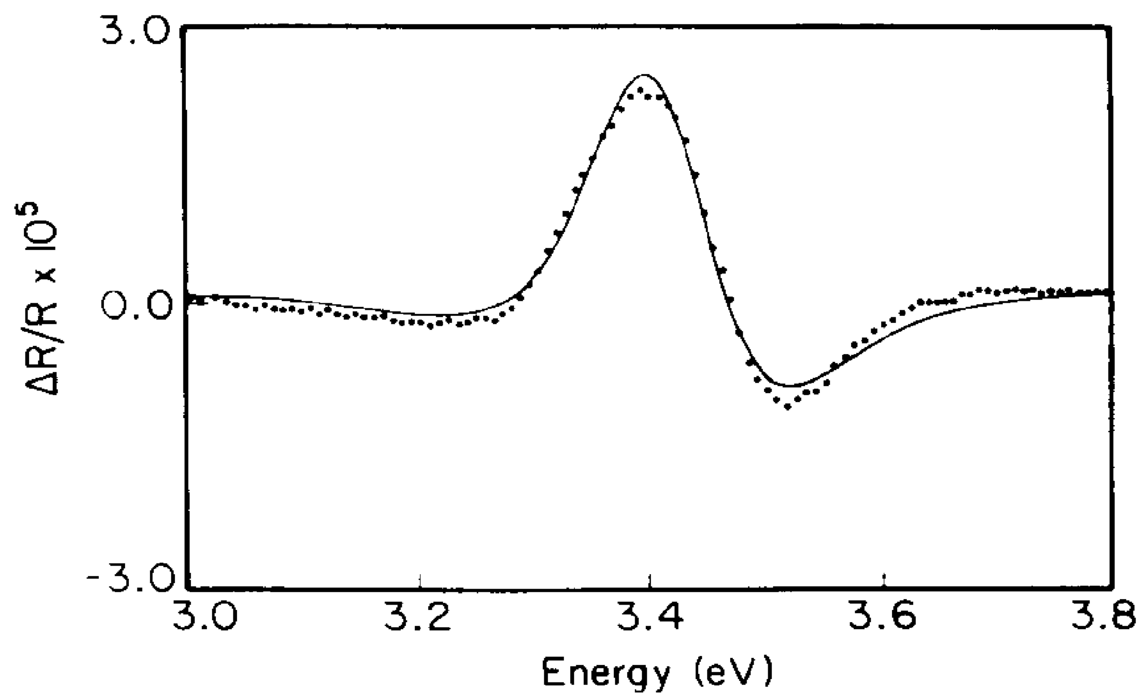

(a)

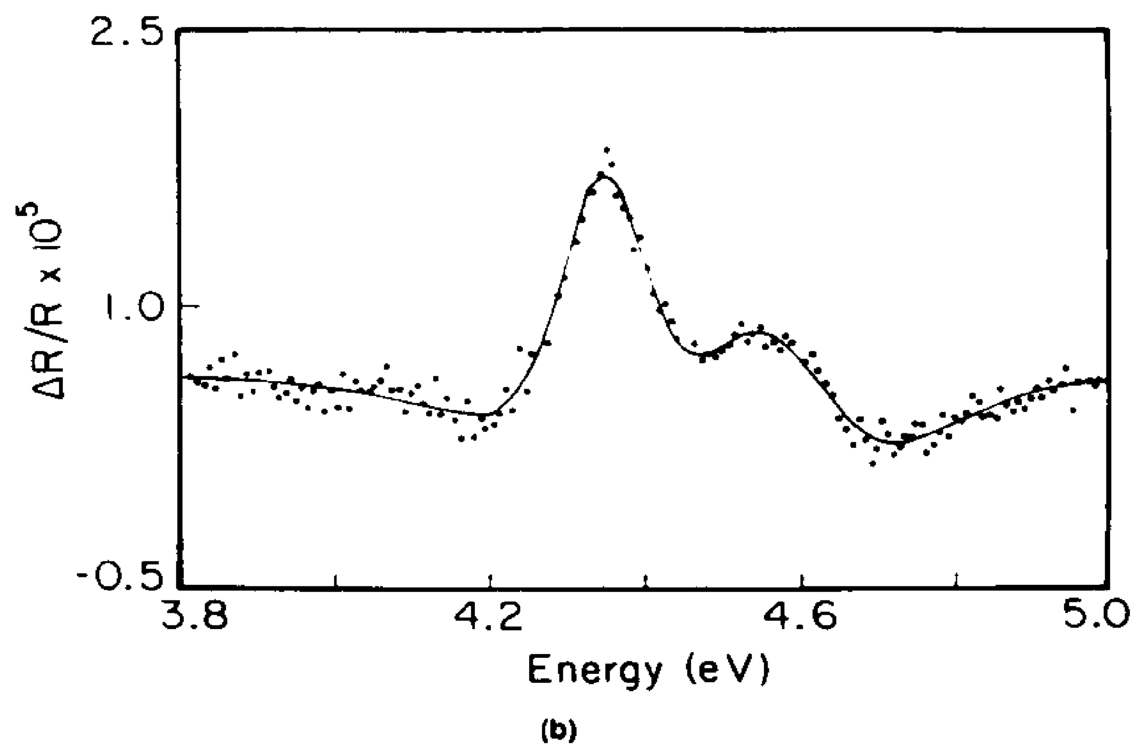

(b)

Figure 4.25 (a) Comparison of observed and calculated E_1 line shape of the PR at 300K of the CF_4 RIE-treated n-Si. (b) The same as (a) for the E_2 region.

TABLE I. Energy gaps and linewidth parameters of PR of Si and various RIE samples at 77K.

Sample	E_1 (eV)	Γ_1 (meV)	E_2 (eV)	Γ_2 (meV)
Si	3.489	87.1	4.382 4.786	135.4 346.8
CHF_3/Ar	3.364 3.494	186.0 89.4	4.377 4.757	124.8 337.8
CF_4	3.360 3.481	126.9 81.5	4.372 4.646	130.6 241.2
$CClF_3/H_2$	3.457	95.1	4.360	171.6
O_2 ash	3.494	67.5	4.390 4.833	92.1 378.9

TABLE II. Energy gaps and linewidth parameters of PR of Si and various RIE samples at 300K.

Sample	E_1 (eV)	Γ_1 (meV)	E_2 (eV)	Γ_2 (meV)
Si	3.446	82.4	4.300 4.335	348.4 113.2
CHF_3/Ar	3.406	145.5	4.336 4.645	156.6 264.2
CF_4	3.421	141.3	4.357 4.600	156.4 245.7
$CClF_3/H_2$	3.372	129.4	4.352 4.427	308.6 191.5
$CClF_3/H_2$ + O_2 ash	3.361	182.9	4.386 4.424	282.7 178.5
O_2 ash	3.418	125.0	4.337 4.626	128.7 284.4

TABLE III. Energy gaps and linewidth parameters of EER and EPR of Si and various RIE samples at 300 K.

Sample	EER		EPR	
	E_1 (eV)	Γ_1 (meV)	E_1 (eV)	Γ_1 (meV)
Si	3.407[a]	112.1[a]	3.407[b]	189.7[b]
Si	3.407	165.6	3.425	172.9
CHF_3/Ar	3.382	321.3	3.417	146.4
CF_4	3.353	246.2	3.427	155.2
$CClF_3/H_2$	3.361	165.2	3.376	145.3
$CClF_3/H_2$ + O_2 ash	3.360	150.1	3.380	150.9
O_2 ash	3.443	92.1	3.431	114.6

[a] Measured in the aqueous electrolyte.
[b] Measured in methanol.

methanolic solution, for the CHF_3/Ar RIE treated Si. The PR and EPR are almost identical but the EER is red shifted with broadening by another factor of 2 with a corresponding increase in Γ to about 270 meV. A similar situation can be observed with CF_4 RIE again.

Figure 4.29 shows the corresponding results for $CClF_3/H_2$ RIE in which the three sets of measurements are almost identical. These results are consistent with the formation of an RIE-modified top layer in which the surface states are isolated from the electrolyte. Figure 4.30 shows the frequency dispersion of the PR and EPR signals for the CHF_3/Ar RIE treated sample. For all other RIE treated

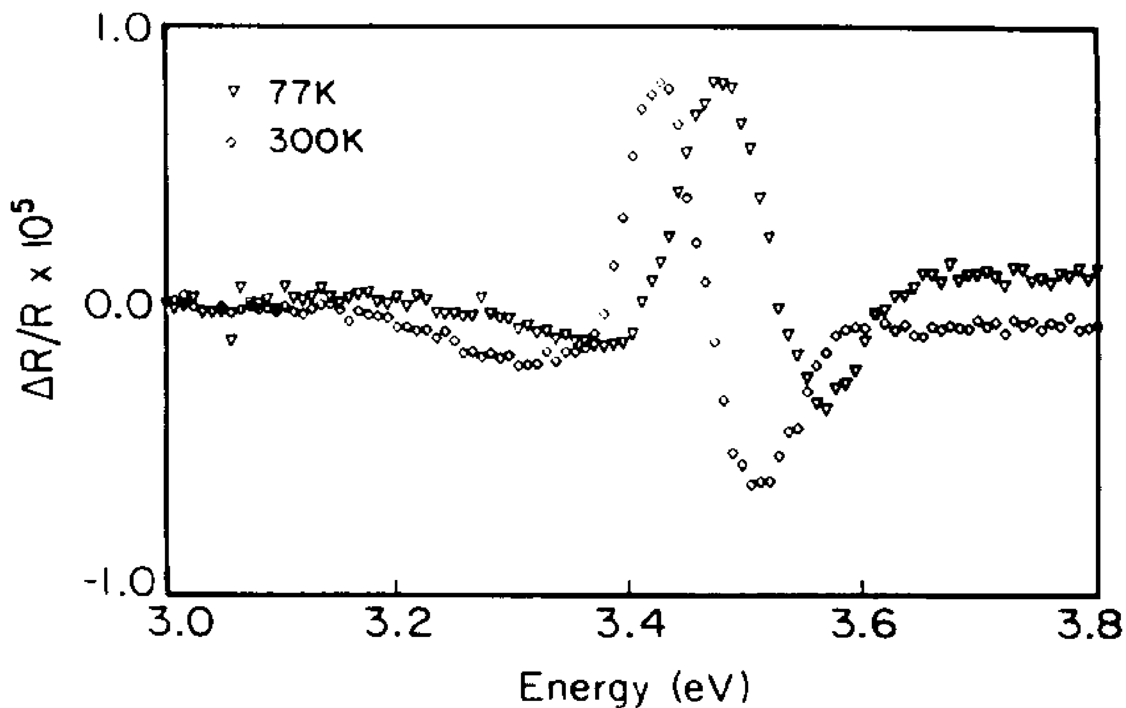

Figure 4.26 Comparison of the PR of n-Si at 77K and 300K. Same conditions as in Fig.4.14. The spectra are normalized for the same amplitude.

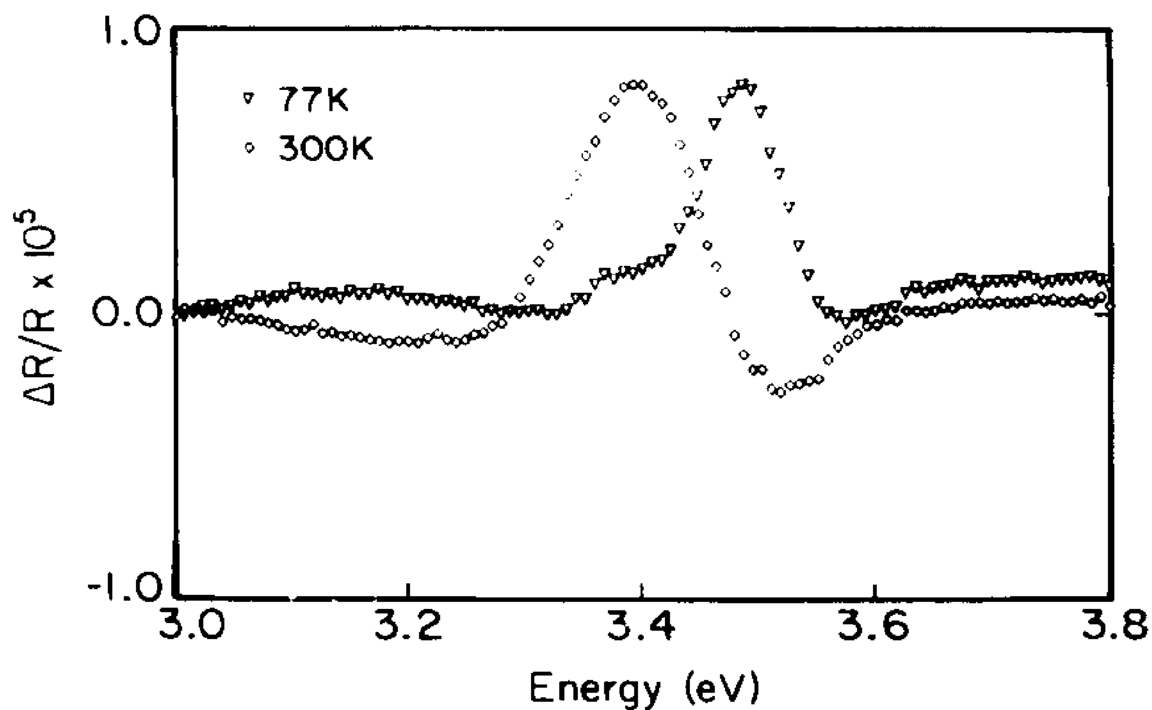

Figure 4.27 Comparison of the PR of CHF_3/Ar RIE-treated n-Si at 77K and 300K.

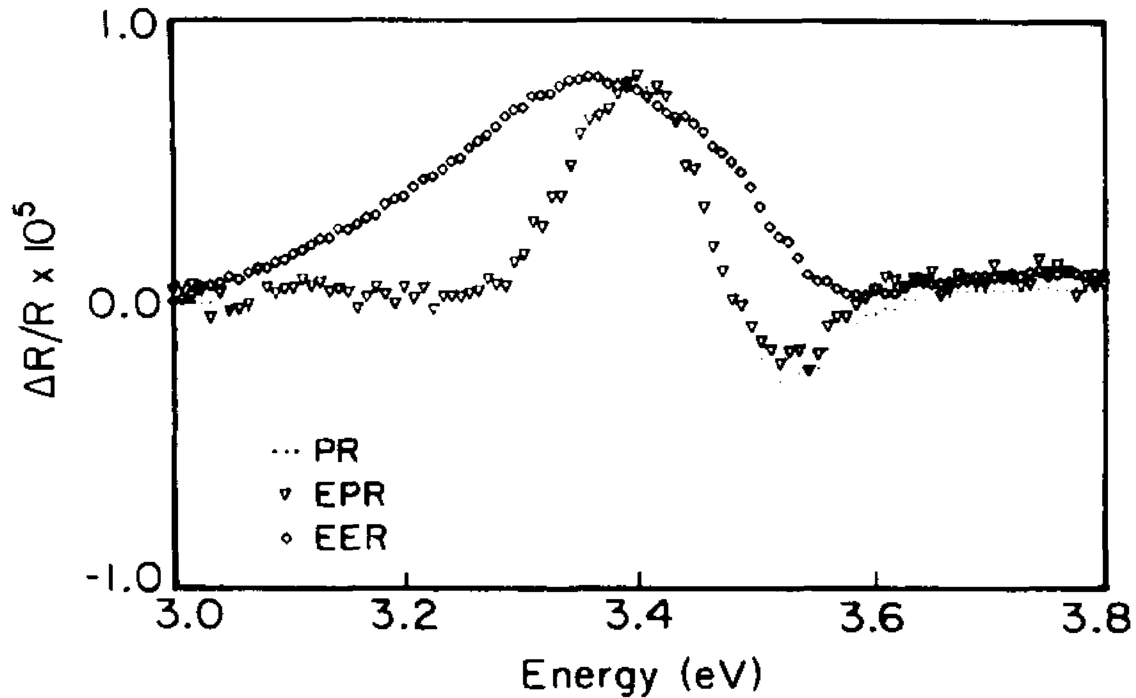

Figure 4.28 Comparison between PR, EPR, and EER for the CHF_3/Ar RIE-treated n-Si. The EPR and the EER were measured in the same methanolic solution as in Fig. 4.16.

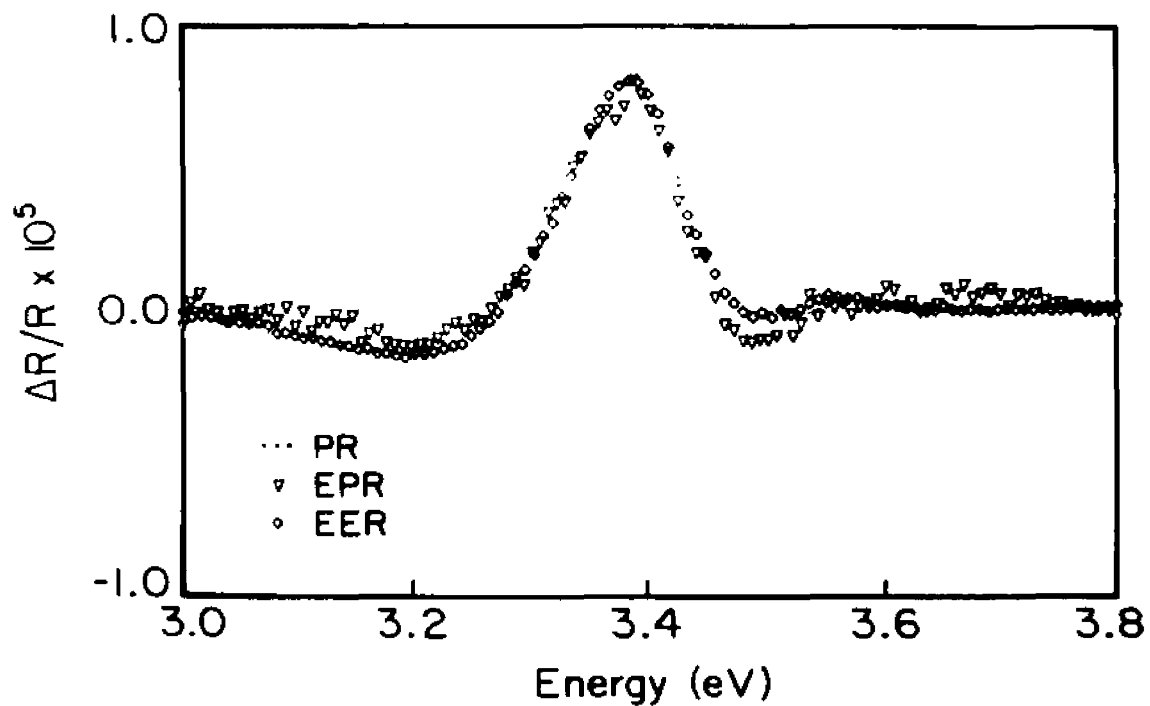

Figure 4.29 The same as Fig. 4.28 for the $CClF_3$/H_2 RIE-treated n-Si.

samples, the dispersions were the same. The electrolyte has no observable effect and in both cases the relaxation times are slower than 50 ms. For CHF_3/Ar RIE and CF_4 RIE samples, there is about 100 Å top layer damaged heavily [see § 4.3.3]. The difference in line shape between the EER and EPR of these samples might result from the difference in the penetration depth of the modulating light and the electric field.

Figure 4.31 shows the dependence of the amplitude of the EER transition on the electrode potential for untreated Si, CHF_3/Ar, and $CClF_3/H_2$ RIE treated samples in the methanolic electrolyte. The $CClF_3/H_2$ behavior is characterized by a 0.15 V negative shift of the flat band with an apparent disappearance of the pinning. A completely different situation is seen with CHF_3/Ar treatment. Over the potential range that is covered here, the EER amplitude is bias independent. A similar situation was observed with the CF_4 etching.

Figure 4.32 presents the bias dependence of the electroreflectance for the $CClF_3/H_2$, $CClF_3/H_2$ + O_2 ash, and O_2 ash RIE samples. Table IV presents the flat-band potentials obtained from these data.

4.3.2 Impedance spectra of Si subjected to various RIE

Figures 4.33(a) and (b) show examples of the impedance spectra at -0.4 V vs Pt, of the CHF_3/Ar [Fig.4.33(a)] and $CClF_3/H_2$ +O_2 ash [Fig.4.33(b)] treated samples. The equivalent circuits representing the impedance results are depicted in the inserts. The impedance spectra calculated based on the equivalent circuits

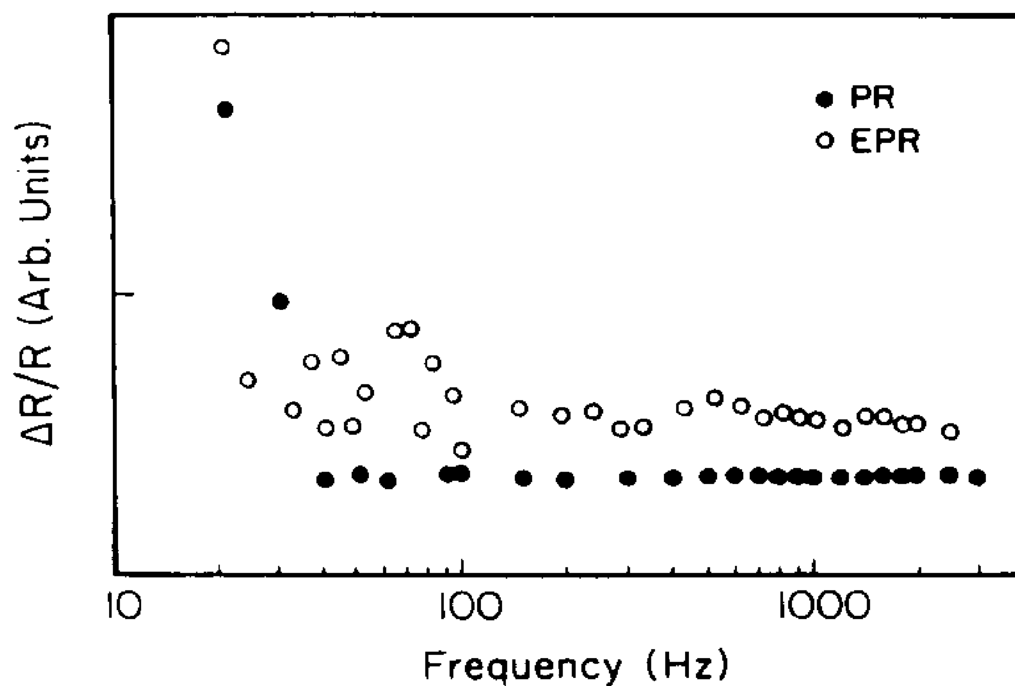

Figure 4.30 Comparison of the frequency dispersion of PR and EPR of CHF_3/Ar RIE-treated n-Si in the methanolic solution.

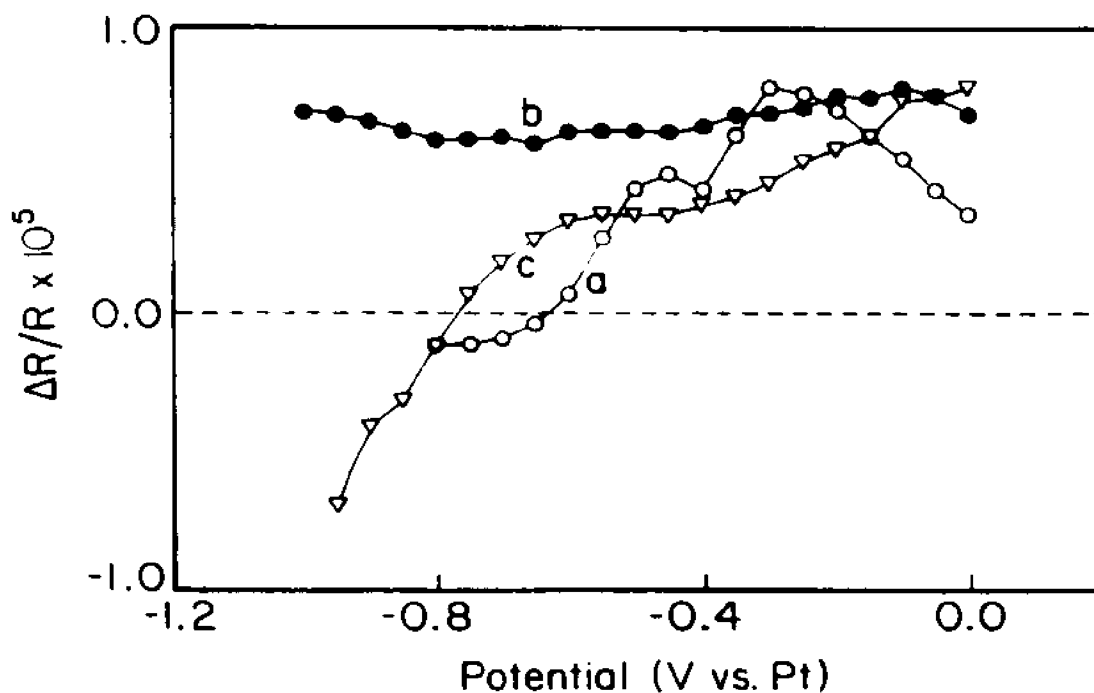

Figure 4.31 Variation of the amplitude of the 3.4 eV EER peak with electrode potential for (a) untreated n-Si, (b) CHF_3/Ar, and (c) $CClF_3/H_2$, RIE-treated samples. The spectra were taken in the methanolic solution that was previously described.

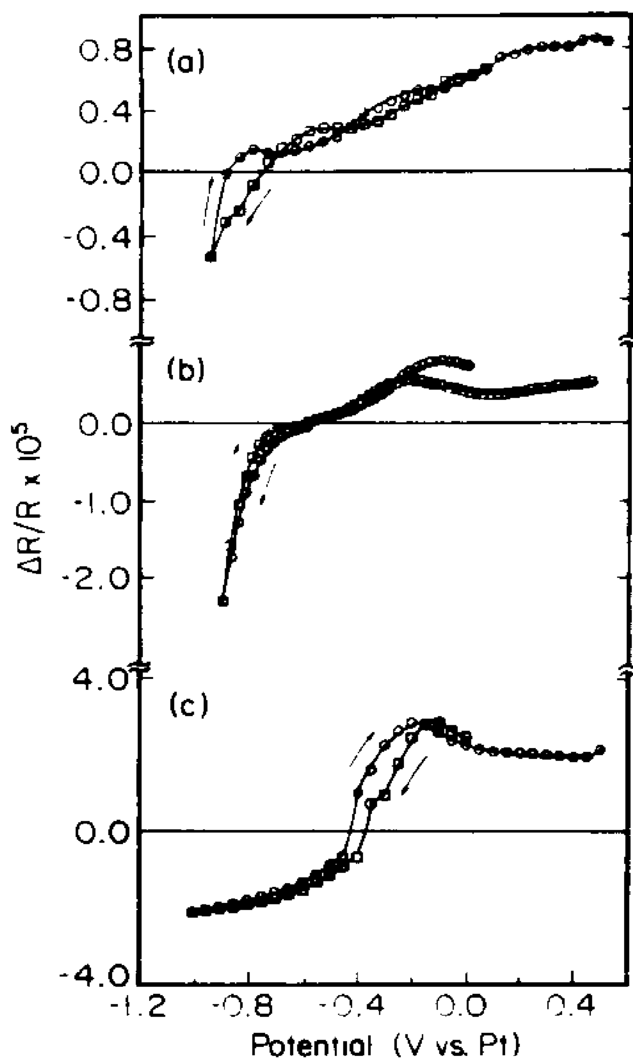

Figure 4.32 (a) Bias dependence of the electroreflectance of the $CClF_3/H_2$ RIE sample. (b) Bias dependence of electroreflectance of the $CClF_3/H_2$ + O_2 ash sample. (c) Bias dependence of the electroreflectance of the O_2 ash sample.

are also given. The spectra of the CF_4 treated samples were similar to the spectra of Fig.4.33(a), and that of $CClF_3/H_2$ RIE and O_2 ash treated samples were similar to the spectra in Fig.4.33(b). The equivalent circuits in all these cases are identical with that applied for the untreated Si in the same electrolyte except that for the CHF_3/Ar and CF_4 etched samples, the CPA element Z_4 is substituted by two

TABLE IV. Flat-band potential V_{fb} obtained from the electroreflectance measurements of Si and various RIE sample

Si Sample	V_{fb} (V vs Pt) based on electroreflectance
original	-0.66
HF etching	-0.51
$CClF_3/H_2$	-0.80
$CClF_3/H_2$ + O_2 ash	-0.67
O_2 ash	-0.40

passive elements, R_1 and C_1. In the case of untreated Si, Z_d was associated with a porous oxide on the Si surface. Z_d or R_1 and C_1 will represent the impedance of the residue layer in all the RIE treatment that have been studied. R_H and C_H account for the electrolyte adsorption. R_3 and C_3 represent a surface state.

The R_2 and C_2 elements showed bias dependence characteristic of an n-type semiconductor. Figures 4.34 and 4.35 depict the Mott-Schottky (MS) plots of C_2 for the Si samples subjected to the various RIE treatments. In Fig.4.34 the behavior of the CHF_3/Ar and CF_4 treated samples is compared to the untreated samples and the behavior of the $CClF_3/H_2$, $CClF_3/H_2$ + O_2 ash, and O_2 ash etched samples is shown in Fig.4.35. Initially the impedance of all the samples was measured over the same potential range of 0.0 - -0.7 V vs Pt. Over most of this range, C_2 for CHF_3/Ar and CF_4 etched samples were potentially independent. This might be interpreted as an indication that C_2 in these cases originates from an

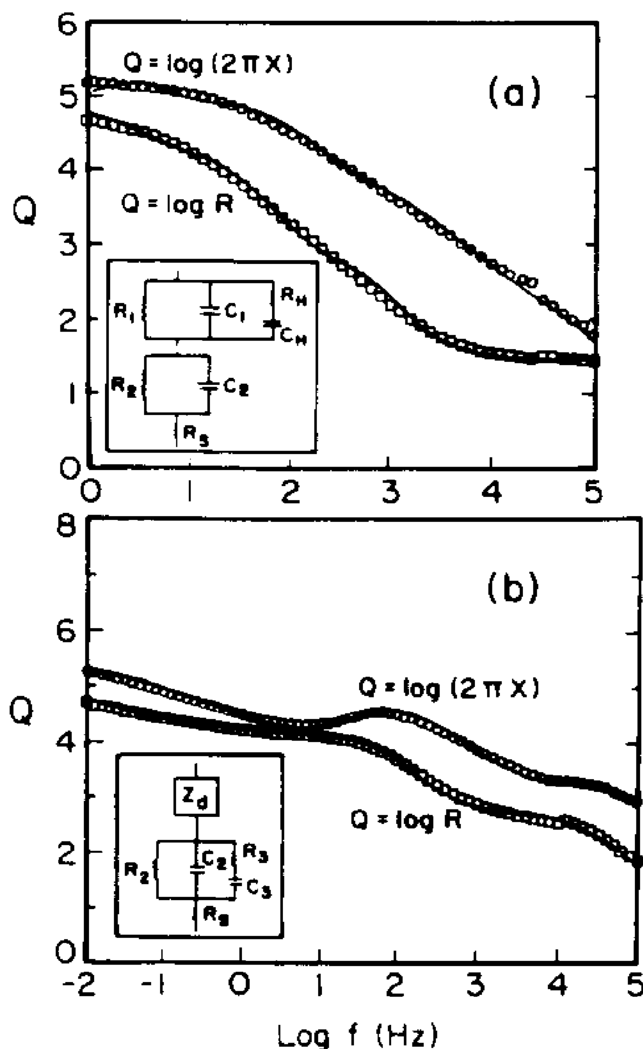

Figure 4.33 Impedance spectrum at -0.4V vs Pt of (a) CHF_3/Ar RIE and (b) $CClF_3/H_2$ RIE + O_2 ash. The equivalent circuits which represent the measured data are shown in the inserts. (□): Re(Z), (O): Im(Z), solid lines: theoretical fits to the proposed equivalent circuit with appropriate values of the elements that are summarized in subsequent figures.

insulating layer. Estimations of the thickness of the layer have shown inconsistencies (~1000 Å for the CHF_3/Ar treated sample) with the optical modulation results and with any other measurement of the damaged layer. An alternative explanation is that C_2 represents the space-charge layer of the semiconductor but over this potential range the Fermi level is pinned by a high concentration of surface states

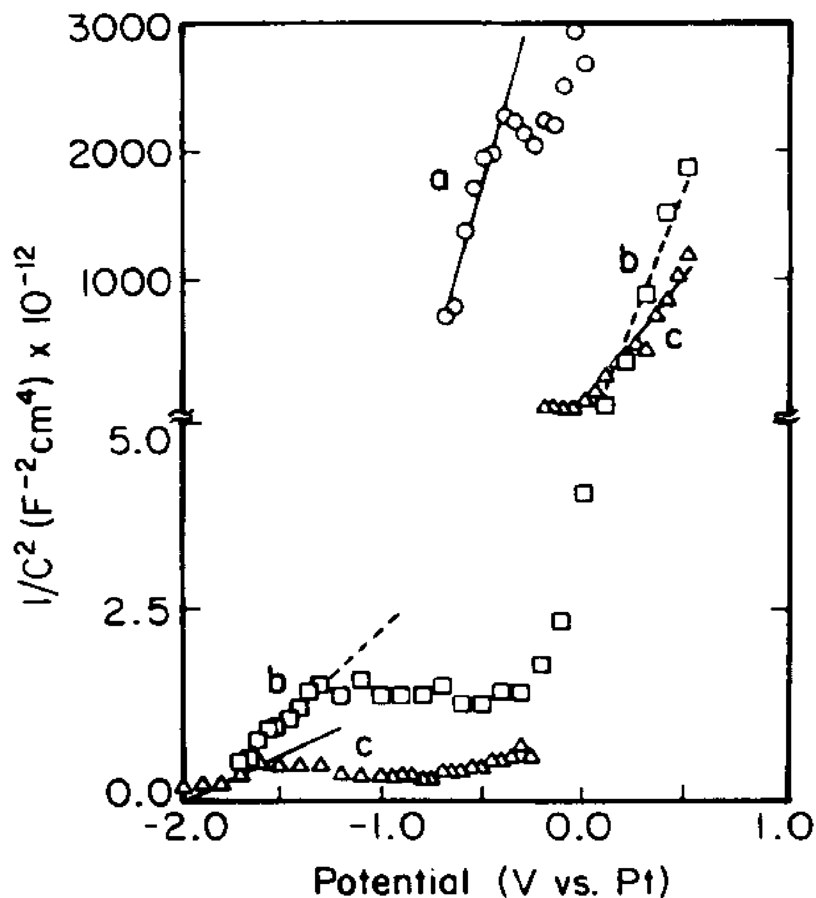

Figure 4.34 **Mott-Schottky plots of (a) original, (b) CHF_3/Ar RIE, and (c) CF_4 RIE samples.**

that were induced by the treatment. This was checked by extending the potential range in both directions. One can observe in Fig.4.34 that in both cases there are two potential ranges for which the Mott-Schottky relation holds. The slopes of these curves at the very positive potentials are very similar to the slope of the untreated Si. In this case the space-charge layer penetrates deep into the semiconductor where there is no damage. The slopes in the negative potential region are much smaller (note the change in scale) that indicates a much higher ionized donor density. This is consistent with electrically active damaged layers that were

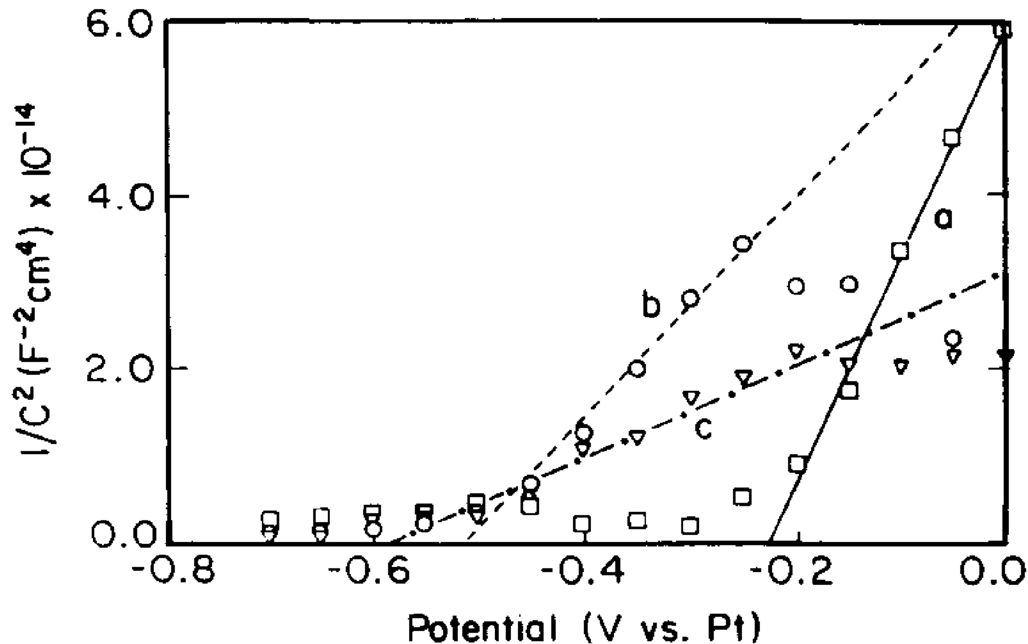

Figure 4.35 **Mott-Schottky plots of (a) $CClF_3/H_2$ RIE, (b) $CClF_3/H_2$ RIE + O_2 ash, and (c) O_2 ash samples.**

induced by the treatments. The results obtained in the far forward bias range have been used to estimate the thickness of the damaged semiconductor regions. In Table V is listed the flat-band potentials and doping densities for all the RIE treated samples in the two potential regions where the Mott-Schottky relation was verified, together with the values obtained for the untreated Si. For the $CClF_3/H_2$, $CClF_3/H_2$ + O_2 ash, and O_2 ash etchings the total high-frequency capacitance continuously increases as the potential changes toward flat-band condition and for the last two RIE procedures pinning was observed in the inversion region (see Fig.4.35). This kind of pinning is consistent with the findings that a superficial oxide layer can be responsible for its appearance.

TABLE V. Flat-band potential V_{fb} and doping density N_d obtained from the impedance measurements of Si and various RIE samples.

Si Sample	First potential region		Second potential region	
	V_{fb} (V vs Pt)	N_d (cm^{-3})	V_{fb} (V vs Pt)	N_d (cm^{-3})
original	-0.862	2.16×10^{15}	---	---
HF etching	-0.761	4.71×10^{15}	---	---
CHF_3/Ar	0.084	2.40×10^{15}	-1.92	4.70×10^{18}
CF_4	-0.032	5.50×10^{15}	-1.99	8.40×10^{18}
$CClF_3/H_2$	-0.243	4.24×10^{15}	-1.020	1.21×10^{17}
$CClF_3/H_2$ + O_2 ash	-0.506	7.27×10^{15}	-0.845	1.28×10^{17}
O_2 ash	-0.600	2.03×10^{16}	---	---

TABLE VI. Short-circuit current density J_{sc} and open-circuit voltage V_{oc} of Si and various RIE samples in methanolic electrolyte for a light intensity of 100 mW/cm^2.

Si Sample	J_{sc} (mA/cm^2)	V_{oc} (V vs Pt)
original	12.4	-0.503
HF etching	16.3	-0.519
CHF_3/Ar	4.1×10^{-3}	-0.125
CF_4	34×10^{-3}	-0.128
$CClF_3/H_2$	3.77	-0.397
$CClF_3/H_2$ + O_2 ash	0.337	-0.307
O_2 ash	40×10^{-3}	-0.231

The comparison of the flat-band potential obtained from the impedance data with that from the electroreflectance (Table IV) shows that they agree very well. The systematic 0.2 V difference in the flat-band potentials can be accounted for by the same reason discussed in §4.1.3.

Table VI presents the short-circuit current density (J_{sc}) and open-circuit voltage (V_{oc}) obtained for all the RIE samples that have been studied and that for an original and an HF etched samples. All the RIE samples had very weak photoresponse except that the $CClF_3/H_2$ RIE samples had mild photoresponse.

4.3.3 The effect of the damage due to RIE

A. Strain due to the damage to the top layer by the RIE.

This part was done in collaboration with Prof. F.H. Pollak.

The most pronounced effect of the RIE treatments on the spectra resulting from the various modulation techniques is the apparent shift in the band edges. This effect can be seen in Figs.4.23 and 4.24 and in the tables I-III. These shifts occur in both E_1 region and E_2 region at both low temperatures and room temperature. It has been established that the most pronounced RIE surface modifications are either thin insulator deposition or a lattice damage [16,17]. Therefore, the most self-consistent interpretation of the spectral shift is that it originates from RIE induced strain in the Si. From Fig.4.23 it can be seen that the effect of CHF_3/Ar RIE is a small shift in the main band and the emergence of a new peak at lower energies. It is obvious from the figure and also can be seen in

the fit parameters presented in Table I, in which the line-width of the main peak remains approximately constant. The same situation is observed with CF_4 RIE etching. With $CClF_3/H_2$ etching it was observed only that a significant red shift of the main peak without resolvable splitting. For any of the samples at room temperature, no splitting and only the shifts and apparent broadening were observed. Since most of the recorded effects of the various RIE treatments are similar it will be assumed that the pressure-induced effects of these treatments are also similar and for the cases in which the splitting is not observed it will be assumed it to be unresolved with separation smaller than $\Gamma/2$. For pure two-dimensional tensile strain, ε, in the plane perpendicular to the <100> direction, the hydrostatic pressure component will produce a shift of the band gap, δE_H, while the uniaxial component will split the intra-band degeneracy of the Λ_3 valence band by an amount $2\delta E_s$. The energies of B_3'' and B_2'' are given by [130]

$$E(B_2'') = E(0) + \delta E_H - \delta E_s \qquad (4.1a)$$

$$E(B_3'') = E(0) + \delta E_H + \delta E_s , \qquad (4.1b)$$

where E(0) is the position of the unstrain peak and [130]

$$\delta E_H = (\sqrt{3}D_1^1/3)[2 + 2S_{12}/(S_{11} + S_{12})]\epsilon \qquad (4.2a)$$

$$\delta E_s = (\sqrt{6}D_3^3/3)[1 - 2S_{12}/(S_{11} + S_{12})]\epsilon . \qquad (4.2b)$$

In Eqs.(4.2) D_1^1 and D_3^3 are the deformation potentials appropriate for hydrostatic pressure and uniaxial strain along the <100> direction, while S_{ij} are the components of the elastic compliance constant. For Si the following numerical values were taken: $D_1^1 = -8$ eV, $D_3^3 = 5$ eV [130], and $2S_{12}/(S_{11}+S_{12}) = -0.77$.

From Fig.4.24 and Table I one can see that for the CHF_3/Ar and CF_4 etchings, the split in the valence band and the shift compensate to result in a very small shift of the major peak. The situation is different with the $CClF_3/H_2$ etched sample in which a relatively large red shift in the peak position can be observed without the corresponding splitting. It is highly unlikely that a different mechanism should apply here. It is more likely, based on the origin of the strain in all cases, that the dimensionality of the problem is only a rough approximation to the distribution of the strain. This contribution can be estimated by a parametrization of the elastic compliance constant such that

$$2S_{12}/(S_{11} + S_{12}) \rightarrow A \ . \qquad (4.3)$$

For the three-dimensional case one deals with pure hydrostatic pressure hence A=1. So if the dimensionality is somewhere between 2 and 3 one expects $1 < A < -0.77$. Equations (4.1) and (4.2) can be solved for ε and A given the shift and the splitting. The results of these calculations are shown in Table VII.

The parameter A deviates significantly from the pure two dimensional case only for $CClF_3/H_2$ RIE case. This might be related to the organic residue of fluorocarbons that was found after this treatment [131].

TABLE VII. Tensile strain and elastic compliance constant parameters for Si subjected to various RIE treatments.

RIE	CHF_3/Ar	CF_4	$CClF_3/H_2$	O_2 ash
$E(B_2'')$ (eV)	3.364	3.360	$E(B_3'')-\Gamma/2$	$E(B_3'')-\Gamma/2$
$E(B_3'')$ (eV)	3.494	3.481	3.457	3.494
$\delta E_{\parallel}$ (eV)	-0.060	-0.0685	-0.056	-0.012
δE_{s} (eV)	0.065	0.0605	0.024	0.017
Shift (eV)	0.005	-0.008	-0.032	0.005
Separation (eV)	0.130	0.121	<0.048	<0.034
ε	0.010	0.010	~0.006	~0.002
A	-0.65	-0.50	~0.02	~ -0.85

Figure 4.36 shows the PR spectra of CHF_3/Ar RIE etched Si and that of a sample subjected to an additional RCA clean after the RIE treatment. The same result was obtained for the CF_4 treated sample. It confirms that RCA cleaning after CHF_3/Ar RIE or CF_4 RIE did not change the PR spectrum. The RCA clean only removes surface contaminants; implanted impurities and lattice damage are not removed. This suggests that the RIE induced strain measured by PR is due to implanted impurities or lattice damage.

The penetration depth of the light might be another probe to check the

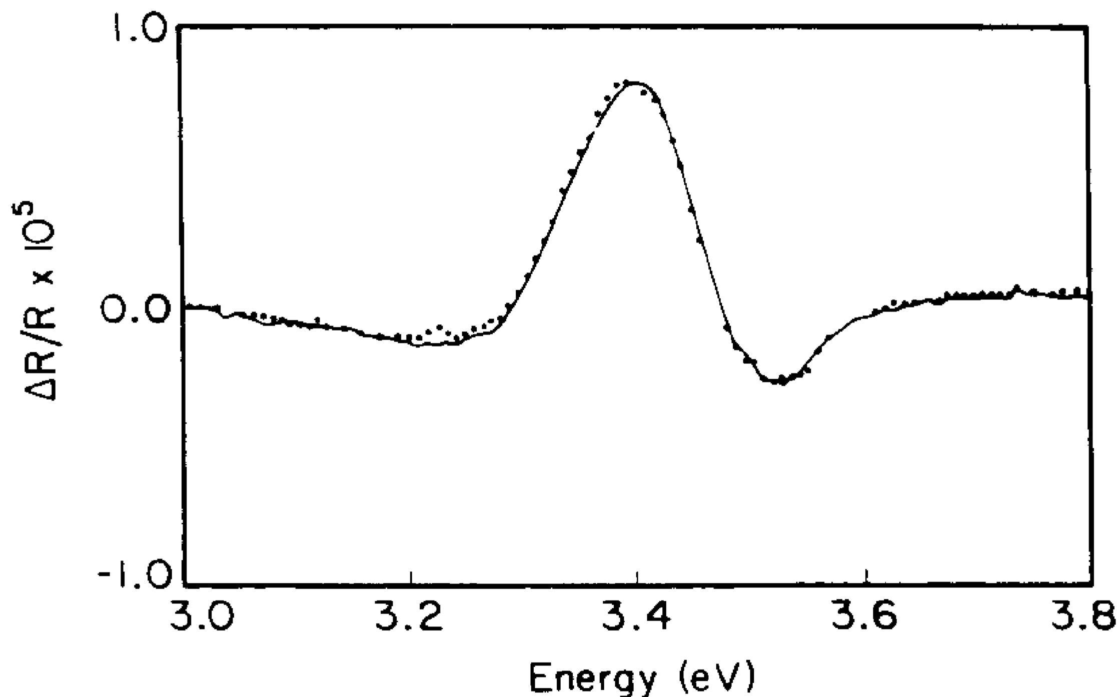

Figure 4.36 The PR of CHF_3/Ar RIE-treated n-Si (points) and of a sample that was cleaned with a second RCA etch following the RIE treatment (solid line).

depth dependence of the modulated reflectivity, and therefore the uniformity of the damaged layer. There are two light beams with different penetration lengths in a PR experiment, the probing and the modulating beams. In PR experiments of Si the modulating beam was always less energetic than the probing beam. From the absorption coefficient of Si [132,133], the penetration depth of the beam with energy 3.4 eV is 107 Å and that with energy 4.3 eV is 42.5 Å. Both are within the serious damaged layer range. Comparison of the results for the E_1 and E_2 peaks might provide some information about the uniformity of the damage within this top layer, but the complexity of the E_2 structure makes it impossible to resolve the splitting, so the strain parameters could not be deduced.

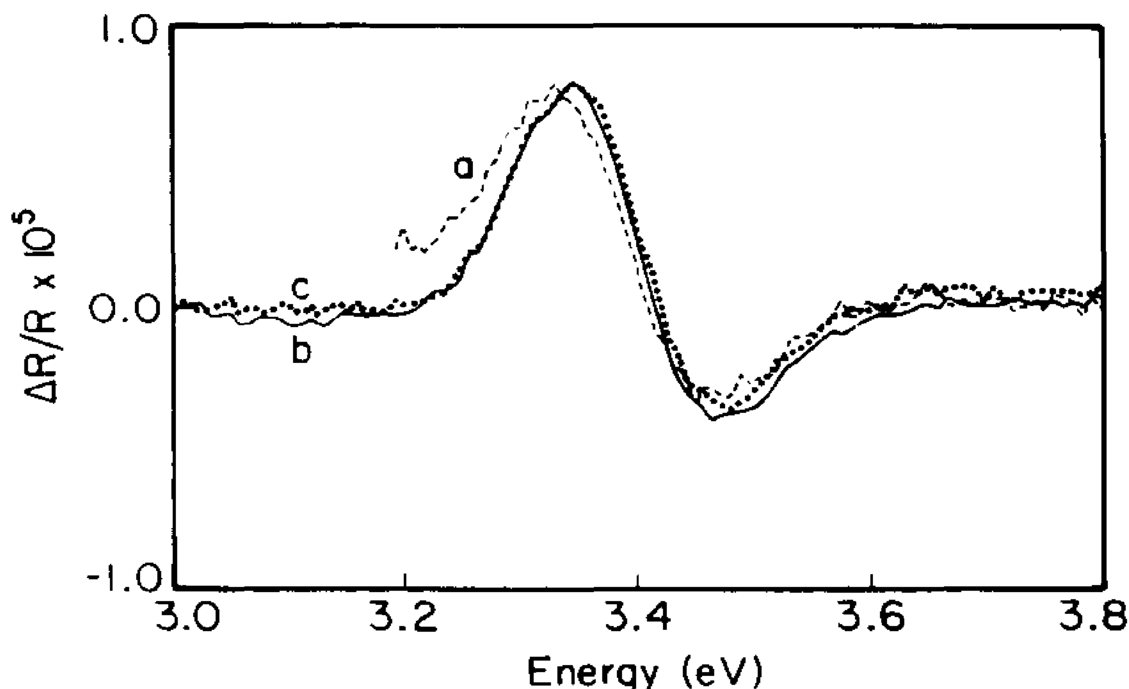

Figure 4.37 EPR at three different wavelength of the modulated beam for the CF_4 RIE-treated n-Si. (a) 4131 Å from Kr-ion laser; (b) 4880 Å from Ar-ion laser; and (c) 6328 Å from He-Ne laser. The spectra are normalized for the same amplitude.

Figure 4.37 shows the normalized EPR spectra of the CF_4 etched sample at three different wavelengths of the pumping beam. The shortest wavelength shows already a small red shift. This wavelength corresponds to the penetration depth of 3000 Å. Unfortunately experimental difficulties precluded experiments with a pumping beam with shorter wavelengths.

B. Accumulation of slow surface states.

The most remarkable results obtained from impedance studies on RIE samples are depicted in Figs.4.34 and 4.35. The shift of the flat-band potentials, consistent with the semiconductor bulk properties, to more positive values is clear evidence that, at equilibrium, positive charges accumulate in the semiconductor

surface after the RIE treatments, which leads to pinning the Fermi level. The unpinning is possible only when large forward potential is applied to the cell, neutralizing these charges on the surface. This is consistent with prior interpretation of barrier lowering in n-type RIE Si Schottky barrier devices [18,131,134,135]. The fact that EER amplitudes of CHF_3/Ar and CF_4 RIE Si are independent of the bias is consistent with a very large negative shift of the flat-band potential. Again, one possible origin for such a shift might be the presence of a thick layer of an insulating material. This will be consistent with the results presented here only if this insulator is completely transparent to photons with energy smaller than 4.5 eV that is inconsistent with surface spectroscopy and RBS measurements of similarly treated samples [136]. An alternative explanation is that these RIE treatments result in surface modifications that give rise to large concentrations of surface states that cause the Fermi level to be pinned (or the band edges to be shifted). However, if the Fermi level is completely pinned in this region the EER signal should vanish. An explanation that is consistent with all these findings is that the Fermi level is pinned by very slow surface states, slower than the modulation frequency such that the EER signal is not pinned by these states, but fast enough to follow the changes in the dc potential. The frequency dispersion of the photoreflectance (PR) signal of the CHF_3/Ar RIE sample did not show any peak that could be related to these states. In addition, the surface states cannot be resolved in the equivalent circuit of the CHF_3/Ar RIE samples. They were observed only through their pinning of the Fermi level.

C. The depth of damage layer.

An objective of this study is to determine the sensitivity and uniqueness of impedance measurements and optical modulation spectroscopies, to elucidate the nature of the damage caused by the RIE treatments and to compare the damage of various treatments. The qualitative conclusions will be cross-checked against prior art in which different analytical techniques were implemented. Attempts at quantitative cross-checks are more troublesome. The samples for the various experiments were cut from commercial large wafers on which the treatments were being routinely performed. The reproducibility of the various physical parameters that were evaluated had been checked and significant variations have been noticed. The results presented here are "typical" but were not subject to any statistical analysis. Wherever possible, the results will be compared with prior work but quantitative aspects of these comparisons (depth of damage layer, concentrations of interface states, etc.) should be accepted with caution.

Table VIII shows the thickness of the residue overlayer (l_1) and of the damaged Si region (l_2), which were evaluated based on the capacitance. In most cases $n\tau/N$, associated with the element Z_d, was used to estimate the capacitance of the overlayer. N, n, and τ were taken from the result at 0V bias. This criterion was employed because these parameters showed bias dependence. Based on the literature [131], it was assumed that for the samples subjected to the O_2 ash treatment, the superficial residue layer is SiO_2, with a dielectric constant equal to 4 [72]. For the other RIE etched samples the minimum and maximum thickness of this

TABLE VIII. Thickness of the residue layer l_1 and silicon damaged region l_2.

Sample	l_1/ε (Å)	l_1 (Å)	l_2 (Å)
CHF_3/Ar	5.7	20-70	131[a]
CF_4	4.6	15-55	76[a]
$CClF_3/H_2$	0.96	4.0-12.0	---
$CClF_3/H_2$ + O_2 ash	4.8	19[b]	---
O_2 ash	5.6	22[b]	---

[a] ε = 12 (for Si).
[b] ε = 4 (for SiO_2).

layer can be evaluated by assuming that it has a dielectric constant between 4 (for SiO_2) and 12 (for Si) [72].

The thickness of damaged region was estimated from the capacitance at the far forward bias where the plateau Mott-Schottky plot exhibited turning. The chemical nature of the damage cannot be discerned using impedance spectroscopy. The results in Table VIII indicate that the damage induced by the CF_4 RIE treatment resulted in a thinner damaged layer and seems not to affect the bulk of the semiconductor so drastically when compared with the CHF_3/Ar RIE treatment, which is consistent with prior work [18,131,134,137,138].

The damage due to the $CClF_3/H_2$ plasma is known to produce a residue layer on the Si surface, to create a permeated layer containing hydrogen at the Si near-surface and to form a layer of damaged Si [131]. Even though this is the case, the existence of photoresponse, or space-charge effects, indicates that the

damage resulted from this plasma is not so deleterious compared with the other RIE treatments in this study. The $CClF_3$ RIE without the presence of H_2 was not investigated, but the notion that H_2 passivates the electrically active states but does not prevent the structural damage [131] is consistent with our results. The estimated thickness of the residue layer from our results was between 4.0 and 12.0 Å. All the thickness values are based on capacitance data under the assumption of the roughness factor of 1. X-ray photoemission spectroscopy (XPS) and ellipsometry measurements of $CClF_3/H_2$ RIE samples as well as impedance measurements on the solid-state devices discussed in §4.4 show that these thicknesses are grossly underestimated. In addition, the capacitance data for the $CClF_3/H_2$ treated samples are based on the low-frequency extrapolation of the Z_d elements. The only explanation that can be consistent with all the available data is that the overlayer in the $CClF_3/H_2$ RIE case is porous. It is also known that post-RIE O_2 ashing removes part of the damage but leave a surface rich in oxygen, probably SiO_2 [131]. The presence of this silicon dioxide overlayer can be responsible for the small photoresponse of the $CClF_3/H_2$ + O_2 ash and O_2 ash treated samples (Table VI). O_2 ashing shifts back the flat-band potential to that of the untreated Si.

Figure 4.38 depicts the bias dependence of the exponent n in the CPA element used to represent the superficial layer on the top of the $CClF_3/H_2$ RIE, $CClF_3/H_2$ RIE + O_2 ash, and O_2 ash samples. As mentioned before, the CPA behavior can originate from structural contributions such as porosity or dynamical

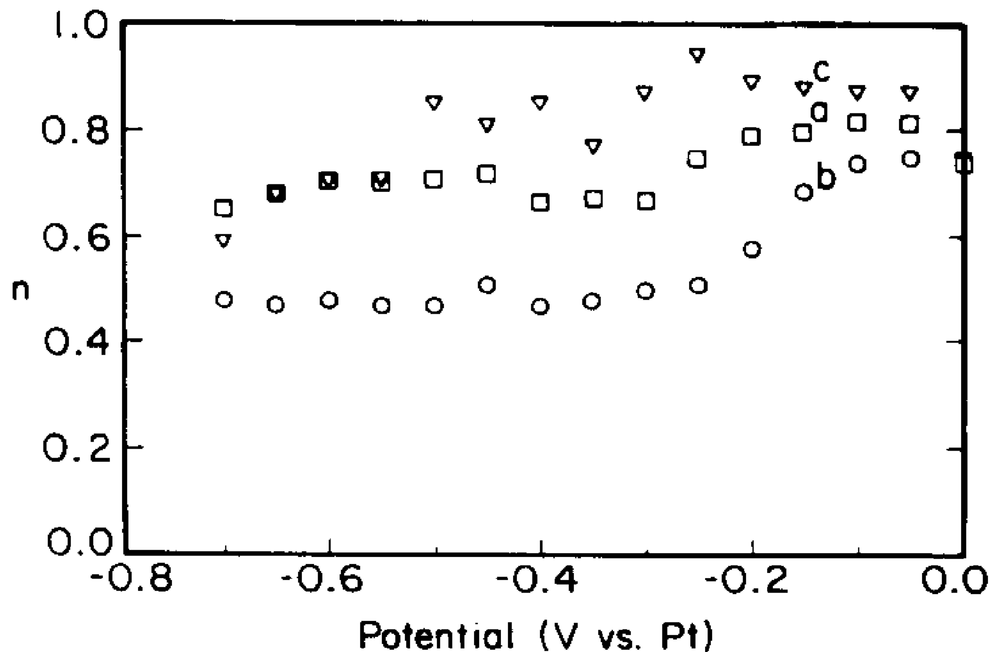

Figure 4.38 Bias dependence of the exponent n of the CPA element. (a) $CClF_3/H_2$ RIE, (b) $CClF_3/H_2$ RIE $+O_2$ ash, and (c) O_2 ash.

contribution such as diffusion. The data here are not sufficient for a clear distinction between the two. As the CPA element in the untreated Si is interpreted to be due to a porous SiO_2 layer, which agrees with volumes of prior study on the untreated Si, it serves as the main basis for the interpretation of this element to arise from the porosity of the top layer. This interpretation is also supported by the fact that the $CClF_3/H_2$ RIE sample showed a reasonable photoresponse (Table VI), which requires good ionic transport to and from the surface of the semiconductor. In addition, following the above discussion, XPS, ellipsometry, and the impedance of the solid-state devices also support interpretation in terms of a porous overlayer on the $CClF_3/H_2$ treated samples. This interpretation conflicts with the observations,

the frequency dispersion of EPR signal and the identity of line shapes of EER, PR, and EPR, that were explained by that the film created by this treatment prevents the electrolyte from interacting with the surface states at the Si surface. One can resolve this conflict by assuming a very thin compact layer between the substrate and the porous layer.

The sample subjected only to the O_2 ashing treatment shows an almost invariant n value very close to 1 ($0.8<n<0.9$) suggesting that the superficial layer is basically an R-C element in parallel. This can correspond to a nonporous insulating layer such as SiO_2 [131] on top of the semiconductor. The poor photoresponse obtained for this sample (Table VI) supports hypothesis of having the nonporous SiO_2 overlayer.

Table IX summarizes the value obtained for the density of states created by the electrolyte adsorption (N_H), the surface states (N_3), and the respective relaxation times, τ_H and τ_3 (at zero potential), for the different RIE processes as well as for an original Si substrate and an HF etched one.

4.3.4 Damage profile analysis

To analyze the damage profile and to understand better the chemistry and nature of the damage layer, the chemical etching for CHF_3/Ar RIE Si and CF_4 RIE Si was used to remove the Si and SiO_2 layer. For the buffered HF solution, the etching rates are 17 Å/s for SiO_2 [72] and 0.43 Å/min for Si<100> [139]. For 2M KOH, the etching rates are 0.05 Å/min for SiO_2 [140] and 5 Å/s for Si [141]. Si

TABLE IX. Density of electrolyte molecules adsorbed in the substrate surface N_H and density of surface states N_3. Relaxation time τ_H related to N_H and relaxation time τ_3 related to N_3 at zero potential.

Si Sample	N_H (cm^{-2})	N_3 (cm^{-2})	τ_H (s)	τ_3 (s)
original	$9.7x10^{15}$	$5.9x10^{11}$	1.3	$8.0x10^{-5}$
HF etching	$3.5x10^{15}$	---	6.0	---
CHF_3/Ar	$1.6x10^{14}$	---	0.075	---
CF_4	$6.2x10^{13}$	---	0.045	---
$CClF_3/H_2$	$3.7x10^{14}$	$5.5x10^{12}$	0.65	$2.3x10^{-4}$
$CClF_3/H_2$ + O_2 ash	---	$6.8x10^{12}$	---	$6.5x10^{-3}$
O_2 ash	$2.1x10^{15}$	$3.3x10^{13}$	0.11	$8.9x10^{-8}$

etching in KOH solution is very anisotropic [139-141], the etching rate in the <100> crystallographic direction is one order of magnitude larger than that in the <111> direction.

The photoresponse was used as the criterion for the "quality" of the semiconductor. Figures 4.39(a) and (b) show the evolution of J_{sc} and V_{oc} in the methanolic solution for the sample subjected to the CHF_3/Ar RIE (1) and CF_4 RIE (2) treatments as a function of the etching time in the buffered HF solution, respectively. The same kind of results is presented in Figs.4.40(a) and (b) for etching with the KOH solution. The bulk of the substrate is assumed to be reached

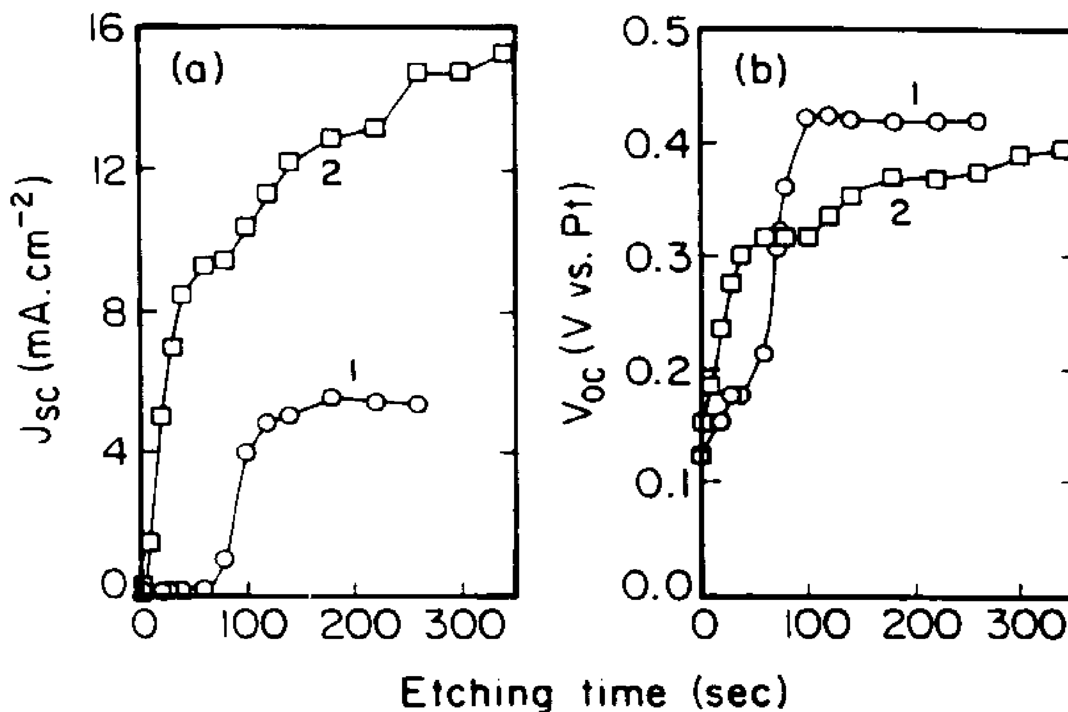

Figure 4.39 (a) Short-circuit current density vs etching time in a buffered HF solution for CHF_3/Ar RIE (1) and CF_4 RIE (2) samples. (b) Open-circuit voltage vs etching time in a buffered HF solution for the same samples.

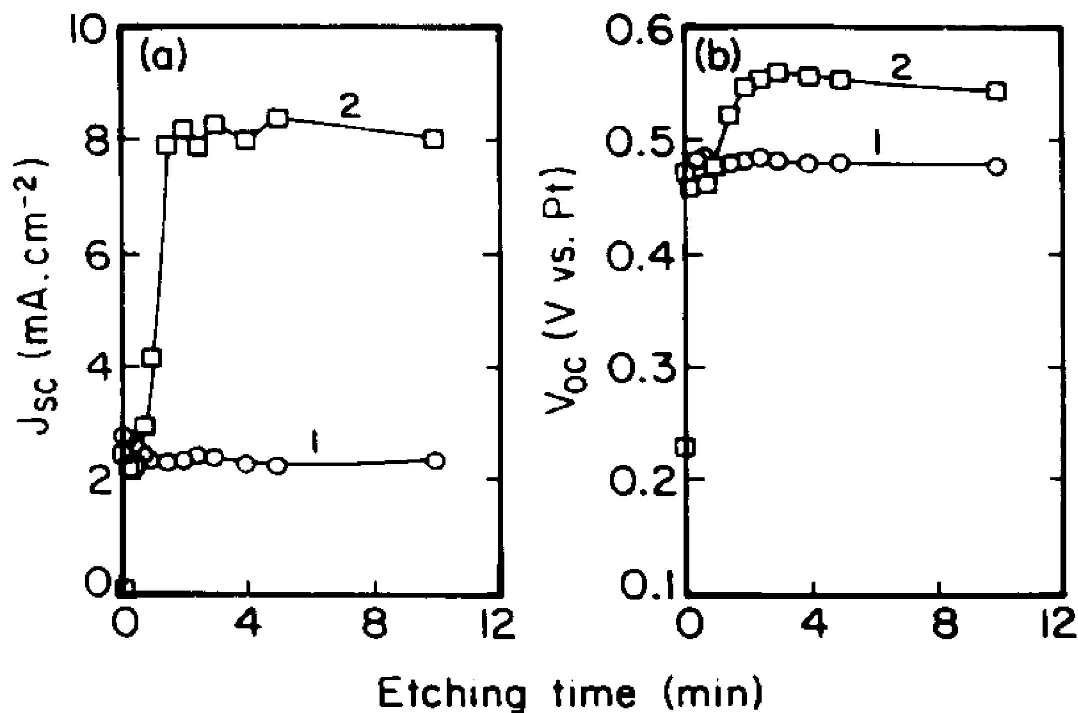

Figure 4.40 The same as Fig. 4.39 for etching with the KOH solution.

when J_{sc} and V_{oc} approach constant values. The final short-circuit current densities obtained after the end of the etching processes for the samples subjected to the CHF_3/Ar RIE are much smaller than the values obtained for the CF_4 RIE samples.

Figure 4.41 shows the photo I-V responses for Si CHF_3/Ar RIE samples and Si CF_4 RIE one after the end of the etching processes in the KOH solution, and that for the original Si substrate as a base for comparison. The turn-on voltage of the RIE samples shifts to more negative values, compared with the result obtained for the original sample. These shifts were associated with the presence of surface states and/or adsorbed electrolyte molecules on the electrode surface. The existence of adsorbed species can be checked using dark current-voltage measurements of the cells. For the CF_4 RIE sample a peak centered on -0.5 V vs Pt has been observed. For the CHF_3/Ar RIE sample the charge was spread over a larger potential range, but also centered on the same potential. The calculated charge density was $3.3\times10^{16}/cm^2$ and $6.5\times10^{15}/cm^2$ for the CHF_3/Ar RIE and the CF_4 RIE samples, respectively. The density for an original Si sample was $1.1\times10^{16}/cm^2$.

An additional etching procedure that was investigated is photoetching. The idea was to use an oxidation/dissolution process, in which the dissolution was the rate-limiting step. For a photoetching process, the parameters that must be adequately balanced are the illumination intensity and the solution concentration. Unfortunately any quantitative results cannot been attained for the following reasons: First, even for the low light intensity (5 mW/cm^2) the oxidation rate was

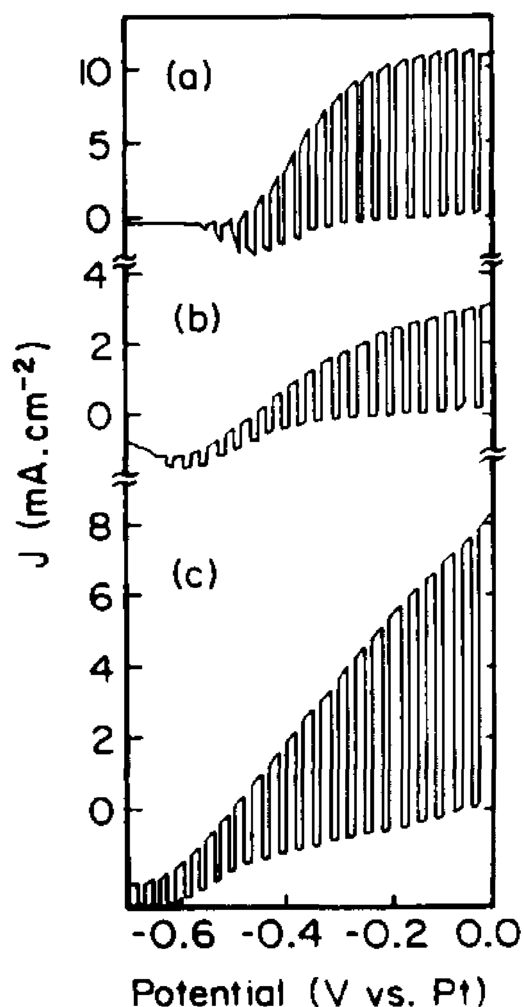

Figure 4.41 Forward sweep of chopped-light-induced photocurrent of (a) original Si substrate. (b) CHF_3/Ar RIE sample after etching process in the KOH solution. (c) CF_4 RIE sample after etching process in the KOH solution. Sweep rate = 10 mV/s.

larger than the dissolution rate. Second, for the 0.5% HF photoetching solution that was used, the dark current density was still too large as compared to the photocurrent.

To perform the measurements, first the potential range was determined, where photoetching proceeded at a constant rate. Then fixing the cell potential in

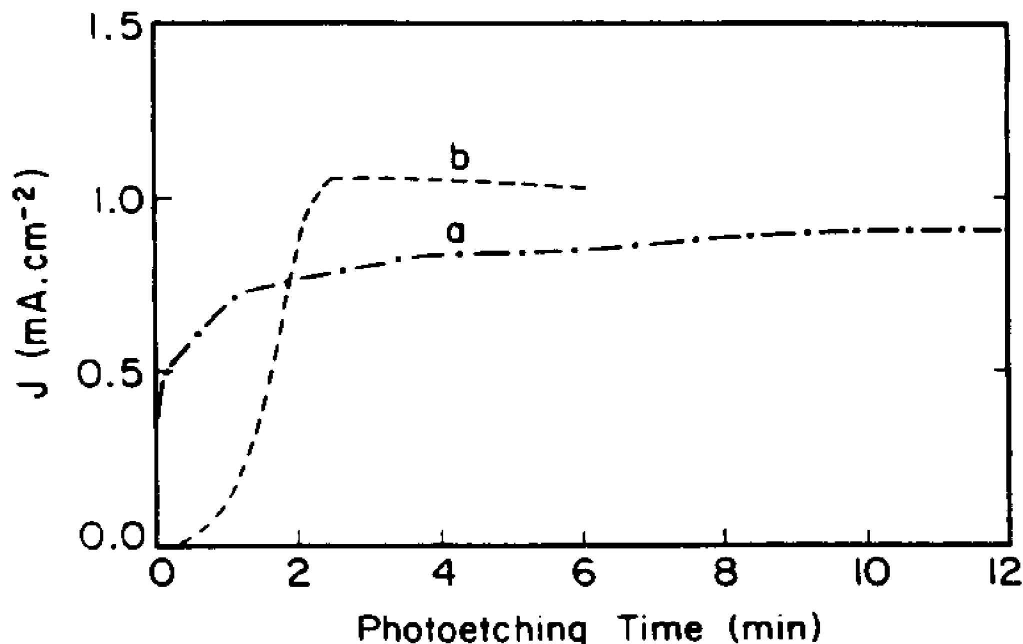

Figure 4.42 Current density vs time during photoetching: (a) CHF_3/Ar RIE and (b) CF_4 RIE.

that range, in our case -0.2 V vs Pt, the current was monitored as a function of time. Figure 4.42 is the results for both RIE treatments.

Based on the thickness of the damaged layer evaluated from the impedance data, it was expected that for the buffered HF solution it will take twice as long to etch away the damage on the CHF_3/Ar treated sample than for the CF_4 RIE sample. This ratio was found to be closer to a factor of 3. This suggests that the surface chemistry of the damaged layers after these treatments is different. This conclusion is also supported by the wet etching results in the 2M KOH solution and by the photoetching results. In the 2M KOH solution (Fig.4.40) a jump in the current density was observed for both samples just after the 1 s etching in the buffered HF solution and after that an almost inactive behavior of the CHF_3/Ar RIE

substrate in the KOH etchant and a small increase in the J_{sc} and V_{oc} values of the CF_4 treated substrate in the same solution were recorded. In the photoetching experiments the evolution of the current density with time for the two samples (Fig.4.42) has very different features. The CHF_3/Ar etched sample presents a jump of the photoresponse in the beginning of the process and a monotonous increase in the current density before reaching a constant value, while the CF_4 etched sample showed a faster and continuous increase. In the photoetching solution (0.5% HF), the behavior of the current density vs time, in the dark and under light, was the same for the CHF_3/Ar RIE sample; for the CF_4 RIE sample, the current density in the dark increased continuously, reaching a value about 30% smaller than that obtained under illumination. So, the sample treated in the CHF_3/Ar plasma seems inactive to the photoetching process.

The limiting current density at the end of the wet chemical etching (either buffered HF or KOH) of the CHF_3/Ar RIE sample never reaches the value of the undamaged Si substrate. For the CF_4 RIE treated sample, the limiting current density agrees with that of the undamaged Si. The behavior of the CHF_3/Ar RIE sample can be associated with the existence of deep impurities. These impurities can be Ar^+ or metal contaminants coming from the reactor chamber [142]. Also, H^+ cannot be discarded as an agent that causes lattice damage, but it was pointed out by Mu et al. [134] that hydrogen passivates its own damage leaving it inactive. Other authors [136] have concluded that in situ O_2 plasma/HF dip cleaning treatment of CHF_3/CO_2 RIE Si surfaces results in the Si surfaces remaining

modified; the residual modifications are shown to be fluorine and carbon contamination and deeper lying modifications as hydrogen-induced extended Si defects. Permeated hydrogen was measured at a depth of more than 2000 Å. This picture is in agreement with our work.

Oehrlein and co-workers [16,138] have proposed a structure for the region near the Si surface subjected to an etching in a CF_4/H_2 plasma by means of a set of complementary experimental techniques. For greater overetching time a 50 Å fluorocarbon overlayer is formed on the Si surface. Going down toward the bulk of the material, there is a 15 Å Si-oxygen layer, an interface rich in silicon carbide and a 30 Å heavily damaged region. Due to the presence of hydrogen in the plasma there is still a 300 Å damaged region that contains hydrogen. For the CF_4 RIE samples, of course, the 300 Å hydrogenated region did not exist. The evaluated thicknesses of the two regions (l_1 plus l_2) contributed to the impedance spectrum are in general agreement with the picture presented by Oehrlein et. al [16, 138]: a fluorocarbon overlayer plus a silicon-oxygen layer plus a heavily damaged region. For the CHF_3/Ar treated substrate, as far as we know, there is not any analogous picture for the damage effects, but from the experimental results in this study, it could be proposed that the top layer of CHF_3/Ar RIE Si consists of a thin polymer overlayer and a 130 Å heavily damaged region.

4.4 Comparison of the liquid junction with solid state devices [113]

The available literature on the electronic properties of reactive ion etched

Si mainly consists of studies of the current-voltage (I-V) characteristics [16,18,131,135] of metal-semiconductor contacts. Capacitance-voltage (C-V) measurements of metal-oxide-semiconductor (MOS) junction [18,143] and deep-level transient spectroscopy (DLTS) measurements [144] are other techniques that also have been used. The MOS C-V measurements were restricted to a few frequency values and were used to determine the generation lifetime and the density of states at the Si/SiO_2 interface, while the DLTS measurements provided information about the energy level and density of traps as well as the thickness of the damaged layer.

In this study, the conventional C-V technique is expanded to a broader frequency analysis by using impedance spectroscopy and the similar methodology to that used for liquid junctions is applied to investigate the effects of RIE on the dielectric properties of Si in Schottky barrier (SB) and MOS configurations. This will facilitate comparison and provide an appropriate baseline for the liquid junction results.

4.4.1 Experimental results of Schottky barrier (SB) devices

Figures 4.43(a) and (b) present the impedance data and the fitting to the equivalent circuits, depicted in the insets, for an original (or control) SB sample and a CHF_3/Ar RIE substrate, with 500 Å Ti metal contact, respectively. The equivalent circuit consistent with CF_4 RIE sample impedance data is the same as that of the original substrate. Figures 4.44(a) and (b) depict similar results for the control

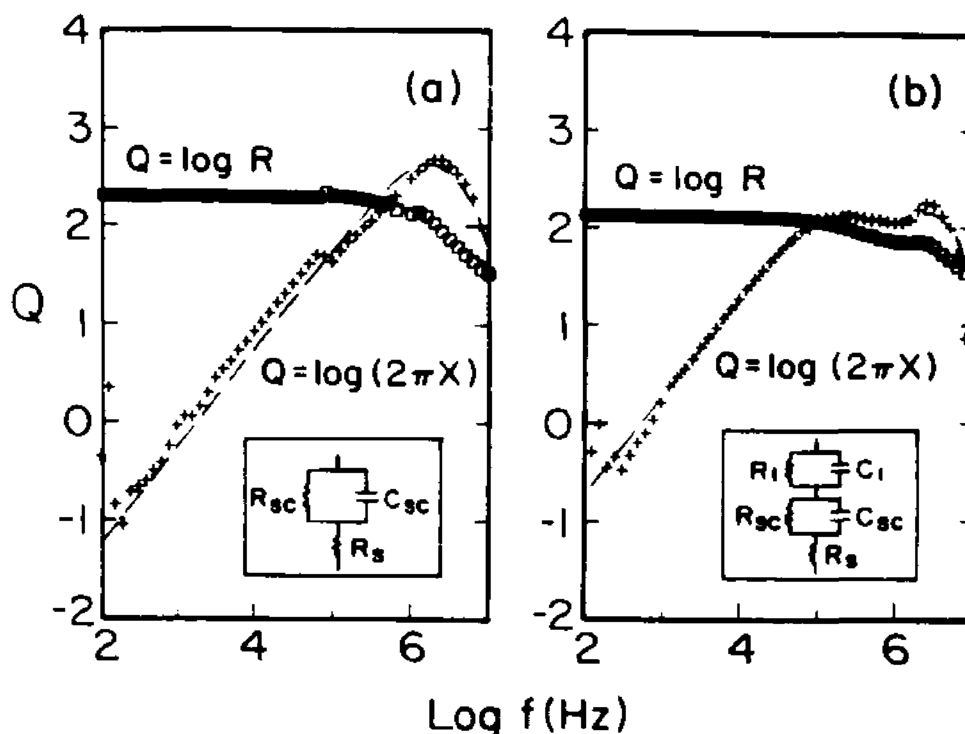

Figure 4.43 (a) Spectra of the real and imaginary parts of the impedance at 0 V of Ti/SB with untreated (control) Si sample. The equivalent circuit that represents the measured data is shown in the inset. The solid lines represent the theoretical fits to the equivalent circuit. (b) The same as (a) for the CHF_3/Ar RIE Ti/SB sample at 0 V.

(bare Si + O_2 ash + HF) and the $CClF_3/H_2$ RIE SB devices with a 5000 Å Al metal contact. The impedance data of the $CClF_3/H_2$ RIE + O_2 ash can be described by the same equivalent circuit as the control. Figure 4.45 shows the impedance data and the fitting to the equivalent circuit of the CHF_3/Ar RIE samples, taken under conditions in which surface states can be observed. For all the devices R_{sc} and C_{sc} represent the resistance and the capacitance of the space-charge region, respectively. R_1 and C_1 represent an insulating overlayer, and R_2 and C_2 are associated with surface states. The insulating overlayer was detected only for the samples subjected to the CHF_3/Ar and $CClF_3/H_2$ RIE treatments.

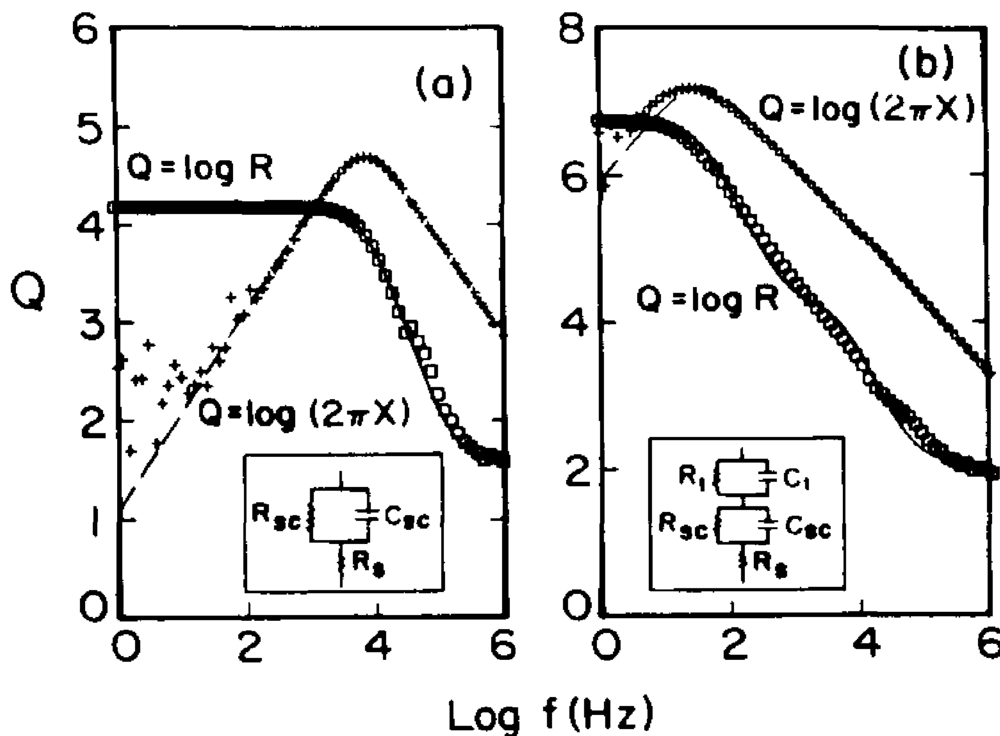

Figure 4.44 (a) The same as Fig. 4.43 (a) for the Al/SB sample at 0 V. (b) The same as (a) for the $CClF_3/H_2$ RIE Al/SB sample.

Figures 4.46(a)-(c) depict the Mott-Schottky plots of C_{sc} for an untreated Si, CHF_3/Ar RIE and CF_4 RIE Ti/SB samples in the same configuration. Figures 4.47(a)-(c) present similar results for the control, the $CClF_3/H_2$ RIE and the $CClF_3/H_2$ RIE + O_2 ash Al/SB samples. The built-in potentials (V_{bi}) and the free-carrier densities (N_d) are given in Table X. This table also includes the barrier heights (V_{bn}) obtained after correcting for the difference in energy between the Fermi level and the bottom of the conduction band [72]. In this table are presented also the series resistances of the devices at zero potential that were derived from the high-frequency limit of the real parts of the impedance data.

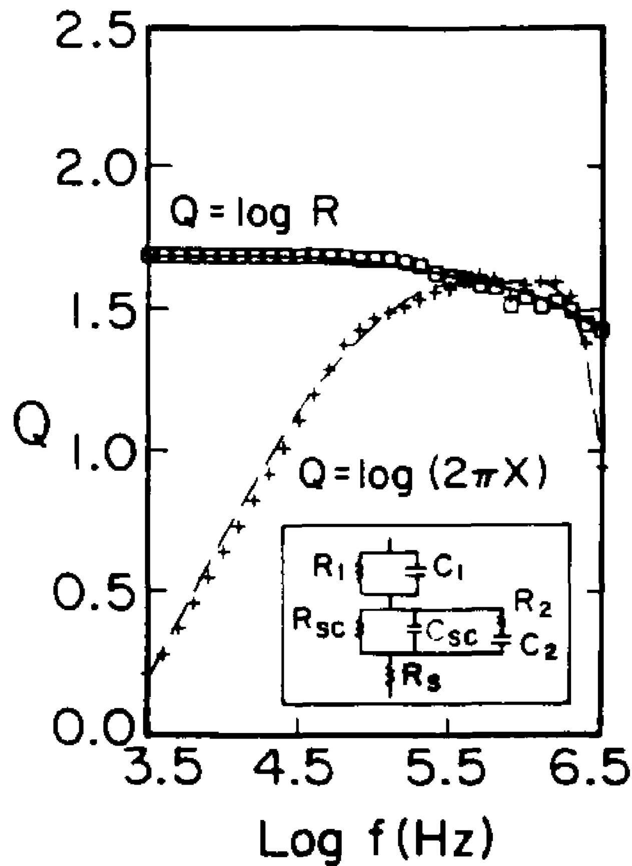

Figure 4.45 **The same as Fig. 4.43 (b) at 0.2 V.**

If the series resistance originates from the space-charge layer, one can estimate its voltage dependence from the current density (J_{sc}) versus voltage (V) characteristics that can represented by [72]

$$J_{sc} = J_{st}[\exp(eV/nk_BT) - 1] , \qquad (4.4)$$

where J_{st} is the saturation current density and n is the diode ideality factor. This will yield

$$\ln R_{sc} = \ln(nk_BT/eJ_{st}) - eV/nk_Bt . \qquad (4.5)$$

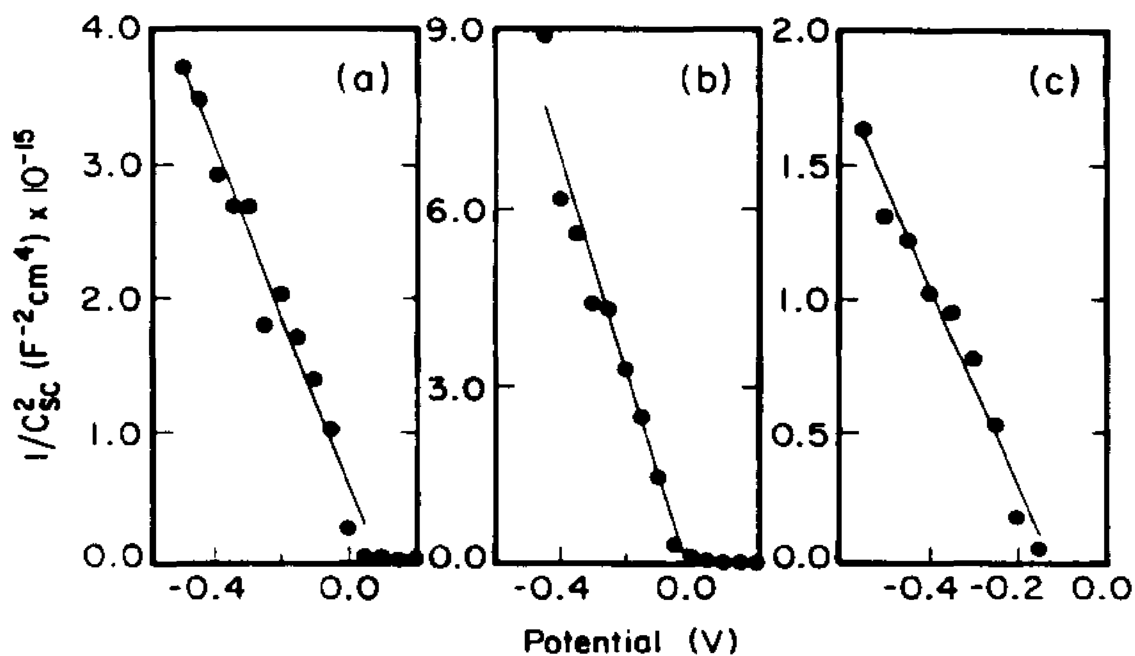

Figure 4.46 Mott-Schottky plot of the space-charge layer capacitance of (a) the original Ti/SB sample, (b) the CHF_3/Ar RIE Ti/SB sample, and (c) the CF_4 RIE Ti/SB sample.

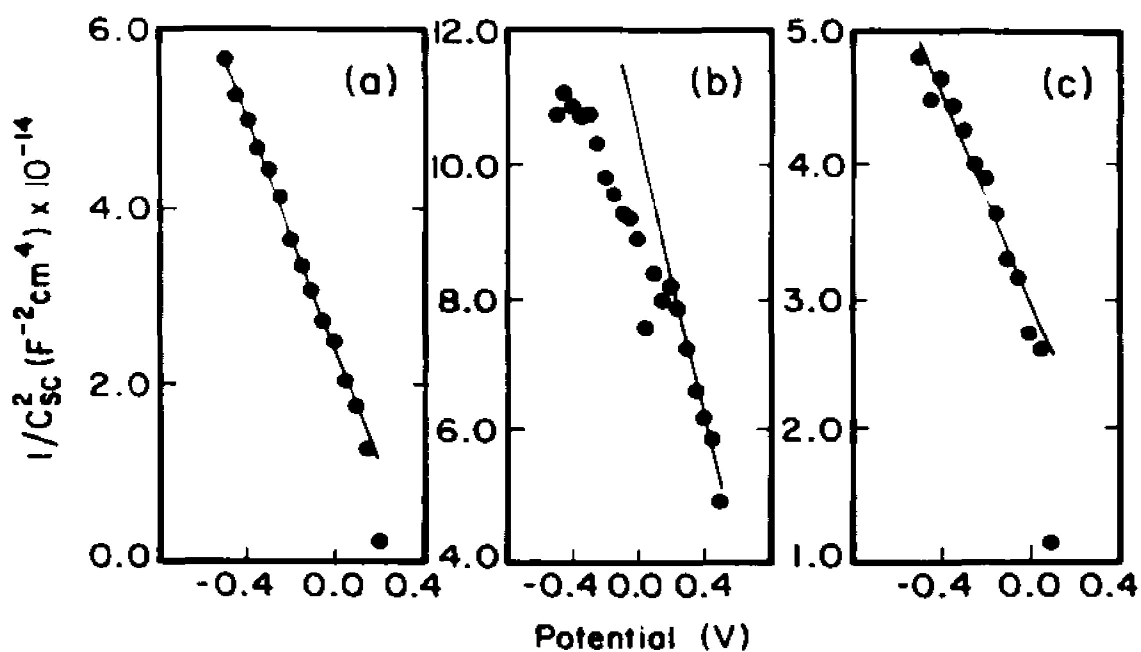

Figure 4.47 Mott-Schottky plot of the space-charge layer capacitance of (a) the original Al/SB sample, (b) the $CClF_3/H_2$ RIE Al/SB sample, and (c) the $CClF_3/H_2$ RIE $+O_2$ ash, Al/SB sample.

TABLE X. Built-in potential V_{bi}, doping density N_d, energy difference between the bottom of the conduction band and the Fermi level V_n, barrier height V_{bn}, and series resistance R_s obtained from the impedance measurements of the SB samples.

Si Sample	V_{bi} (V)	N_d (cm^{-3})	V_n (V)	V_{bn} (V)	R_s (Ω)
Original	0.159	2.04×10^{15}	0.201	0.360	38
CHF_3/Ar	0.040	7.71×10^{14}	0.226	0.266	32
CF_4	-0.097	3.12×10^{15}	0.190	0.090	25
Original[a]	0.356	1.69×10^{16}	0.146	0.502	30
$CClF_3/H_2$	1.000	1.10×10^{16}	0.157	1.160	44
$CClF_3/H_2$ + O_2 ash	0.754	2.92×10^{16}	0.132	0.886	70

[a] Al metal contact.

Figures 4.48(a)-(c) show the dependence of the space-charge layer resistance on the applied dc potential for an original Si, the CHF_3/Ar RIE, and the CF_4 RIE Ti/SB samples, respectively. Similar results are shown in Figs.4.49(a)-(c) for the samples with Al metal contacts. All the values for the series resistance under reverse-bias conditions were corrected for the shunt resistance (R_{sh}). In both figures the linear regression of the experimental data with Eq.(4.5) in some potential range was obtained. In Table XI are presented the results of this analysis together with the values for the barrier height obtained from J_{st}, using the thermionic emission theory [72]:

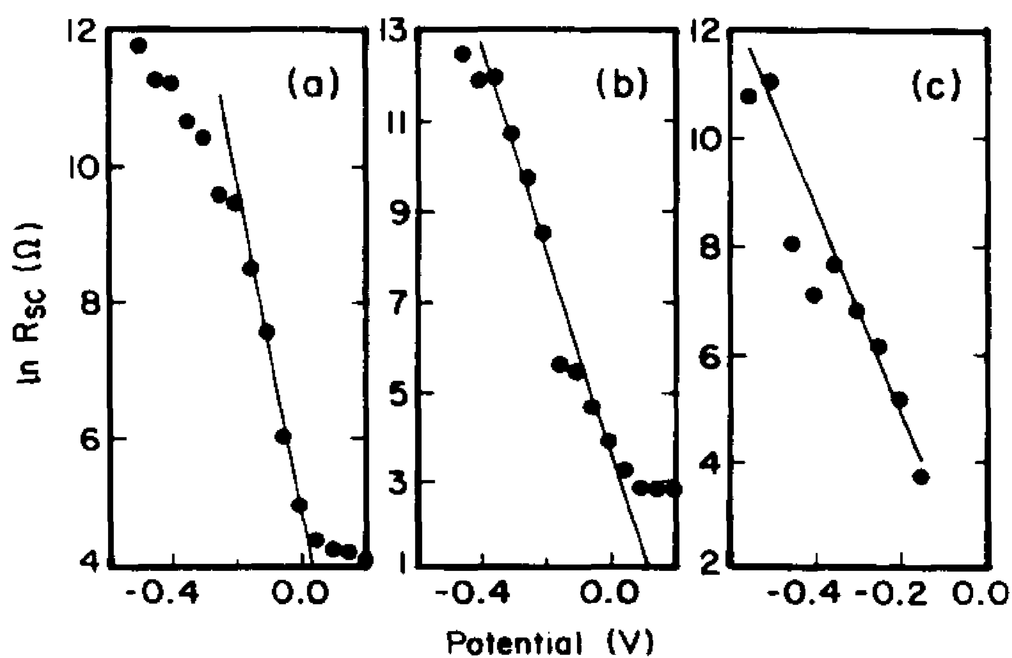

Figure 4.48 ln R_{sc} vs bias voltage for (a) the original Ti/SB, (b) the CHF_3/Ar RIE Ti/SB, and (c) the CF_4 RIE Ti/SB.

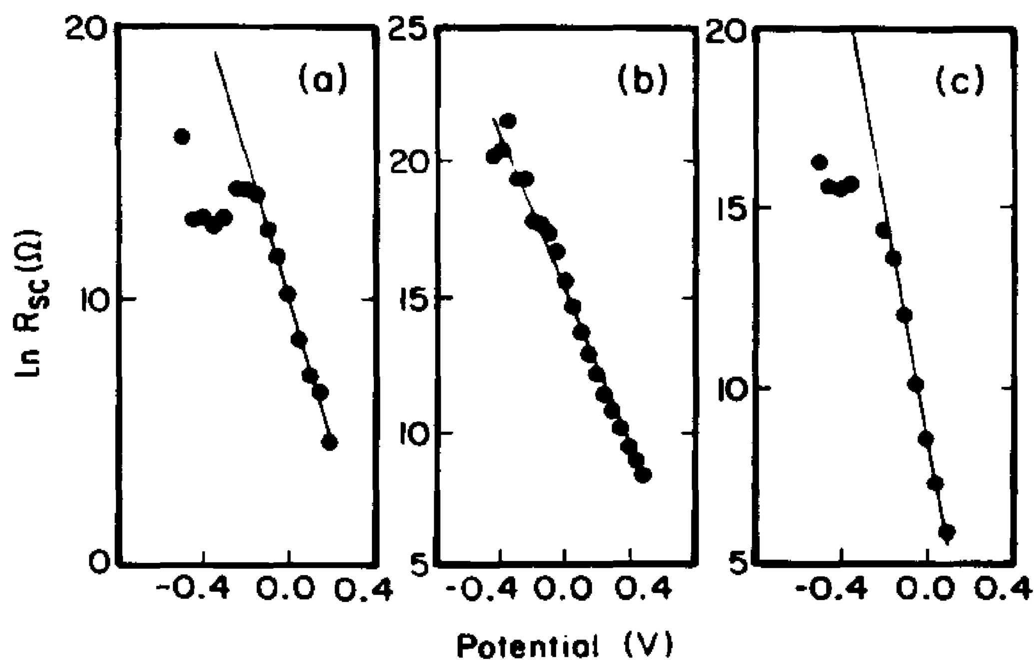

Figure 4.49 (a) The same as Fig. 4.48 (a) for the original Al/SB. (b) The same as (a) for the $CClF_3/H_2$ RIE Al/SB. (c) The same as (a) for the $CClF_3/H_2$ RIE $+O_2$ ash Al/SB.

TABLE XI. Diode ideality factor n, saturation current density J_{st}, barrier height V_{bn}, and shunt resistance R_{sh}, calculated based on the impedance results and thermionic emission theory for the SB devices.

Si Sample	n	J_{st} (A/cm^2)	V_{bn} (V)	R_{sh} (Ω)
Original	1.58	0.0159	0.546	4500
CHF_3/Ar	1.69	0.0596	0.512	5900
CF_4	2.02	2.47	0.415	370
Original*	1.49	0.21	0.479	$4.8x10^4$
$CClF_3/H_2$	2.74	0.25	0.475	$2.3x10^7$
$CClF_3/H_2$ + O_2 ash	1.20	0.194	0.481	$3.1x10^5$

* Al metal contact.

$$J_{st} = A^{**} T^2 \exp(-eV_{bn}/k_BT) \ , \qquad (4.6)$$

where A^{**} is the effective Richardson constant (A) for thermionic emission. In this case, A^{**}/A=2.1 [72].

Figures 4.50(a)-(b) depict the current density versus voltage characteristics of the various devices. A barrier height decrease is evident in the sample subjected to the CF_4 RIE treatment [Fig.4.50(a)], while a shift in the J-vs-V plot to large forward bias in the case of the $CClF_3/H_2$ RIE indicates the presence of an insulating layer [Fig.4.50(b)]. Figures 4.51(a) and (b) show the fitting of the experimental data for a CHF_3/Ar RIE and a $CClF_3/H_2$ RIE sample, respectively, to Eq. (4.4) after correcting for the series resistance. The CF_4 treated sample was

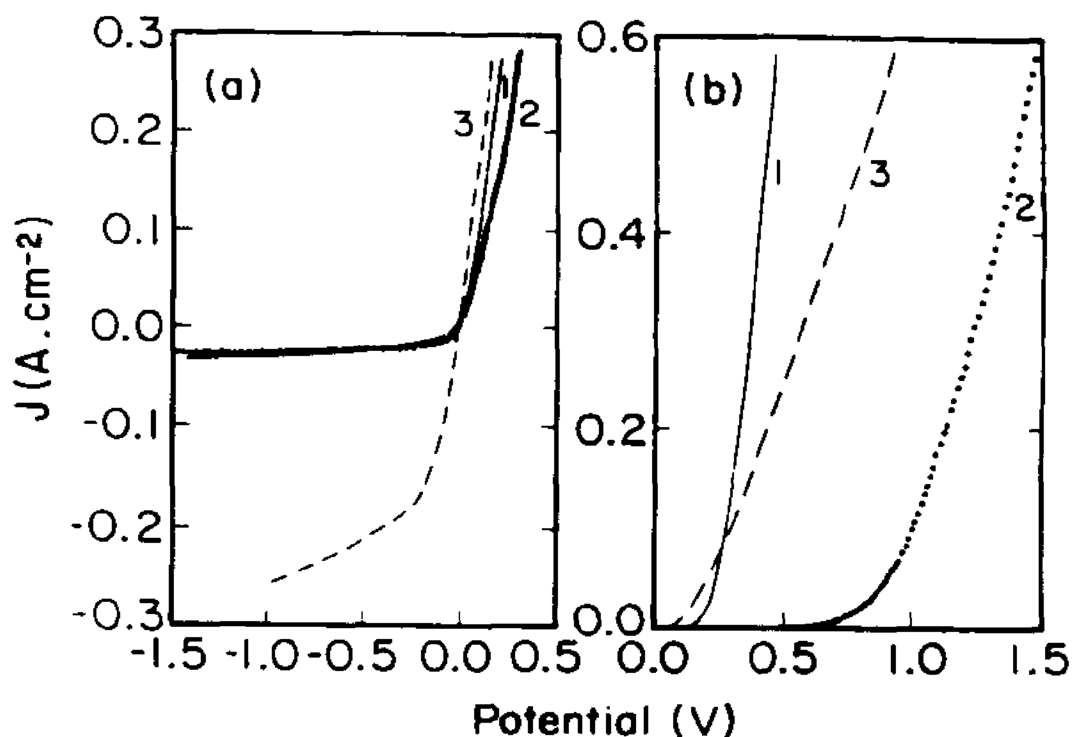

Figure 4.50 (a) Current density vs voltage characteristics of the Ti/SB devices: (1) original, (2) CHF_3/Ar RIE, and (3) CF_4 RIE. (b) The same as (a) for the Al/SB devices: (1) original, (2) $CClF_3/H_2$ RIE, and (3) $CClF_3/H_2$ RIE + O_2 ash.

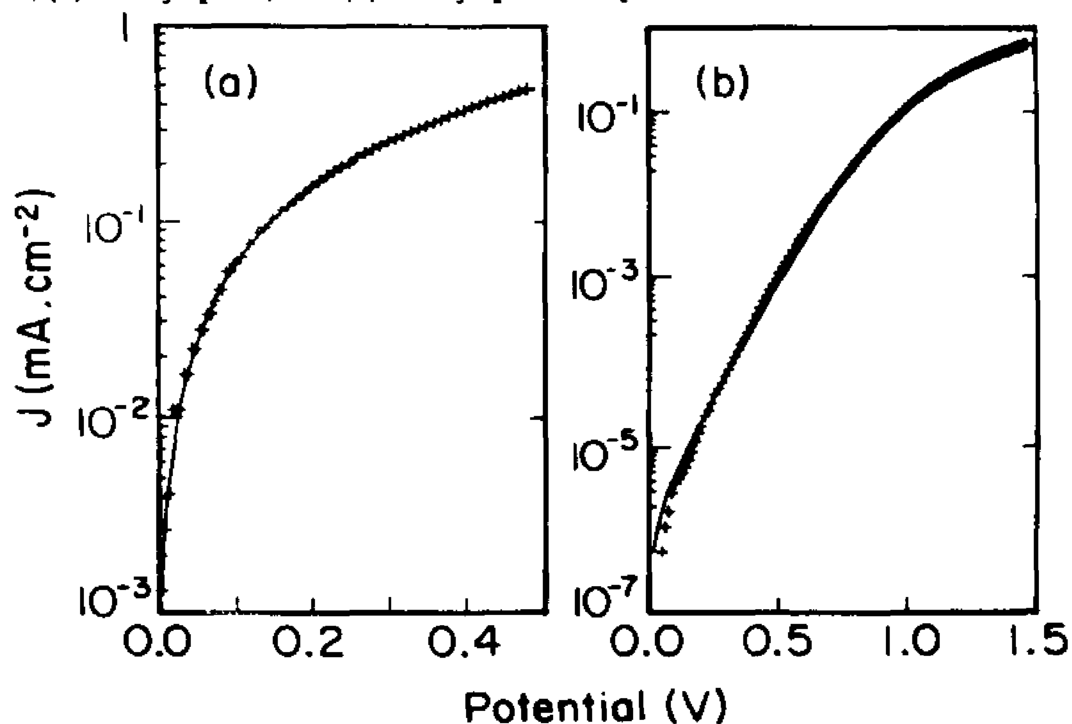

Figure 4.51 Current density vs voltage characteristics in the forward-bias region (+) and the theoretical fit to Eq.(4.4) (solid line) for (a) CHF_3/Ar RIE Ti/SB, and (b) $CClF_3/H_2$ RIE Al/SB.

TABLE XII. Diode ideality factor n, saturation current density J_{st}, barrier height V_{bn}, and series resistance R_s, calculated based on the current-voltage results and thermionic emission theory for the SB devices.

Si Sample	n	J_{st} (A/cm^2)	V_{bn} (V)	R_s (Ω)
Original	1.15	0.0191	0.541	18.5
CHF_3/Ar	1.30	0.0142	0.549	42.0
CF_4				42.3
Original[a]	1.25	4.7×10^{-5}	0.697	15.0
$CClF_3/H_2$	3.18	1.6×10^{-6}	0.784	41.5
$CClF_3/H_2$ + O_2 ash	1.23	4.35×10^{-4}	0.639	65.0

[a] Al metal contact.

ohmic. Table XII shows the values of the various parameters obtained from these measurements. The barrier height was extracted again by assuming thermionic emission.

Figures 4.52(a) and (b) show the comparison between the photoreflectance (PR) spectra of Si and Si/Ti SB devices for the original (or control) samples and for the samples subjected to the $CClF_3/H_2$ RIE process, respectively. In both cases broadening of the peaks is observed in addition to the red shift when the metal contact is present (more pronounced for the treated sample). The comparison between SB structures made on untreated silicon, $CClF_3/H_2$ RIE, and O_2 ashed samples are shown in Fig. 4.52(c); a more pronounced peak broadening and red

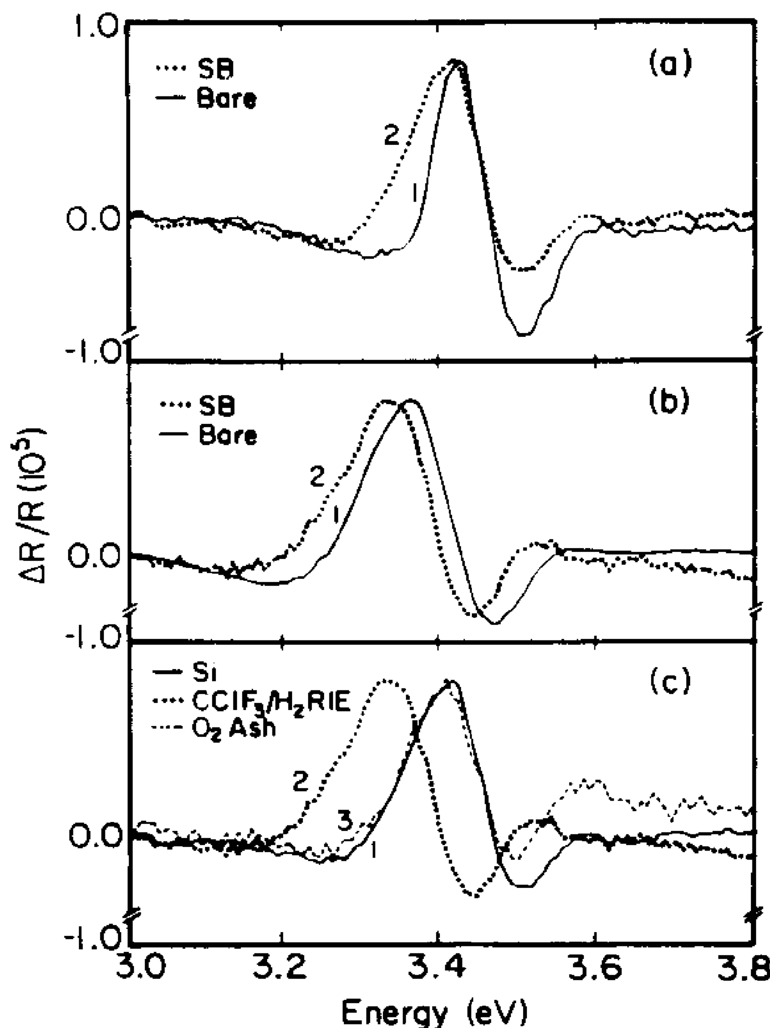

Figure 4.52 Photoreflectance spectra of (a) bare Si (1) and untreated Ti/SB (2); (b) bare $CClF_3/H_2$ RIE Si (1) and $CClF_3/H_2$ RIE Al/SB (2); (c) Ti/SB devices with untreated Si (1), $CClF_3/H_2$ RIE (2), and O_2 ash (3).

shift are observed for the RIE treated sample, while O_2 ashing seems not to affect the barrier properties. The line-shape parameters obtained from the fitting of the PR results for two dimensional critical points are shown in Table XIII.

4.4.2 Experimental results of metal-oxide-semiconductor (MOS) devices

The MOS devices for this study were subjected to the CHF_3/Ar and CF_4 RIE

TABLE XIII. Fitting parameters for the photoreflectance of SB. E_1 is the energy gap and Γ_1 the phenomenological broadening parameter related to the lifetime of the majority carriers.

Sample	E_1 (eV)	Γ_1 (meV)
Original[a]	3.417	119.6
$CClF_y/H_2$	3.343	142.1
O_2 ash	3.391	119.7

[a] Ti metal contact.

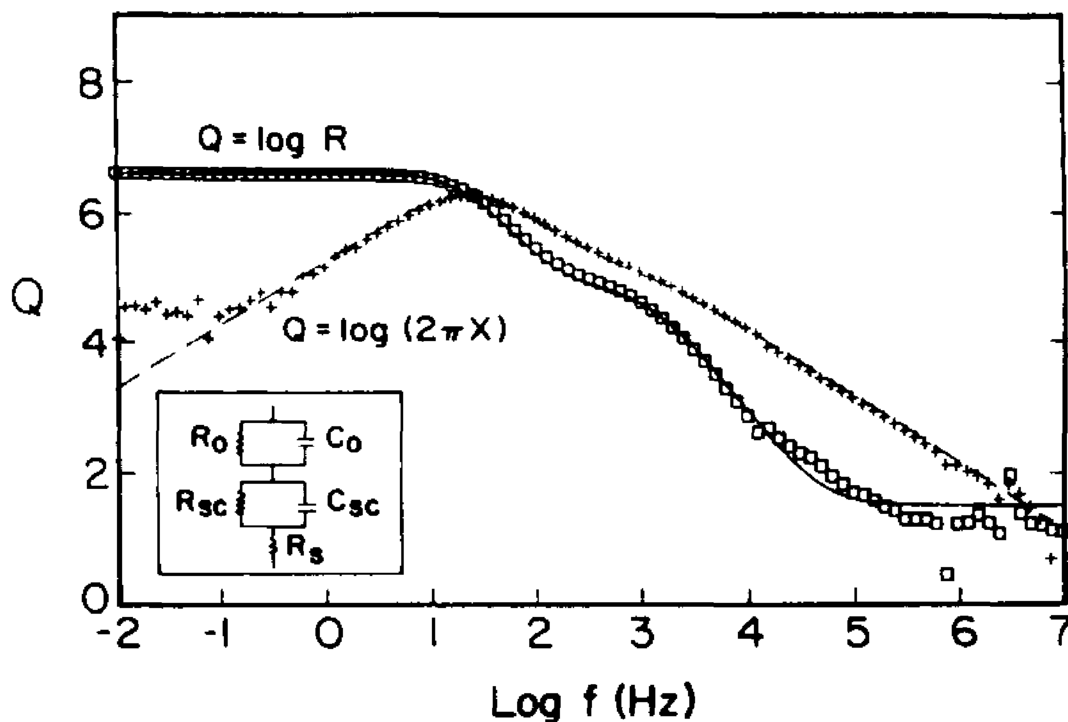

Figure 4.53 Impedance spectra of MOS device with untreated Si at -0.5 V. The equivalent circuit is shown in the inset with the theoretical fits to this circuit (solid lines).

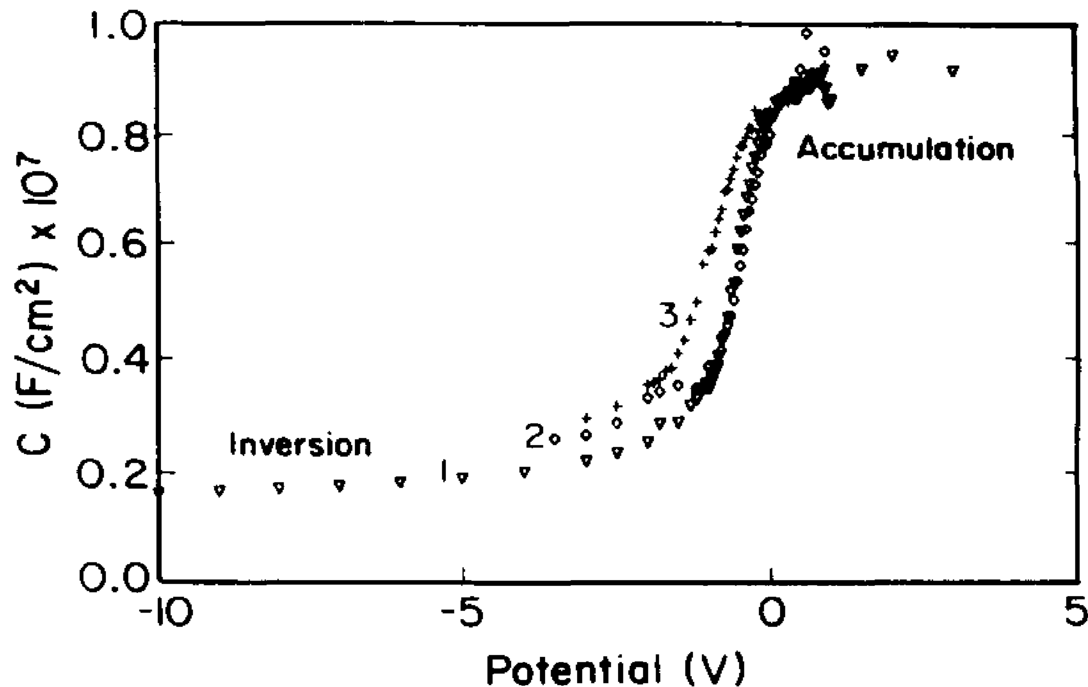

Figure 4.54 High-frequency capacitance C vs voltage for MOS devices with (1) untreated Si, (2) CHF_3/Ar RIE, and (3) CF_4 RIE.

treatments. Figure 4.53 shows the impedance data in the depletion region of a MOS control sample with the equivalent circuit used to interpret these data. The same configuration of equivalent circuit was found not only to fit the impedance data over the entire voltage range from depletion to accumulation for untreated Si but also to fit the impedance spectra of all the RIE treated samples.

Figure 4.54 shows the high-frequency capacitance, C, of the samples, which is the combination of the oxide capacitance, C_o, and the space-charge layer capacitance, C_{sc}:

$$\frac{1}{C} = \frac{1}{C_o} + \frac{1}{C_{sc}} \ . \qquad (4.7)$$

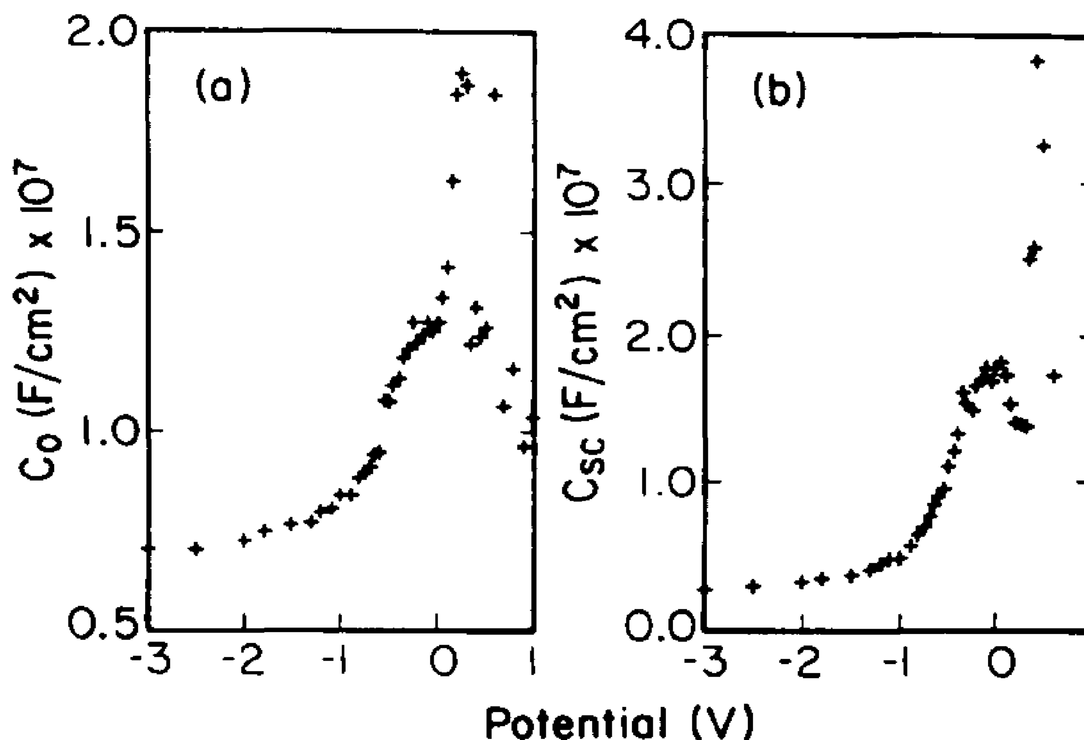

Figure 4.55 The voltage dependence of the oxide layer capacitance, C_o, (a), and the space-charge layer capacitance, C_{sc}, (b), of the MOS device with the untreated Si.

Figures 4.55(a) and (b) present the relationship of C_o and C_{sc} of the original MOS sample, respectively, with bias. As one can see, the oxide capacitance is bias dependent. An equivalent circuit with a constant oxide capacitance and a surface state parallel to the space-charge layer elements was tried to represent the impedance data, but it did not suit for the impedance results over entire applied potential range.

Figures 4.56(a)-(c) are the Mott-Schottky plots of C_{sc} for the original, the CHF_3/Ar RIE, and the CF_4 RIE MOS samples, respectively. The values for V_{bi} and N_d are also listed in Table XIV.

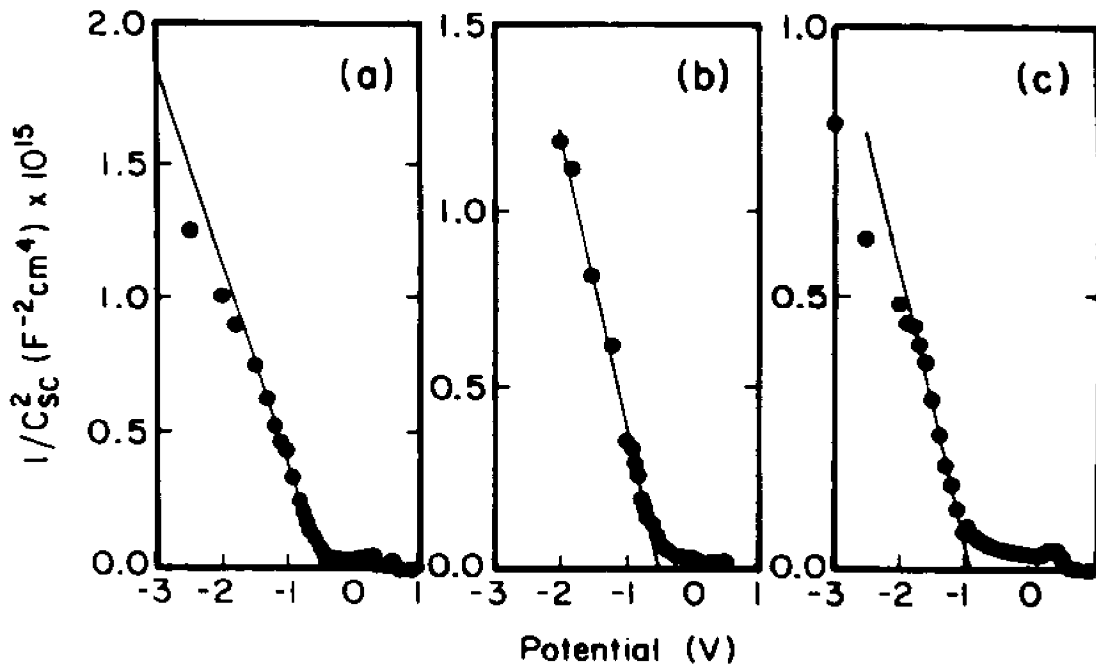

Figure 4.56 Mott-Schottky plot of C_{sc} of (a) the untreated MOS sample, (b) the CHF_3/Ar RIE MOS sample, and (c) the CF_4 RIE MOS sample.

TABLE XIV. Built-in potential V_{fb}, doping density N_d, and thickness of the oxide layer l_o of the MOS samples. SCL denotes space-charge layer.

		V_{bi} (V)	N_d (10^{-16} cm^{-3})	l_o (Å)
Original	SCL	-0.42	1.63	
	oxide	0.23	9.23	498
CHF_3/Ar	SCL	-0.45	1.49	
	oxide	0.28	8.26	410
CF_4	SCL	-0.85	2.35	
	oxide	0.21	16.90	372

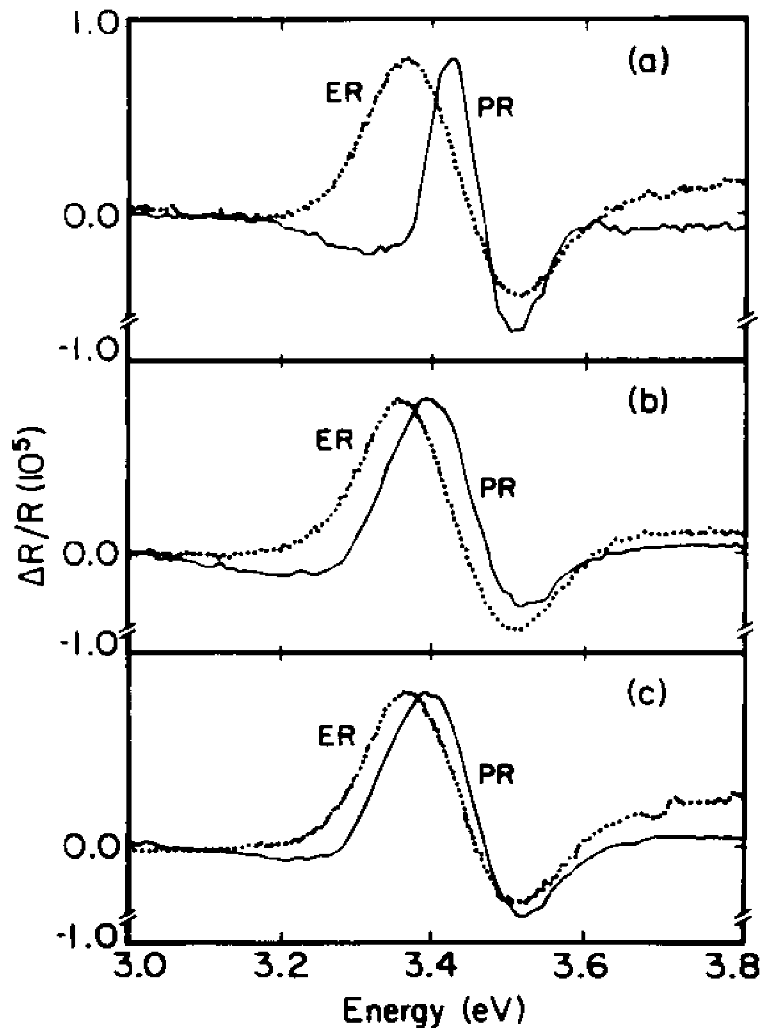

Figure 4.57 Electroreflectance (ER) spectra of (a) a MOS device with untreated Si, (b) a CHF_3/Ar RIE MOS sample, and (c) a CF_4 RIE MOS sample, and photoreflectance (PR) spectra of bare Si.

The electroreflectance (ER) of the MOS devices constructed from the original Si, the CHF_3/Ar RIE, and the CF_4 RIE samples did not show any significant differences. Figure 4.57(a) shows the ER signal (at 0V) obtained for the control MOS sample and the photoreflectance (PR) of the bare substrate. Analogous comparisons are shown in Figs.4.57(b) and (c) for the samples subjected to the CHF_3/Ar and CF_4 RIE treatments, respectively. The fitting of the experimental data

TABLE XV. Fitting parameters for electroreflectance and photoreflectance of the bare and MOS samples.

Sample		E_1 (eV)	Γ_1 (meV)
Bare Si (PR)	Si	3.446	82.4
	CHF_3/Ar	3.406	145.5
	CF_4	3.421	141.3
MOS (ER)	Si	3.411	155.4
	CHF_3/Ar	3.403	157.9
	CF_4	3.399	152.8

with the Aspnes's third-derivative function for two-dimensional critical points is presented in Table XV. For the non-RIE samples the ER line shape of MOS is broader than that of the PR of bare Si, and the ER peak shifts to a lower energy. For the RIE treated samples there is no significant difference between the MOS ER and bare PR results.

4.4.3 Comparison of SB with liquid junction

From the impedance data of the SB devices, the residue overlayer, due to the RIE process, was detected for the CHF_3/Ar RIE and $CClF_3/H_2$ RIE samples. The thickness of this layer, as a function of its unknown dielectric constant (l/ε), was calculated to be 5.8 Å/ε for the CHF_3/Ar RIE and 92 Å/ε for the $CClF_3/H_2$ RIE treated samples. For the CHF_3/Ar RIE samples the agreement with the liquid junction data (5.7 Å/ε) is excellent. For the $CClF_3/H_2$ RIE samples the evaluated

thickness of the residue layer based on liquid junction (0.96Å/ε) is much less than that from SB. As pointed in §4.3, it results from the overlayer produced by $CClF_3/H_2$ RIE treatment is porous. In the LJC configuration the electrolyte can penetrate through this layer and as a result the real contact area is much larger than the geometric area, which is reflected in the capacitance measurements as a thinner residue layer. In contrast, in the present SB configurations, the metal deposits on the crests of the residue, in which case the contact area is much smaller than the geometric area and as a result the thickness is overestimated.

The contribution due to surface states was detected on Schottky devices only over a small potential region, in the forward bias, for the control SB sample and the CHF_3/Ar RIE one. Their densities at 0.2 V are 1.8×10^{13} and 9.4×10^{13} cm^{-2}, respectively. The surface state densities of the SB devices are larger than the densities of these states in the LJC configuration (5.9×10^{11} cm^{-2} for the untreated samples), probably due to interactions of these states with the electrolyte. On the other hand, measurements of the frequency dispersion of the EPR signal carried out on a bare Si substrate showed a surface state with the same relaxation time as that obtained from the impedance data of the SB untreated sample. No surface states could be detected for the sample subjected to CHF_3/Ar RIE in the LJC configuration and for those subjected to the CF_4 RIE in both configurations. For the $CClF_3/H_2$ RIE substrate in the SB configuration a surface state density of 1.7×10^{11} cm^{-2} was obtained, while this value in the LJC configuration was equal to 5.5×10^{12} cm^{-2}. As the density of surface states is inversely proportional to the sample area,

these values are underestimated in the SB configuration and overestimated in the LJC one, due to porosity.

The results presented in Table X show that the doping densities (N_d) obtained for the SB devices with Ti metal contacts agree very well with the sample resistivities and with the values obtained from the measurements in the LJC. For the set of SB devices with the Al metal contacts the N_d values are larger. The built-in potentials and, consequently, the barrier heights have decreased after the CHF_3/Ar and CF_4 RIE processes. This effect was also observed for the samples in the LJC configuration and by other authors [18,131,134,135] and was interpreted in terms of an accumulation of positive charges at the semiconductor surface after the RIE treatments. For the $CClF_3/H_2$ RIE treatment an increase in the barrier height was observed in comparison with the control SB device. This result indicates the presence of an insulating overlayer, which is in agreement with that in the LJC configuration. The Mott-Schottky plot [Fig.4.47(b)] shows pinning in the reverse bias region, which is another indication of an insulating overlayer. O_2 ashing partially removes the damage, shifting the barrier height toward the value of the control SB device, which was observed in the LJC configuration.

The photoreflectance results shown in Figs.4.52(a)-(c) for the untreated and $CClF_3/H_2$ RIE SB devices show spectral features similar to those in the LJC configuration and in contact with air; the spectral changes were interpreted in terms of tensile strain caused by surface damage.

From the results on the space-charge resistance as a function of the applied

bias and the I-V measurements (table XI and XII), it is concluded, looking particularly at the ideality factors, that the diffusion and the recombination currents are comparable for most of the devices that were analyzed here. For the Ti/SB samples, the barrier height values, calculated using the thermionic emission theory, are much larger than those obtained from the direct impedance results (Table X) and are not sensitive to the RIE treatments. In addition, the values of the ideality factors and the saturation currents obtained from the impedance measurements (Table XI), which were taken mostly in the reverse bias region, and the current measurements (Table XII), which were taken mostly in the forward bias region, do not fully agree. The resultant barrier height derived from the impedance experiments is in good agreement with the value calculated from the potential distribution of the R_{sc} based on the thermionic emission theory only for the control SB sample with Al metal contact. This strongly suggests that other current transport mechanisms, in addition to thermionic emission, take place. These mechanisms can include tunneling through the barrier, recombination in the space-charge region, and minority carriers in the interface. This is a subject for further investigation.

Looking at I-V characteristics of the two sets of SB devices, the presence of the insulating overlayer due to the $CClF_3/H_2$ RIE treatment [Fig.4.50(b)] is evident by the positive shift of the threshold bias. O_2 ash probably removes this layer, but still some deviation from the control device characteristics is observed, which could be related to structural damage. The I-V curves of the Ti/SB diodes

[Fig.4.50(a)] show that the CF_4 RIE treatment is responsible for more damage compared with the CHF_3/Ar RIE process. On the other hand, the results on liquid junction cell indicate that the CHF_3/Ar RIE treatment is more deleterious than the CF_4 RIE. The reason may be that the by-products of these two treatments are completely different and could be washed out by the cleaning procedure before the metal deposition. Unfortunately, the available data do not permit further speculation on the possible reasons for the difference.

4.4.4 Comparison of MOS devices with liquid junction

The MOS devices seem to be less affected by the RIE procedures when compared with the SB devices. Both impedance and modulation spectroscopy measurements did not show any significant differences between the control MOS sample and the RIE treated ones. This result suggests that the presence of the oxide layer masks the possible effects due to the RIE damage. This is consistent with prior observation that RIE damage and contaminations can be removed by oxidation [137]. This interpretation is supported by comparing the modulation spectroscopy results obtained for a bare Si substrate and a control MOS device. The fact that the ER of MOS obtained from the untreated substrate have line-shape and peak position different from that of PR of the bare substrate [Fig.4.57(a)] confirms that after growing the oxide layer on the Si surface some strain may be induced and this effect might be so strong that it masks the RIE damage. The possibility of loss of crystallinity has been discarded as a main factor

influencing the optical results, because the shifting and splitting of the photoreflected peak instead of broadening have been observed at low temperature (77K). In the case of the impedance results, the observed bias dependence of the "oxide layer" capacitance can be interpreted in terms of impurities and/or a combination of the proper oxide plus interface plus damaged region.

X-ray photoelectron spectroscopy (XPS) studies [145-149] have shown that an interfacial transition layer, a few angstroms thick, is formed on both sides of the Si/SiO_2 interface, to relax the stress produced due to oxide formation. In these regions both compositional and structural transitions take place: on the Si side two silicon layers are displaced, while on the oxide films, the structural changes take place within 30 Å of the interface. In addition to the atomic displacements at the interface, related to the possible presence of electronic states, the existence of abrupt interfaces and intermediate oxidation states of silicon (such as SiO, Si_2O, and Si_2O_3) were found. All of these findings are strictly dependent on the oxidation and post-annealing conditions of the oxide growth as well as on the crystallographic orientation of the base substrate.

The values of doping density obtained from MOS measurements (Table XIV) are 1 order of magnitude higher than those obtained for the samples in the LJC and the SB device configurations probably because the impurities diffuse to the bulk of the semiconductor during the oxide growth process [150]. The thickness of the oxide layer, calculated using the impedance results (Table XIV) and the SiO_2 dielectric constant, agrees very well with the 500 Å value specified during the oxide

growth processing step.

Except for the fact that in the liquid junction configurations one has to take into account the contribution of the electrolyte to the potential distribution, similar potential distribution is expected for all the solid junction configurations that were analyzed, with or without an insulating layer.

In summary, the applicability of liquid junctions as an ex situ powerful tool to characterize electronic materials is demonstrated. In terms of sensitivity of the dielectric properties to the RIE treatments, the liquid junction is the most sensitive, followed by SB devices, with the MOS configuration exhibiting the least sensitivity. One of the main advantages in further pursuit of these analytical techniques is their suitability for analysis of the real surfaces, rather than surfaces that have already passed through device processing, which may have altered properties.

CHAPTER 5

SURFACE OPTIMIZATION OF n-$CuInSe_2$

5.1 Experimental results [115-117]

5.1.1 Photoelectrochemical performance characteristics

Figure 5.1 shows an example of the experimental results that has motivated this study. It compares the photoelectrochemical performance characteristics of n-$CuInSe_2$ in polyiodide solution of an unetched, etched, and etched + oxidized electrode. The Br_2/MeOH etch cleans the surface and leads to some Cu-depletion in the near surface region [43]. Subsequent air oxidation further improve the photo I-V characteristics [43]. A full analysis of these curves will not be attempted in this study. Instead, attention will be focused on the changes in the EER and impedance as a function of the surface treatment and on the information that EER and impedance can provide to help understanding the improvements in performance resulting from the surface optimization.

5.1.2 Electrolyte electroreflectance (EER)

Figure 5.2 shows the EER spectra of $CuInSe_2$ in aqueous polysulfide at different electrode potentials. One can observe three transitions, marked as A, B, and C, located at 1.02, 1.175, and 1.26 eV, respectively. Peaks A and C correspond to the low temperature spectrum that was reported by Shay et al. [151] and were assigned by them to the direct gap transition and its spin orbit splitting. The

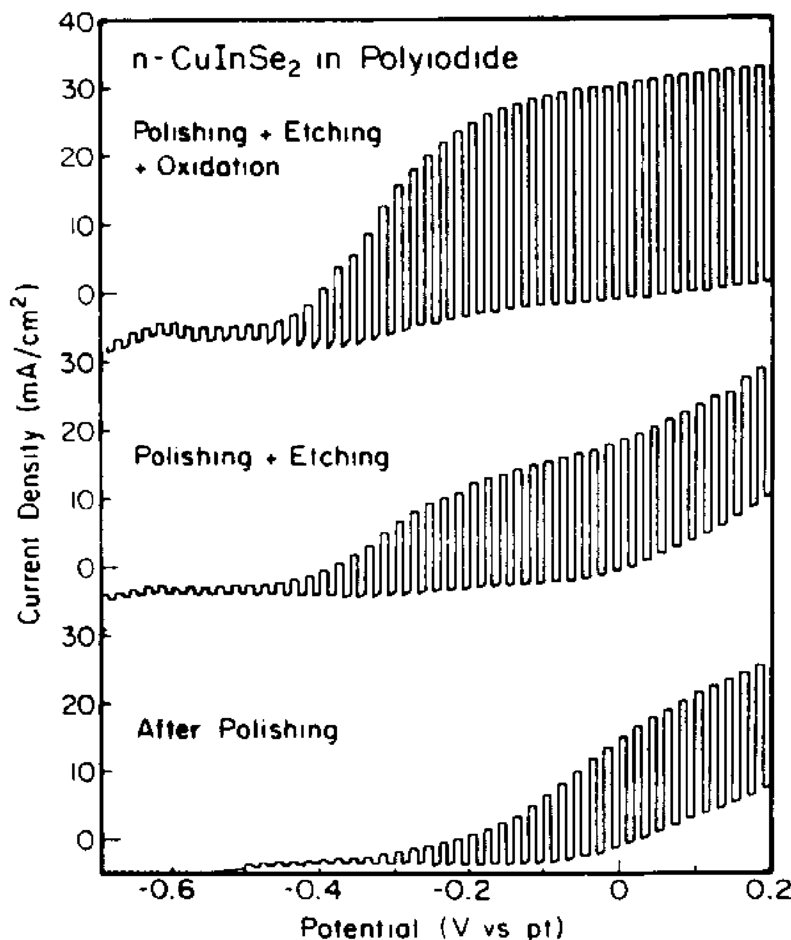

Figure 5.1 Current-potential response curves with chopped white light for n-$CuInSe_2$ in polyiodide solution with the following composition: 6M KI + 0.1M CuI_2 + 0.1M InI_3 + 0.0125M I_2 at pH 6.0. W/X source with intensity of 100 mW/cm^2. Etching in 2% Br_2/methanol solution for 60s. Oxidation for 2h at 150°C in air.

position of peak B is at higher energy than the one observed for the crystal field splitting; as a result, the origin of this transition is uncertain. One also can see in the same figure that, as long as the potential stays in depletion (U > - 0.2 V vs Pt), the shape of the spectra is not affected by the potential of the electrode. In addition, at electrode potentials slightly negative of - 0.5 V vs Pt the phase inverts, indicating that the system was shifted from depletion to accumulation.

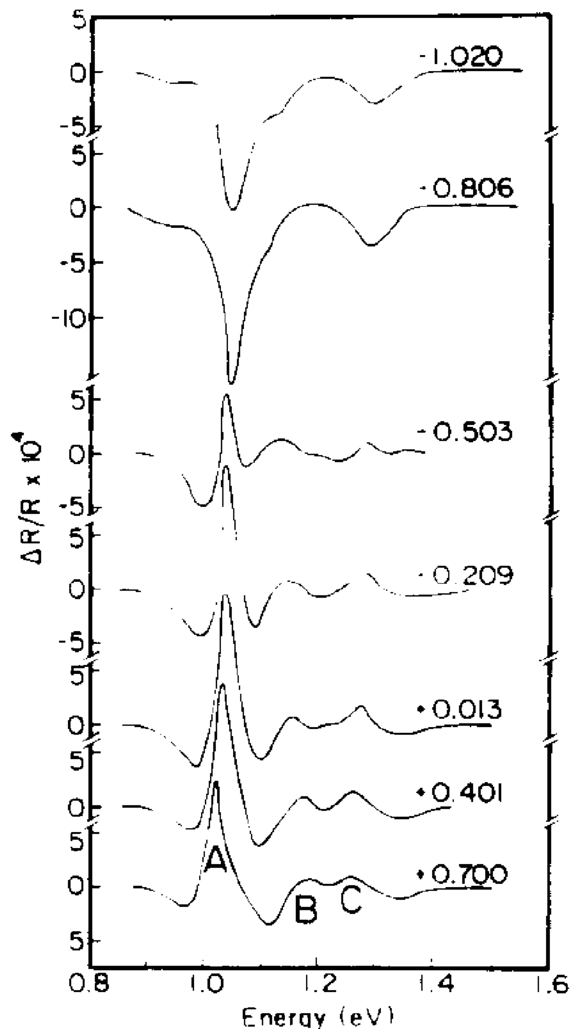

Figure 5.2 EER spectra of n-$CuInSe_2$ in 1/1/1M aqueous polysulfide as function of electrode potential vs Pt. Modulation amplitude: 0.20 V.

In figure 5.3 we present a similar set of spectra in polyiodide solution. The spectral features are unaffected by the change in electrolyte. The flat-band potential is shifted to more negative values vs the solution potential. At very positive potentials (strong depletion), some broadening of the high energy lines is observed.

In figures 5.4 and 5.5 we show the variation of the amplitudes of the peaks

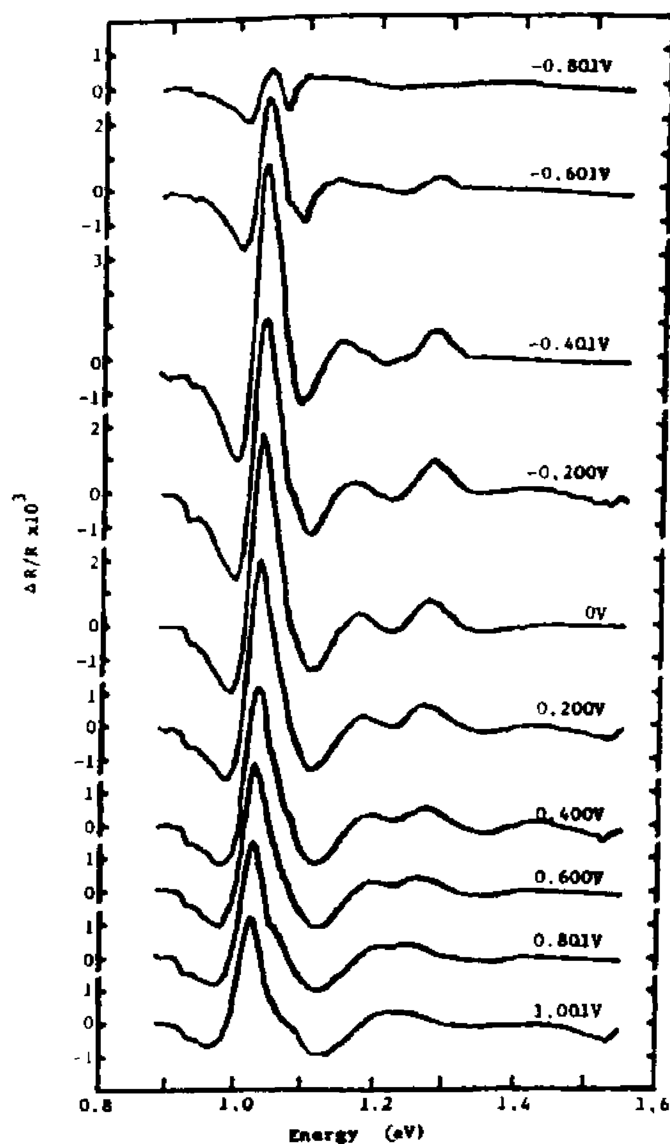

Figure 5.3 **EER spectra of n-CuInSe$_2$ in aqueous polyiodide with the same composition in Fig. 5.1.**

in the EER spectrum in polysulfide solution before and after etching the crystal in 2% Br$_2$/methanol solution for 60 s. One can observe that prior to etching the amplitude does not change sign at negative potentials; rather, it peaks around a potential of - 0.2 V vs Pt, the amplitude decreases sharply as the bias is going to reverse. This behavior is identical with the one previously observed for electro-

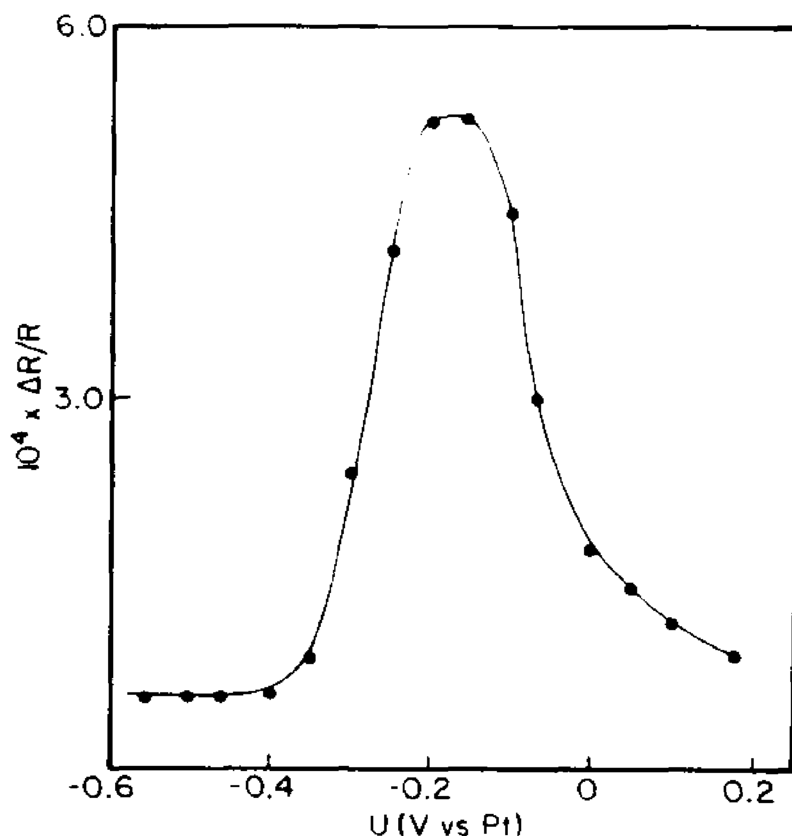

Figure 5.4 **Variation of the amplitude of peak A from Fig. 5.2 with the electrode potential, before etching.**

deposited CdSe [123] and single crystal $CdIn_2Se_4$ [106] in the same electrolyte. There it was interpreted in terms of pinning of the Fermi level (or unpinning of the band edges).

After etching, the pinning of the Fermi level is almost completely removed. One can observe a sharp phase change at a potential of - 0.62 V vs the solution potential, which one can identify with the flat-band potential. Under reverse bias conditions, the amplitude is approximately independent of the potential of the electrode. All three peaks behave in a similar way.

Figure 5.6 shows the corresponding measurements in polyiodide solution.

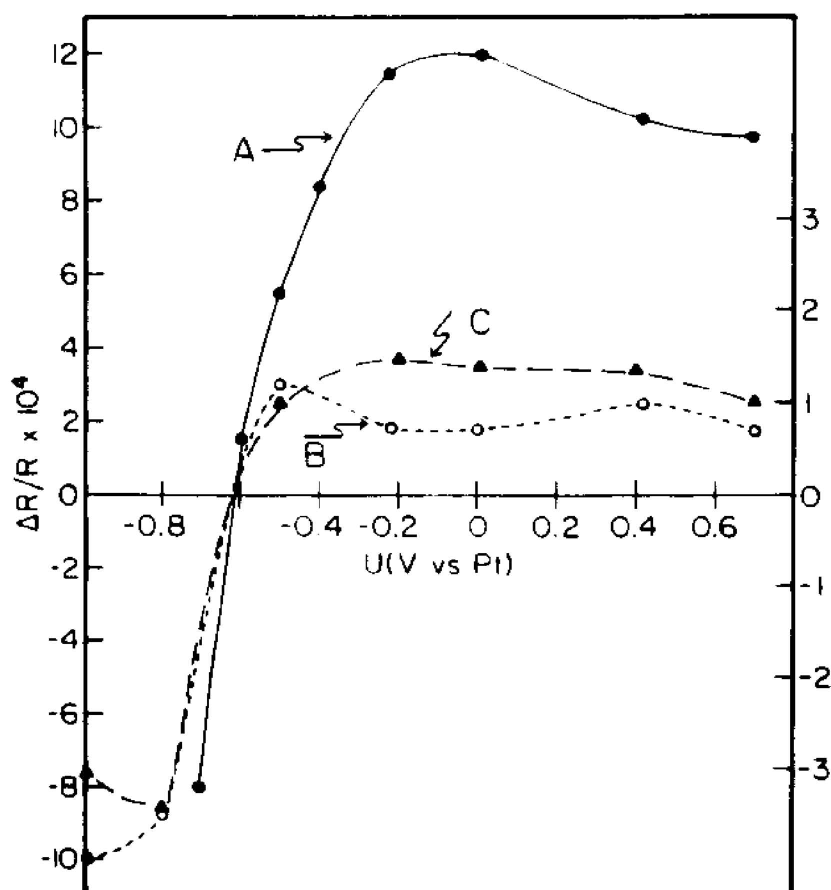

Figure 5.5 **Variation of the amplitude of the three EER peaks in Fig. 5.2 with electrode potential after etching in Br_2/methanol and wash in 10% KCN.**

In this electrolyte, even before etching, the Fermi level at reverse bias is only slightly pinned, the phase inversion is sharp, and the flat-band potential is shifted to - 0.70 V vs the solution potential. As with the polysulfide case, etching unpins the Fermi level as is observed by the decrease in the dependence of the EER peak amplitude on the electrode potential as reverse bias conditions were approached. Changes in roughness can explain the decrease in the absolute magnitude of the EER signal with etching, but this aspect needs further exploration.

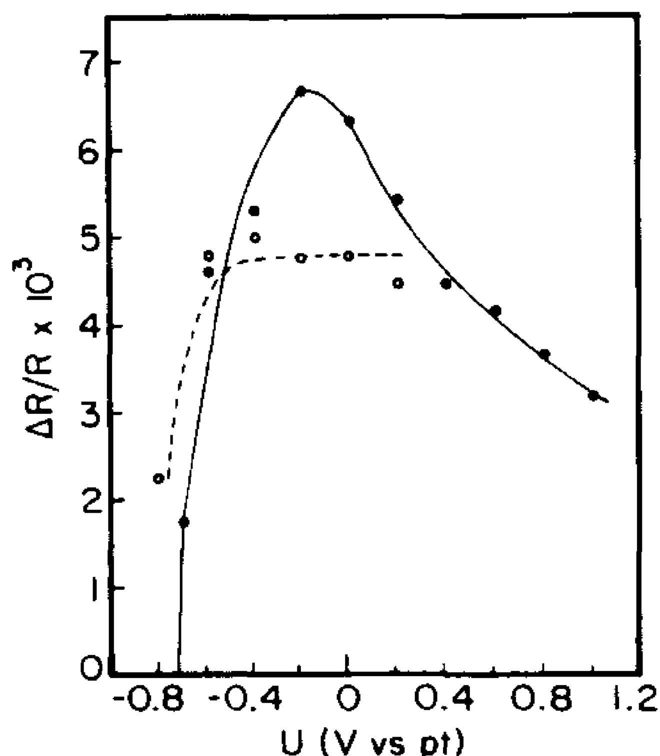

Figure 5.6 Variation of the amplitude of the low energy EER peak from Fig. 5.3 with electrode potential, before (solid line) and after (broken line) etching.

Figure 5.7 shows the EER spectra of n-$CuInSe_2$ in aqueous polyiodide electrolyte after oxidation for 1.5 h at 150°C. The three distinct peaks are seen clearly only at - 0.4 V vs Pt. At - 0.2 V vs Pt, the high energy peaks are broadened such that the whole high energy region, from 1.5 eV down to the main peak, looks like one broad peak. As the bias shifts to reverse, the amplitude of the broad peak decreases considerably, and, although some traces of the original high energy peaks can be spotted, the only distinctive remaining peak is that due to the direct band-edge. In addition, considerably higher voltage modulation was needed to obtain a reasonable signal-to-noise ratio than was necessary to similar experi-

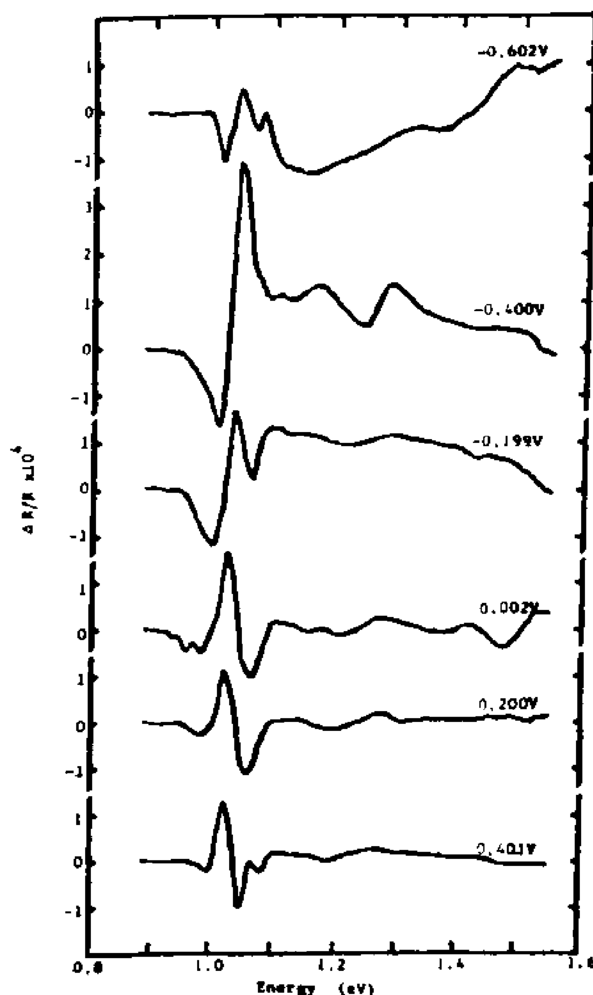

Figure 5.7 EER spectra of n-$CuInSe_2$ in aqueous polyiodide with the same composition as in Fig. 5.1 after oxidation for 1.5h at 150°C.

ments with unoxidized electrodes. In attempt to gain some insight into this behavior, the EER spectra of unoxidized $CuInSe_2$ and of oxidized $CuInSe_2$ was compared with that of $CuInSe_2$, on which surface a thin layer of electrodeposited indium was air oxidized, in figure 5.8. These data all were taken at the same electrode potential. One can see that there is a close correspondence between the EER behavior of the oxidized sample and the one with the indium oxide.

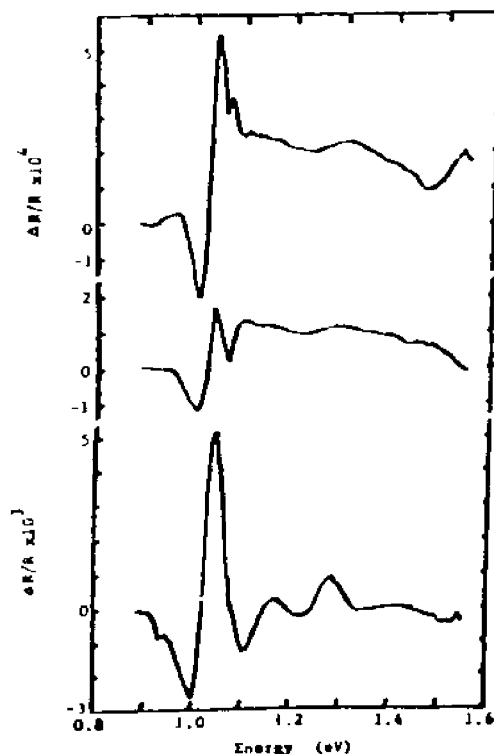

Figure 5.8 Comparison of EER spectra of n-$CuInSe_2$ in aqueous polyiodide. Top: With a layer of indium oxide; potential = -0.245V vs Pt; modulation = 2.25 V_{p-p}. Middle: After oxidation for 1.5h at 150°C; potential = -0.2V vs Pt; modulation = 0.4 V_{p-p}. Bottom: As received; potential = -0.2V vs Pt; modulation = 0.2 V_{p-p}.

Figure 5.9 shows the variation of the EER signal with the modulating voltage amplitude, from which one can observe that the linear dependence is maintained up to 0.5 V, more than twice as large as normal operating modulation amplitude, which was mostly around 0.2 V. Based on the low field approximation theory of EER [152] the spectral line shape function $L(\hbar\omega)$ [Eq.(2.130)] can be used to fit the spectra.

The four parameters that determine the line shape were fitted to the low energy peak of the etched crystal in the polysulfide solution. Since the overlap with the higher energy peaks is not being taken into account, more weight was put on

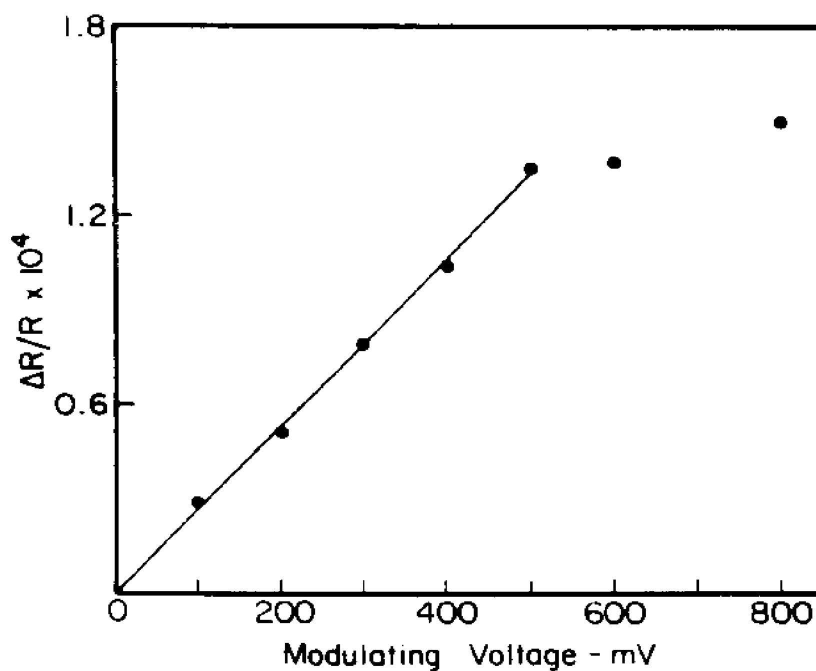

Figure 5.9 The amplitude of peak A from Fig. 5.2 as a function of the modulation amplitude.

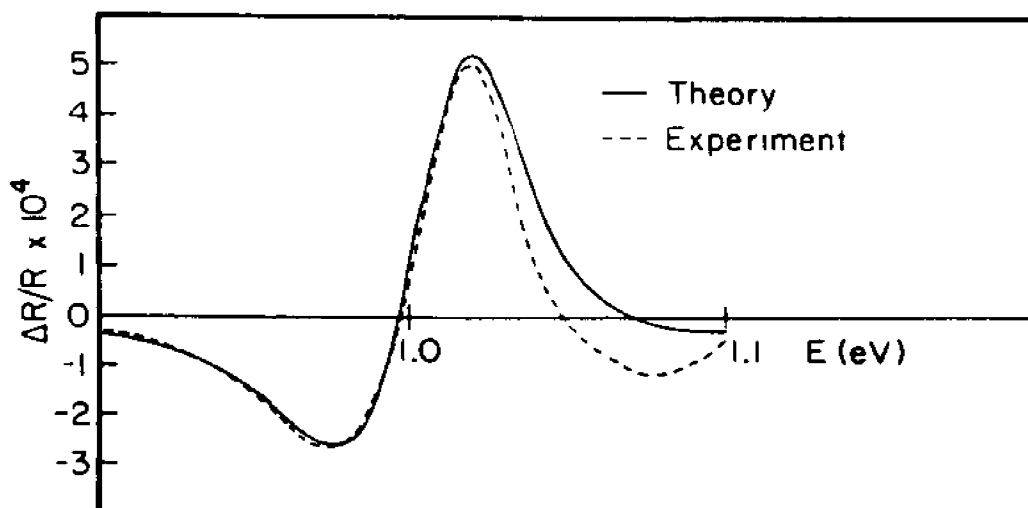

Figure 5.10 Comparison of observed and calculated line shape of peak A in Fig. 5.2. Potential = -0.2V vs Pt.

the low energy side of the peak, compared to the high energy tail. Figure 5.10 shows the results of the fit, using the following parameters: $n = 2.5$, $E_g = 1.01$ eV, $\theta = 275°$, and $\Gamma = 0.04$ eV. The value of the band-gap of the direct transition and the dimensionality of the critical point are in agreement with the low temperature studies [151].

5.1.3 Impedance

The impedance spectrum of the unetched crystal in polyiodide did not give any comprehensible results. The curves for the impedance spectrum of the etched crystal in the same electrolyte are shown in Fig.5.11. They resemble closely the spectrum of an abrupt junction interface observed with other photoelectrochemical systems [55]. Accordingly, it was analyzed using the technique of relaxation spectrum analysis [76] for parallel RC elements. The equivalent circuit is shown as an insert in the figure. Only the two fastest elements (C_{ss} and C_{sc}) were evaluated. The box with the question mark symbolizes additional information in the low frequency range that was not analyzed. The dependence of the two capacitance elements on the electrode potential is shown in Figs.5.12 and 5.13. The space-charge capacitance, C_{sc}, obeys the Mott-Schottky relation over a limited potential range. The doping level evaluated from the slope of this line is 2.7×10^{17} cm^{-3}, and the intercept is - 0.69 V vs the solution potential. This intercept must be corrected for the potential drop across the Helmholtz layer [55] for evaluation of the flat-band potential. However, the doping level is small enough for this

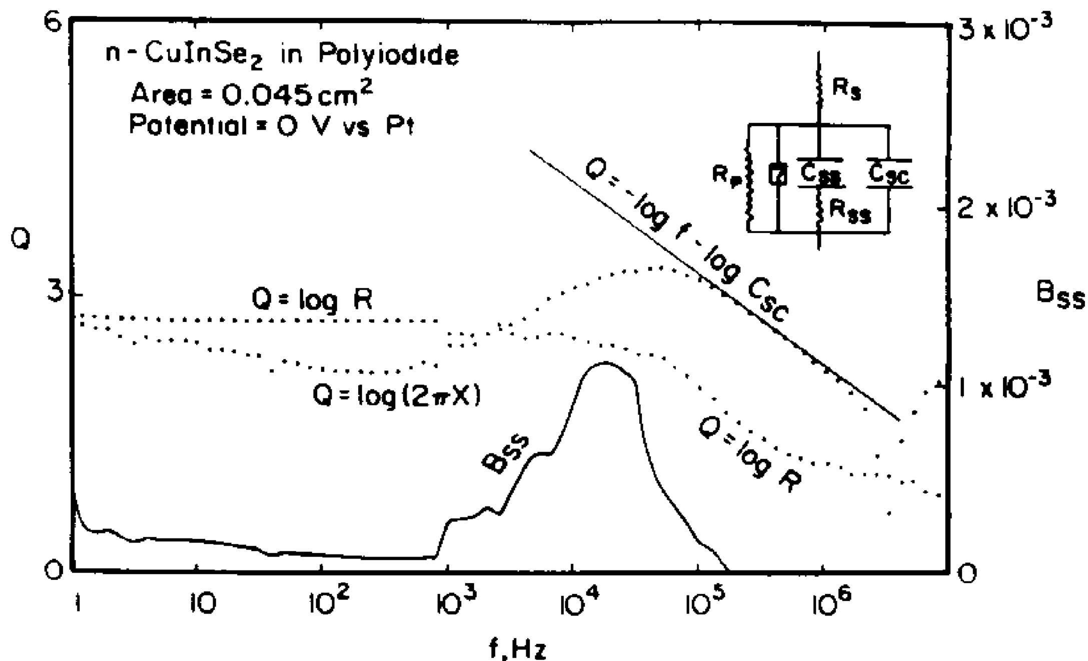

Figure 5.11 Impedance response curves for n-$CuInSe_2$ in polyiodide solution with the same composition as in Fig. 5.1. In the right-hand corner is the equivalent circuit constructed in the manner explained in the text.

correction to be negligible. As a result, the intercept of - 0.69 V vs Pt can be considered as a good measure of the flat-band potential, in excellent agreement with the EER results.

Figure 5.13 shows the dependence of C_{ss} on the electrode potential. The data were fitted to a Gaussian distribution of surface states, centered on two electrode potentials: one at - 0.52 V vs Pt, the other one at - 0.25 V vs Pt. From Fig.5.13, it was evaluated that the states close to the flat-band have a distribution width of 0.10 eV and an area density of 2.3×10^{12} cm^{-2}, while the second type of state has a width of 0.17 eV and an area density of 2.6×10^{12} cm^{-2}. If 10^{15} cm^{-2} is taken as a typical density for a monolayer, both states are present in fraction of a percent of a monolayer.

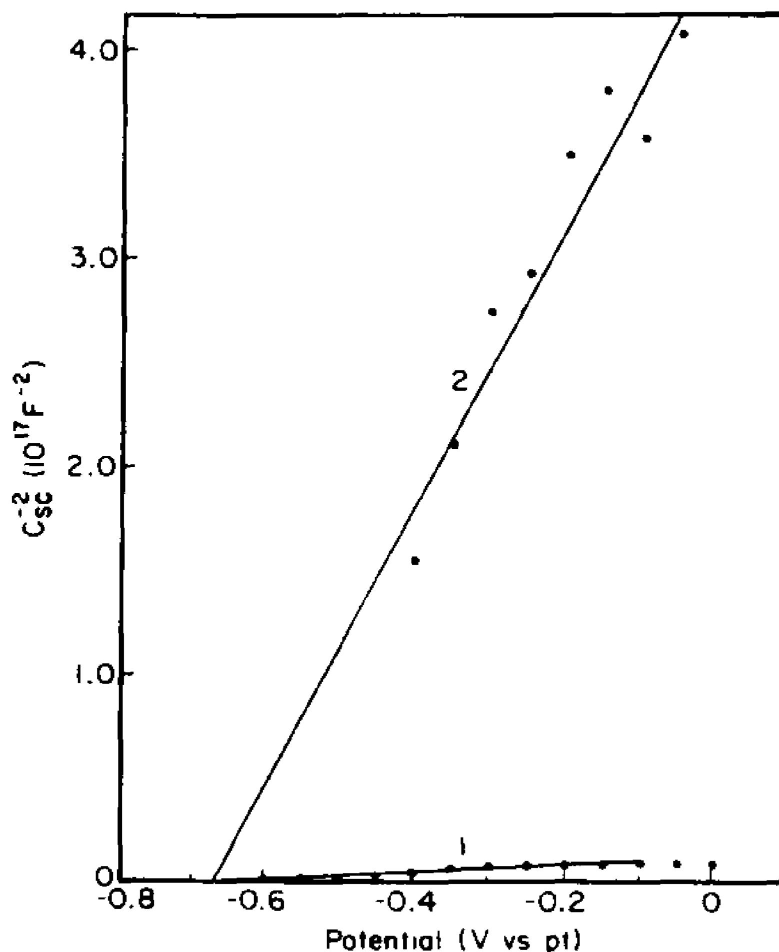

Figure 5.12 Mott-Schottky plots of C_{sc} (curve 1) and C_t (curve 2). The data for C_{sc} were taken from the high frequency response of spectra like the one presented in Fig. 5.11. The data for C_t were taken from the high frequency peak of the imaginary part in a response like the one shown in Fig. 5.14.

Figure 5.14 shows the impedance spectra of the crystal after heating in air for 1 h at 150°C. By comparing Fig.5.11 with Fig.5.14, one can observe large changes in the shape of both the real and the imaginary parts that take place upon oxidation. The origin of these changes can be deducted from the shape of the imaginary part and the assumed structure of the modified interface. If it is assumed that the oxidized layer has dielectric properties different from those of the

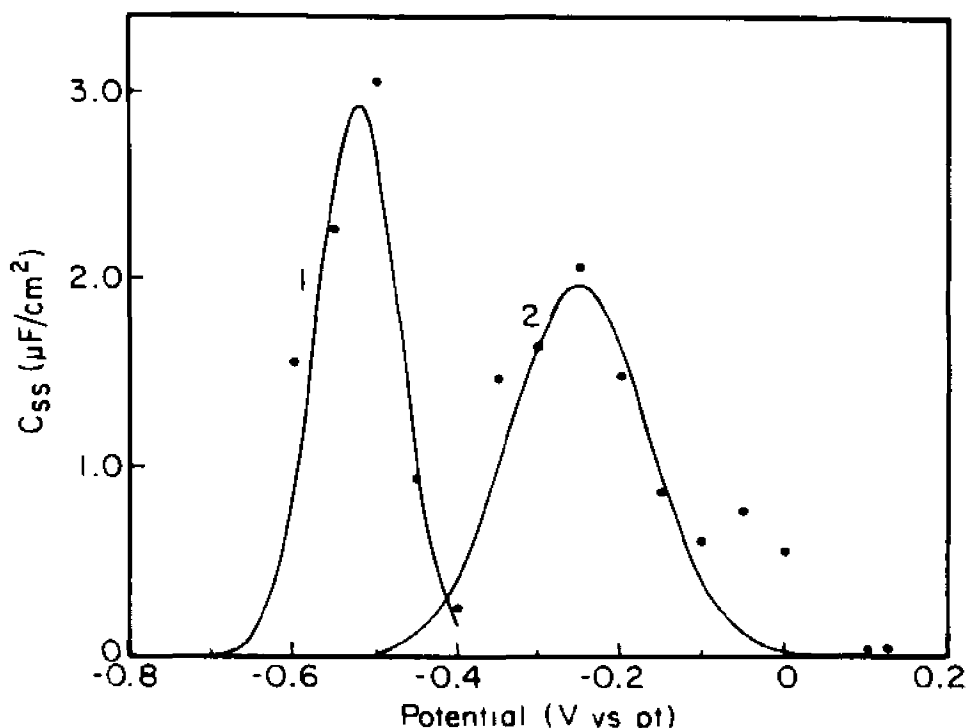

Figure 5.13 Variation of C_{ss}, taken from response curves like the one shown in Fig. 5.11, with electrode potential. The solid line is a theoretical fit to superposition of two Gaussian line shapes.

unoxidized crystal, then the resulting interface can be described, to a first-order approximation, by two circuit elements that are connected in series, with both elements capable of accumulating charge; therefore, some form of capacitive element will be associated with each circuit element.

The general case of an arbitrary number of such circuit elements, each characterized by a single capacitive element connected in parallel to a shunt resistance, which characterizes the relaxation time of the particular charge accumulation mode, has already been addressed [153]. The result of such an analysis was that the imaginary part of the impedance takes the following general form

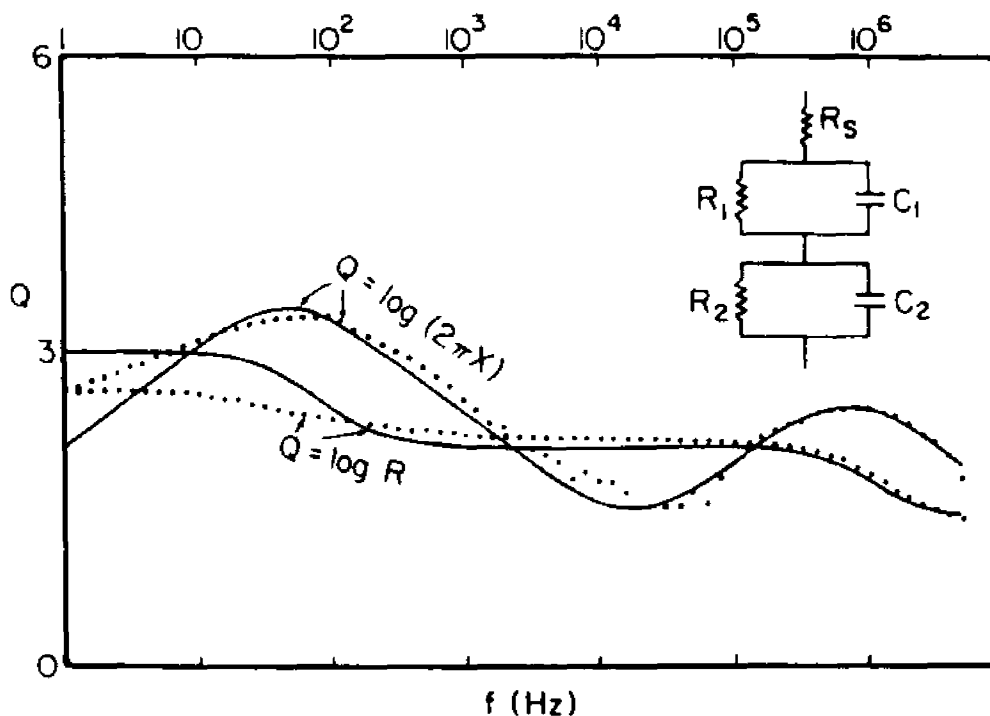

Figure 5.14 The impedance spectra of the n-$CuInSe_2$ crystal after heating in air for 1h at 150°C. In the right-hand corner is the equivalent circuit constructed as a reference point in a manner explained in the text. The full line is a theoretical fit to this equivalent circuit, based on Eq. (5.1). The parameters of the equivalent circuit were adjusted to fit only the imaginary part.

$$X = -\sum_{i=1}^{n} \frac{\omega R_i \tau_i}{1 + (\omega \tau_i)^2} , \qquad (5.1)$$

where R_i is the shunt resistance of each RC element and τ_i is its relaxation time.

It is predicted by Eq.(5.1) that, for this mode of the interface, the imaginary part of the impedance will consist of a superposition of Lorentzian peaks from which, if the resolution is good enough, one can derive the values of the individual passive elements. The data presented in Fig.5.14 suggest that two peaks are involved. Consistent with the anticipated simple model of the oxidized interface, it

is expected that one RC element will be associated with the space-charge layer of $CuInSe_2$ while the other peak is associated with the oxidized interface, which, based on chemical and surface spectroscopic evidence, appears to be some form of indium oxide. Regardless of the actual composition of the oxidized layer, it is expected to have dielectric properties different from those of the space-charge layer of $CuInSe_2$, and to be in series with the latter. Figure 5.14 also shows the fit of the experimental data to Eq.(5.1) for n=2. The high frequency peak fits the expected line shape very well, while significant deviations are observed at the low frequency tail of the low frequency peak. Furthermore, the figure also shows that, by taking the parameters that were fitted to the imaginary part and using them without further adjustment to plot the real part of the impedance, there is a good fit at the high frequency end of the spectrum and there are relatively large deviation in the low frequency part.

It is possible, of course, to assume that the chemistry (composition) and physics (charge accumulation modes and their relaxation) of the oxidized layer are more complicated, in such a way that enough parameters will be available to fit the model to the experimental data. However, the uniqueness of such an interpretation will always be open to question and such a model will not serve any useful purpose. Such an approach will be avoided.

The high frequency parts of the real part of the impedance in Figs.5.11 and 5.14 show that in spite of the observation that in both cases the frequency is not high enough to arrive at an unambiguous value for the series resistance of these

systems, the oxidation does not have a major effect on the series resistance, which in both cases is controlled by the electrolyte.

Figure 5.12 (curve 2) shows the Mott-Schottky plot of the capacitance that was derived from the high frequency peak (C_1). For potentials that are at least 0.3 V positive to flat-band, the fit is reasonable. Negative to this potential, we could not obtain any interpretable data. The flat-band potential that one obtains from the intercept of this curve remains at - 0.69 V vs the solution potential, which is identical with the one obtained for the same crystal before oxidation, as can be seen in Fig.5.12 (curve 1). The doping level, however, is reduced to 7.5×10^{15} cm^{-3}, which is more than an order of magnitude smaller than that before oxidation. Following an additional 1 h oxidation, the doping level is further reduced to 2.45×10^{15} cm^{-3}.

Figure 5.15 shows the impedance spectrum of a solid state configuration, in which $CuInSe_2$ is oxidized by heating the crystal in air for 2 h at 150°C, and the Ag metal contacts the oxide layer. When comparing with the results obtained with the liquid junction cell (Fig.5.14), one observes that the low frequency peak, present in the latter, disappeared, while the high frequency peak is still present.

Figure 5.16 shows the Mott-Schottky plot of the capacitance derived from the high frequency part of the low frequency peak of the imaginary part in the impedance spectrum (Fig.5.14) of n-$CuInSe_2$ after heating for 1 h at 150°C in air.

Figure 5.17 shows the dependence of the high frequency capacitance of the solid state configuration on the bias voltage. The capacitance still obeys the Mott-

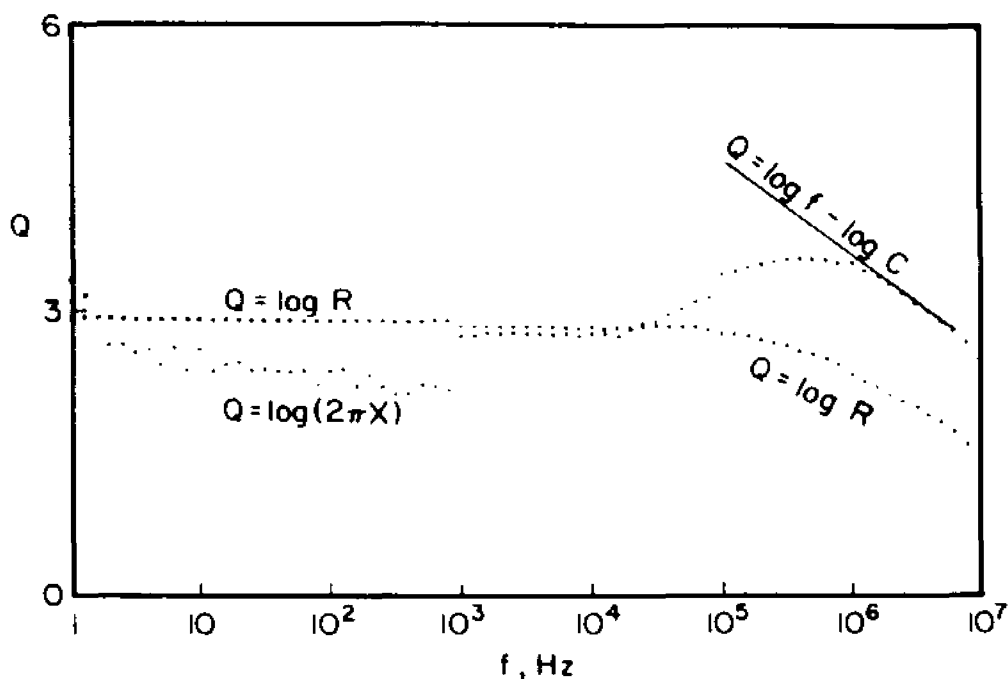

Figure 5.15 Impedance response curve of the surface-oxidized, n-$CuInSe_2$ with Ag front contact without electrolyte, prepared after heating the etched semiconductor in air for 2h at 150°C.

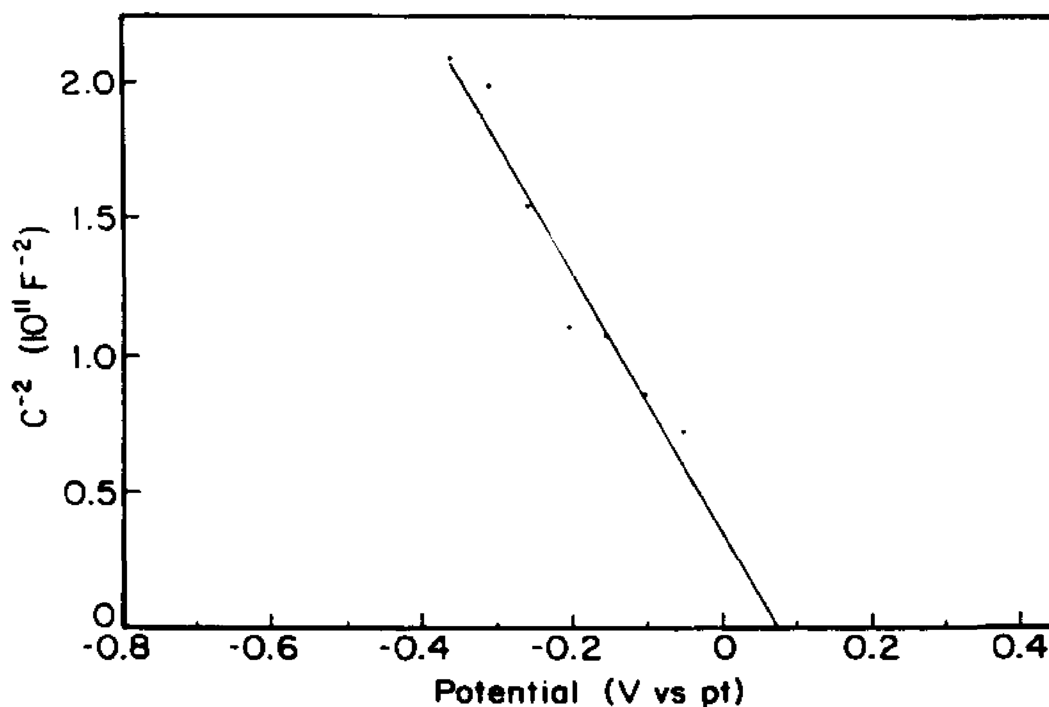

Figure 5.16 Mott-Schottky plot of the capacitance taken from the high frequency part of the low frequency peak of the imaginary part in the impedance response like the one shown in Fig. 5.14. Electrode area is 0.045 cm^2.

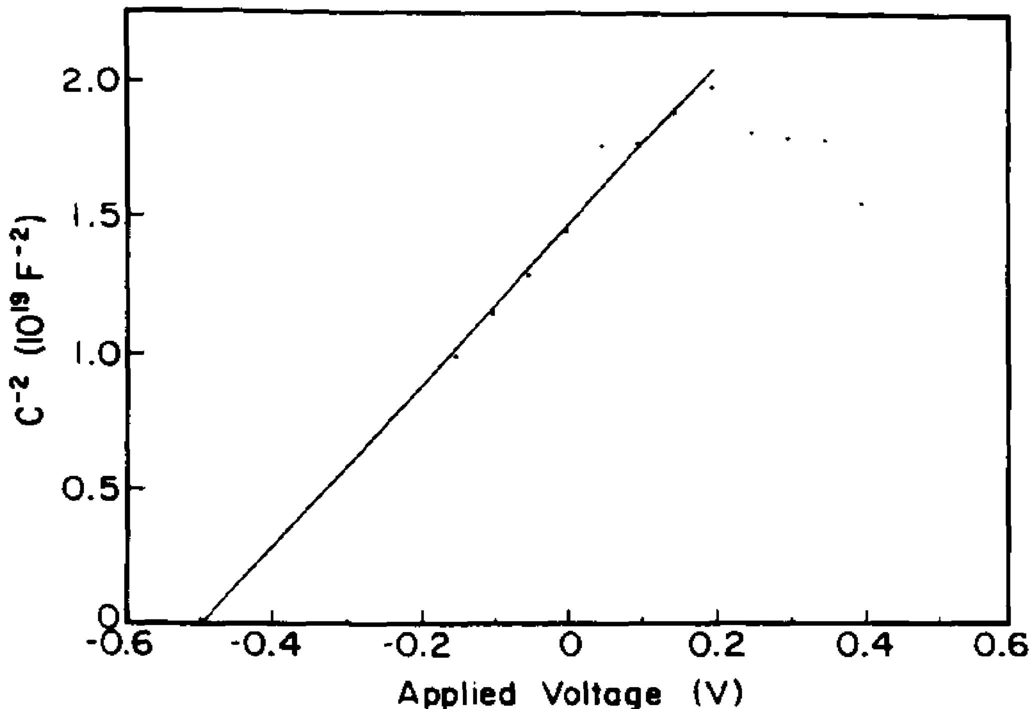

Figure 5.17 Mott-Schottky plot of capacitance taken from the high frequency response of spectra like the one presented in Fig. 5.15. The voltage is applied between the back and the front contacts of the solid-state device. Electrode area is 0.020 cm^2.

Schottky relation over a reasonable potential range, The doping level, evaluated from the slope of this line, is 1.2×10^{15} cm^{-3} and the intercept is - 0.52 V, based on a value of the dielectric constant of 13.6 [37,154], characteristic for $CuInSe_2$.

Figure 5.18 shows the dark I-V curve of the solid state configuration. The electrode arrangement for this experiment is shown in the insert of the figure. It is important to mention that the curve is independent of the polarity of the contacts.

When the light was shone onto the surface of the solid state junction, no photoresponse was observed in the I-V characteristics.

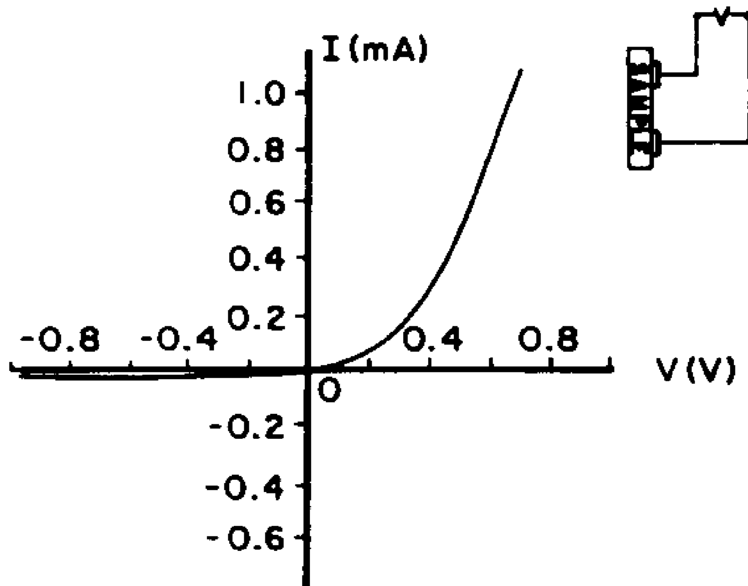

Figure 5.18 Dark I-V characteristics of the n-$CuInSe_2$ solid-state junction without electrolyte, after heating in air for 2h at 150°C. The insert represents the arrangement of the electrode.

5.2 Discussion [115-117,155]

5.2.1 Effects of chemical etching

The EER data suggest that the main effect of etching the crystal was to remove the pinning of the Fermi level. Although this effect is much more pronounced in polysulfide solution, it is common to both the polysulfide and the polyiodide solutions.

Following the procedure that was described in §2.2.6 [106], one can calculate the variation of the flat-band potential with the electrode potential. Furthermore, if one assumes an energy distribution for the surface states, one can calculate some useful parameters such as density, mean energy, and energy width of these surface states. This was done for the unetched sample in polysulfide

solution, based on the data shown in Fig.5.4 and by assuming a Gaussian energy distribution for the surface states. Figure 5.19 shows the plots of P/(1-P) for unetched $CuInSe_2$ as a function of U. The results show that the pinning is due to a monolayer of states (10^{15} cm^{-2}) located at U_t = +0.17 V vs Pt with a standard deviation with respect to the center of the distribution of 0.1 eV. These results are almost identical with those reported earlier for electrodeposited CdSe [123] and single crystal $CdIn_2Se_4$ in the same electrolyte [106]. It was interpreted there [106] that these states are due to the chemisorbed polysulfide ions on the surface of the crystal. It is believed to be valid also in the present case. The similarity in the flat-band potential in all these cases also suggests similar surface chemistry.

Based on the photoluminescence data [156] the energy position of the surface states corresponds to a Se-related defect: V_{Se}, if a covalent defect model is assumed; and Se_{i}, if an ionic model is considered. The possibility of the iso-valent acceptor O_{Se} cannot be excluded, either.

The role of etching here is not to clean the surface states but to change their relaxation times from relatively fast states to very slow ones (slower than the modulation frequency, which is 50 Hz). If the dominant relaxation mechanism of these states is through bulk imperfections in the crystal, then preferential removal of these imperfections by the oxidative etch can provide a mechanism that will be consistent with the EER data and the improvement in performance.

Impedance data show that the formation of an abrupt junction after etching and that etching removes most of the surface states from the interface such that

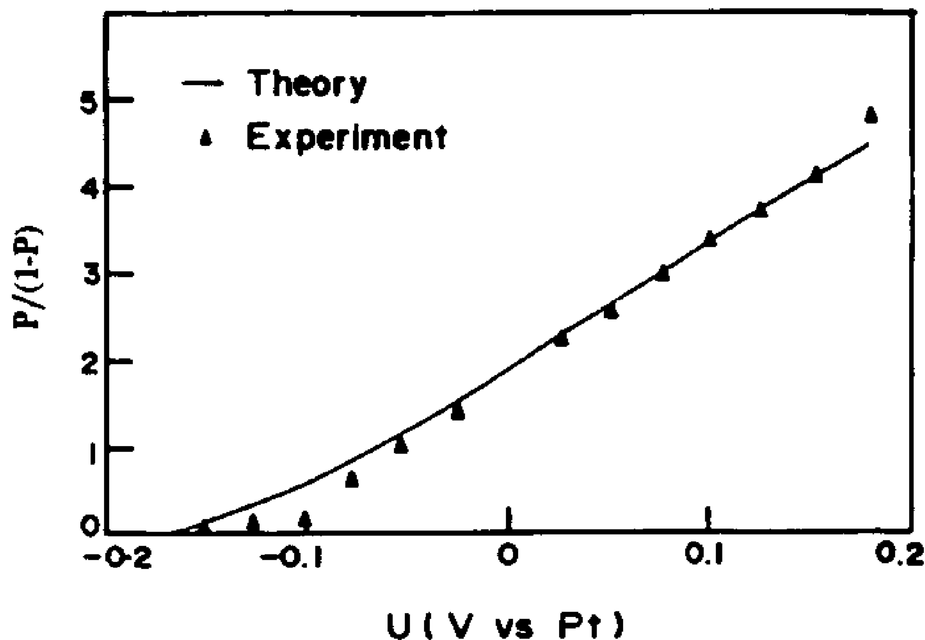

Figure 5.19 Plot of P/(1-P) vs potential U for untreated $CuInSe_2$.

less than 1% of a monolayer of states remains. Two states were identified: one centered at 0.17 eV below the conduction band and one centered at 0.44 eV below the conduction band, which puts it close to the center of the gap.

To check the validity of the above deductions, the photo I-V curves shown in Fig. 5.1 was simulated using, as far as possible, the numerical values obtained from the impedance measurements. The simplest simulation of this type is that of monochromatic light-induced I-V curves. Unfortunately, by the time it was realized that such an experiment was essential, the crystal used for all the quantitative measurements was not suitable for further experiments, therefore, the data taken with white light was used, and the response characteristics was calculated by integrating over the spectral output of the light source and the absorption spectrum over the entire spectral range. For $CuInSe_2$ this approach has the advantage that

it avoids the uncertainty in the absorption coefficient (esp. at wavelength > 1100nm), caused by the very strong wavelength dependence and the resulting sensitivity of the absorption coefficient to very small calibration errors in the wavelength measurement. This requires absorption measurements on the same sample in the very same setup, used for obtaining the monochromatic I-V.

Accordingly, the photoinduced current will be given by [57]

$$J = -K \int_{\lambda_{min}}^{\lambda_{max}} e\Phi(\lambda) \frac{\lambda}{hc} \frac{dI}{d\lambda} \, d\lambda \ , \qquad (5.2)$$

where K is a normalization constant for the total light intensity, e is the electronic charge, $\Phi(\lambda)$ is the monochromatic quantum efficiency at wavelength λ, h is the Plank constant, and I is the monochromatic light intensity of the source.

Based on the modified Gartner model including surface recombination [61], the monochromatic quantum efficiency $\Phi(\lambda)$, is given by Eq.(2.49). Neglecting the reflected loss, it becomes

$$\Phi = \frac{S_t}{S_r + S_t} \left[1 - \frac{e^{-\alpha W}}{1 + \alpha L_p} \right] . \qquad (5.3)$$

Assuming that only the surface state closest to the conduction band, i.e., that centered at 0.17 eV below conduction band, is responsible for the surface recombination, and that this process is limited by the availability of minority carriers, the rate constant for surface recombination S_r is given by Eq.(2.44)

$$S_r = \frac{k_r N_t}{2}\left[1 - erf\left(\frac{U - U_t}{\sqrt{2}\sigma}\right)\right] . \qquad (2.44)$$

The absorption coefficients α were taken from the literature [157], and the spectral output of the lamp $dI/d\lambda$ was measured. K was adjusted to give the total light intensity that was 100 mW/cm^2. The doping density N_d, the flat-band potential U_{fb}, and the most probable potential of surface state U_t were taken from the impedance data. As a cross check for consistency, σ was taken as free parameter. The best fit of Eq.(5.2) to the I-V characteristics that were presented in Fig.5.1 for the etched crystal, is shown in Fig.5.20 for minority carrier diffusion length L_p = 0.04 µm, the ratio between the rates of surface recombination and charge transfer to the electrolyte $k_r N_t / S_t$ = 23.2, and the width of the Gaussian energy distribution of the surface state σ = 0.12 eV, which is consistent with the one obtained from impedance measurements (0.10 eV).

5.2.2 Effects of air oxidation

The most significant results from the EER experiments are the need for a nearly 8 times higher modulation voltage compared with the etched samples, and the similarity between the spectra for oxidized samples and for samples onto which a layer of oxidized In was deposited. This, together with data from surface analysis [42] suggests that air oxidation leads to the formation of some form of indium oxide. As the direct optical band gap of In_2O_3 is above 2 eV [158], the presence

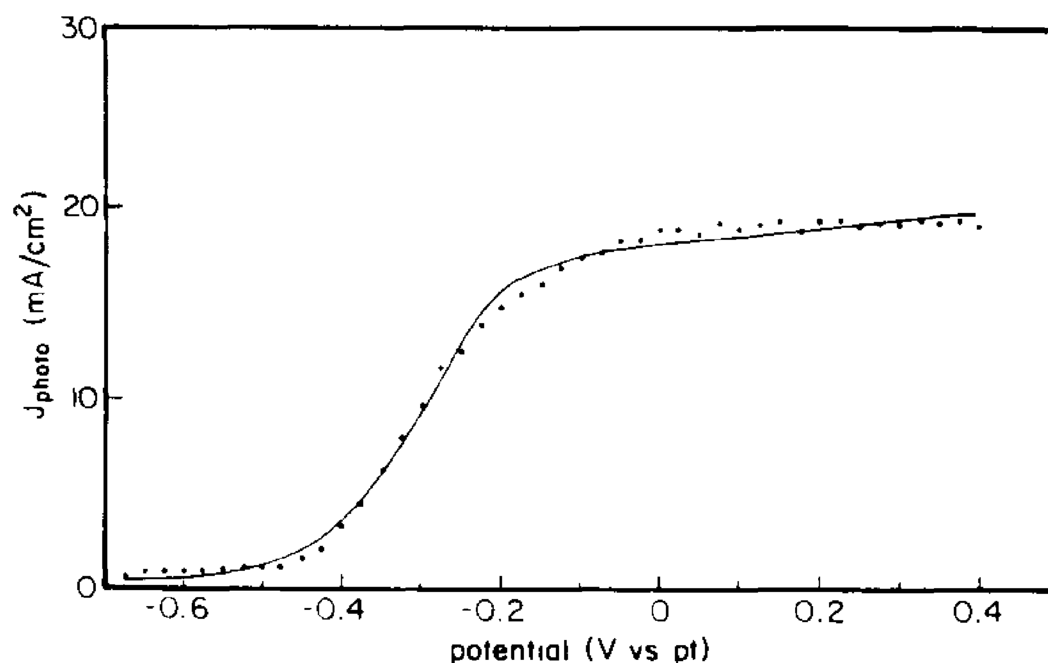

Figure 5.20 Comparison of experiment (dotted line) and theory (solid line) for the light induced current-voltage characteristics of etched n-$CuInSe_2$ in the same electrolyte as in Fig. 5.1. The theoretical curve was calculated by using Eq. (5.2) in the manner explained in the text.

of such a film is not expected to affect the EER data in the spectral range studied here. The increased modulation voltage that is needed suggests that a significant part of this voltage falls over the oxide film, implying this film to be poorly conducting. From the EER and photo I-V results, it was shown that the oxide layer is transparent to the incoming illumination in the visible portion of the spectrum and also transparent to the charge transfer at the interface of the semiconductor with the electrolyte.

It was found that the flat-band potential is unaffected by the oxidation but that the effective doping level is reduced by more than an order of magnitude. The experimental light-induced current-voltage curve for the oxidized sample was fitted assuming that the only change that took place upon oxidation of the crystal was

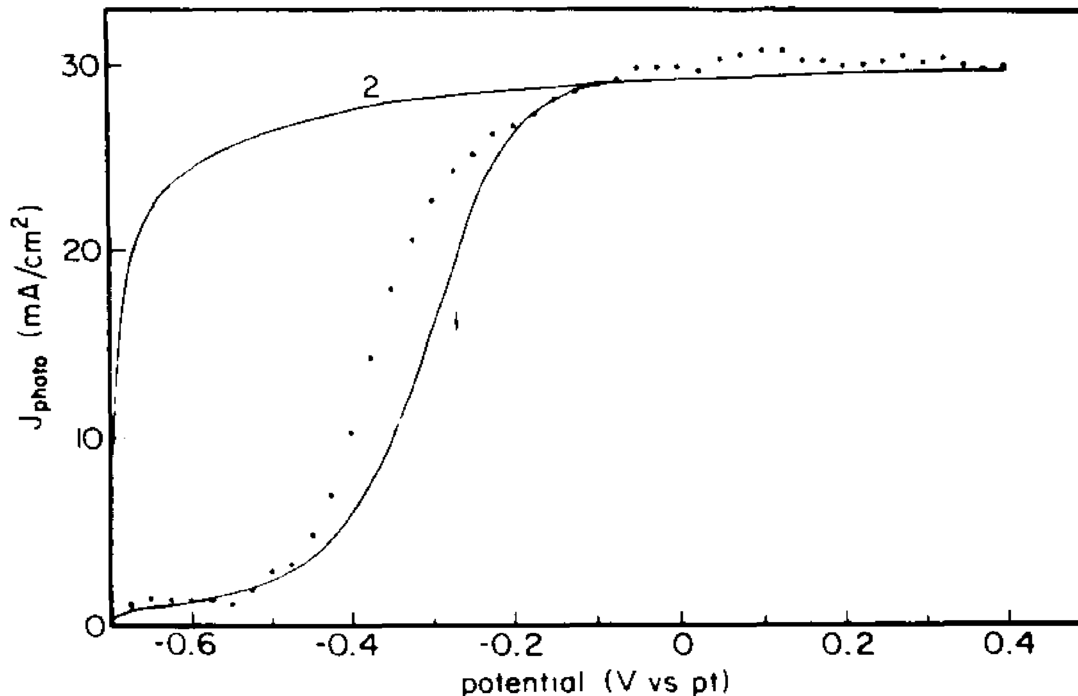

Figure 5.21 The same fit between theory and experiment as the one shown in Fig. 5.20, but for the oxidized $CuInSe_2$ crystal. Curve 1 shows the behavior with the same parameters as the one found for etched crystal except for the effective doping level, which was taken from the data in Fig. 5.12 to be $7.5X10^{16}cm^{-3}$. Curve 2 was calculated by using the same parameters but with no surface recombination.

the reduction in the doping level and using the modified doping level taken from the impedance data of the oxidized crystal into Eq.(5.2). The result is presented in curve 1 in Fig.5.21. The same figure also shows the experimental data. The agreement between experiment and theory is impressive, considering that this is a parameter-free fit.

The assumption that there is no change in surface recombination upon oxidation of the crystal is not based on the impedance data shown in Fig.5.14. States with relaxation times of less than 0.4 μs are completely masked by the contribution to the impedance from the oxide layer. The small shift of the

experimental data in Fig.5.21 toward negative potentials can be interpreted as a very limited cleaning of the surface due to the formation of the oxide layer. However, any quantitative evaluation of this effect is too speculative to pursue further.

Curve 2 in Fig.5.21 shows the effect of complete elimination of surface recombination on the performance characteristics of the cell: more than a 50% improvement in the open-circuit voltage is expected. This can be accomplished either by further reduction in the concentration of recombination centers at the surface, or, alternatively, by further improvement in the charge transfer rate to the electrolyte.

These results thus show that virtually all of the improvement in behavior after air oxidation can be ascribed to a reduction in net donor density, which leads to a widening of the space charge layer (up to 10-fold, after prolonged oxidation). This allows essentially all the incident radiation below ca. 1150 nm to be absorbed in the space charge layer, thus eliminating the influence of the bulk recombination mechanisms.

The above analysis has been selected as a "case study" for identification of surface states and effects of surface modification on semiconductor-electrolyte interfaces by means of impedance spectroscopy, in the book "Impedance Spectroscopy" edited by J. Ross Macdonald [75].

5.2.3 Nature of oxidized layer

Comparing Fig.5.14 with Fig.5.11, the main feature of the spectrum of the oxidized sample is the presence of two peaks in the imaginary part of the impedance. In §5.1.2, an equivalent circuit of two series elements was used, each element was composed of a capacitor connected in parallel to a resistor. One circuit element represents the space charge layer of $CuInSe_2$, while the other is associated with the oxidized interface. Comparison with computer-generated Lorentzian curves showed that the high frequency peak has an ideal Lorentzian line-shape, while the low frequency peak is not Lorentzian [116]. The significant deviations observed in the low frequency region suggest that the behavior on the oxidized interface cannot be described in the same manner as the space charge layer, nor can it be described in terms of any other charge accumulation mode with a well-defined relaxation time.

Important information is provided by the behavior of the low frequency peak in the impedance spectra as a function of the electrode potential. The high frequency part of these peaks has a slope of -1 at potential values between - 0.05 and - 0.35 V vs the solution potential. This region was used to evaluate the capacitance of the element [76]. The Mott-Schottky plot in Fig.5.16 is characteristic for a p-type material with a flat-band potential of +0.1 V vs the solution potential and doping density of 10^{22} cm^{-3} (based on a value for the dielectric constant of 2.3, characteristic for In_2O_3 [159]), indicative of a highly degenerate semiconductor.

If these results are to be taken literally, then one might expect the space

charge layer to be located in the semiconductor, near the conductive oxide, with no direct contact with the electrolyte and the device to operate as a solid state photovoltaic cell, in series with the electrochemical cell. If so, the photovoltaic response and the impedance should be preserved in the absence of the electrolyte. The fact that the low frequency peak disappeared and the high frequency peak was similar to that with electrolyte (Fig.5.15) indicates that the low frequency peak resulted from the interaction between oxidized layer and the electrolyte. The consistency of the doping level evaluated from Mott-Schottky plot of the solid state junction (Fig.5.17) with that of the liquid junction confirms that the high frequency peak certainly represents the space charge layer between the $CuInSe_2$ and the oxidized layer. If the oxide layer were conductive, the I-V curve of the solid state junction would be ohmic. Otherwise, the I-V curve will show a blocking feature, and from Fig.5.18, it is evident that the latter is the case. From the above, it can be deduced that the low frequency peak is associated with the oxidized layer in conjunction with the electrolyte, since the oxidized layer alone is a poor conductor and there is no photoresponse for solid state junction. Thus, the hypothesis that the device operates as a solid state photovoltaic cell, in series with the electrochemical cell in which the role of the electrolyte is only to provide ohmic contact, is not valid.

The chemical nature of the layer is also important. On the one hand, it has been reported that polycrystalline p-$CuISe_3Se^0$ was grown by some type of photoassisted electrochemical transformation of the $CuInSe_2$ surface in Cu con-

taining acidic iodide solution [34,36]. On the other hand, ESCA and Auger analyses on samples used in systems like those discussed here [42] have indicated that Cu is absent from the resulting surface layer and that the oxidized layer is some form of indium oxide. However, indium oxide is unknown in p-type form.

Therefore, one was faced with the following situation: by oxidation of the surface a new layer is formed, it has p-type character and is conductive when in a liquid junction cell and is an insulator when in a solid state device. Also, it contains only indium and oxygen, but indium oxide is unknown in p-type form.

Figure 5.22 indicates a possible explanation for this behavior. It shows several electron beam-induced current (EBIC) scans across the junction of an n-$CuInSe_2$/oxidized surface/metal test device. It is clear from the picture that some EBIC response is seen at the interface, but this response is not continuous, i.e., we have "shorts" across the junction. In view of these results, the most suitable approach to this problem is to assume that the oxide layer is porous. When it is "dry", it is nonconducting, but when it is immersed in the electrolyte, the conductivity of the "mixed" interface layer results from ionic conductivity of the electrolyte within the pore structure. When the $CuInSe_2$ with oxidized layer works as a solid state device, the porous or discontinuous structure of the oxidized layer made measurements of a photoresponse impossible. However, the silver paint as electrode penetrates through the structure to make contact with the substrate and short circuit the oxidized layer in the measurement of solid state junctions. As a

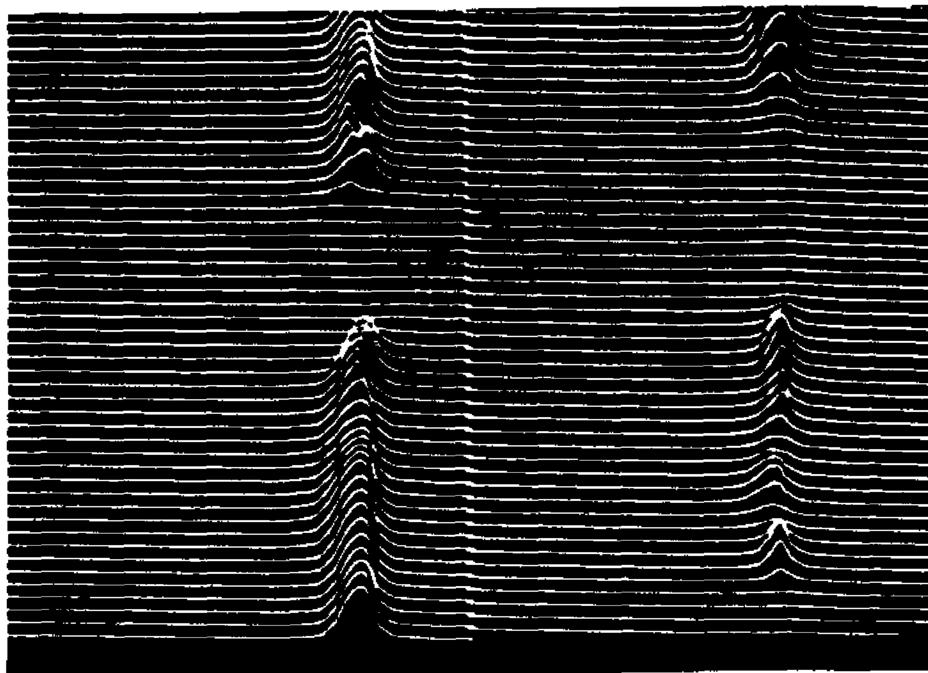

Figure 5.22 Electron beam-induced current traces across the cleaved junction of an n-$CuInSe_2$/oxidized surface layer + oxidized In/Ti device. The right-hand part shows the region directly below that shown on the left-hand side. Each side shows a ca. 25 μm length of the junction. Beam voltage: 10 kV; beam current: 15 pA. Junction region: Ti on the right; the junction stretches from the Ti, through the In(ox) into the $CuInSe_2$.

result, in the impedance spectrum of the solid state junction, only the high frequency peak, representing the space charge layer, remains, and the low frequency peak disappears. When the crystal with oxidized layer was mounted in a liquid junction photoelectrochemical cell, the electrolyte filled the pore space, forming a continuous (vide infra) conducting phase. This porous oxidized layer flooded by the electrolyte is conductive because of the ionic conductivity of the electrolyte within the pores. Thus, the normal operation of photoelectrochemical solar cell is ensured, and the dielectric characteristics observed in the low frequency region is explained.

5.2.4 Effective medium description of oxidized layer-electrolyte composite

Following our discussion in Chapter 2, the differential effective medium approximation was used for simulating the impedance spectra of the oxidized $CuInSe_2$/electrolyte system. According to the theory described in §2.1.5, the complex dielectric function of the composite is implicitly expressed by the equation (2.94)

$$P = \left(\frac{\epsilon_b - \epsilon}{\epsilon_b - \epsilon_a}\right)\left(\frac{\epsilon_a}{\epsilon}\right)^d , \qquad (5.4)$$

where P is the porosity, ϵ, ϵ_a, and ϵ_b are the complex dielectric constants of the composite, the conductive medium and the insulating medium, respectively, and d is a parameter between 0 and 1, which is known as depolarization factor or screening factor, dependent on the geometry of the inclusion in the composite.

Neglecting the dielectric loss, the complex dielectric constant for the low frequency regime may be written as

$$\epsilon = K - j\frac{4\pi\sigma}{\omega\epsilon_o} = |\epsilon| e^{-j|\theta|} , \qquad (5.5)$$

where K is the dielectric constant, σ is the conductivity, ω is the angular frequency, ϵ_o is the permittivity of vacuum, and $|\epsilon|$ and $|\theta|$ are the modulus and the argument of the complex dielectric constant, respectively. Substituting the complex dielectric constant of the conductive medium and that of the insulating medium into Eq.(5.4), one can get the $|\epsilon|$ and $|\theta|$ of the composite as a function of dielectric

characteristics of its constituents and two parameters, the depolarization factor, d, and the porosity, P. Therefore, the impedance of the element corresponding to the oxide-electrolyte composite may be expressed as follows

$$Z_1 = R_1 + jX_1 = -j\frac{L}{gA\omega\epsilon_o\epsilon}, \qquad (5.6)$$

where L is the thickness of the layer, g is the roughness factor, and A is the area of sample. Considering the impedance of the space charge layer

$$Z_2 = \frac{R_2}{1+\omega^2\tau^2} - j\frac{\omega\tau R_2}{1+\omega^2\tau^2}, \qquad (5.7)$$

where R_2 is the shunt resistance of RC element, representing the space charge layer, and τ is its relaxation time, the total impedance of the cell, Z, is given by

$$Z = R_s + Z_1 + Z_2, \qquad (5.8)$$

where R_s is the series resistance. Obviously, the relaxation spectrum of the impedance Z_1 depends on the geometric factors of the layer (L, g, A), the dielectric and conductive characteristics of the constituents (K_a, σ_a, K_b, and σ_b) and the microstructure of the layer (P, d).

Figure 5.23 shows the theoretical fit based on Eq.(5.5)-(5.8). The same Lorentzian fit parameters R_2 and C_2 as in Fig.5.14 have been used (R_2 = 118.15Ω, C_2 = 1.90×10^{-9} F). For the solution, K_a = 80.1 and σ_a ~ 0.900 $\Omega^{-1}cm^{-1}$ have been taken from the literature [161]. The adjustable parameters are: the ratio L/g of

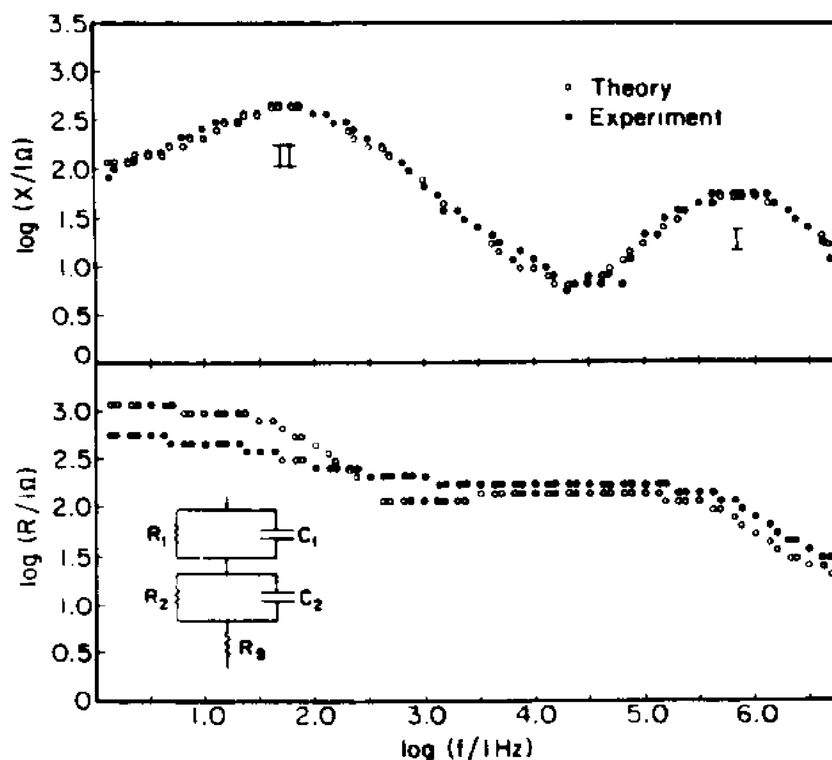

Figure 5.23 The impedance spectra of n-$CuInSe_2$, after heating in air for 1h at 150°C, in polyiodide solution with the same composition as in Fig. 5.1. Solid circles represent experimental points and circles represent theoretical results based on Eq. (5.5) and (5.8).

thickness to roughness, the conductivity σ_b and dielectric constant K_b of the oxidized phase, the porosity P, and the depolarization factor d. The adjustable parameters were fitted by means of least squares fitting of nonlinear model for the imaginary part of the impedance. It is seen from Fig.5.23 that the fit of the imaginary part of the impedance spectrum is acceptable, resulting in the following set of parameters: P = 19.9%, d = 0.2, σ_b = 8.8×10^{-12} $\Omega^{-1}cm^{-1}$, K_b = 3.2, and L/g = 6.0×10^{-9} cm. Using these parameters, without further adjustment, to plot the real part of the impedance, there is good agreement in the high frequency region of the spectrum, and a reasonable one in the low frequency region.

The low conductivity of the oxidized phase, derived from the fitting, supports

the appropriateness of the model. The dielectric constant of the oxidized phase is also reasonably close to the value 2.3 given in the literature for In_2O_3 [159]. The depolarization factor indicates that the geometrical shape of the inclusion in the composite lies between needles with axes parallel to the field (d = 0) and sphere (d = 1/3) [91]. The value of porosity and thickness to roughness ratio are also reasonable (e.g., to a thickness of 10^{-6} cm, comparable with that obtained by a spraying technique [158], would correspond to a roughness of 1000).

5.2.5 Potential distribution of the $CuInSe_2$/polyiodide system

Based on the above analysis, a picture of the potential distribution of the etched $CuInSe_2$/aqueous polyiodide electrolyte system and oxidized $CuInSe_2$/ aqueous polyiodide electrolyte system is shown in Figure 5.24. The flat-band potential is -0.69 V vs Pt (the solution potential). The energy gap is 1.01 eV. There are two surface states which occupy less than 1% of a monolayer: one is centered at 0.17 eV below the conduction band and the other one at 0.44 eV below the conduction band. After oxidation, there is a porous oxide layer covered on the surface. Since it is porous, the flat-band potential is unchanged. The main effect of the oxidation is that the doping density is reduced. As a result, the space charge layer in the semiconductor is widened.

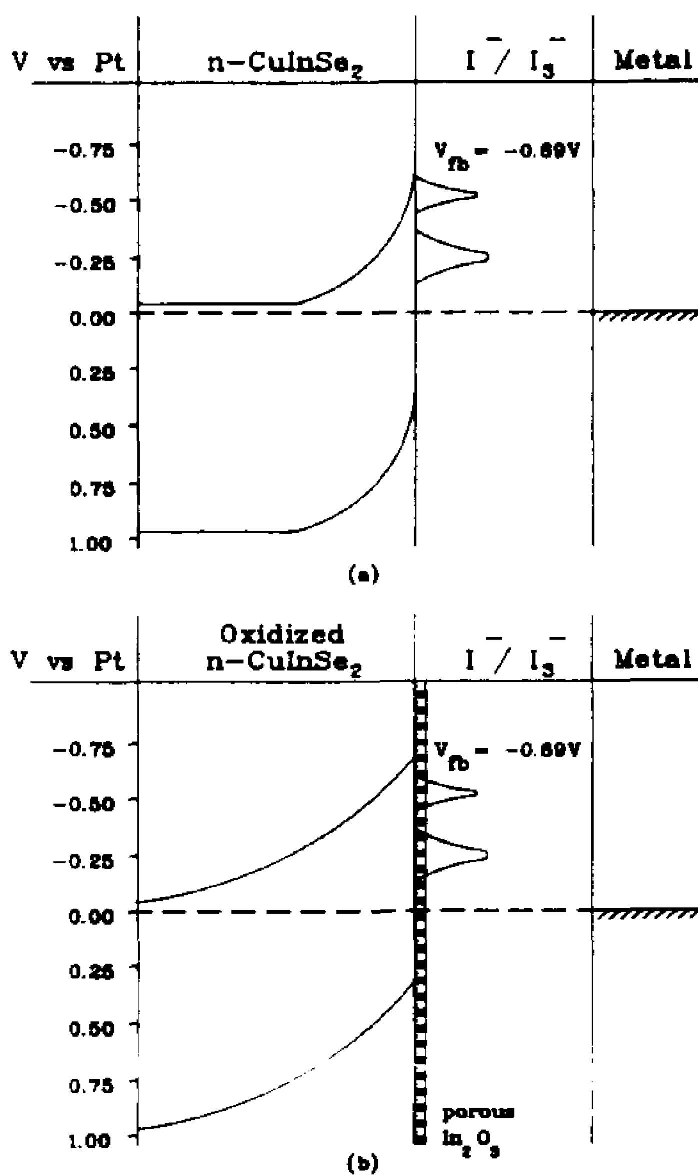

Figure 5.24 The band structure diagrams of n-$CuInSe_2$ in polyiodide solution before and after heating in air.

CHAPTER 6

n-InSe AND ITS PHOTO-MODIFICATION

6.1 Experimental results

6.1.1 Photoreflectance

Figure 6.1 shows the photoreflectance spectrum of the unmodified n-InSe in the energy range between 1.1 and 1.3 eV with a 6328 Å pumping beam. The spectrum exhibits one doublet, similar to the doublet observed in the electroreflectance spectrum of the InSe/Pt Schottky barrier [162].

Figure 6.2 shows the spectra, in the same energy range, of the photo-modified electrodes with different modification times. The intensity of the signal decreases drastically with the modification time, i.e., with increase in the thickness of the modified layer. The amplitude of the peak of the sample with modification time of 20 min was reduced to one-tenth of that of the unmodified one. A small shift of the peak to higher energy is also observed, which can be interpreted to be due to the stress caused by lattice mismatch between the top layer and the bulk [130].

The PR spectra of the modified InSe with two different pumping wavelengths is shown in Fig.6.3. No significant difference in the line-shapes was observed with pumping beams with energy of 1.96 eV (6328 Å) and 1.83 eV (6764 Å). Since the two PR spectra were not taken at the same point on the sample, the shift of the peak can be interpreted in terms of nonhomogeneity of the modification

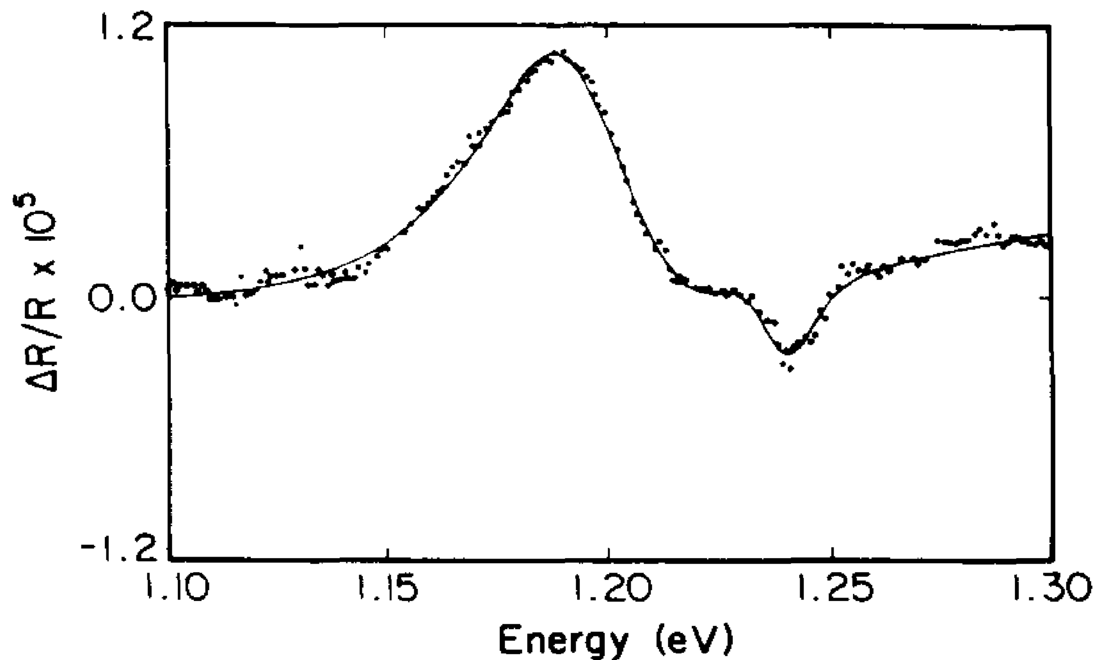

Figure 6.1 Photoreflectance spectrum of n-InSe in the low energy range and a theoretical fit to the line-shape function. Modulation source -- 6328 Å He-Ne laser; modulation frequency -- 517 Hz. Fitting parameters: E_{ex} = 1.196 eV, Γ_{ex} = 0.033 eV; E_g = 1.238 eV, Γ = 0.016 eV.

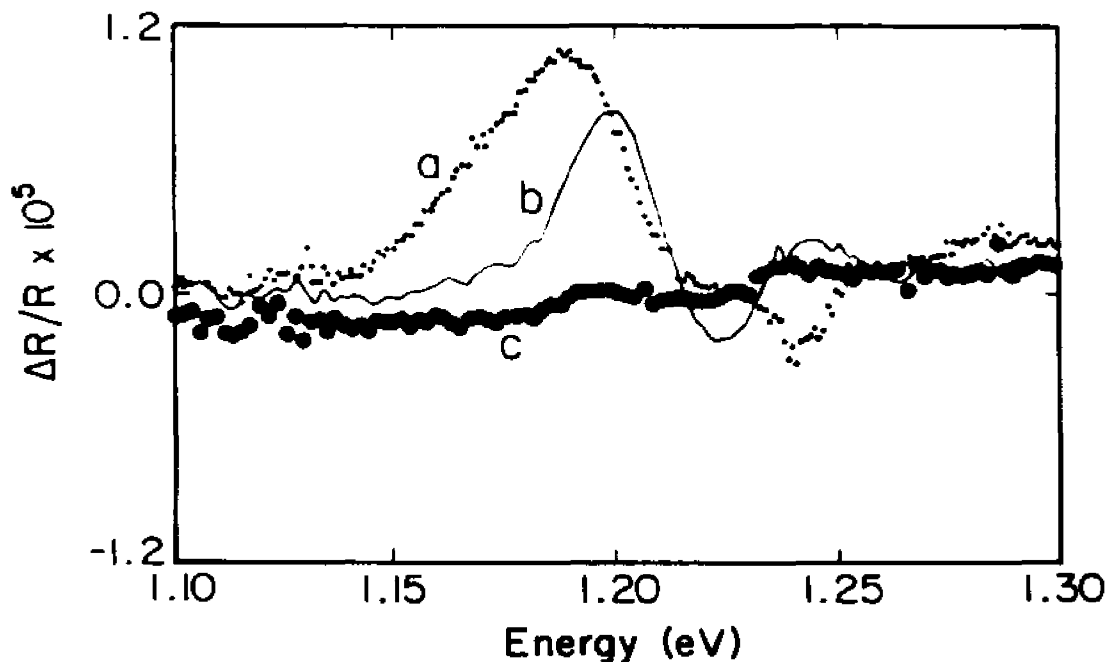

Figure 6.2 Comparison of PR of n-InSe and photomodified InSe after treatment in the polyiodide electrolyte containing Cu^+ with different modification time. a) n-InSe; b) modified InSe with modified time of 10 min.; c) modified InSe with modified time of 20 min. Same conditions as in Fig. 6.1.

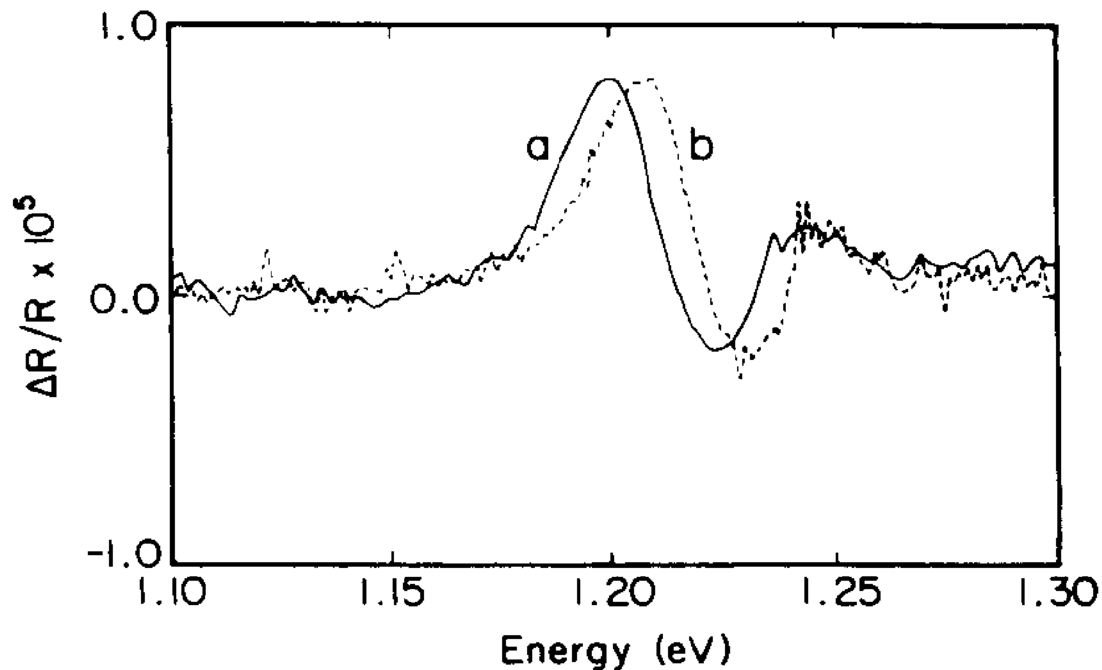

Figure 6.3 PR of photomodified n-InSe at different wavelengths of the modulated beam. a) 6328 Å from He-Ne laser, and b) 6764 Å from Kr ion laser. The spectra are normalized for the same amplitude.

of InSe electrode, which leads to the different stress on different points of the sample. Figure 6.4 shows the PR spectra of the modified InSe and unmodified InSe in the higher energy range between 1.8 and 2.1 eV. InSe does not exhibit any signal in this regime, while the photomodified one shows a broad peak with a maximum at 1.93 eV.

The best fit curve of spectral line shape function to the experimental spectrum of InSe is shown in Fig.6.1. The higher energy peak was assigned to a direct gap with two dimensional critical point (n=3), energy gap, E_g, of 1.238 eV, and line-width parameter, Γ, of 15.6 meV. The energy gap is consistent with the published value obtained from adsorption spectra [163]. The lower energy peak was assigned to an excitonic transition (n=2) with E_{ex} = 1.196 eV and Γ = 32.7

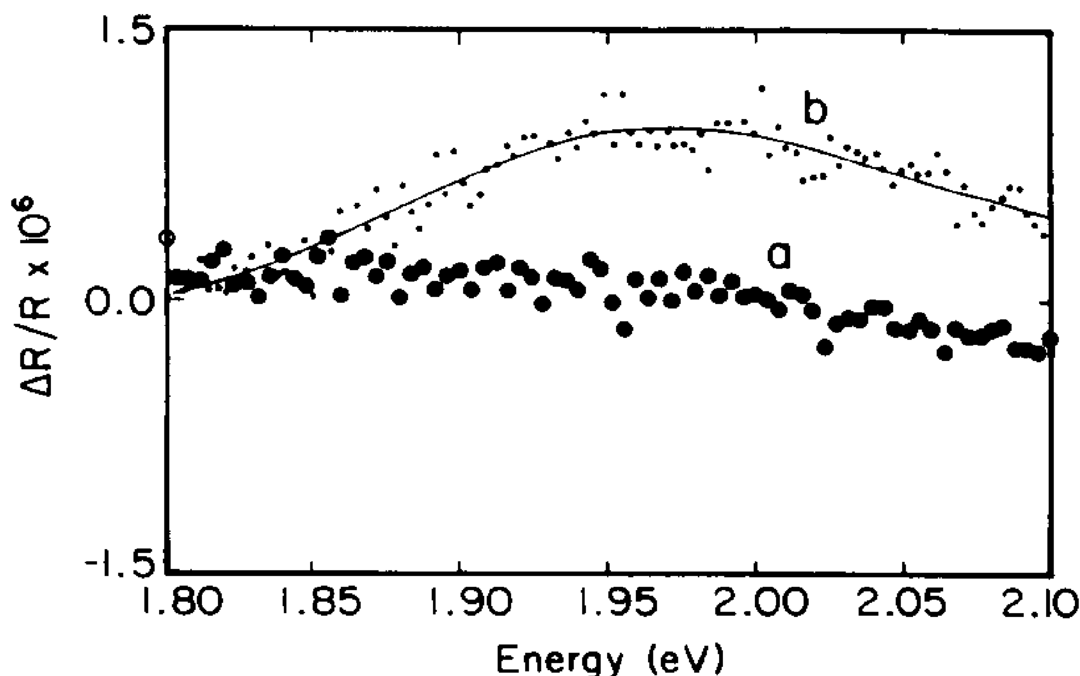

Figure 6.4 Photoreflectance spectra of a) InSe and b) photomodified InSe; in the high energy range, and the theoretical fit (solid line) of the line-shape of the spectrum of the modified InSe. Modulation source -- 4067 Å Kr ion laser; modulation frequency -- 516 Hz. Fitting parameters: E_g = 1.93 eV; Γ = 0.221eV.

meV. From this analysis, the binding energy of the exciton is 42 meV. This is larger than the commonly accepted value (14.5 meV) [163] but is consistent with published results (ΔE_{ex} = 37 meV) [164]. The discrepancy might be due to the dimensionality of the exciton. Godzaev and Sernelius [165] have calculated the binding energies for three-dimensional and two-dimensional excitons for direct and indirect transitions in InSe and obtained the following theoretical values for the direct excitons: $\Delta E_{ex}(3D)$ = 15.1 meV and $\Delta E_{ex}(2D)$ = 59.2 meV. Our value of the binding energy (42 meV) lies in between. This can be interpreted as mixed dimensionality, but is still an open question that requires further research. After modification the binding energy of the exciton is reduced to 31 meV (E_g = 1.234

eV, E_{ex} = 1.203 eV). The reduction of the binding energy may be due to the effects of the strain resulting from the top modified later.

6.1.2 Impedance

Figure 6.5 shows the impedance spectra of unmodified InSe in the electrolyte 1M KI/0.05M I_2/2M H_2SO_4 at the following electrode potentials: a) - 0.1 V vs Pt and b) +0.3 V vs Pt. The spectra under positive and negative potentials have significantly different features. At positive potentials the spectra can be represented in terms of passive (frequency-independent) elements. At negative potentials the imaginary part does not exhibit the -1 slope at the high frequency end and the real and imaginary parts of the impedance are parallel to each other over a few orders of magnitude of frequency; this is characteristic of an apparent constant phase angle (CPA) behavior.

A typical impedance spectrum of a modified InSe electrode in the same electrolyte at a potential of - 0.05 V vs Pt is shown in Fig.6.6. There is no significant difference between positive and negative potentials. The impedance spectra were analyzed using the technique of relaxation spectrum analysis [73,76] and the equivalent circuits are shown in the inserts.

For InSe, the space charge capacitance can be determined only under reverse bias conditions. The Mott-Schottky plot of C_{sc} is shown in Fig.6.7(a). The doping level, evaluated from the slope of the line, is $2.9\times10^{15}/cm^3$ and the flat-band potential, from the intercept, is - 0.33 V vs the solution potential.

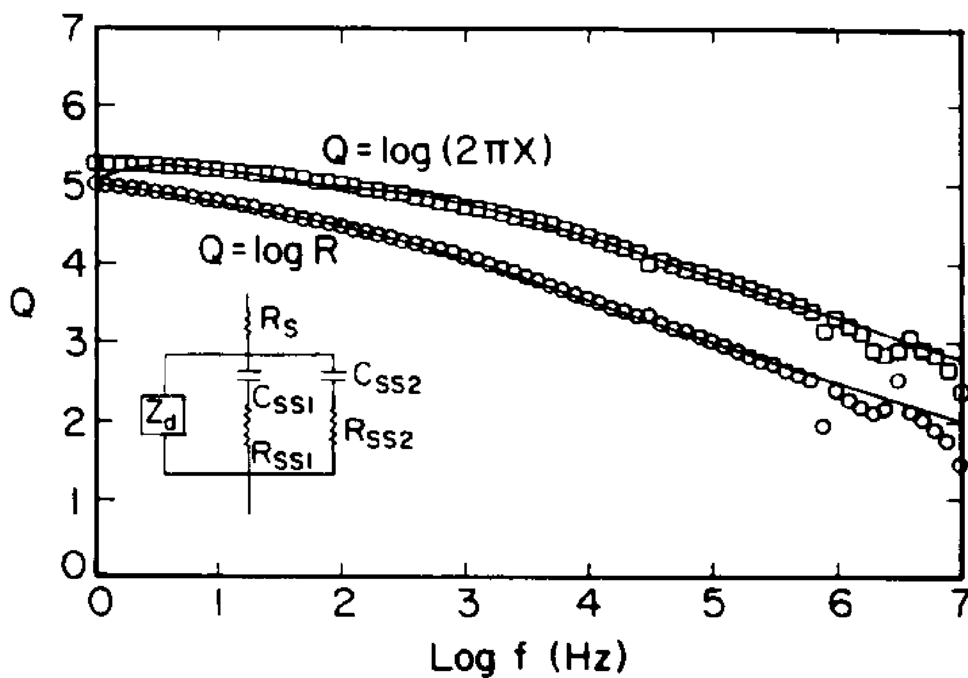

(a)

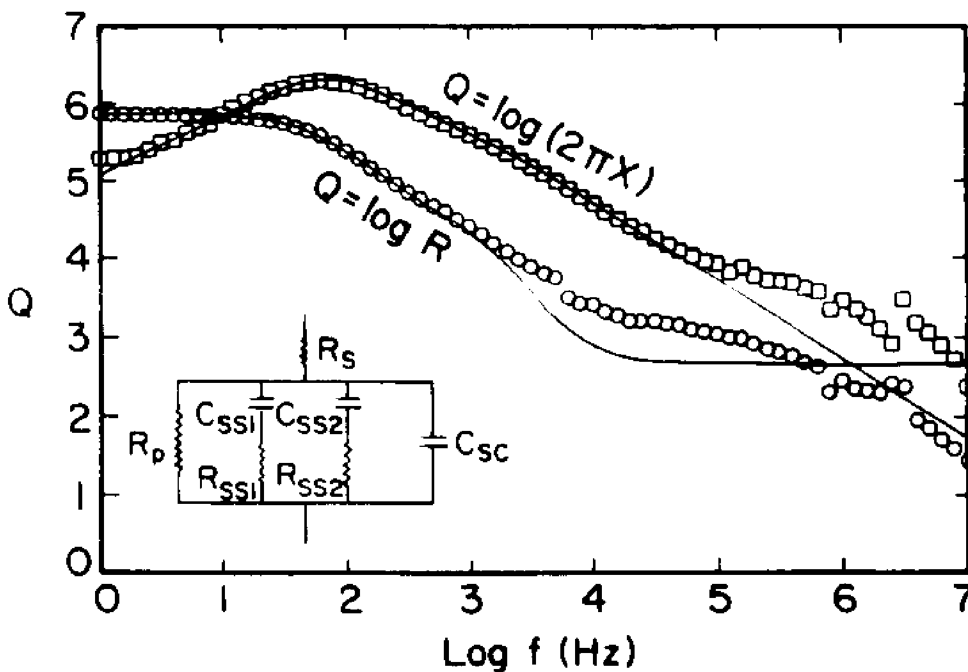

(b)

Figure 6.5 The impedance spectra of n-InSe in the electrolyte: 1M KI/0.05M I_2/2M H_2SO_4 at potential of a) -0.1 V vs Pt, and b) +0.3V vs Pt. Electrode area is 0.12 cm^2. The solid lines are the theoretical fit to the equivalent circuit shown in the insert.

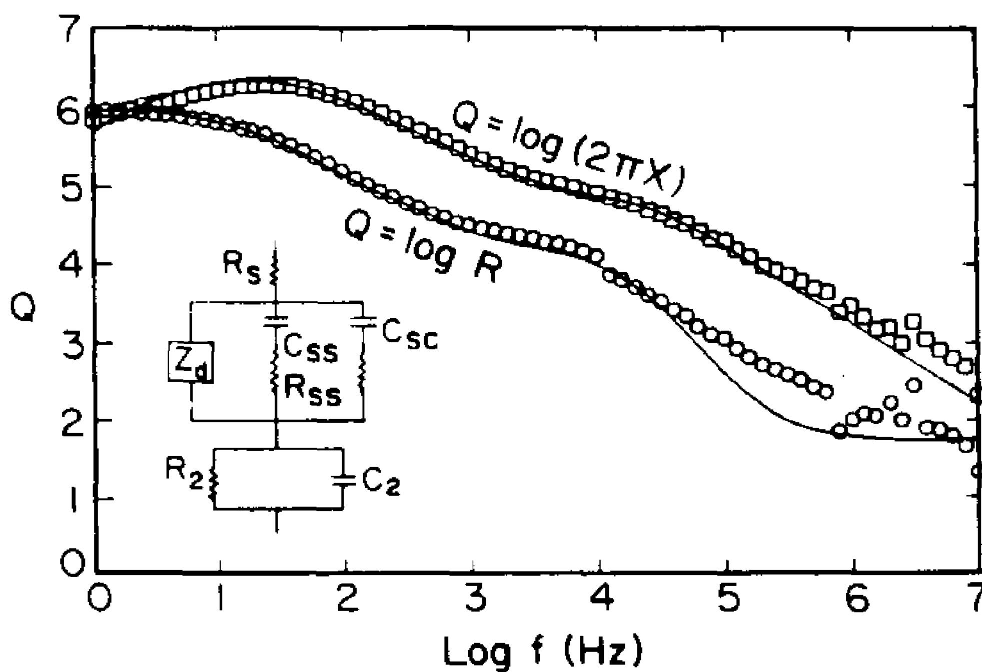

Figure 6.6 The impedance spectra of modified InSe in the same electrolyte as in Fig. 6.5 at potential of -0.05 V vs Pt. Electrode area is 0.257 cm^2. The solid lines are theoretical fits to the equivalent circuit shown in the insert.

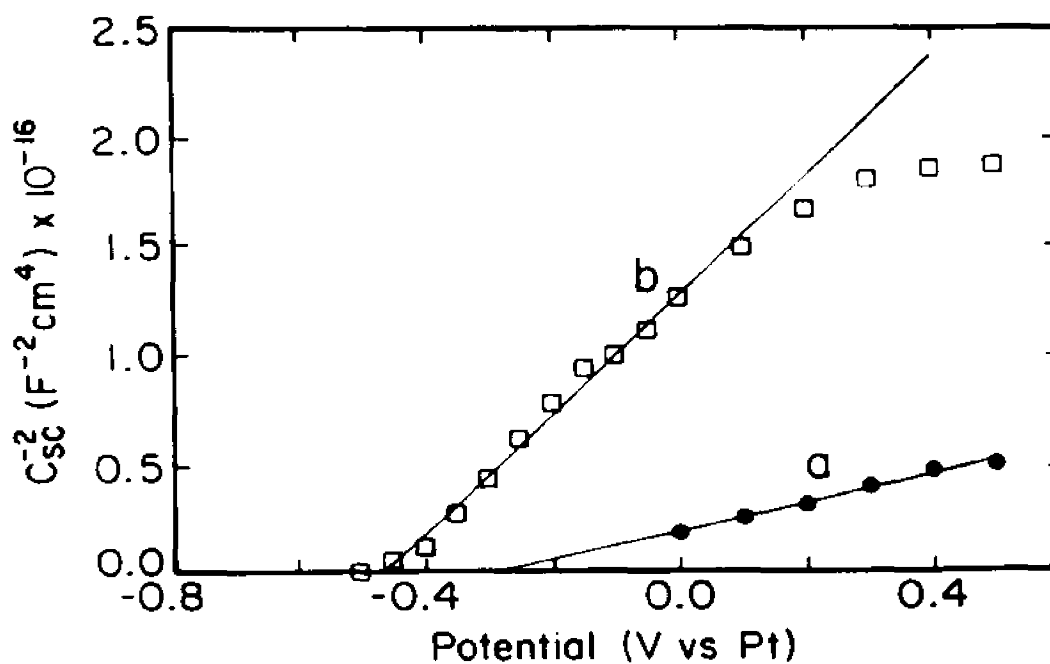

Figure 6.7 Mott-Schottky plots of C_{sc} for a) InSe and b) modified InSe.

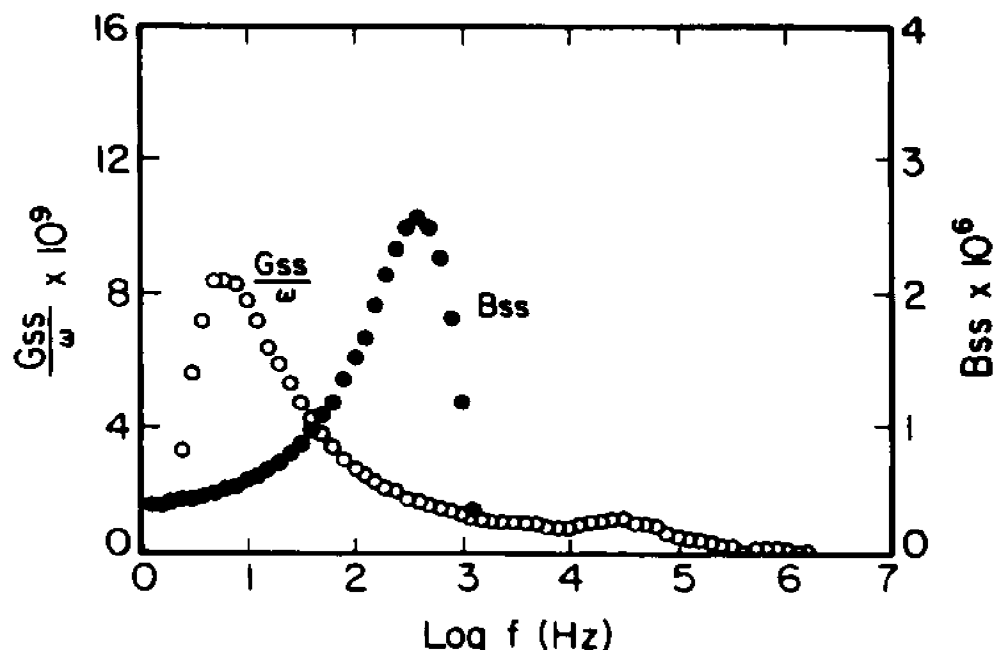

Figure 6.8 G_{ss}/ω and B_{ss} spectra of n-InSe in the same electrolyte as in Fig. 6.5. Electrode potential: 0 V vs Pt. The capacitive and resistive elements of the surface states are evaluated from the amplitude and the position of the peak.

Figure 6.8 shows typical G_{ss}/ω and B_{ss} spectra, from which the C_{ss} and R_{ss} were evaluated [76]. As a result, two surface state elements were assigned, with relaxation time of 1 ms and 10 ms, respectively. The dependence of the surface state capacitances, C_{ss1} and C_{ss2}, on the electrode potential is shown in Figs.6.9 and 6.10. The data were fitted to a Gaussian distribution of surface states [56]. For the fast surface state the distribution is centered on - 0.23 V vs Pt with area density of $1.05\times10^{13}/cm^2$ and width of 0.11 eV. For the slow surface state the distribution is centered on - 0.21 V vs Pt with area density of $3.12\times10^{13}/cm^2$ and width of 0.13 eV. If $10^{15}/cm^2$ is taken as the typical density for a monolayer, both states occupy a small fraction of a monolayer.

The modified InSe could not be represented in terms of a single junction

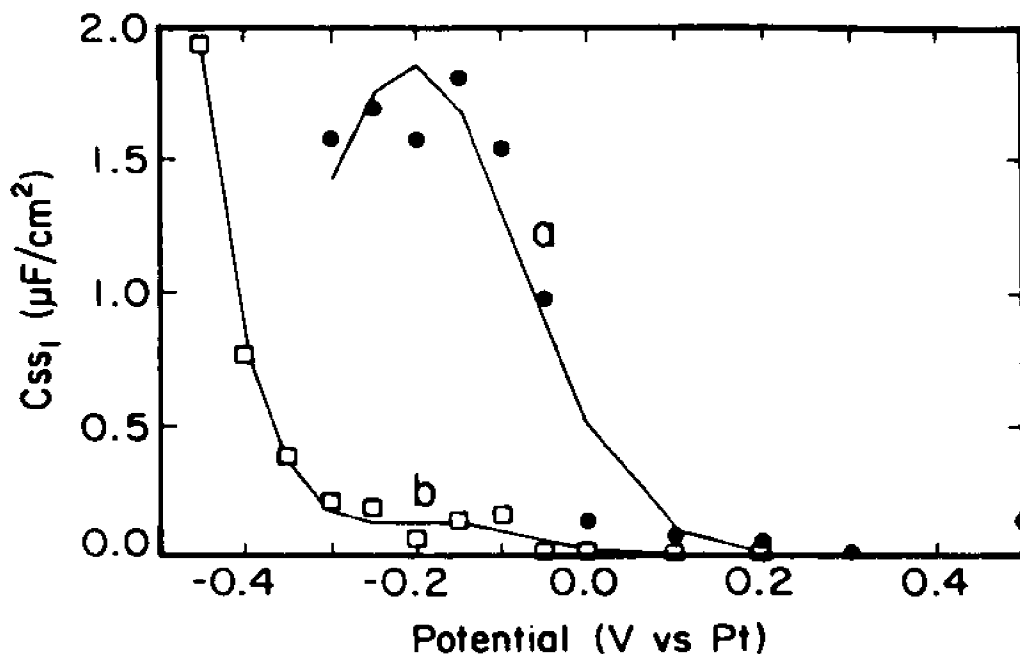

Figure 6.9 Variation of C_{ss1} of the slow surface states, with electrode potential for a) n-InSe and b) modified InSe. The solid lines are theoretical fits to Gaussian line shapes.

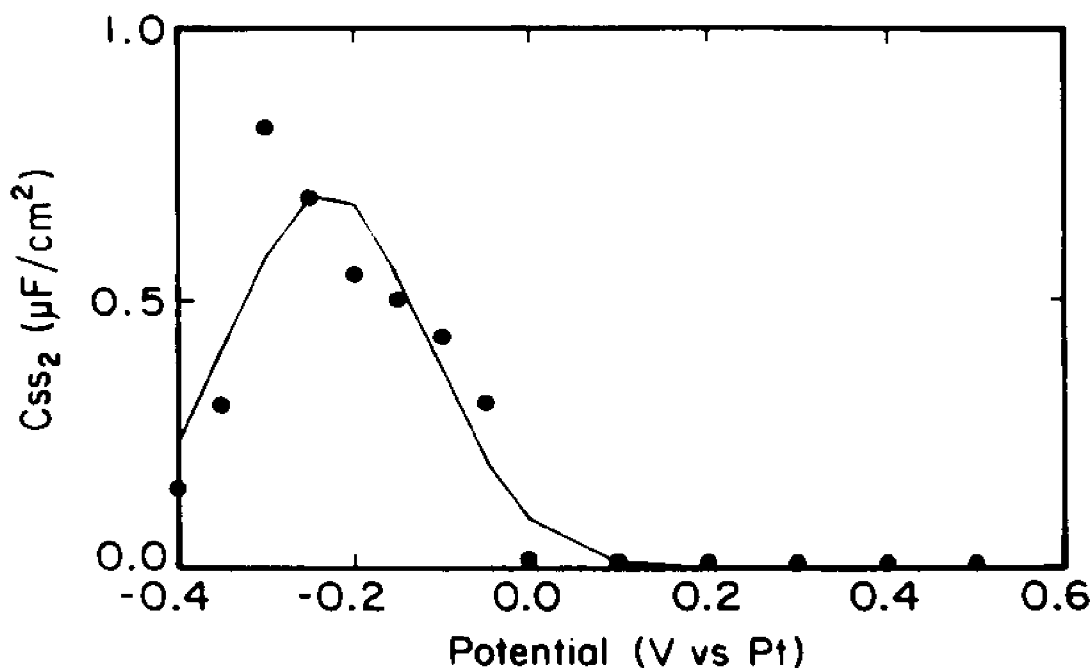

Figure 6.10 Variation of C_{ss2} of the fast surface states, with electrode potential for n-InSe. Fast surface states of the modified InSe electrode were not observed. The solid line is a theoretical fit to a Gaussian line shape.

interface. Following the evidence that was presented for the formation of a $CuISe_3$ top layer, resulted from the modification in the $I^-/I_2/Cu^+/HI$ electrolyte, the modified interface can be described by a circuit element composed of R_2, C_2, connected in series with the space charge layer of InSe (insert of Fig.6.6). A fit procedure was used to find the circuit parameters. As a result, it was found that R_2 and C_2 were almost unaffected by changes in the electrode potential.

After removing the R_2C_2 element from the total impedance, the same procedure, as described for the unmodified InSe, was followed to extract the other parameters of the equivalent circuit. The space charge capacitance of InSe also obeys the Mott-Schottky relationship with doping density of $7.26\times10^{14}/cm^3$ and flat-band potential of - 0.51 V vs Pt [Fig.6.7(b)]. The doping density is reduced to 25% of the unmodified semiconductor, and flat-band potential is shifted by about 0.18 V.

After modification the fast surface state disappears and only the slow surface state remains. The dependence of the capacitive element, which is associated with this state, on electrode potential is shown in Fig.6.9(b). The fit to a Gaussian distribution gives a distribution around - 0.17 V vs Pt with area density of $7.51\times10^{11}/cm^2$ and a width of 0.1 eV. Compared with InSe, this state is distributed around the same potential, with approximately the same width, except that the density is reduced by more than an order of magnitude.

6.2 Discussion

6.2.1 Effects of photo-modification

A. The formation of top layer $CuISe_3$

Comparison of the photoreflectance spectra of InSe with that of modified InSe in the higher energy range 1.8-2.1 eV shows that there is some difference resulting from the modification. The theoretical fit to the broad single peak of modified InSe shows a three-dimensional critical point with E_g = 1.93 eV and Γ = 221 meV. $CuISe_3$ is reported to be a semiconductor with a band gap of 2 eV [166]. This supports the X-ray diffraction result [45] that the top layer is $CuISe_3$, similar to the $CuInSe_2$ case. The broad width is probably associated with the poor semiconducting quality of the film [127]. However, the very low signal-to-noise ratio and the structureless feature introduce much uncertainty in any attempt for further interpretation.

From the capacitance C_2 representing the modified layer and taking $6.6 \leq \varepsilon \leq 10$ for the dielectric constant of $CuISe_3$ [37], the thickness of the $CuISe_3$ top layer was estimated to be between 2 μm and 3 μm. This is consistent with the SEM measured value [45] and the value for the n-$CuInSe_2$ case [37].

B. The reduction of doping density

From the analysis of Mott-Schottky plot of InSe and modified InSe, it is followed that after modification, the flat-band potential is shifted by about - 0.18 V and the doping density is reduced to 25% of the unmodified InSe. The negative shift of the flat-band potential might lead to the observed increase in the open-

circuit voltage [45]. The reduction in the doping density leads to a widening of the space charge layer, allowing most of the incident light to be absorbed well within the space charge layer, thus eliminating the influence of bulk recombination mechanisms. As a result, the photocurrent increases after the modification. It is the similar mechanism to that of $CuInSe_2$ discussed in §5.2.2.

C. Cleaning the interface of trapping centers.

From photoreflectance, it was found that the intensity of the PR signal decreases drastically with the modification time, i.e., with an increase in the thickness of the modified layer. It can be interpreted either in terms of absorption of the pumping beam by the modified layer or in terms of removal of surface states by the modification that, in the absence of an electrolyte, will force the crystal to be pinned at flat-band. To be able to distinguish between these possibilities, A krypton laser line at 6764 Å was used for the pumping beam, which is equivalent to 1.83 eV, below the band-gap of $CuISe_3$. The results, given in Fig.6.3, show that the photoreflectance spectrum did not change. In addition, the same variations of signal intensity with thickness were observed. Since the top film is transparent to a pumping beam with photon energy below its energy gap, it is a strong argument against an interpretation in terms of attenuation of the pumping beam at the top layer, but rather in favor of cleaning of the interface of trapping centers. This conclusion is confirmed further by comparing the surface state density before and after modification from analysis of the impedance data.

The analysis of the impedance data shows that after modification, the fast

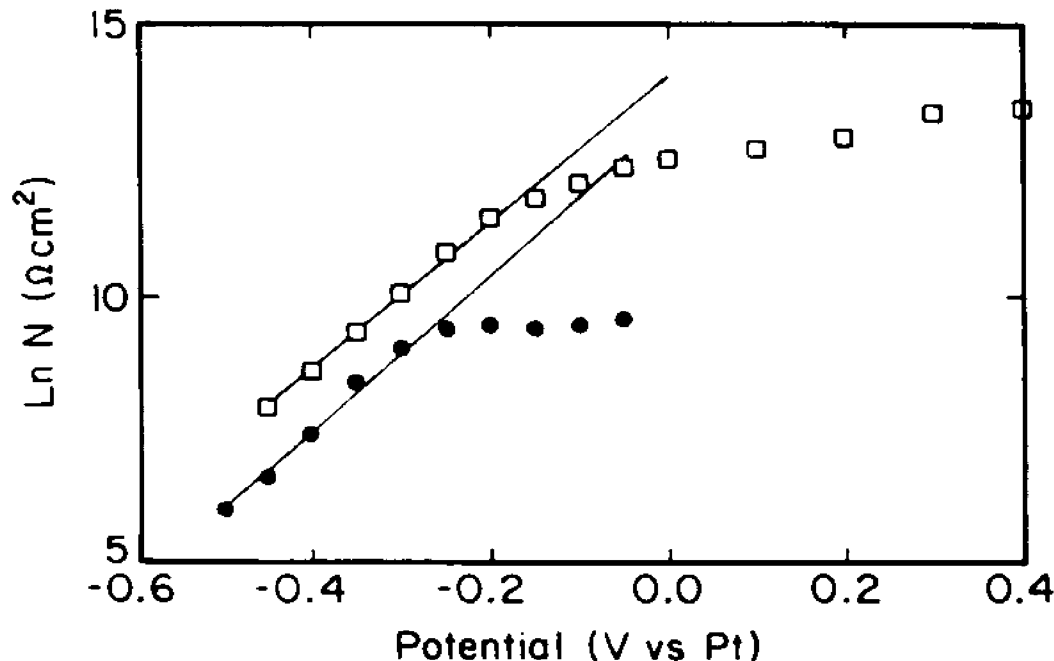

Figure 6.11 Variation of the CPA parameter N with the electrode potential for n-InSe (circles) and modified InSe (squares). The solid lines are the theoretical fits to Eq. (6.3).

surface state with relaxation time of 1 ms is removed and the density of the slow surface state with relaxation time of 10 ms is reduced by more than an order of magnitude. It again suggests that the modified layer acts as a window that cleans the interface of trapping centers.

6.2.2 Origin of the CPA element

In the equivalent circuit of the InSe/electrolyte system, there is a CPA element Z_d. For InSe, n is nearly independent of potential, with values between 0.50 and 0.55. For the modified InSe, n also has a value between 0.45 and 0.55 in forward bias. Figure 6.11 shows that in the forward bias, >0.2 V, there is a linear dependence of ln N on potential for InSe and modified InSe with nearly the same

slope. In forward bias, <0.2 V, and in the reverse bias region, N is almost independent of potential for both InSe and modified InSe.

These similarities of behavior of n and N strongly suggest that the mechanism governing the CPA behavior in the impedance spectra of InSe and modified InSe may be the same. This behavior, the voltage dependence of N and the appearance of this element parallel to the space charge capacitance, excludes contribution from a composite dielectricum at the interface and from diffusion of the electrolyte. The only source that seems to be consistent with these observations is diffusion of the minority carriers [72]. However, we are not aware of any other claim for observing diffusion capacitance in a liquid junction device where the situation seems to be similar to Schottky barriers, which are assumed to be unable to store minority carriers [167]. In calculating the diffusion impedance the abrupt junction approximation for p-n junction [72] was followed, which was modified by incorporating the dependence of the concentration of the minority carriers on the electrode potential in the following form

$$p = p_{no} \exp\left[\frac{e(U - U_{fb})}{m k_B T}\right], \qquad (6.1)$$

where p is the minority carriers' concentration, p_{no} is the equilibrium density of the minority carriers at the field-free regime, k_B is the Boltzmann constant, e is the electron charge, T is the temperature, U is the electrode potential, U_{fb} is the flat-band potential, and "m" is an ideality factor that parameterizes the deviation from abrupt junction. Incorporating Eq.(6.1) into the treatment in §2.1.4 yields the

following expression for the diffusion impedance Z_d

$$Z_d = \frac{mk_BT}{e}\frac{L_p}{eD_pp_{no}}(1+j\omega\tau_p)^{-0.5}\exp\left[\frac{-e(U-U_{fb})}{mk_BT}\right], \qquad (6.2)$$

where L_p, D_p, and τ_p are diffusion length, diffusion coefficient, and lifetime of the minority carriers and ω is the angular frequency.

Incorporating Eq.(2.70) into Eq.(6.2) one obtains

$$N = N_o e^{-\frac{eU}{mk_BT}}, \qquad (6.3)$$

where

$$N_o = \frac{mk_BT}{e}\frac{\tau_p}{eL_pp_{no}}\exp\left(\frac{eU_{fb}}{mk_BT}\right). \qquad (6.4)$$

From the fit parameters, $p_{no}L_p/\tau_p$ was evaluated as 6.3×10^9 $s^{-1}cm^{-2}$ and 4.2×10^8 $s^{-1}cm^{-2}$, respectively, for InSe and modified InSe. If it was taken that L_p = 10 μm and τ_p = 13 μs [168], the density of minority carrier p_{no} will be $8.1\times10^7/cm^3$ and $5.4\times10^6/cm^3$ for InSe and modified InSe, respectively. Values of m were estimated as 2.66 and 2.87, respectively, for the two samples. The values found for p_{no} are higher than expected; the reason might be oversimplifications in the model or differences in the transport parameters compared to those taken from Ref.[168].

6.2.3 Potential distribution of InSe- and modified InSe-polyiodide system

Figures 6.12 (a) and (b) show the potential distribution of InSe/aqueous polyiodide and modified InSe/aqueous polyiodide system. For InSe/aqueous polyiodide system, the flat-band potential is - 0.33 V vs Pt. The energy gap is 1.24 eV. There are two surface states: the fast one with the relaxation time of 1 ms is centered at 0.1 eV below the conduction band and the slow one with the relaxation time of 10 ms at 0.12 eV below the conduction band. Both states occupy about 1% of a monolayer.

After photo-modification, the flat-band potential is shifted to - 0.51 V vs Pt. A layer of $CuISe_3$ with thickness of 2-3 μm is formed on the surface. The fast surface state is removed completely and the density of slow surface state is reduced by more than one order of magnitude. The reduction of doping density to 25% of unmodified InSe makes the width of space charge layer double.

6.2.4 The characteristics of modified layer $CuISe_3$

The implication from the $CuInSe_2$ work [35-39] are that since $CuISe_3$ is a p-type material, the rectifying junction is a solid state n-p junction that derives the charge separation process.

From the analysis of impedance spectra, the semiconducting properties of the modified layer are not confirmed. The equivalent capacitance representing the layer is voltage independent and the layer is characterized as an insulator. The high energy photoreflectance results provide some indications about semiconduct-

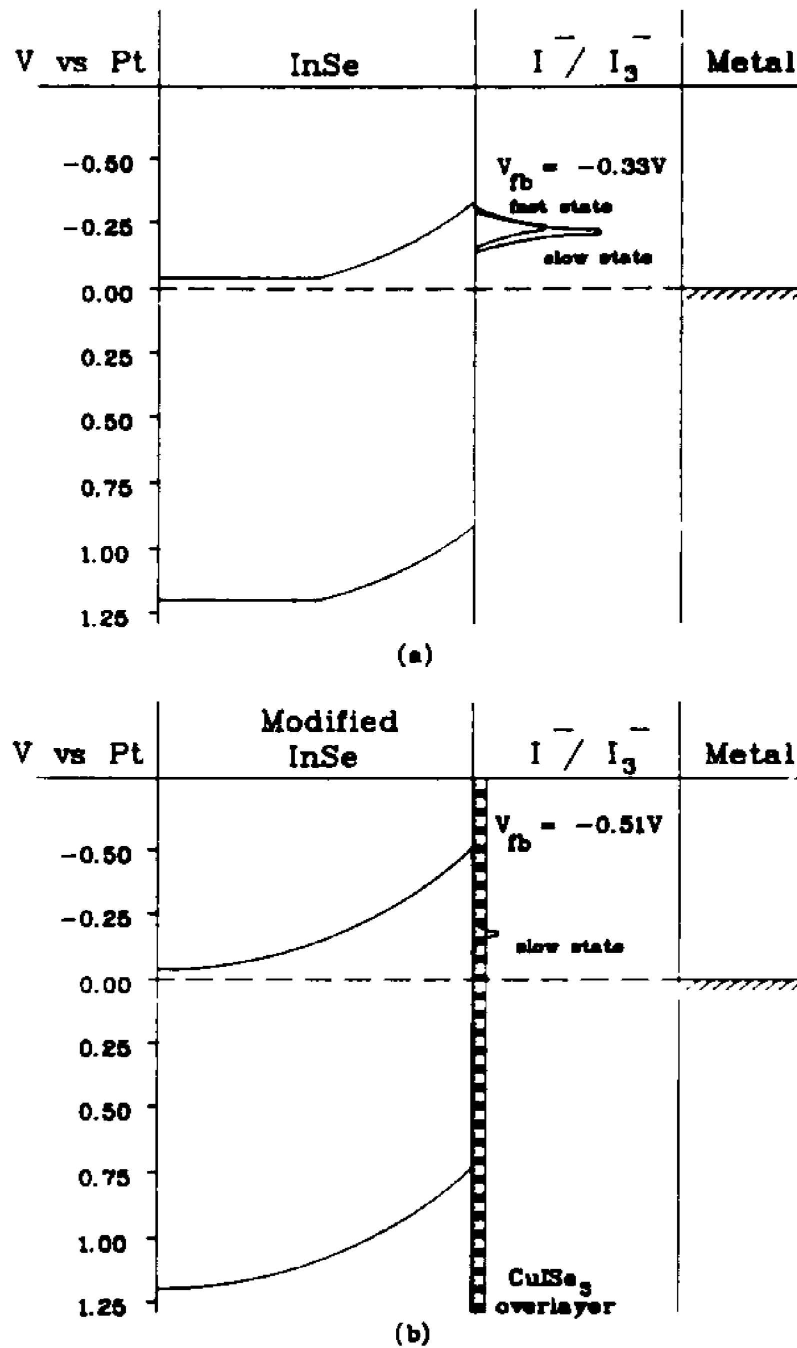

Figure 6.12 The band structure diagrams of n-InSe and modified InSe in polyiodide solution.

ing properties but width of that signal suggests poor electronic transport properties.

Recently, the rectifying junction between n-InSe and modified p-$CuISe_3$ layer is demonstrated by photoresponse and EBIC measurements of InSe/$CuISe_3$-Se°/ metal solid state devices [48]. The EBIC signal is observed only for the junctions corresponding to modified films of 0.4 to 0.7 μm. When the film has a thickness larger than 1μm no EBIC signal is found. It indicates that the interphase film is highly resistive and consistent with the results of impedance spectra. The fact that the quantum yield of n-InSe/p-$CuISe_3$-Se°/polyiodide system at 850 nm is forty times higher than that observed for corresponding solid state devices [48] leads to the suggestion that interphase may be porous. When it is "dry", it is semi-insulating. When it is immersed into the electrolyte, the ionic conductivity of the electrolyte entered into the layer will make contribution and as a result, the photoresponse is improved far more. Of course, the issue is still open and needs more experimental evidence.

A marked difference between the effects of the modified layer of ⊥ n-InSe and that of $CuInSe_2$ is in the stabilization of these systems. The modification appears to result in almost complete stabilization of $CuInSe_2$, while only partial stabilization (a few hours) is observed with ⊥ n-InSe. First, it seems that the mechanism of film synthesis is different, because with $CuInSe_2$ part of the Cu could be provided by the crystal. This may result in the formation of a film that seals defects in the surface efficiently. On the contrary, with InSe this does not seem to be the case. Secondly, the reason for this difference might reside in the

crystal structure. In the layered compounds the photocorrosion, starting at steps, may propagate laterally in the crystal causing delamination of the layers, a process that cannot be competed successfully by the formation of a $CuISe_3$-Se° interphase of sufficient density to stop further penetration of the electrolyte. If this hypothesis is supported by direct experimental verification, it will have an important consequence on the feasibility of stabilizing lamellar compounds by surface modification.

CHAPTER 7

CONCLUSIONS AND FUTURE WORK

7.1 Conclusions

In this study, liquid junctions were used to characterize silicon and silicon subjected to various RIE; $CuInSe_2$ and its surface optimization; and InSe and its photo-modification. Impedance spectroscopy and modulation spectroscopy such as EER, PR, and EPR were the major methodologies that were used for investigating the dielectric properties of the semiconductors and their interface with the ambients. It was shown that the above experimental techniques provide information about the flat-band potential, doping density, Fermi level pinning, the density and distribution of surface states, energy gap and broadening parameter related to the lifetime of majority carriers, etc. The effective medium analysis of the frequency dispersion of the impedance provides the information on the microstructure of the composite at the interface. The analysis of the CPA elements reveals the origin of disorder such as diffusion of minority carriers. The change of the line shape of the modulation spectrum provides a sensitive probe for analyzing the tensile strain, the quality of the crystal, etc. Both techniques can be complementary and cross-checked, which comprise a versatile system of characterization for the dielectric properties of semiconducting materials.

7.1.1 Silicon and silicon subjected to various RIE

The liquid junctions consisting of n-type <100> Si in methanolic solutions of ferrocene derivatives with $LiClO_4$ as the supporting electrolyte have been analyzed by means of a complementary set of impedance spectroscopy, modulation spectroscopy, and current-voltage measurements. The main conclusions out of this analysis are that:

The Fermi level is partially pinned due to surface states at a potential about 0.2 eV below the conduction band and is completely pinned at potentials positive to mid-gap; the surface states are coupled with the oxide layer; HF etching removes oxide layer and reduces the Fermi level pinning.

The effects of various contact media on the photoreflectance of Si were studied. The changes in line shape of PR signal upon introduction of the electrolyte are reversible. These changes are electrolyte dependent, being more pronounced in the methanolic solutions than in the aqueous electrolytes. The methanol itself proved to be the constituent driving these changes. The effect of the electrolyte is interpreted to be due to modifications of the kinetics of equilibration between the surface states and the space-charge layer. This is supported by the frequency dispersion experiments in which it was demonstrated that the presence of the methanolic electrolyte causes a decrease in the relaxation time of the surface states by more than an order of magnitude.

The Fermi level pinning behavior is different for EER and EPR. It may be connected with the different carriers that are responsible for the modulated electric

field in both cases.

The effects of various RIE treatments of Si, including CHF_3/Ar, CF_4, $CClF_3/H_2$, $CClF_3/H_2$ $+O_2$ ash, and O_2 ash, were investigated by modulation spectroscopies (EER, EPR, PR) and impedance spectroscopies. Except for the $CClF_3/H_2$ RIE sample, all RIE samples exhibited poor photoresponse. The most pronounced effect of the RIE treatments on the modulation spectroscopy is the shift of the transition energy and splitting or broadening of the peaks. These spectral changes were interpreted in terms of tensile strain of the order of 1% caused by the surface damage. In all the cases except for $CClF_3/H_2$ RIE, the strain is two dimensional.

CHF_3/Ar and CF_4 RIE show shifts of the flat-band potential, which are associated with the accumulation of positive charges at the semiconductor interface. It means that they introduce an apparent damaged layer into the Si substrate. The CHF_3/Ar RIE results in deeper damage, which cannot be removed by the wet etching.

The thickness of the residue layer and damaged layer resulting from various RIE were estimated. Based on the analysis of the damaged layer and residue layer due to various RIE, the order of the damage is $CHF_3/Ar > CF_4 > CClF_3/H_2$. The residue overlayer on the $CClF_3/H_2$ RIE sample is porous. The O_2 ashing partially recovers the surface damage by removing the implanted charges but is responsible for the formation of an insulating oxide overlayer.

The results on the liquid junction interfaces were compared with that of the

Schottky barrier device and the metal-oxide-semiconductor device configurations. In terms of the sensitivity of the dielectric properties to the RIE treatments, the liquid junction is the most sensitive, followed by SB devices, with the MOS configuration exhibiting the least sensitivity.

7.1.2 $CuInSe_2$ and its surface optimization

Impedance spectroscopy and electrolyte electroreflectance were used to investigate the dielectric properties of the interface between n-$CuInSe_2$ and aqueous polyiodide electrolyte and the improvements in the photoelectrochemical performance due to chemical etching and low temperature oxidation.

The etching removes most of the surface states from the interface such that less than 1% of a monolayer of states remains. Two states were identified: one centered at 0.17 eV below conduction band and one centered at 0.45 eV below conduction band. The flat-band potential of the etching $CuInSe_2$ was - 0.69 V vs Pt, which was unaffected by the oxidation.

The most important effect resulting from the oxidation of the surface were the reduction in the doping level by more than one order of magnitude, which results in the increased width of the space-charge layer on the semiconductor side of the interface.

The fitting of the experimental light-induced current-voltage curve shows two factors to be responsible for the improvements in performance: the reduction in effective doping level and the cleaning of the surface states.

The oxidized layer is porous and insulating. The analysis of the impedance relaxation spectrum through differential effective medium theory shows that the conductivity of the oxide lies in the dividing region between semiconductor and insulator, the porosity is about 20%, and the microstructure of the composite lies between needle and spherical grain. Therefore, the ionic conductivity of the electrolyte plays a role in the n-$CuInSe_2$ photoelectrochemical solar cell with modified interfaces.

7.1.3 InSe and its photo-modification

The photoreflectance and impedance measurements of n-InSe and modified InSe electrodes demonstrate that a modified layer was generated at the surface of a n-InSe electrode, in the presence of copper polyiodide electrolyte under illumination, which is consistent with $CuISe_3$ with an energy gap of 1.93 eV and a thickness of 2-3 μm, which suggests that there is very little difference between the chemistry of the surface modification of $CuInSe_2$ and that of cleaved surface of n-InSe when both are carried in acidic polyiodide solution in the presence of Cu^+ ions under similar conditions. This layer acts as a window that cleans the surface of trapping centers by removing the fast surface state with relaxation time of 1 ms, and reducing the slow surface state with relaxation time of 10 ms by more than an order of magnitude. It is our contention that this is the predominant mechanism for the observed improvements in the photoelectrochemical response. Also, the reduction of the doping density contributes to the improvement in performance.

7.2 Future work

The techniques that were used in this work for in situ characterization of semiconductors, are mainly dielectric and optical, which are macroscopic in nature and highly sensitive to the model adopted for the particular system. The uniqueness of the model is checked by using different macroscopic techniques on an identical system and arriving at a model agreed with all the results quantitatively. The alternative way to establish the relationship of the properties of materials with their structure is to characterize in situ the materials by microscopic measurements. But most of the microscopic techniques such as electron microscopes (SEM, TEM, STEM), electron diffraction techniques (LEED, RHEED), or electron spectroscopies (XPS, UPS, AES) can be operated only in ultra-high vacuum.

Scanning tunneling microscope (STM) is the only method that may be applied to in situ investigate electronic information on a sub-nanometric scale. STM can be used in vacuum, air, and various aqueous and non-aqueous electrochemical environments. It gives us an opportunity to investigate the effect of different media on the density and distribution of surface electronic states. The information provided by STM on surface roughness, surface defects, adsorption and desorption, and their chemical identification will help for building a correct model to explain the results obtained by macroscopic characterization techniques.

One exclusive feature of STM is the possibility to be combined with other techniques. The combination of the STM with surface photovoltage can probe non-equilibrium carrier distribution created by optical excitation of semiconductors with

high spatial resolution. The combination of STM with impedance can probe the charge accumulation and transfer modes on the interface with high spatial resolution. The STM also can be combined with the electrochemical measurements to yield useful information on charge transfer on electrode/electrolyte interface. These combination of in situ micro- and macroscopic measurements could provide greatly insight in the relationship of properties of materials with their structure.

On the other hand, the methodology in this study can be extended to various materials or devices that were not characterized by the techniques used in this work. One of those is the characterization of electrochromic films. The charge carriers in the electrochromic films include electrons and ions. The dielectric behavior of materials with mixed conduction mechanisms is very interesting. To distinguish and separate the contribution of electrons and ions to the macroscopic dielectric and optical properties are challenging topic.

APPENDIX

PUBLICATIONS RELATED TO THE DISSERTATION

1. W.M. Shen, W. Siripala, M. Tomkiewicz, and D. Cahen, "Electrolyte Electroreflectance Study of Surface Optimization of n-$CuInSe_2$ in Photoelectrochemical Solar Cells", J. Electrochem. Soc., **133,** 107-112 (1986).

2. W.M. Shen, M. Tomkiewicz, and D.Cahen, "Impedance Study of Surface Optimization of n-$CuInSe_2$ in Photoelectrochemical Solar Cells", J. Electrochem. Soc., **133,** 112-116 (1986).

3. W.M. Shen, B. Aurian-Blajeni, M. Tomkiewicz, and D. Cahen, "Dielectric Properties of the Interfacial Layer on n-$CuInSe_2$ in Photoelectrochemical Solar Cells", J. Electrochem. Soc., **133,** 930-934 (1986).

4. D. Cahen, Y.W. Chen, R. Noufi, R. Ahrenkiel, R. Matson, M. Tomkiewicz, and W.M. Shen, "n-$CuInSe_2$ Photoelectrochemical Cells", Solar Cells, **16,** 529-548 (1986).
   also:
   D. Cahen, Y.W. Chen, R. Noufi, R. Ahrenkiel, R. Matson, M. Tomkiewicz, and W.M. Shen, "n-$CuInSe_2$ Photoelectrochemical Cells", in 'Copper Indium Diselenide for Photovoltaic Applications' (Materials Science Monographs, **37**), edited by T.J. Coutts, L.L. Kazmerski, and S. Wagner (Elsevier Science Publishers, 1986), pp 529-548.

5. D. Cahen, M. Tomkiewicz, W.M. Shen, and R.J. Matson, "The n-type Copper Indium Selenide (n-$CuInSe_2$) Photoelectrochemical Cells: Solid State or Solid-liquid Junctions?", Proc. 18th IEEE Photovoltaic Spec. Conf., Los Vegas, Oct. 1985, 1665-1670.

6. C. Levy-Clement, D. Sedaries, W.M. Shen, and M. Tomkiewicz, "Modified Photoelectrodes: n-InSe/Copper-Polyiodide Interface", in 'Photoelectrochemistry and Electrosynthesis on Semiconducting Materials", edited by D.S. Ginley, A.J. Nozik, N. Armstrong, K. Honda, A. Fujishima, T. Sakata, and T. Kawai, The Electrochem. Soc. Proc. **88-14** (1987), 250-257.

7. M. Tomkiewicz and W.M. Shen, "System's Approach to Photoelectrochemistry", in 'Photoelectrochemistry and Electrosynthesis on Semiconducting Materials", edited by D.S. Ginley, A.J. Nozik, N. Armstrong, K. Honda, A. Fujishima, T. Sakata, and T. Kawai, The Electrochem. Soc. Proc. **88-14** (1987), 468-476.

8. C. Levy-Clement, D. Sedaries, N. Le Nagard, A. Marbeuf, J. Rioux, M. Neumann-Spallart, C. Godart, W.M. Shen, and M. Tomkiewicz, "Photo-electrochemistry of Lamellar Chalcogenides", Proceedings of the International Colloquim on Layered Compounds, edited by D. Guerard and P. Lagranbe (1988), 305-310.

9. D. Sedaries, C. Levy-Clement, M. Neumann-Spallart, M.A. Ryan, C. Pettenkofer, H.J. Lewerenz, W.M. Shen, M. Tomkiewicz, and A. Jakubowicz, "Investigation of Photo-modified Semiconductor/Electrolyte Interfaces: the Indium Selenide/Copper Iodide Selenide-Selenium/Polyiodide (n-InSe/$CuISe_3$-Se^0/Polyiodide) System", J. Chim. Phys. Phys.-Chim. Biol., **86,** 1265-1276 (1988).

10. M.C.A. Fantini, W.M. Shen, M. Tomkiewicz, and J.P. Gambino, "Liquid Junctions for Characterization of Electronic Materials: I. The Potential Distribution at the Si/Methanol Interface", J. Appl. Phys., **65,** 4884-4890 (1989).

11. W.M. Shen, M.C.A. Fantini, M. Tomkiewicz, and J.P. Gambino, "Liquid Junctions for Characterization of Electronic Materials: II. Photoreflectance and Electroreflectance of n-Si", J. Appl. Phys., **66,** 1759-1764 (1989).

12. W.M. Shen, M.C.A. Fantini, F.H. Pollak, M. Tomkiewicz, H.J. Leary, and J.P. Gambino, "Liquid Junctions for Characterization of Electronic Materials: III. Modulation Spectroscopies of Reactive Ion Etching of Si", J. Appl. Phys., **66,** 1765-1771 (1989).

13. M.C.A. Fantini, W.M. Shen, M. Tomkiewicz, and J.P. Gambino, "Liquid Junctions for Characterization of Electronic Materials: IV. Impedance Spectroscopy of Reactive Ion Etched Si", J. Appl. Phys., **66,** 2148-2155 (1989).

14. M.C.A. Fantini, W.M. Shen, M. Tomkiewicz, and J.P. Gambino, "Liquid Junctions for Characterization of Electronic Materials: V. Comparison with Solid-state Devices Used to Characterize Reactive Ion Etching of Si", J. Appl. Phys., **66,** 4846-4853 (1989).

15. W.M.Shen, M. Tomkiewicz, C. Levy-Clement, and D. Sedaries, "Photo-reflectance and Impedance Study of InSe and Modified InSe", J. Electro-chem. Soc., **137,** 2656-2661 (1990).

BIBLIOGRAPHY

1. S.R. Kurtz and J.M. Olson, Proc. 19th IEEE photovoltaic Spec. Conf., New Orleans, LA, May 4-8, 1987, p. 823.

2. M. Tomkiewicz, Proc. SPIE, **452,** p.120 (1983).

3. E. Bacquerel, C.R., Acad. Sci. Paris, **9,** 561 (1839).

4. W.H. Brattain and C.G.B. Garrett, Bell System Tech. J., **34,** 129 (1955).

5. A. Fujishima and K. Honda, Nature (London), **238,** 37 (1972).

6. A.J. Nozik, Ann. Rev. Phys. Chem., **29,** 189 (1978).

7. H. Gerischer, in 'Solar Energy Conversion', Topics in Appl. Phys., edited by B.O. Seraphin, Vol. **31,** (Berlin Springer Verlag, 1979), p. 115.

8. R.H. Wilson, CRC Crit. Rev. in Solid State and Mater. Sci., **10,** 1 (1980).

9. M. Tomkiewicz and H. Fay, Appl. Phys., **18,** 1 (1979).

10. R. Memming, in 'Topic in Current Chemistry, Vol. **143,** Electrochemistry II',edited by E. Steckhan (Springer-Verlag, Berlin, 1988), p. 79.

11. N.S. Lewis, Ann. Rev. Mater. Sci., **14,** 95 (1984).

12. C.M. Gronet, N.S. Lewis, G. Cogan, and J. Gibbons, Proc. Natl. Acad. Sci. USA, **80,** 1152 (1983).

13. M.L. Rosenbluth, C.M. Lieber, and N.S. Lewis, Appl. Phys. Lett., **45,** 423 (1984).

14. J.F. Gibbons, G.M. Cogan, C.M. Gronet, and N.S. Lewis, Appl. Phys. Lett., **45,** 1095 (1984).

15. M.L. Rosenbluth and N.S. Lewis, J. Am. Chem. Soc., **108,** 4689 (1986).

16. G.S. Oehrlein, Phys. Today, **39,** 1 (October, 1986).

17. S.J. Fonash, Solid State Technol., **28,** 201 (April, 1985).

18. S.W. Pang, Solid State Technol., **27,** 249 (April, 1984).

19. S.M. Pang, Micrcelectron. Eng., **5,** 351 (1986).

20. G.S. Oehrlein, Mater. Sci. Eng., **B4,** 441 (1989).

21. S.J. Fonash, J. Electrochem. Soc., **137,** 3885 (1990).

22 W.S. Chen and R.A. Mickelsen, Proc. SPIE, **248,** 62 (1981).

23. S. Wagner, J.L. Shay, P. Migliorato, and H.M. Kasper, Appl. Phys. Lett., **25,** 434 (1974).

24. D. Haneman, CRC Crit. Rev. in Solid State and Mater. Sci., **14,** 377 (1988).

25. Solar Cells, Special issue on $CuInSe_2$, Vol. **16** (1986).

26. Y. Mirovsky and D. Cahen, Appl. Phys. Lett., **40,** 727 (1982).

27. D. Cahen, Y. Mirovsky, and R. Tenne, in 'Solid State Chemistry, 1982', Studied in Inorganic Chemistry, Vol. **3,** edited by S.R. Metselaar, H.J. Heijligers, and J. Schoonman, (Elsevier, Amsterdam, 1983), p. 173.

28. Y. Mirovsky, G. Djemal, and D. Cahen, Il. Nuovo Cimento, **D2,** 2039 (1983).

29. Y. Mirovsky, R. Tenne, D. Cahen, G. Sawatzky, and M. Polak, J. Electrochem. Soc., **132,** 1070 (1985).

30. D. Cahen, G. Dagan, Y. Mirovsky, G. Hodes, W. Giriat and M. Lubke, ibid., **132,** 1062 (1985).

31. D. Cahen, G. Dagan, G. Hodes, Y. Mirovsky, Y.W. Chen, J.C.W. Folmer, P.J. Ireland, R. Noufi, J.A. Turner, K.J. Bachmann, S. Endo, C. Rincon, G.A. Sawatzky, and M. Tomkiewicz, Prog. Cryst. Growth Charact., **10,** 263 (1985).

32. S. Menezes, H.J. Lewerenz, and K.J. Bachmann, Nature (London), **305,** 615 (1983).

33. K.J. Bachmann, S. Menezes, R. Kotz, M. Fearheily, and H.J. Lewerenz, Surf. Sci., **138,** 475 (1984).

34. S. Menezes and H.J. Lewerenz, J. Electrochem. Soc., **131,** 2462 (1984).

35. S. Menezes, H.J. Lewerenz, G. Betz, K.J. Bachmann, and R. Kotz, J. Electrochem. Soc., **131,** 3030 (1984).

36. S. Menezes, Appl. Phys. Lett., **45,** 148 (1984).

37. H.J. Lewerenz and E.R. Kotz, J. Appl. Phys., **60,** 1430 (1986).

38. S. Menezes, Solar Cells, **16,** 255 (1986).

39. S. Menezes, J. Electrochem. Soc., **134,** 2771 (1987).

40. D. Cahen, Y.W. Chen, P.J. Ireland, R. Noufi, J.A. Turner, K.J. Bachmann, and C. Rincon, Proc. 17th IEEE Photovolt. Spec. Conf., New York (1984), p. 786.

41. D. Cahen and Y.W. Chen, Appl. Phys. Lett., **45,** 746 (1984).

42. D. Cahen, P.J. Ireland, L.L. Kazmerski, and F.A. Thiel, J. Appl. Phys., **57,** 4761 (1985).

43. D. Cahen, Y.W. Chen, R. Noufi, R. Ahrenkiel, R.J. Matson, M. Tomkiewicz, and W.M. Shen, Solar Cells, **16,** 529 (1986).

44. D. Cahen and Y. Mirovsky, J. Phys. Chem., **89,** 2818 (1985).

45. C. Levy-Clement, D. Sedaries, W.M. Shen, and M. Tomkiewicz, in 'Photoelectrochemistry and electrosynthesis on semiconducting materials', edited by D.S. Ginley, A.J. Nozik, N. Armstrong, K. Honda, A. Fujishima, T. Sakata, and T. Kawai eds., The Electrochem. Soc. Proc. **88-14** (1987), p. 250.

46. C. Levy-Clement, in 'Photochemical Energy Conversion', edited by J.R. Norris,Jr., and D. Meisel, Proc. of 7th International Conference on Photochemical Conversion and Storage of Solar Energy, (1988), p. 267.

47. D. Sedaries, C. Levy-Clement, M. Neumann-Spallart, and M. Tomkiewicz, J. Electroanal. Chem., **269,** 283 (1989).

48. D. Sedaries, C. Levy-Clement, M. Neumann-Spallart, M.A. Ryan, C. Pettenkofer, H.J. Lewerenz, W.M. Shen, M. Tomkiewicz, and A. Jakubowicz, J. Chim. Phys. Phys.-Chim. Biol., **86,** 1265 (1988).

49. H. Gerischer, J. Electroanal. Chem. Interfacial Electrochem., **58,** 263 (1975).

50. H. Gerischer, Surf. Sci., **18,** 97 (1969).

51. S.R. Morrison, The Chemical Physics of Surfaces (Plenum, New York,

1977).

52. W.P. Gomes and F. Cardon, Prog. Surf. Sci., **12,** 155 (1982).

53. W.Schottky, Z. Phys., **113,** 367 (1939); **118,** 539 (1942).

54. N.F. Mott, Proc. R. Soc. London, Ser. **A171,** 27 (1939).

55. M. Tomkiewicz, J. Electrochem. Soc., **126,** 1505 (1979).

56. M. Tomkiewicz, Surf. Sci., **101,** 286 (1980).

57. H.J. Hovel, in 'Semiconductors and Semimetals', Vol. **11,** Solar Cells, edited by R.K. Willardson and A.C. Beer (Academic Press, New York, 1975), Chap. 2.

58. W.W. Gartner, Phys. Rev., **116,** 84 (1959).

59. R.H. Wilson, J. Appl. Phys., **48,** 4292 (1977).

60. M.A. Butler, J. Appl. Phys., **48,** 1914 (1977).

61. M. Tomkiewicz, J. Electrochem. Soc., **127,** 1518 (1980).

62. J. Reichman, Appl. Phys. Lett., **36,** 574 (1980).

63. F. El Guibaly, K. Calbow, and B.L. Funt, J. Appl. Phys., **52,** 3480 (1981).

64. F. El Guibaly and K. Calbow, Can. J. Phys., **59,** 1682 (1981).

65. F. El Guibaly and K. Calbow, J. Appl. Phys., **53,** 1737 (1982).

66. S. Chandra, S.L. Singh, and N. Khare, J. Appl. Phys., **59,** 1570 (1986).

67. H. Kobayashi and H. Tsubomura, J. Electroanal. Chem., **272,** 37 (1989).

68. P. Lemasson, J. Crystal Growth, **72,** 405 (1985).

69. D. Guyomard, J. de Chim. Phys., **83,** 355 (1986).

70. J.-N. Chazalviel, Electrochim. Acta, **33,** 461 (1988).

71. M. Tomkiewicz, in 'Photoelectrochemical Solar Cells' edited by K.S.V. Santhanam, and M. Sharon (Elsevier, Amsterdam, 1988), Chap. 3a.

72. S.M. Sze, Physics of Semiconductor Devices, 2nd ed. (Wiley, New York, 1981).

73. M.C.A. Fantini, W.M. Shen, M. Tomkiewicz, and J.P. Gambino, J. Appl. Phys., **65,** 4884 (1989).

74. D.W. Davidson and R.H. Cole, J. Chem. Phys., **19,** 1484 (1951).

75. J.R. Macdonald, Impedance Spectroscopy (Wiley, New York, 1987).

76. M. Tomkiewicz, J. Electrochem. Soc., **126,** 2220 (1979).

77. M. Kramer and M. Tomkiewicz, J. Electrochem. Soc., **131,** 1283 (1984).

78. M. Tomkiewicz and B. Aurian-Blajeni, J. Electrochem. Soc., **135,** 2743 (1988).

79. S.H. Liu, Phys. Rev. Lett., **55,** 529 (1985).

80. W.M. Shen, M. Tomkiewicz, D. Sedaries, and C. Levy-Clement, J. Electrochem. Soc., **137,** 2656 (1990).

81. D.E. Aspnes, J. de Physique, **44,** Supplement au n 12, C10-3 (1983).

82. D.E. Aspnes, J.B. Theeten, and F. Hottier, Phys. Rev., **B20,** 3292 (1979).

83. D.E. Aspnes, Am. J. Phys., **50,** 704 (1982).

84. H.A. Lorentz, Theory of Electrons, 2nd ed. (Teubner, Leipzig, 1916), Chap.4.

85. L. Lorenz, Ann. Phys. Chem. (Leipzig), **11,** 70 (1880).

86. J.C. Maxwell-Garnett, Philos. Trans. R. Soc. London, **203,** 385 (1904); **A205,** 237 (1906).

87. D.A.G. Bruggeman, Ann. Phys. (Leipzig), **24,** 636 (1935).

88. R.W. Cohen, G.D. Code, M.D. Coutts, and B. Abeles, Phys. Rev., **B8,** 3689 (1973).

89. A.N. Norris, P. Sheng, and A.J. Callegari, J. Appl. Phys., **57,** 1990 (1985).

90. P. Sheng and A.J. Callegari, in 'Phys. and Chem. of Porous Medium ',

edited by D.L. Johnson and P.N. Sen, AIP Conf. Proc. No. **107** (AIP, New York, 1984), p. 144.

91. P.N. Sen, C. Scala, and M.H. Cohen, Geophysics, **46,** 781 (1981).

92. M. Cardona, Modulation Spectroscopy (Academic Press, N.Y., 1969).

93. B.O. Seraphin, in 'Semiconductors and Semimetals', Vol. **9,** Modulation Techniques, edited by R.K. Willardson and A.C. Beer (Academic Press, N.Y., 1972), Chap. 1.

94. Y. Hamakawa and T. Nishino, in 'Optical Properties of Solids: New Developments', edited by B.O. Seraphin (North Holland, Amsterdam, 1976), Chap. 6.

95. D.E. Aspnes, in 'Handbook of Semiconductors', edited by M. Balkanski, Vol. **2** (North Holland, Amsterdam, 1980), Chap. 4A.

96. F.H. Pollak, Proc. SPIE, **276,** 142 (1981).

97. F. Bassani and G.P. Parravicini, Electronic States and Optical Transitions in Solids (Pergamon Press, Oxford 1975), Chap. 5.

98. D.E. Aspnes, J. Opt. Soc. Am., **63,** 1380 (1973).

99. B.O. Seraphin and N. Bottka, Phys. Rev., **139,** A560 (1965).

100. F.H. Pollak and O.J. Glembocki, Proc. SPIE, **946,** 2 (1988).

101. F.H. Pollak, in 'Photoelectrochemistry: Fundamental Processes and Measurement Techniques', edited by W.L. Wallace, A.J. Nozik, S.K. Deb, and R.H. Wilson, Softbound Proceedings Series, (The Electrochemical Society, Pennington, N.J. 1982), p. 608.

102. R. Glosser and N. Bottka, Proc. SPIE, **794,** 88 (1987).

103. N. Bottka, D.K. Gaskill, R.S. Sillmon, R. Henry, and R. Glosser, J. Electron. Mater., **17,** 161 (1988).

104. B. Pettinger, H.R. Schoppel, T. Yokoyama, and H. Gerischer, Ber. Bunges. Phys. Chem., **78,** 1024 (1974).

105. V.A. Myamlin and Y.V. Pleskov, Electrochemistry of Semiconductors (Plenum Press, New York, 1967), Chap. 1.

106. M. Tomkiewicz, W. Siripara, and R. Tenne, J. Electrochem. Soc., **131,** 736 (1984).

107. H. Shen, Z. Hang, S.H. Pan, F.H. Pollak, and J.M. Woodall, Appl. Phys. Lett., **52,** 2058 (1988).

108. W.M. Shen, M.C.A. Fantini, M. Tomkiewicz, and J.P. Gambino, J. Appl. Phys., **66,** 1759 (1989).

109. M. Tomkiewicz and W.M. Shen, in 'Photoelectrochemistry and Electrosynthesis on Semiconducting Materials', edited by D.S. Ginley, A.J. Nozik, N. Armstrong, K. Honda, A. Fujishima, T. Sakata, and T. Kawai, The Electrochem. Soc. Proc. **88-14** (1987), p. 468.

110. H. Shen, P. Parayanthal, Y.F. Liu, and F.H. Pollak, Rev. Sci. Inst., **58,** 1429 (1987).

111. W.M. Shen, M.C.A. Fantini, F.H. Pollak, M. Tomkiewicz, H.J. Leary, and J.P. Gambino, J. Appl. Phys., **66,** 1765 (1989).

112. M.C.A. Fantini, W.M. Shen, M. Tomkiewicz, and J.P. Gambino, J. Appl. Phys., **66,** 2148 (1989).

113. M.C.A. Fantini, W.M.Shen, M. Tomkiewicz, and J.P. Gambino, J. Appl. Phys., **66,** 4846 (1989).

114. W.M.R. Divigalpitiya, S.R. Morrison, G. Vercruysse, A. Praet, and W.P. Gomes, Solar Energy Mater., **15,** 141 (1987).

115. W.M. Shen, W. Siripara, M. Tomkiewicz, and D. Cahen, J. Electrochem. Soc., **133,** 107 (1986).

116. W.M. Shen, M. Tomkiewicz, and D. Cahen, J. Electrochem. Soc., **133,** 112 (1986).

117. W.M. Shen, B. Aurian-Blajeni, M. Tomkiewicz, and D. Cahen, J. Electrochem. Soc., **133,** 930 (1986).

118. C. Rincon, J. Gonzalez, and G. Sanchez Perez, Phys. Status Solidi, **B108,** K19 (1981).

119. K.J. Bachmann, M. Fearheiley, Y.H. Shing, and N. Tran, Appl. Phys. Lett., **44,** 407 (1984).

120. See, for example, M. Cardona, K.L. Shaklee, and F.H. Pollak, Phys. Rev., **154,** 696 (1967).

121. See, for example, K. Kondo, and A. Moritani, Phys. Rev., **B14,** 1577 (1976).

122. H. Gerischer, in 'Faraday Discussion of The Chemical Society', No. **70,** Photoelectrochemistry (1980), p. 98.

123. R.P. Silberstein, F.H. Pollak, J.K. Lyden, and M. Tomkiewicz, Phys. Rev., **B24,** 7397 (1981).

124. J.W. Fanst,Jr. and E.D. Palik, J. Electrochem. Soc., **130,** 1413 (1983).

125. J.L. Vossen and W. Kern, in Thin Film Processes (Academic, New York, 1978), Chap. V.

126. K. Kondo and A. Moritoni, Phys. Rev., **B15,** 812 (1977).

127. P.M. Raccah, J.W. Garland, Z. Zhang, U. Lee, D.Z. Xue, L.L. Abels, S. Ugur, and W. Wilinsky, Phys. Rev. Lett., **53,** 1958 (1984).

128. J.W. Garland, H. Abad, M. Viccaro, and P.M. Raccah, Appl. Phys. Lett., **52,** 1176 (1988).

129. O.J. Glembocki, B.V. Shanabrook, and W.T. Beard, Surf. Sci., **174,** 206 (1986).

130. F.H. Pollak and G.W. Rubloff, Phys. Rev. Lett., **29,** 789 (1972).

131. X.C. Mu, S.J. Fonash, G.S. Oehrlein, S.N. Chakravarti, C. Parks, and J. Keller, J. Appl. Phys., **59,** 2958 (1986).

132. D.E. Aspnes and A.A. Studna, Phys. Rev., **B27,** 985 (1983).

133. See, for example, S.M. Sze, in 'Physics of Semiconductor Devices', 2nd ed. (Wiley, New York, 1981), p. 750.

134. X.C. Mu, S.J. Fonash, A. Rohatgi, and J. Rieger, Appl. Phys. Lett., **48,** 1147 (1986).

135. A.Rohatgi, P. Rai-Choudhury, S.J. Fonash, P. Lester, R. Singh, P.J. Caplan, and E.H. Poindexter, J. Electrochem. Soc., **133,** 408 (1986).

136. G.S. Oehrlein, G.J. Scilla, and S.J. Jeng, Appl. Phys. Lett., **52,** 907 (1988).

137. G.S. Oehrlein, J. Appl. Phys., **59,** 3053 (1986).

138. G.S. Oehrlein, R.M. Tromp, J.C. Tsang, Y.H. Lee, and E.J. Petrillo, J. Electrochem. Soc., **132,** 1441 (1985).

139. W. Kern and C.A. Deckert, in 'Thin Film Process', edited by J.L. Vossen and W. Kern (Academic, New York, 1978), Chap. V-1.

140. E.D. Palik, J.W. Faust,Jr., H.F. Gray, and R.F. Greene, J. Electrochem. Soc., **129,** 2051 (1982).

141. O.J. Glembocki, R.E. Stahlbush, and M. Tomkiewicz, J. Electrochem. Soc., **132,** 145 (1985).

142. R. Stander, in Materials Research Corporation-Reactive Ion Etching Systems, Sec. 9 of the Basics of Plasma Etching, Technical Report.

143. A.M. Goodman, J. Appl. Phys., **34,** 329 (1963).

144. H. Matsumoto and T. Sugano, J. Electrochem. Soc., **129,** 2823 (1982).

145. T. Hattori and T. Nishina, Surf. Sci., **86,** 555 (1979).

146. T. Hattori and T.Suzuki, Appl. Phys. Lett., **43,** 470 (1983).

147. T. Suzuki, M. Muto, M. Hara, K. Yamabe, and T. Hattori, Jpn. J. Appl. Phys., **25,** 544 (1986).

148. H. Yamagishi, N. Koike, K. Imai, K. Yamabe, and T. Hattori, Jpn. J. Appl. Phys., **27,** L1398 (1988).

149. T. Hattori, Extended Abstracts of the 20th (1988 International) Conference on Solid State Devices and Materials, Tokyo, Japan (1988).

150. K. Sakamoto, J. Appl. Phys., **61,** 1553 (1987).

151. J.L. Shay, B. Tell, H.M. Kasper, and L.M. Schiavone, Phys. Rev., **B7,** 4485 (1973).

152. D.E. Aspnes, Surf. Sci., **37,** 418 (1973).

153. M. Hepel and M. Tomkiewicz, J. Electrochem.Soc., **132,** 32 (1984).

154. P.W. Li, R.A. Anderson, and R.H. Plovnick, J. Phys. Chem. Solids, **40,** 333

(1979).

155. D. Cahen, M. Tomkiewicz, W.M. Shen, and R.J. Matson, Proc. 18th IEEE Photovoltaic Spec. Conf., Los Vegas, Oct. 1985, p. 1665.

156. F. Abou-Elfotouh, D.J. Dunlavy, D. Cahen, R. Noufi, L.L. Kazmerski, and K.J. Bachmann, Prog. Cryst. Growth Charact., **10,** 365 (1985).

157. W. Horig, H. Neumann, H. Sobotta, B. Schumann, and G. Kuhn, Thin Solid Films, **48,** 67 (1978).

158. A. Raza, O.P. Agnihotri, and B.K. Gupta, J. Phys. D, **10,** 1871 (1977).

159. A.A. Studna and G.J. Gualtieri, Appl. Phys. Lett., **39,** 965 (1981).

160. P.N. Sen, W.C. Chew, and D. Wilkinson, in 'Phys. and Chem. of Porous Medium', edited by D.L. Johnson and P.N. Sen, AIP Conf. Proc. No. **107** (AIP, New York, 1984), p. 52.

161. CRC Handbook of Chemistry and Physics, 58th ed., R.C. Weast, editor, CRC press, Inc. (1977-1978).

162. C. Levy-Clement, D. Sedaries, J. Rioux, and M. Tomkiewicz, 6th ICPS Conf. Proc., Abs. C-33 (1986).

163. J. Camassel, P. Merle, and H. Mathieu, Phys. Rev., **B17,** 4718 (1978).

164. M.V. Andriyashik, M.Yu. Sakhnovskii, V.B. Timofeev, and A.S. Yakimova, Phys. Status Solidi, **28,** 277 (1968).

165. M.O. Godzaev and B.E. Sernelius, Phys. Rev., **B33,** 8568 (1986).

166. A. Rabenau and H. Rau, Solid State Commun., **7,** 1281 (1969).

167. See, for example, R.H. Rhoderick, in 'Metal-Semiconductor Contacts' (Clarendon Press, Oxford, 1980).

168. M. Di Giulio, G. Micocci, A. Rizzo, and A. Tepore, J. Appl. Phys., **54,** 5839 (1983).